Fractional Flux Quanta in High-T$_c$/Low-T$_c$ Superconducting Structures

Ph.D. committee

Chairman	
prof. dr. G. van der Steenhoven	University of Twente
Secretary	
prof. dr. G. van der Steenhoven	University of Twente
Supervisor	
prof. dr. ir. J.W.M. Hilgenkamp	University of Twente
Members	
prof. dr. C.C. Tsuei	IBM T.J. Watson Research Center
prof. dr. ir. J.E. Mooij	Delft University of Technology
prof. dr. K.J. Boller	University of Twente
prof. dr. ir. H.J.W. Zandvliet	University of Twente
dr. ir. W.G. van der Wiel	MESA$^+$ Institute for Nanotechnology

Cover
Front: scanning SQUID microscopy images of 0- and π-rings containing no flux or one fractional flux quantum, respectively. Stripe: optical micrograph of an RSFQ circuit containing a π-ring-based toggle flip-flop. Back: scanning SQUID microscopy image of two antiferromagnetically coupled fractional flux quanta in a double corner junction. The illustrations correspond to figures 5.5(c), 6.3(b) and 7.4(c), respectively.

The research described in this thesis was performed in the Faculty of Science and Technology and the MESA$^+$ Institute for Nanotechnology at the University of Twente, in collaboration with the IBM T.J. Watson Research Center in Yorktown Heights (USA) and the Technische Universität Ilmenau (Germany). This work is part of the research programme of the Dutch Foundation for Fundamental Research on Matter (FOM), which is financially supported by the Netherlands Organization for Scientific Research (NWO). Additional support was provided by the European Science Foundation (ESF) PiShift programme and the NanoNed programme of the Dutch Technology Foundation (STW).

Fractional Flux Quanta in High-T$_c$/Low-T$_c$ Superconducting Structures
Ph.D. Thesis, University of Twente
Printed by Gildeprint Drukkerijen
ISBN 978-90-9024316-0

FRACTIONAL FLUX QUANTA IN HIGH-T_C/LOW-T_C SUPERCONDUCTING STRUCTURES

PROEFSCHRIFT

ter verkrijging van
de graad van doctor aan de Universiteit Twente,
op gezag van de rector magnificus,
prof. dr. H. Brinksma
volgens besluit van het College voor Promoties
in het openbaar te verdedigen
op donderdag 25 juni om 15:00 uur

door

Cornelis Johannes Maria Verwijs

geboren op 27 januari 1979
te Roosendaal en Nispen

Dit proefschrift is goedgekeurd door de promotor:

Prof. dr. ir. J.W.M. Hilgenkamp

dubium sapientiae initium
(doubt is the origin of wisdom)

René Descartes (1596-1650)

Contents

Chapter 1

Introduction

Superconductors can be divided roughly in two classes: the high-critical temperature (T_c) superconductors and the low-T_c superconductors. Ironically, the superconductors that require more sophisticated cooling mechanisms such as helium liquefaction were discovered first in 1911 [1–3], while superconductors that can be cooled simply by immersion in liquid nitrogen were only discovered a little over 20 years ago [4]. This can be attributed to the higher complexity of the high-T_c superconductors which can only be artificially fabricated. The difference between high- and low temperature superconductors is not merely restricted to a different transition temperature, however. The physical properties of these two classes are fundamentally different. In fact, whereas the theory of low-temperature superconductors has more or less matured since the introduction of the BCS theory in 1957 [5], the mechanism of superconductivity in the high-T_c superconductors has still not been unravelled.

Given the different nature of the two superconducting classes, the question arises what would happen when these superconductors are brought into contact. It turns out that this leads to remarkable physics, as is illustrated in figure 1.1. In figures 1.1(a) and 1.1(b) the schematics of two rings, consisting partly of a high-T_c superconductor (shown in red) and partly of a low-T_c superconductor (shown in blue) are depicted, where we implicitly assume that the high-T_c superconductor has a d-wave pairing symmetry and the low-T_c superconductor an s-wave symmetry. The contacts between these superconductors (shown in yellow) are so-called Josephson junctions. The only difference between the two rings is the position where the connection between the different materials is made. When we cool these rings down below their transition temperatures, an interesting phenomenon occurs, which can be observed in figures 1.1(c) and 1.1(d), where the magnetic field just above the ring is superimposed on the schematics of the respective rings (the magnetic fields shown are in fact real data sets obtained from the samples discussed in chapter 5). In the absence of any external magnetic fields or currents one of the rings clearly shows a magnetic field, which is absent in the other ring. This magnetic flux is caused by a circulating current which has started to flow spontaneously in the ring and its magnitude corresponds exactly to half of a magnetic flux quantum (one flux quantum $\Phi_0 = 2.07 \cdot 10^{-15}$ Wb).

The spontaneously generated half-integer flux quantum is the macroscopic manifestation of the quantum mechanical wavefunction which can be used to describe the quantum processes that take place in the superconductors, and can not be explained classically. It arises due to a mismatch in the order parameter symmetries of the isotropic low-T_c

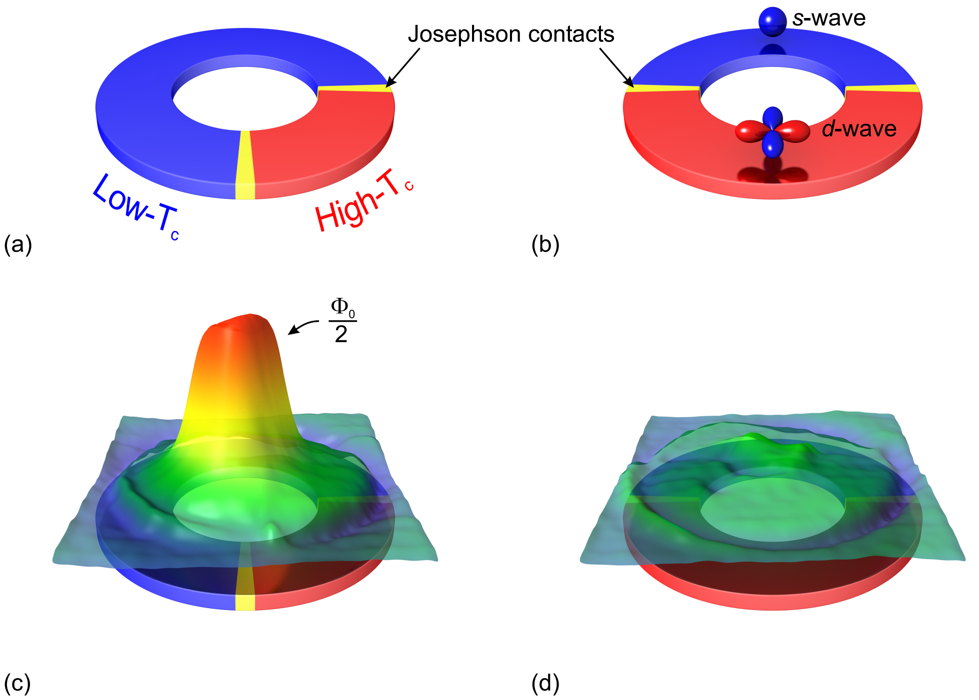

Figure 1.1: (a)-(b) Schematic of a ring connecting a high-T_c superconductor to a low-T_c superconductor in two different geometries. (c)-(d) Magnetic field profile superimposed on the ring schematics. One of the rings displays a spontaneously generated half-integer flux quantum.

superconductor and the high-T_c superconductor which was assumed to have a d-wave symmetry, i.e. a phase difference π occurs for orthogonal directions in k-space. This property is exploited in the ring of figure 1.1(a) and as a result the phase of the wavefunction, when going around the ring, picks up an extra phase π compared to, for example, the ring in figure 1.1(b). The single-valuedness of the superconducting wavefunction dictates that this phase difference needs to be compensated for, which, provided the inductance of the ring is large enough, is realized through the generation of a half-integer flux quantum. The phenomenon of spontaneously generated half-integer magnetic flux quanta in structures combining superconductors with conventional and unconventional pairing symmetries was first recognized by Geshkenbein, Larkin and Barone [6, 7].

This thesis focuses on the spontaneously generated flux in $YBa_2Cu_3O_{7-\delta}$/Nb hybrid superconducting structures. Strictly speaking, as will be discussed in section 2.10, the spontaneously generated flux in such structures will only correspond to a half-integer flux quantum in the large inductance limit; the half-integer flux quanta will not be fully formed for smaller inductances. Keeping this in mind, the terms 'half-integer' and 'fractional' will be used more or less interchangeably throughout this thesis. We will present experiments where the fractional flux quanta are used for a fundamental study of the order parameter symmetry in the cuprate superconductor $YBa_2Cu_3O_{7-\delta}$ (YBCO) as well as for the realization of a novel logic circuit element in superconducting digital electronics. Experiments have been performed using superconducting π-rings as described in the above, in and so-called corner junctions, where the spontaneous flux is generated at a d-wave-induced discontinuity point in a long Josephson junction.

The outline of the thesis is as follows: in chapter 2 a brief introduction is given to superconducting loops containing Josephson junctions. After a brief historical introduction to superconductivity several key aspects that are of importance to our experiments, such as fluxoid quantization and the Josephson effect, are presented. The DC SQUID, which was used as a magnetic field sensor in most experiments described in this thesis, will also be discussed here. The chapter closes with a description of the effect of intrinsic π-phase shifts in superconducting Josephson loops and the formation of fractional flux quanta in such structures.

Chapter 3 is concerned with the actual realization of π-phase shifts through the unconventional order parameter symmetry of YBCO. First, the well-known spherical harmonics are used to describe the order parameter symmetry in three dimensions. Then the two-dimensional projections are discussed as well as a few considerations with respect to conventions in current-day literature. Finally, it is shown how the superconductors YBCO and niobium can be combined in order to obtain the desired half-flux quantum effect.

In chapter 4 the experimental realization of the YBCO/Nb ramp-type Josephson structures is discussed. YBCO is a member of the so-called *cuprate* superconductors, in which superconductivity is believed to occur in the copper-oxygen planes. The superconducting properties of YBCO depend crucially on the crystal growth and are highly sensitive to oxygen deficiencies. Considerations associated with the material properties of YBCO and Nb are discussed as well as the processing steps required for reliable and reproducible Josephson contacts between the two superconductors.

Chapter 5 is concerned with the angle-resolved determination of the YBCO pairing symmetry. In these experiments scanning SQUID microscopy was performed on an array of YBCO/Nb rings with one of the junction angles varying. With these phase-sensitive experiments a quantitative analysis of the s-wave admixture to the predominantly d-wave order parameter symmetry in YBCO as well as an upper bound to possible complex admixtures is given.

Chapter 6 deals with the integration of π-rings in a novel logic circuit element for digital superconducting electronics. First several general concepts of rapid single flux quantum technology (RSFQ) are presented, followed by the design of an RSFQ test circuit containing a toggle flip-flop based on d-wave-induced spontaneously generated half-integer flux quanta. The correct operation of this device was experimentally determined and will be presented.

Chapter 7 is concerned with the on-chip manipulation and detection of half-integer flux quanta in double corner junctions. In the ground state these corner junctions are characterized by two antiferromagnetically coupled half-integer magnetic flux quanta. The sine-Gordon equation is used to describe these junctions and the phase- magnetic flux- and current-profiles are derived analytically for both the single and the double corner junction. The predicted response to a transport current is discussed. In conclusion, the experimental observation of a controlled toggling between the two ground states in the double corner junctions is presented.

Chapter 2

Superconducting loops containing Josephson junctions

2.1 Introduction

Spontaneously generated flux in superconducting loops containing Josephson junctions and an intrinsic π-phase shift (π-rings) form the basis of this thesis. The objective of this chapter is discuss why these loops act as they do and to place them in a proper context. After a brief discussion of superconductivity in general, one of its most striking properties, fluxoid quantization, will be presented. Fluxoid quantization stands at the heart of all superconducting interferometers, of which the DC SQUID will briefly be reviewed. Along the way, the Josephson junction will be introduced, as well as its analogy to a pendulum in the RCSJ model. With the discussion of the effect of π-phase shifts all elements for a proper understanding of π-rings have been presented. How these π-phase shifts are physically implemented will be left for later chapters.

2.2 Superconductivity

In 1908 the Dutch physicist Heike Kamerling Onnes managed the first successful liquefaction of helium at the Physical Laboratory in Leiden (which would later be named after him and still bears his name to this day) [8]. This achievement enabled the Leiden group to enter an until then unexplored temperature regime down to the boiling point of liquid helium (4.2 K at standard pressure). By reducing the pressure on the helium bath the base temperature could even be lowered further down to approximately 1.5 K. Resistivity measurements were performed on different metals in this regime to gain insight into the low temperature behavior of metals which was at that time heavily debated.

Only three years later, in 1913, Kamerlingh Onnes and his assistant Gilles Holst discovered that the resistance of solid mercury suddenly drops to zero when it is cooled below its critical temperature T_c of 4.2 K [1–3]. Though it was Holst who performed the actual measurement, usually only Kamerlingh Onnes is credited for the discovery [9]. Incidentally, Holst would later become not only the first employee (1914) but also the first director (1926) of the prestigious Philips Physics Laboratory ('Nat.Lab.') [10]. With their experiment Kamerlingh Onnes and Holst had found the first of a new class of materials:

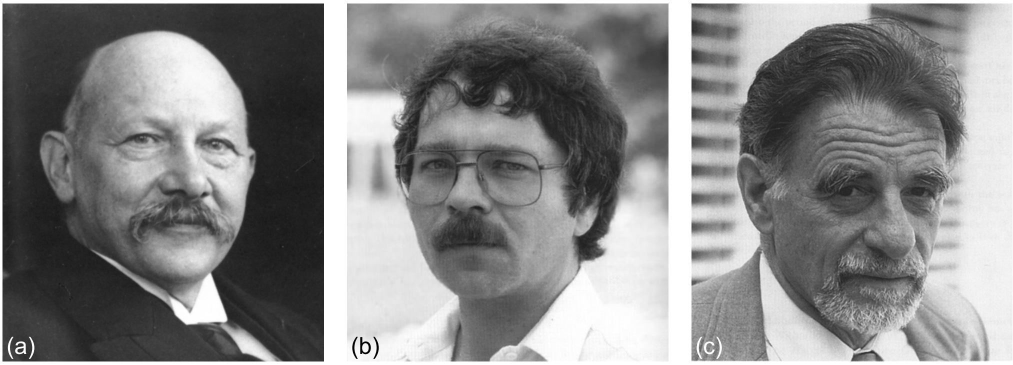

Figure 2.1: Discoverers of low-T_c and high-T_c superconductivity: (a) Heike Kamerlingh Onnes, (b) Johannes Georg Bednorz and (c) Karl Alex Müller.

the *superconductors*. The importance of materials that can carry currents without dissipation was immediately recognized and soon the search for superconductivity in other materials had started. Already by December 1912 Kamerlingh Onnes had demonstrated that superconductivity can be achieved in tin (3.8 K) and lead (6 K, later raised to 7.2 K) as well [11]. In 1913 Kamerlingh Onnes was awarded the Nobel prize "for his investigations on the properties of matter at low temperatures which led, inter alia, to the production of liquid helium" [12].

In the early days the Leiden group had a monopoly on superconductivity research simply because it was the only group in the world capable of liquifying helium. This changed after the first world war when in 1923 a helium liquefier, based on the Leiden design, started operation at the University of Toronto. Four years later a helium liquefier capable of producing 10 liters per hour was started at the Physikalisch-Technische Reichsanstalt (PTR) near Berlin under the direction of Walther Meissner [13]. Many different compounds were tested for superconductivity and in 1930 a new record-T_c was obtained in NbC: 10.3 K [14, 15]. Later that year, superconductivity was discovered in pure niobium, which was found to become superconducting at 8.5 K [16] (later this was raised to 9.25 K). Niobium-based technology is currently the standard for superconducting digital electronic circuits [17].

For two decades superconductors were thought to be merely ideal conductors, until in 1933 Walther Meissner and Robert Ochsenfeld demonstrated that in fact superconductors differ from ideal conductors in that they actively expel magnetic fields [18]. This effect is known as the *Meissner-Ochsenfeld effect*. Meanwhile efforts were made to develop a theory of superconductivity that could explain the experimentally observed phenomena: in 1935 the brothers Fritz and Heinz London proposed a two-fluid model in which they introduced two equations in addition to Maxwell's equations, which would later be named after them, to govern the electromagnetic fields in superconductors [19]. In 1950 Ginzburg and Landau developed a macroscopic theory that described superconductivity in terms of an order parameter Ψ and provided a derivation for the London equations [20]. The theoretical efforts culminated in 1957 through the development of the BCS theory which provides the current understanding of the nature of low-T_c superconductivity [5]. In BCS theory, named after its founders Bardeen, Cooper and Schrieffer, the charge carriers are

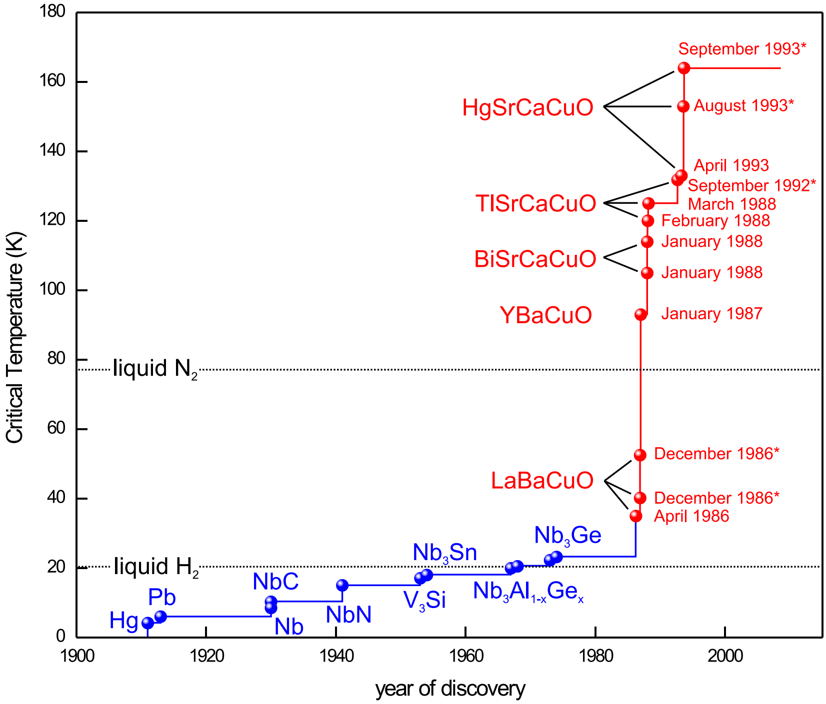

Figure 2.2: Development of the highest known critical temperature T_c in time. Data points indicated with an asterisk ($*$) are measured under hydrostatic pressure [1–4, 11, 14–16, 22, 25, 26, 29, 30, 34–42, 61–67].

pairs of electrons that are bound via electron-phonon interactions. The electron pairs behave as bosons and collectively occupy a single superconducting state which is separated from the normal states by an energy gap. Bardeen, Cooper and Schrieffer were awarded the 1972 Nobel prize for their development of the BCS theory [21].

Meanwhile superconductivity was found in many new compounds. In 1954 superconductivity was discovered Nb_3Sn (18 K) by Matthias *et al.* [22]. The high critical current density of Nb_3Sn makes it of the most popular materials today for large scale applications such as superconducting magnets in Magnetic Resonance Imaging (MRI) systems or particle accelerators such as the Large Hadron Collider (LHC). The International Thermonuclear Experimental Reactor (ITER) which is currently being built will require more than 500 tons of Nb_3Sn wire [23, 24]. For over a decade Nb_3Sn remained the highest-T_c superconductor until in 1967-1978 the liquid hydrogen (boiling point 20.3 K) barrier was broken through the discovery of superconductivity in $Nb_3Al_{1-x}Ge_x$ [25, 26].

For about thirty years after the introduction of the BCS theory the theory of superconductivity was thought to be complete. During that period McMillan had published a paper on the transition temperature in strong-coupled superconductors [27]. Using a model which was based on BCS theory, he was able to calculate transition temperatures within an accuracy of a few percent. For sensible input parameters the transition temperatures never exceeded 40 K, and soon an upper limit on T_c in the 30-40 K regime was silently assumed [28, 29]. The surprise was therefore great when in 1986 Johannes Georg Bednorz and Karl Alex Müller reported signatures for superconductivity at 35 K [30]. This result was even more remarkable considering the fact that it had been observed in a Ba-La-Cu-O compound, a ceramic material that is only a moderate conductor at room temperature. The initial scepticism about the discovery was soon dispelled however, as groups around the world reproduced the experiment [31]. Bednorz and Müller were awarded the 1987 Nobel prize for basically what is now known as high-T_c superconductivity [32].

The discovery of the high-T_c superconductors had given the field a new impulse, as can be seen in figure 2.2. Within a year a T_c of 93 K was observed in an Y-Ba-Cu-O compound [4]. With a transition temperature comfortably above the boiling point of liquid nitrogen (77 K) cooling down could be greatly facilitated. Using X-ray analysis the stoichiometry of the superconducting phase was soon determined to be $\mathrm{YBa_2Cu_3O_{7-\delta}}$ [33]. The maximum critical temperature was increased even further with the discovery of superconductivity in different copper-oxide compounds (or *cuprates* for short). In 1998 the bismuth- and thallium-based cuprates raised the highest T_c to 114 K and 125 K, respectively [34–38], and in 1992 the T_c of the latter was increased to 131.8 K under a pressure of 150 kbar [39]. Interestingly, the highest transition temperatures today are achieved in cuprates which are based on mercury, the element that initiated the field of superconductivity [40–42]. At the moment of writing the highest T_c is 164 K, observed in $\mathrm{HgBa_2Ca_2Cu_3O_{8+\delta}}$ under a pressure of 310 kbar [42].

Besides the cuprates, several new types of compounds were found to exhibit superconductivity, such as BaKBiO [43, 44], alkali metal doped fullerenes [45–49], the borocarbides [50–56], magnesium diboride [57], carbon nanotubes [58] and, most recently, iron arsenide based compounds [59, 60]. In terms of critical temperature however, these superconductors can not (yet) compete with the cuprates: at the moment of writing none of these shows superconductivity at liquid nitrogen temperature.

A little over twenty years after its discovery , the origin of high-T_c superconductivity is still not understood and a matter of heavy debate. There are many interesting differences between high-T_c and low-T_c superconductors, however. One of the most striking differences is in the symmetry of the order parameter. How the difference in order parameter symmetry is used for the spontaneously generated half-integer magnetic flux quanta described in this thesis will be the topic of section 3.3.

2.3 Fluxoid quantization

Superconductivity is a quantum phenomenon that manifests itself on a macroscopic scale. The ensemble of all electrons participating in the superconducting ground state (the superconducting *condensate*) can be described by a single macroscopic quantum wavefunction

$$\Psi(\mathbf{r},t) = |\Psi(\mathbf{r},t)|\, e^{i\theta(\mathbf{r},t)} \tag{2.1}$$

with $|\Psi(\mathbf{r},t)|$ the amplitude and $\theta(\mathbf{r},t)$ the phase at position $\mathbf{r}$ and time t. The probability density $\Psi^*\Psi$ is related to the total number of charge carriers $N^\star$ by the normalization condition

$$\int \Psi^*(\mathbf{r},t)\Psi(\mathbf{r},t)dV = N^\star \tag{2.2}$$

Because the number of charge carriers involved in the superconducting condensate is large $\Psi^*\Psi$ can be interpreted [68] as the local charge carrier density $n^\star$.

The macroscopic wavefunction obeys the Schrödinger equation for a charged particle in an electromagnetic field [69]

$$i\hbar\frac{\partial\Psi}{\partial t} = \left[\frac{1}{2m^\star}\left(\frac{\hbar}{i}\nabla - q^\star\mathbf{A}\right)^2 + q^\star\phi\right]\Psi \tag{2.3}$$

Here $m^\star$ and $q^\star$ are the mass and charge of the charge carriers, and $\mathbf{A}(\mathbf{r},t)$ and $\phi(\mathbf{r},t)$ are the magnetic vector potential and scalar potential, which are related to the magnetic and electric fields $\mathbf{B}$ and $\mathbf{E}$ by

$$\mathbf{B} = \nabla\times\mathbf{A} \tag{2.4}$$

and

$$\mathbf{E} = -\nabla\phi - \frac{\partial\mathbf{A}}{\partial t} \tag{2.5}$$

respectively.

Multiplying equation (2.3) by Ψ^* and subtracting its complex conjugate yields

$$\frac{\partial}{\partial t}\left(\Psi^*\Psi\right) = -\nabla\cdot\left[\frac{\hbar}{2m^\star i}\left(\Psi^*\nabla\Psi - \Psi\nabla\Psi^*\right) - \frac{q^\star}{m^\star}\left|\Psi\right|^2\mathbf{A}\right] \tag{2.6}$$

Upon multiplication with $q^\star$ we recognize this as the electromagnetic continuity equation

$$\frac{\partial\rho_s}{\partial t} = -\nabla\cdot\mathbf{J}_s \tag{2.7}$$

with ρ_s the charge density and

$$\mathbf{J}_s = \frac{\hbar q^\star}{2m^\star i}\left(\Psi^*\nabla\Psi - \Psi\nabla\Psi^*\right) - \frac{q^{\star 2}}{m^\star}\left|\Psi\right|^2\mathbf{A} \tag{2.8}$$

the current density. Equation (2.8) is known as the second Ginzburg-Landau equation and can also be obtained from a phenomenological treatment where the free energy of a superconductor is expanded in powers of Ψ [20]. It is also consistent with the microscopic BCS theory (in 1959 Gor'kov showed that the Ginzburg-Landau theory is derivable as a limiting case of the BCS theory [70]).

Substituting equation (2.1) into equation (2.8) we find

$$\Lambda\mathbf{J}_s + \mathbf{A} = \frac{\hbar}{q^\star}\nabla\theta \tag{2.9}$$

with

$$\Lambda \equiv \frac{m^\star}{n^\star q^{\star 2}} \tag{2.10}$$

This result shows that the phase of the superconducting condensate is related not only to the current but also to the magnetic field via the vector potential $\mathbf{A}$, which becomes more apparent when we integrate equation (2.9) around a closed contour Γ:

$$\oint_\Gamma \Lambda\mathbf{J}_s\cdot d\mathbf{l} + \oint_\Gamma \mathbf{A}\cdot d\mathbf{l} = \frac{\hbar}{q^\star}\oint_\Gamma \nabla\theta\cdot d\mathbf{l} \tag{2.11}$$

Using Stokes' Theorem to identify the middle term as the magnetic flux

$$\oint_\Gamma \mathbf{A}\cdot d\mathbf{l} = \int_S (\nabla\times\mathbf{A})\cdot d\mathbf{S} = \int_S \mathbf{B}\cdot d\mathbf{S} \equiv \Phi \tag{2.12}$$

and realizing that the integral of $\nabla\theta$ around any closed contour has to be an integer times 2π to ensure the single-valuedness of the wavefunction (2.1), we find the celebrated fluxoid quantization condition:

$$\oint_{\Gamma} \Lambda \mathbf{J}_s \cdot d\mathbf{l} + \Phi = \mathrm{n}\Phi_0 \tag{2.13}$$

In which

$$\Phi_0 \equiv \frac{h}{|q^\star|} = \frac{h}{2e} = 2.07 \cdot 10^{-15}\ \mathrm{Wb} \tag{2.14}$$

is the *magnetic flux quantum.*

Consider the integration contour Γ depicted in figure 2.3. When the path is chosen in the bulk superconductor where the magnetic field is expelled, the current density $\mathbf{J}_s$ is zero and we find that the flux in the hole is quantized

$$\Phi = \mathrm{n}\Phi_0 \tag{2.15}$$

The experimental confirmation in 1961 [71] was the first experimental evidence that the charge carriers in a superconductor (the Cooper pairs) carry a charge of $q^\star = -2e$. It is important to note that equation (2.15) is a special case. In general, the *fluxoid*, defined as the left-hand side of equation (2.13), is quantized, not the flux. Another important aspect is that Φ stands for the total flux, which is a sum of the externally applied flux and the self-generated flux.

2.4 London penetration depth and coherence length

Two important material properties are the London penetration depth λ_L and the coherence length ξ. The London penetration depth is the characteristic length scale over which magnetic fields can penetrate into a superconductor. This can be easily seen by taking the curl of equation (2.9) and expressing $\mathbf{J}_s$ in terms of the magnetic field $\mathbf{B}$ using Maxwell's equations, which yields

$$\nabla^2 \mathbf{B} = \frac{\mu_0}{\Lambda} \mathbf{B} \tag{2.16}$$

The solution for a magnetic field oriented along the z-axis penetrating the superconducting semispace $x > 0$ is $B_z = B_0 \exp(-x/\lambda_L)$ with

$$\lambda_L = \sqrt{\frac{\Lambda}{\mu_0}} \tag{2.17}$$

The coherence length is the typical length scale over which variations in the order parameter Ψ occur. It can be derived from and was first introduced in the Ginzburg-Landau theory [20]. Sometimes the coherence length is referred to as the 'size of a Cooper pair': within the BCS model it can be regarded as the distance over which electrons 'feel' each other through electron-phonon interactions. The ratio of the London penetration depth and the coherence length

$$\kappa = \frac{\lambda}{\xi} \tag{2.18}$$

is known as the *Ginzburg-Landau parameter.* The Ginzburg-Landau parameter determines if a superconductor is type I ($\kappa < 1/\sqrt{2}$) or type II ($\kappa > 1/\sqrt{2}$). For a type

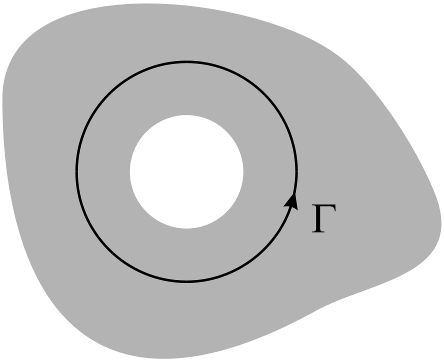

Figure 2.3: Integration path Γ in a bulk superconductor.

I superconductor the surface energy σ_{ns} of a normal metal-superconductor interface is positive and perfect diamagnetism occurs below the critical temperature T_c and critical field B_c [72]. For a type II superconductor the surface energy σ_{ns} is negative. Below the lower critical field B_{c1} it acts as a type I superconductor, but between the lower critical field B_{c1} and the upper critical field B_{c2} the external magnetic field is only partly excluded and a mixed state exists in which flux is penetrating the superconductor through quantized vortices that have a normal core with a radius of the order ξ. These vortices are known as Abrikosov vortices, after the physicist who first predicted them [73]. The flux carried by a single Abrikosov vortex corresponds to exactly one flux quantum Φ_0.

2.5 Gauge invariance

The vector- and scalar potentials $\mathbf{A}$ and ϕ from which the electromagnetic fields $\mathbf{E}$ and $\mathbf{B}$ can be determined are not uniquely defined. In fact, Maxwell's equations are invariant under the *gauge transformation*

$$\begin{aligned} \mathbf{A} &\longrightarrow \mathbf{A} + \nabla\chi \\ \phi &\longrightarrow \phi - \frac{\partial\chi}{\partial t} \end{aligned} \tag{2.19}$$

as can be readily seen from equations (2.4) and (2.5). However, upon inspection of equation (2.9) this seems to suggest that the experimentally measurable quantity j_s depends on the gauge chosen which should of course not be the case. The solution to this paradox lies in the fact that for the Schrödinger equation (2.3) to be gauge invariant the phase θ needs to be transformed along with the potentials in the following way

$$\begin{aligned} \mathbf{A} &\longrightarrow \mathbf{A} + \nabla\chi \\ \phi &\longrightarrow \phi - \frac{\partial\chi}{\partial t} \\ \theta &\longrightarrow \theta - \frac{2\pi}{\Phi_0}\chi \end{aligned} \tag{2.20}$$

2.6 Josephson junctions

A Josephson junction is a weak link between two superconductors where superconductivity is suppressed. In the junction the wavefunctions of the two superconductors overlap, leading to interesting interference effects. In the absence of a magnetic vector potential $\mathbf{A}$ the current flowing through the junction is related to the phase drop between the two wavefunctions via

$$I_s = I_c \sin\left(\theta_1 - \theta_2\right)_{\mathbf{A}=0} \tag{2.21}$$

It is emphasized that this relation only holds when $\mathbf{A} = 0$. It could not be the general equation for the current through a junction, because the current through the junction is directly related to the phase difference $\theta_1 - \theta_2$. But the phase difference depends on the gauge chosen via equation (2.20) whereas the supercurrent I_s is an experimentally measurable, and thus gauge invariant, quantity. Equation (2.21) can be written in its gauge invariant form by defining the gauge such that

$$\mathbf{A}' = \mathbf{A} + \nabla\chi = 0 \tag{2.22}$$

This results in a phase difference

$$\theta_1' - \theta_2' = \theta_1 - \theta_2 + \frac{2\pi}{\Phi_0} \int_{\mathbf{r}_1}^{\mathbf{r}_2} \nabla\chi \cdot d\mathbf{l} \tag{2.23}$$

Using $I_s = I_s' = I_c \sin\left(\theta_1' - \theta_2'\right)_{\mathbf{A}'=0}$ together with (2.22) and (2.23) we find

$$I_s = I_c \sin\varphi \tag{2.24}$$

with φ the *gauge invariant phase difference*, defined by

$$\varphi \equiv \theta_1 - \theta_2 - \frac{2\pi}{\Phi_0} \int_{\mathbf{r}_1}^{\mathbf{r}_2} \mathbf{A} \cdot d\mathbf{l} \tag{2.25}$$

Though it is not entirely correct, in this thesis the (gauge invariant) phase difference φ over a junction will often be simply referred to as the 'phase' of a junction. The voltage over the junction is related to the gauge invariant phase via

$$V = \frac{\Phi_0}{2\pi} \frac{d\varphi}{dt} \tag{2.26}$$

Equations (2.24) and (2.26) were first predicted by Brian D. Josephson [74, 75] and are now known as the first and second Josephson equation, respectively. The energy stored in a junction can be calculated straightforwardly from these equations by integrating the work needed to change the phase from 0 to φ:

$$U_J = \int_0^t IV dt = \frac{\Phi_0 I_c}{2\pi} \int_{\varphi_0}^{\varphi} \sin(\varphi) \frac{d\varphi}{dt} dt \tag{2.27}$$

or

$$U_J = E_J \left(1 - \cos\varphi\right) \tag{2.28}$$

with

$$E_J \equiv \frac{\Phi_0 I_c}{2\pi} \tag{2.29}$$

the *coupling energy* (the integration constant was chosen to give $U_J = 0$ for $\varphi = 0$).

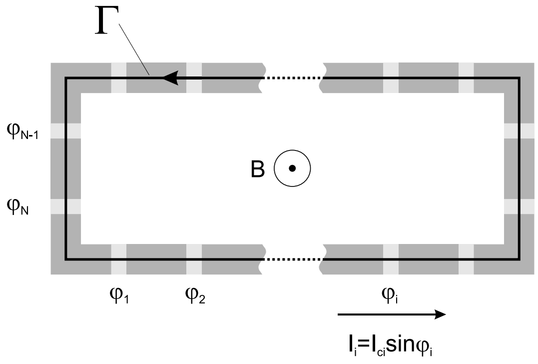

Figure 2.4: Integration path Γ in a superconducting loop containing multiple Josephson junctions with phases $\varphi_1 ... \varphi_N$ and in a magnetic field B.

2.7 Fluxoid quantization in a multi-junction loop

The fluxoid quantization condition for a loop containing N Josephson junctions can now easily be derived by integrating the gradient of the phase $\nabla\theta$ around the loop along the contour as shown in figure 2.4. Using equations (2.9) and (2.25) we find

$$\oint \nabla\theta \cdot d\mathbf{l} = -\frac{2\pi}{\Phi_0}\int_{\Gamma'} \Lambda \mathbf{J}_s \cdot d\mathbf{l} - \frac{2\pi}{\Phi_0}\oint \mathbf{A}\cdot d\mathbf{l} - \sum_{i=1}^{N} \varphi_i \tag{2.30}$$

where Γ' denotes the contour Γ with the Josephson junctions excluded. The first integral on the right-hand side can be ignored when the superconducting leads are sufficiently thick so $\mathbf{J}_s = 0$ along the contour Γ'. Then, again using the single-valuedness of the wavefunction and Stokes' theorem equation (2.30) simplifies to

$$\frac{1}{2\pi}\sum_{i=1}^{N} \varphi_i + \frac{\Phi}{\Phi_0} = \mathrm{n} \tag{2.31}$$

This equation can be thought of as the fluxoid quantization condition of multi-junction loops with thick leads. It elegantly shows that the sum of the normalized phase and flux is quantized.

2.8 RCSJ model

The two Josephson equations are sufficient for describing the DC characteristics of a weak link. For a proper description of the voltage state, the physical junction is usually modelled as an ideal junction shunted by a resistor and a capacitor, see figure 2.5(a). This model is known as the resistively and capacitively shunted junction (RCSJ) model. Kirchhoff's law for this shunted junction reads

$$I = C\frac{dV}{dt} + I_c \sin\varphi + \frac{V}{R} \tag{2.32}$$

Inserting (2.26), using the dot-convention for the time-derivative and rearranging terms this yields

$$\ddot{\varphi} + \frac{1}{RC}\dot{\varphi} + \omega_p^2 \left(\sin\varphi - \frac{I}{I_c} \right) = 0 \tag{2.33}$$

with

$$\omega_p = \sqrt{\frac{2\pi}{\Phi_0} \frac{I_c}{C}} \tag{2.34}$$

the *plasma frequency.* This equation is reminiscent of the equation of motion for a rigid pendulum of length ℓ and mass m on which an external torque τ is exerted, as illustrated in figure 2.5(b). The equation of motion for this system reads

$$\ddot{\varphi} + \gamma\dot{\varphi} + \omega_0^2 \left(\sin\varphi - \frac{\tau}{mg\ell} \right) = 0 \tag{2.35}$$

Here φ is the angle of the pendulum with respect to the vertical axis, γ is a damping-coefficient, and

$$\omega_0 = \sqrt{\frac{g}{\ell}} \tag{2.36}$$

is the resonance frequency of the pendulum. The properties of a Josephson junction can be conveniently described in terms of the damped pendulum model (the equivalence of the two systems was demonstrated experimentally by Hansma and Rochlin [76]). The externally applied torque and the pendulum angular frequency are related to the total current through and voltage over the junction (2.26) as

$$\begin{array}{ccc} \tau & \longleftrightarrow & I \\ \omega & \longleftrightarrow & \dfrac{2\pi}{\Phi_0} V \end{array} \tag{2.37}$$

For torques smaller than a critical torque $mg\ell$ the pendulum assumes an equilibrium position and a static situation arises. Correspondingly, for currents smaller than the critical current I_c the phase adjusts to the current and no voltage appears over the junction. When the torque is released the pendulum will start oscillating at its resonance frequency ω_0. The movement of the pendulum will be damped because of friction which scales linearly with the angular velocity. Analogously, junction phase oscillations are described by the plasma frequency ω_p and damping is characterized by the RC time. The product of these is known as the quality factor

$$Q = \omega_p RC = \sqrt{\beta_C} \tag{2.38}$$

A more commonly used damping parameter is the square of the quality factor

$$\beta_C = \frac{2\pi}{\Phi_0} I_c R^2 C \tag{2.39}$$

β_C is known as *the Stewart-McCumber parameter* [77, 78].

When the external torque exceeds the critical torque the pendulum enters the dynamical state where it keeps rotating. Correspondingly, when the Josephson junction is biased above its critical current it enters the voltage state. Though this is a dynamical process, these oscillations take place at very high frequencies (typically hundreds of GHz)

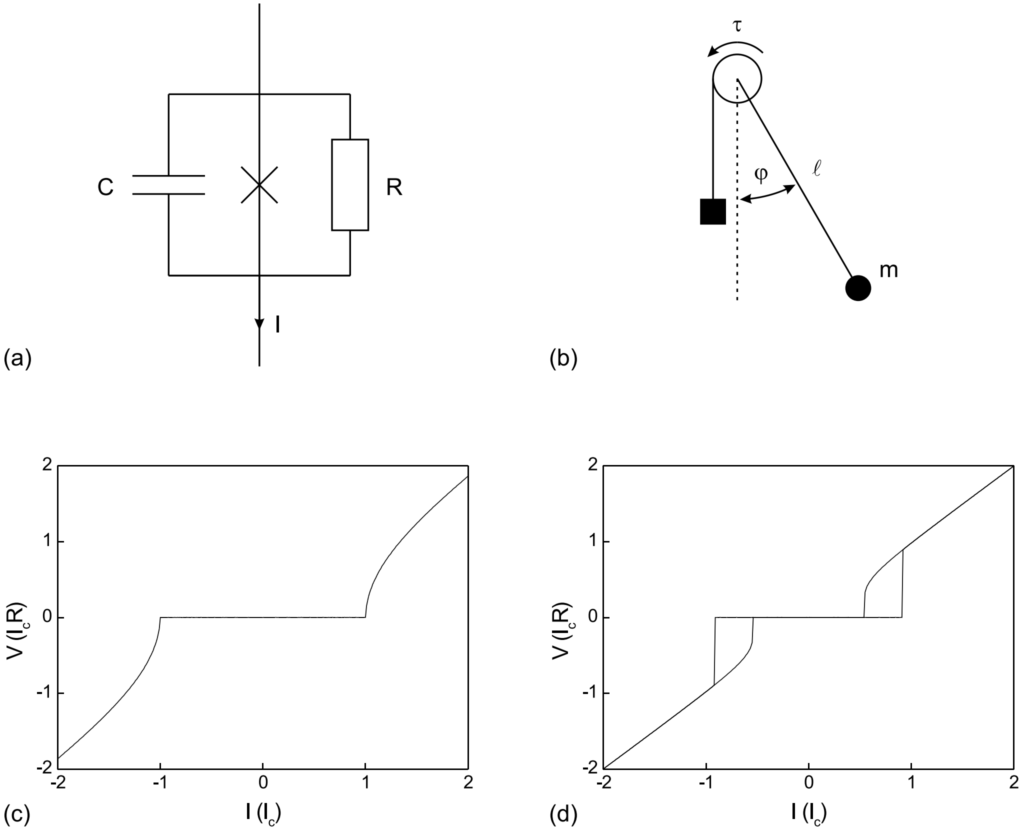

Figure 2.5: (a) Schematic of a resistively and capacitively shunted Josephson junction. (b) Mechanical analogon: a rigid pendulum with mass m, length ℓ on which an external torque τ is exerted. (c) IV characteristic of an overdamped junction ($\beta_C = 0.5$). (d) IV characteristic of an underdamped junction ($\beta_C = 5$).

and an average DC current and voltage will be measured. Equation (2.33) can be solved to obtain the IV characteristics of a Josephson junction. In the limit of strong damping ($\beta_C \ll 1$) the problem reduces to a first order differential equation and the analytical solution, for $I > I_c$, is given by

$$V = I_c R \sqrt{\left(\frac{I}{I_c}\right)^2 - 1} \tag{2.40}$$

This solution interpolates smoothly between $V = 0$ at the critical current to Ohm's law ($V = IR$) for $I \gg I_c$.

In general the solution to equation (2.33) has to be computed numerically. The IV for an overdamped junction $\beta_C < 1$ is shown in figure 2.5(c). For underdamped ($\beta_C > 1$) junctions equation (2.33) is bistable in a regime below I_c, resulting in a hysteretic IV characteristic as depicted in figure 2.5(d). In this regime the built-up momentum of the pendulum can overcome the damping due to friction, and the pendulum will not stop rotating until the potential energy gained upon completing a cycle is smaller than the energy lost due to dissipation. This happens at a torque that is smaller than the critical torque, and in the junction equivalent this current is known as the *retrapping current* I_r. It should be noted that in any real experiment the observed critical current and retrapping current will differ from their respective RCSJ values due to thermal fluctuations and macroscopic quantum tunnelling [79].

The separation between the overdamped and underdamped regime is usually defined at $\beta_C = 1$. Mathematically however, the transition between hysteretic and non-hysteretic behavior of equation (2.33) occurs at a Stewart-McCumber parameter which is slightly smaller. Many authors have numerically calculated the bifurcation curve $\beta_C(I_r/I_c)$, but interestingly the value $\beta_C(1)$ is rarely mentioned explicitly [78, 80–83]. From Barone and Paternò [84] a value $\beta_C^{-1/2} = 1.15$ or $\beta_C = 0.756$ is obtained.

2.9 DC SQUID

One famous example of a multi-junction loop is the 2-junction loop, also known as the direct current superconducting quantum interference device (DC SQUID). This device is the most sensitive magnetic field sensor that is currently available [85–87]. SQUIDs are employed in a broad variety of fields, ranging from the non-destructive inspection of fatigue cracks in airplanes to the monitoring of heart- and brain activity and from astronomy to geological surveying [87–90]. SQUIDs are good candidates for the detection of half-integer flux quanta and therefore play a central role in all experiments described in this thesis.

2.9.1 Critical current of a SQUID

A schematic of a DC SQUID is depicted in figure 2.6(a). The total current I is related to the currents through the individual junctions via Kirchhoff's law

$$I = I_{c1} \sin \varphi_1 + I_{c2} \sin \varphi_2 \tag{2.41}$$

Taking into account the direction of I_2, the fluxoid quantization condition (2.31) reduces to

$$\frac{1}{2\pi} (\varphi_1 - \varphi_2) + \frac{\Phi}{\Phi_0} = \mathrm{n} \tag{2.42}$$

Because the two phases are related via the magnetic field, the maximum dissipationless current that a SQUID can support is a function of the magnetic flux. Combining (2.41) and (2.42) we find

$$I_{max} = \sqrt{(I_{c1} - I_{c2})^2 + 4 I_{c1} I_{c2} \cos^2 \left(\pi \frac{\Phi}{\Phi_0} \right)} \tag{2.43}$$

I_{max} is the critical current of the SQUID[1]. It should be noted, however, that the flux Φ in this equation is the actual flux threading the SQUID loop, which is the sum of the externally applied flux Φ_e and the self-generated flux

$$\Phi = \Phi_e + L_1 I_{c1} \sin \varphi_1 - L_2 I_{c2} \sin \varphi_2 \tag{2.44}$$

---

[1] To avoid confusion with the critical currents of SQUID junctions I_{max} is used here instead of I_c

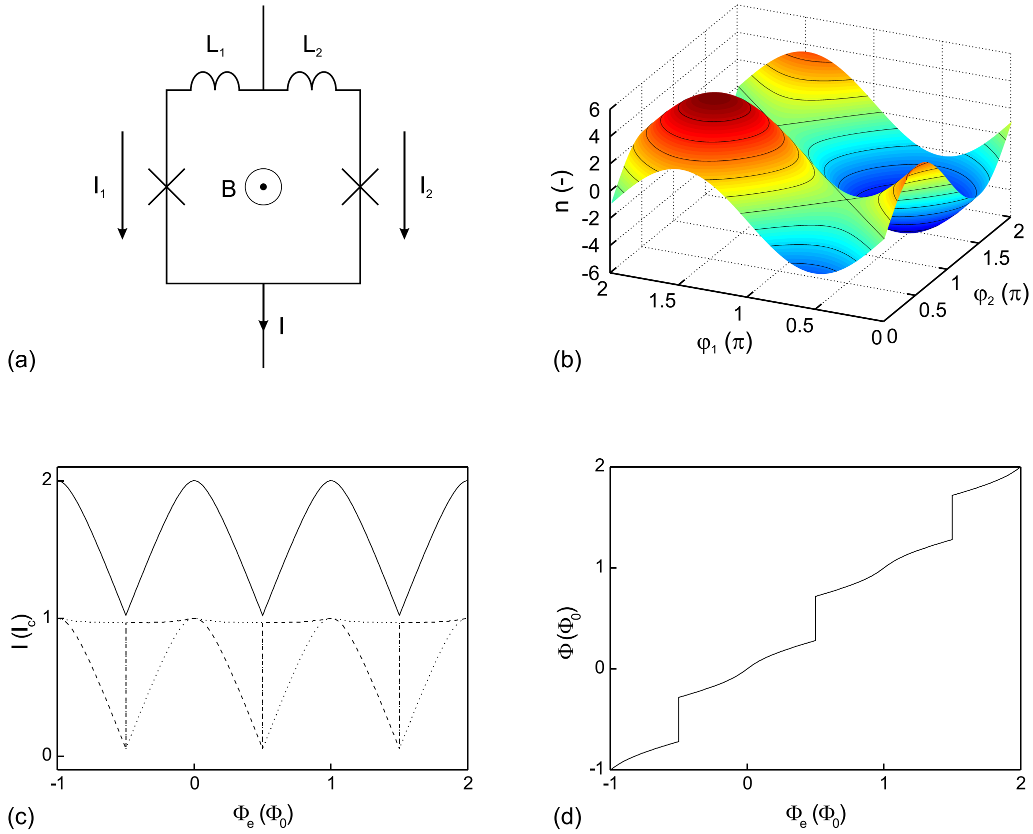

Figure 2.6: (a) Schematic of a DC SQUID. (b) Fluxoid number n as a function of the phases φ_1 and φ_2. The contours for which n is integer indicate the solutions that satisfy the fluxoid quantization condition. (c) The critical current (solid line) and currents through junctions 1 and 2 (dashed and dotted lines, respectively) as a function of the externally applied magnetic flux Φ_e ($\beta_L = 3$). (d) The total magnetic flux through the SQUID loop as a function of the externally applied magnetic flux Φ_e ($\beta_L = 3$).

In general, the critical current of a SQUID as a function of the *externally applied* magnetic field cannot be calculated analytically because $\Phi(\Phi_e)$ cannot be written in an explicit form. The critical current can be calculated numerically, however. One possible method is to define a grid of φ_1 and φ_2 (both defined between 0 and 2π), and calculate the total flux and the fluxoid number n on each point for a given external flux Φ_e. The allowed solutions lie on the contours for which n is integer, as indicated by the solid lines in figure 2.6(b). The critical current is then given by the solution that maximizes equation (2.41). The resulting current and flux are depicted in figures 2.6(c) and 2.6(d) for a symmetric SQUID with equal junction critical currents ($I_{c1} = I_{c2}$) and branch inductances ($L_1 = L_2 = L/2$).

The SQUID critical current has a periodicity of one flux quantum and has maxima at $\Phi_e = \mathrm{n}\Phi_0$. The total flux in the SQUID ring as a function of the externally applied magnetic flux shows step-like behavior reminiscent of the flux quantization in bulk super-

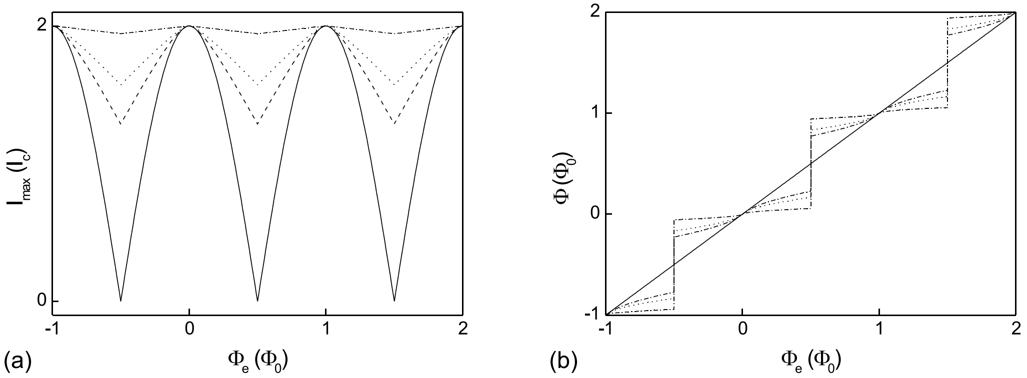

Figure 2.7: (a) Critical current and (b) total magnetic flux through the SQUID loop versus the externally applied magnetic flux. Solid lines: $\beta_L = 0$, dashed lines: $\beta_L = 5$, dotted lines: $\beta_L = 10$, dash-dotted lines: $\beta_L = 100$.

conducting rings. When a flux is applied the SQUID reacts by generating a circulating current to counteract that flux. When the flux becomes too large, however, the circulating current changes sign and the self-generated flux adds to the external flux, bringing the total flux towards the next integer number of flux quanta. The transition point occurs at $\Phi_e = (\mathrm{n} + \frac{1}{2})\Phi_0$. This can also be recognized in the behavior of the currents through the individual branches: when an integer number of flux quanta is applied, there is no screening current and the maximum transport current is achieved when $I_1 = I_2 = I_c$. For non-zero fields however the aforementioned circulating current will add to the current in one junction and subtract from the current in the other junction. The maximum current is achieved when one of the junctions reaches I_c. The other junction will then be separated from its critical current by an amount equal to twice the circulating current. The sign-change of the circulating current when the externally applied flux reaches $(\mathrm{n} + \frac{1}{2})\Phi_0$ can clearly be observed.

The SQUID behavior and the influence of the screening currents are described by the *screening parameter*

$$\beta_L \equiv \frac{2\pi L I_c}{\Phi_0} \tag{2.45}$$

For SQUIDs with a small screening parameter ($\beta_L \ll 1$) the influence of the screening currents is negligible and the flux through the SQUID equals the external flux $\Phi \approx \Phi_0$. For a SQUID with $\beta_L = 0$ and equal junctions equation (2.43) reduces to

$$I_{max} = 2I_c \left| \cos\left(\pi \frac{\Phi_e}{\Phi_0}\right) \right| \tag{2.46}$$

In figure 2.7 the critical current and flux are shown for several values of the screening parameter. The curve for $\beta_L = 0$ is identical to equation (2.46). For higher values of β_L the SQUID screens external fields more effectively.

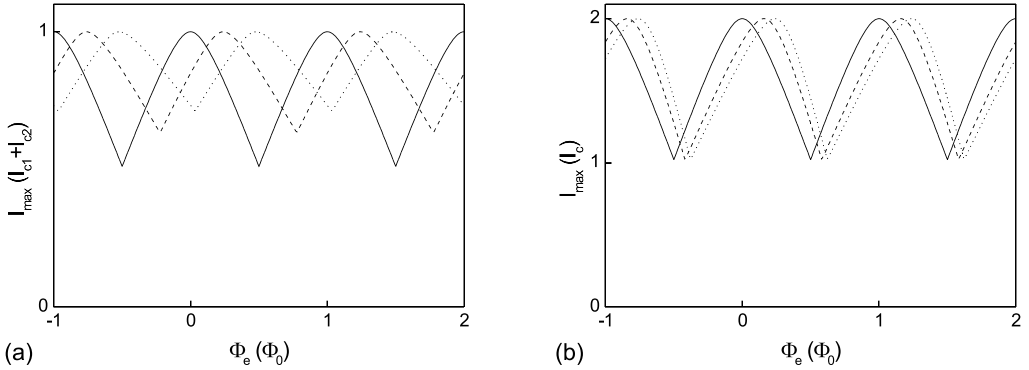

Figure 2.8: Effect of asymmetries on the SQUID critical current. (a) $\beta_L = 3$, $\lambda = 1$. Solid line: $\kappa = 1$, dashed line: $\kappa = 2$, dotted line: $\kappa = 3$. (b) $\beta_L = 3$, $\kappa = 1$. Solid line: $\lambda = 1$, dashed line: $\lambda = 2$, dotted line: $\lambda = 3$.

2.9.2 Asymmetric SQUID

Most SQUIDs contain asymmetries, whether intentional or because of microscopic irregularities due to fabrication. An asymmetry in the junction critical currents or branch inductances will affect the critical current of the SQUID. In figure 2.8 the critical current is plotted for a screening parameter $\beta_L = 1$ and different ratios of the junction critical currents ($\kappa = I_{c2}/I_{c1}$) and branch inductances ($\lambda = L_2/L_1$). For the calculations β_L was defined using I_{c1} for the critical current: $\beta_L = 2\pi L I_{c1}/\Phi_0$. In general, the maximum critical current for an asymmetric SQUID is not obtained at zero external flux. Combining equations (2.41), (2.42) and (2.44) we find that the SQUID can always obtain its maximum critical current $I_{c1} + I_{c2}$. This is achieved when ($\varphi_1 = \varphi_2 = \pi/2$)

$$\frac{\Phi_e^\star}{\Phi_0} = \frac{\beta_L(\kappa\lambda - 1)}{2\pi(\lambda + 1)} + \mathrm{n} \tag{2.47}$$

This shift of the maximum can be explained by the interplay between the external field, the screening current and the junction critical currents. For a SQUID with symmetric inductances ($\lambda = 1$) the current through the junctions can be regarded as the superposition of half the applied current and the screening current, which has an opposite sign for each junction and depends on the externally applied magnetic field. At zero field there will be no screening currents and therefore the maximum critical current $I_{c1} + I_{c2}$ cannot be reached at $\Phi_e = 0$ for $I_{c1} \neq I_{c2}$ (unless in the special case $\beta_L = 0$). When I_{c2} is slightly larger than I_{c1} ($\kappa \gtrsim 1$) the maximum transport current can be sent when the screening current is $(I_{c2} - I_{c1})/2$, which occurs for $\Phi_e \gtrsim 0$. For larger asymmetries κ a larger screening current and thus a larger external field is required to overcome the difference in critical currents.

When the asymmetry is not located in the junctions ($\kappa = 1$) but in the inductances, the shift of the maximum critical current can be explained by realizing that the maximum coincides (for a small externally applied flux) with a total magnetic flux $\Phi = 0$, see equation (2.43). When the maximum SQUID critical current $2I_c$ is reached, the self-generated flux at the moment of switching will be $I_c L_1(1 - \lambda) \neq 0$. Since the sum of the externally applied flux and the self-generated flux should be equal to the total magnetic flux the maximum can not be achieved at $\Phi_e = 0$ but at the external flux as defined in equation (2.47). SQUID asymmetries also cause a shift of the position where the minimum critical current is obtained. Moreover, the modulation is influenced by the asymmetry in the critical current, but is independent of any asymmetry in the inductances [91].

2.9.3 SQUID in the voltage state

The modulation of the SQUID critical current with the enclosed flux is what makes a SQUID suitable as a flux sensor. The modulation can be detected by reading out the critical current directly, for example by ramping up the current through the SQUID until a voltage appears. A far more easy method however, which was also used in our experiments, is to use the SQUID in the voltage state. To describe this behavior the SQUID is modelled as a parallel connection of two RCSJ junctions. Each of the junctions satisfies equation (2.33) and the relation between the junction phases and the externally applied magnetic field is described by (2.42) and (2.44). For a completely symmetric SQUID ($I_{c1} = I_{c2} = I_c$, $C_1 = C_2 = C$, $R_1 = R_2 = R$ and $L_1 = L_2 = L/2$) these equations reduce to

$$\begin{cases} \beta_C \ddot{\varphi}_1 + \dot{\varphi}_1 + \sin\varphi_1 - \frac{1}{2}\frac{I}{I_c} - \beta_L^{-1}\left(\varphi_2 - \varphi_1 - 2\pi\frac{\Phi_e}{\Phi_0}\right) = 0 \\ \beta_C \ddot{\varphi}_2 + \dot{\varphi}_2 + \sin\varphi_2 - \frac{1}{2}\frac{I}{I_c} + \beta_L^{-1}\left(\varphi_2 - \varphi_1 - 2\pi\frac{\Phi_e}{\Phi_0}\right) = 0 \end{cases} \tag{2.48}$$

were the derivatives are with respect to the normalized time $\omega_p^2 RCt$. Asymmetries can be introduced quite straightforwardly (see, for example, the SQUID Handbook [87]). For any applied current I and magnetic flux Φ_e the coupled differential equations (2.48) can be solved to obtain the phases $\varphi_1(t)$ and $\varphi_2(t)$ as a function of time. From the averages of the phases and the time-derivative of the phases the DC current and voltage can be calculated for each junction. In figure 2.9(a) the IV-characteristic of a SQUID is shown for two values of the external magnetic flux. For $\Phi_e = 0$ the SQUID has a maximum critical current of twice the junction critical current I_c and for $\Phi_e = \Phi_0/2$ the SQUID critical current is at a minimum.

When a SQUID is operated in the voltage mode a constant current I is applied and the voltage over the SQUID is measured. The measured voltage modulates with the applied magnetic field as indicated in figure 2.9(b). Operated in this way, the SQUID acts as a flux-to-voltage transducer. The SQUID is most sensitive when operated on the steep rising (or falling) edges where the SQUID is just biased above its critical current. A flux-locked loop technique can be used to keep the SQUID at this optimal working point [92]. Another interesting feature that can also be observed from figure 2.9 is that the voltage modulation for small bias currents is inverted with respect to the voltage modulation for high bias currents. This behavior can be attributed to LC resonances which are caused by the nonlinear interaction of the ac Josephson current with the resonant circuit formed by the loop inductance L and the junction capacitance C [93–95]. Using the second Josephson equation (2.26) the resonance frequency can be translated to a resonance voltage

$$V_{\mathrm{res}} = \frac{\Phi_0}{2\pi\sqrt{LC/2}} \tag{2.49}$$

Using (2.39) and (2.45) the resonance voltage can be expressed in terms of β_C, β_L and

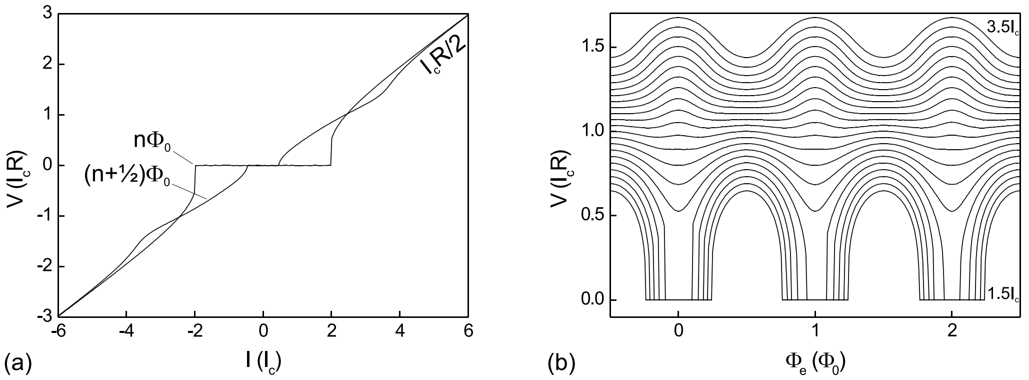

Figure 2.9: (a) IV characteristic of a symmetric DC SQUID, calculated for an applied field corresponding to a maximum critical current $\Phi_e = \mathrm{n}\Phi_0$ and for a field corresponding to a minimum critical current $\Phi_e = (\mathrm{n} + \frac{1}{2})\Phi_0$. (b) Measured voltage over a DC SQUID operated in the voltage mode for different values of the applied current I. I_c denotes the junction critical current in both figures and calculations were performed for a SQUID with $\beta_L = 1$ and $\beta_C = 1$.

the I_cR-product as

$$V_{\text{res}} = \sqrt{\frac{2}{\beta_C \beta_L}} I_c R \tag{2.50}$$

which corresponds to a (normalized) resonance voltage of 1.41 for figure 2.9.

2.10 π-rings

A π-ring is a superconducting ring that contains an intrinsic phase shift π (a review of π-phase shift Josephson structures has been given by Hilgenkamp [96]). This π-phase shift can be established in several different ways. The phase shift can be incorporated in the junction itself, for example by using SFS junctions [97, 98], SIFS junctions [99] or by controlling the energy distribution of current-carrying states in SNS junctions [100]. This type of junction is known as the π-junction. The current through a π-junction is related to its phase via $I = I_c \sin(\varphi + \pi) = -I_c \sin\varphi$ and is therefore sometimes said to have a negative critical current. Another way to obtain a π-phase shift in a superconducting ring is by the inclusion of a second loop containing a trapped fluxoid [101, 102]. The π-rings that were used in our experiments however were established by exploiting the $d_{x^2-y^2}$-wave pairing symmetry of the cuprate superconductors [103, 104], which will be discussed in section 3.3. Because we use rings containing two different superconducting materials our rings have a minimum of 2 Josephson junctions.

A schematic of a π-ring is depicted in figure 2.10(a). The π-phase shift is represented as a separate element. The following discussion also holds if the π-phase shift is incorporated in one of the junctions, provided the phase of the π-junction is diminished by π in the current-phase relationship (*not* in the fluxoid quantization condition), and the separate

π-phase shift is removed. The fluxoid quantization condition (2.31) for a π-ring reads

$$\frac{1}{2\pi}(\varphi_1 + \varphi_2 + \pi) + \frac{\Phi}{\Phi_0} = \mathrm{n} \tag{2.51}$$

One glance at this equation shows that the ground state of a 'normal' 2-junction ring, no flux and all-zero phases, is no longer an allowed solution. The extra π-phase shift has to be compensated for if n is to be an integer. This can be accomplished by a rearrangement of the phases over the junctions and the flux threading the loop. Exactly how these are affected depends on the characteristics of the ring, and in particular on the screening parameter β_L (2.45). For rings with a small screening parameter ($\beta_L \ll 1$) the produced flux will be negligible, even when the maximum current I_c flows through the ring, so the additional π-phase shift arises over the phases of the junctions. When the screening parameter is very large ($\beta_L \gg 1$) however, a very small change in phase will result in the spontaneous generation of a half-flux quantum, leaving the phases almost zero. This regime is known as the *large inductance limit*. The half-flux quantum can have positive or negative polarity, corresponding to a phase shift of $\pm\pi$.

2.10.1 π-ring in an external magnetic field

We will now discuss how a π-ring responds to an external magnetic flux Φ_e. In the following, we will assume $I_{c2} = \kappa I_{c1}$ with $\kappa \geq 1$. The phases φ_1 and φ_2 are directly related via the requirement that the currents through each of the junctions is the same

$$I = I_{c1} \sin\varphi_1 = I_{c2} \sin\varphi_2 \tag{2.52}$$

Thus we find for φ_2 (modulo 2π)

$$\varphi_2 = \begin{cases} \arcsin\left(\kappa^{-1} \sin\varphi_1\right) \\ \pi - \arcsin\left(\kappa^{-1} \sin\varphi_1\right) \end{cases} \tag{2.53}$$

The total energy of a π-ring is given by the sum of the energy stored in the Josephson junctions (2.28) and the energy stored in the generated magnetic field

$$U = E_{J1}(1 - \cos\varphi_1) + E_{J2}(1 - \cos\varphi_2) + \frac{1}{2}LI^2 \tag{2.54}$$

Given φ_1, the energy difference between the two solutions for φ_2 is

$$U(\varphi_{2b}) - U(\varphi_{2a}) = \frac{\Phi_0}{\pi}\sqrt{I_{c2}^2 - I^2} \tag{2.55}$$

which is always positive. The second solution of equation (2.53) will therefore always be one of higher energy. This does not imply that this solution can be dismissed, however, because in general when φ_{2b} satisfies the fluxoid quantization condition (2.51), φ_{2a} will not and vice versa.

The flux Φ in (2.51) has two contributions: the externally applied flux Φ_e and the self-generated flux LI

$$\Phi = \Phi_e + LI \tag{2.56}$$

Equations (2.51), (2.52), (2.53), (2.54) and (2.56) can be solved numerically to obtain the spontaneously generated current, the total flux, and the phases for the ground state

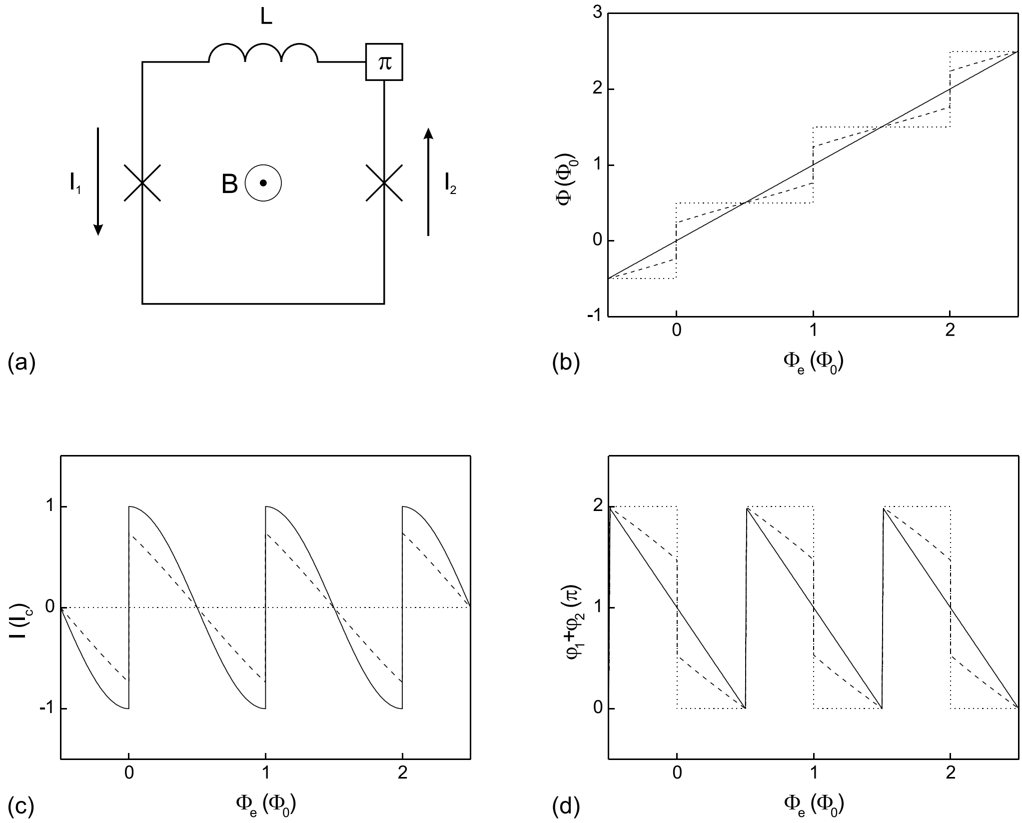

Figure 2.10: (a) Schematic of a π-ring. (b) Total flux threading the loop, (c) spontaneously generated current, and (d) sum of the phases for a π-ring. Solid lines: $\beta_L = 0$, dashed lines: $\beta_L = 2$, dotted lines: $\beta_L = 10000$

of a π-ring as a function of the externally applied magnetic flux. The result of this calculation for a π-ring with equal junctions is plotted in figures 2.10(b)-(d) for different values of the screening parameter β_L. In the small inductance limit the external field cannot be screened, even for circulating currents close to the critical current, and thus the total magnetic flux is equal to the externally applied magnetic flux. The phases over the junctions and the externally applied flux combined compensate for the π-phase shift. In the large inductance limit the phases remain approximately zero and only a fraction of the critical current is sufficient to generate a flux which is quantized as $(\mathrm{n} + \frac{1}{2})\Phi_0$.

2.10.2 Ground state without external flux

We now consider the ground state of an asymmetric π-ring in the absence of an external magnetic field. In figures 2.11(a)-(c) the phases, flux and circulating current are plotted as a function of the screening parameter for different critical current ratios κ (β_L is defined based on I_{c1}). For asymmetric junctions ($\kappa > 1$) a clear transition is observed between currentless solution $\varphi_1 = \pi$, $\varphi_2 = 0$ and $I = \Phi = 0$ for $\beta_L \leq \beta_L^\star$ and a ground state characterized by spontaneously generated currents producing a flux that asymptotically approaches a half-flux quantum for $\beta_L > \beta_L^\star$. In the following, we will derive an analytical expression for $\beta_L^\star$. Substitution of φ_2 from (2.51) into (2.52) and using $\beta_L \Phi_0 \sin\varphi_1/2\pi$ for the self-generated flux (and thus for the total flux as the externally applied field is assumed to be zero) yields

$$\sin\varphi_1 = \kappa \sin(\varphi_1 + \beta_L \sin\varphi_1) = f(\varphi_1) \tag{2.57}$$

$f(\varphi_1)$ and $\sin\varphi_1$ are depicted in figure 2.11(d). At the intersections equation (2.52) is satisfied. The currentless solutions $\varphi_1 = \{0, \pi, 2\pi\}$ are valid solutions of equation (2.57), regardless of κ or β_L. For the currentless solutions $\Phi = 0$ and the fluxoid quantization condition (2.51) reads $\varphi_1 + \varphi_2 + \pi = 2\pi\text{n}$. Realizing that we have assumed $I_{c2} > I_{c1}$ we find that indeed $(\varphi_1, \varphi_2) = (\pi, 0)$ is the solution that minimizes the total energy (2.54).

Non-zero solutions of (2.57) exist only when $f(\varphi_1)$ and $\sin\varphi_1$ have additional intersections. For symmetry reasons only the interval $0 \leq \varphi \leq \pi$ needs to be considered. Because $\kappa \geq 1$ and $\beta_L \geq 0$, the slope at the origin $f'(0) = \kappa(1 + \beta_L)$ will be larger than 1. Thus $f(\varphi_1) > \sin\varphi_1$ for $\varphi_1 \downarrow 0$. At $\varphi_1 = \pi$ both $\sin\varphi_1$ and $f(\varphi_1)$ cross the β_L-axis. If at this point the slope $f'(\pi)$ is larger than -1, $f(\varphi_1) < \sin\varphi_1$ for $\varphi_1 \uparrow \pi$ and therefore the two lines must have crossed *above* the β_L-axis (that is, a non-zero current solution), because $\sin\varphi_1 > 0$ for $0 < \varphi_1 < \pi$. The condition $f'(\pi) > -1$ can be written as $\beta_L > \beta_L^\star$ with

$$\beta_L^\star = 1 - \kappa^{-1} \tag{2.58}$$

We have demonstrated that for $\beta_L > \beta_L^\star$ non-zero solutions exist. In the following we will show that these solutions do not exist for screening parameters *smaller* than $\beta_L^\star$. This will be proven by demonstrating that on the interval $0 < \varphi_1 < \pi$ the function $f(\varphi_1)$ is always larger than $\sin\varphi_1$ when $\beta_L < \beta_L^\star$. In general, the inequality

$$-\cos(\varphi_1 + x)\sin x < x \qquad 0 < x < \pi \tag{2.59}$$

is true for any φ_1 when $0 < x < \pi$ (the requirement for x will be checked later). Making use of the trigonometric relation $\sin a - \sin b = 2\cos(\frac{a+b}{2})\sin(\frac{a-b}{2})$ equation (2.59) can be rewritten to

$$\sin\varphi_1 - \sin(\varphi_1 + 2x) < 2x \qquad 0 < x < \pi \tag{2.60}$$

Multiplying both sides with κ, substituting

$$x \equiv \frac{\beta_L \sin\varphi_1}{2} \tag{2.61}$$

and rearranging terms we obtain

$$\kappa(1 - \beta_L)\sin\varphi_1 < \kappa\sin(\varphi_1 + \beta_L \sin\varphi_1) \equiv f(\varphi_1) \tag{2.62}$$

Since we are considering the case $\beta_L < 1 - \kappa^{-1}$ (which lies between 0 and 1) on the interval $0 < \varphi_1 < \pi$ the condition $0 < x < \pi$ is automatically satisfied. Moreover, under these conditions the left-hand side of equation (2.62) is larger than $\sin\varphi_1$ so we obtain

$$\sin\varphi_1 < f(\varphi_1) \tag{2.63}$$

Thus we have shown that for $\beta_L < \beta_L^\star$ no non-zero solutions exist and only the currentless solutions are allowed below this threshold.

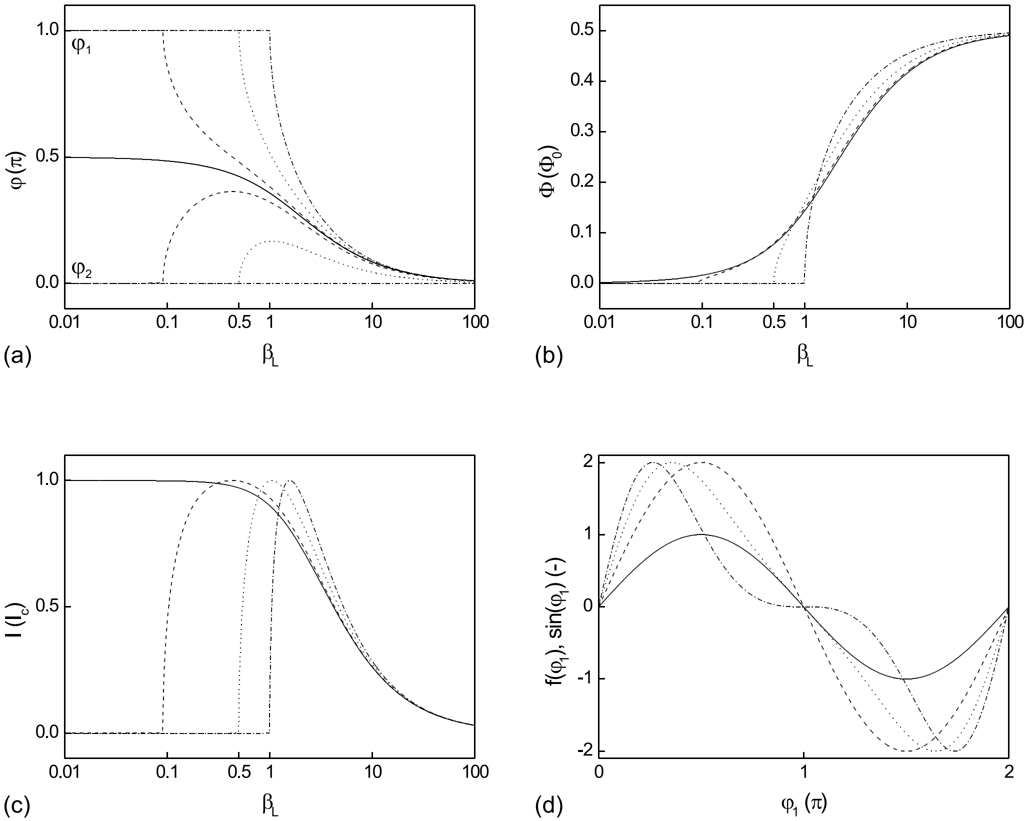

Figure 2.11: (a) Phases, (b) flux and (c) current of the ground state of a π-ring as a function of the screening parameter β_L for different values of $\kappa \equiv \frac{I_{c2}}{I_{c1}}$. When the junctions are asymmetric the ground state is currentless when the screening parameter is below a threshold value $\beta_L^\star$. Solid lines: $\kappa = 1$, dashed lines: $\kappa = 1.1$, dotted lines: $\kappa = 2$, dash-dotted lines: $\kappa = 10000$. (d) Graphical representation for the solutions of equation (2.57), plotted for $\kappa = 2$ and different values of β_L. Solid line: $\sin\varphi_1$, dashed line: $f(\varphi_1)$ for $\beta_L = 0$, dotted line: $f(\varphi_1)$ for $\beta_L = 0.5$, dash-dotted line: $f(\varphi_1)$ for $\beta_L = 1$.

2.11 Josephson inductance

From the Josephson equations (2.24) and (2.26) the relation between the voltage over a junction and the time derivative of the current flowing through that junction can easily be derived to read

$$V = L_J \frac{dI}{dt} \tag{2.64}$$

with

$$L_J = \frac{\Phi_0}{2\pi\sqrt{I_c^2 - I^2}} \tag{2.65}$$

Thus it follows directly from the Josephson relations that a Josephson junction acts as a non-linear inductor. L_J is known as the *Josephson inductance*.

2.12 Summary

In this chapter we have briefly reviewed some of the key aspects of superconducting loops containing Josephson junctions. We have discussed how the phenomenon of fluxoid quantization in such loops can be used to realize a DC SQUID, one of the most sensitive sensors currently in existence. The DC SQUID plays a central role in almost all experiments described in this thesis. Incorporating an intrinsic π-phase shift in superconducting loops containing Josephson junctions was shown to lead to an altered ground state, which for large screening parameters leads to spontaneously generated flux corresponding to a fraction of a flux quantum (increasing to half a flux quantum in the large inductance limit). Though we have presented several consequences of intrinsic π-phase shifts, the mechanism by which such a π-phase shift can be incorporated was not discussed. How this phase shift was realized in the devices discussed in this thesis will be the topic of the next chapter.

Chapter 3

d-wave-induced half-integer magnetic flux quanta

3.1 Introduction

In the previous chapter several basic properties of superconducting rings containing Josephson junctions were discussed. In section 2.10 it was shown that when such rings contain an intrinsic π-phase shift, the ground state of such a ring is characterized by the spontaneous generation of fractional flux quanta, which grow asymptotically to $\Phi_0/2$ in the large inductance limit. For the experiments discussed in this thesis the unconventional order parameter symmetry of $YBa_2Cu_3O_{7-\delta}$ (YBCO) is exploited in order to realize such a π-phase shift. In this chapter the pairing symmetries of YBCO and Nb are discussed, as well as how the difference in order parameter symmetry can be used to obtain π-loops.

3.2 Order parameter symmetry

In this section a brief introduction is given to the concept of order parameter symmetry. Whereas in the field of superconductivity many authors start out by directly considering the symmetry of the superconducting gap Δ, a slightly different approach is taken here. The concept of order parameter symmetry is introduced via the quantum mechanical wavefunction $\Psi(\mathbf{r}, t)$ and the spherical harmonics $Y_\ell^m(\varphi, \theta)$ which can be used to describe its symmetry. The first subsections are concerned with the general 3D symmetry functions. In the later sections the projection of these functions onto the two-dimensional plane and in particular the normalization of these functions is considered.

3.2.1 3D order parameter symmetry

As was discussed in section 2.3 the superconducting condensate can be described by a complex wavefunction $\Psi(\mathbf{r}, t)$ which has an amplitude $|\Psi(\mathbf{r}, t)|$ and a phase $\theta(\mathbf{r}, t)$. When expressed in spherical coordinates, this wavefunction can conveniently be expressed as a linear combination of the *spherical harmonics* $Y_\ell^m(\varphi, \theta)$

$$\Psi(r, \varphi, \theta, t) = \sum_{\ell, m} Y_\ell^m(\varphi, \theta)\psi_\ell^m(r, t) \qquad (3.1)$$

$Y_0^0 = \sqrt{\frac{1}{4\pi}}$	$Y_2^{\pm 2} = \sqrt{\frac{15}{32\pi}} \sin^2\theta e^{\pm 2i\varphi}$
$Y_1^0 = \sqrt{\frac{3}{4\pi}} \cos\theta$	$Y_3^0 = \sqrt{\frac{7}{16\pi}} (5\cos^3\theta - 3\cos\theta)$
$Y_1^{\pm 1} = \mp\sqrt{\frac{3}{8\pi}} \sin\theta e^{\pm i\varphi}$	$Y_3^{\pm 1} = \mp\sqrt{\frac{21}{64\pi}} \sin\theta (5\cos^2\theta - 1) e^{\pm i\varphi}$
$Y_2^0 = \sqrt{\frac{5}{16\pi}} (3\cos^2\theta - 1)$	$Y_3^{\pm 2} = \sqrt{\frac{105}{32\pi}} \sin^2\theta \cos\theta e^{\pm 2i\varphi}$
$Y_2^{\pm 1} = \mp\sqrt{\frac{15}{8\pi}} \sin\theta \cos\theta e^{\pm i\varphi}$	$Y_3^{\pm 3} = \mp\sqrt{\frac{35}{64\pi}} \sin^3\theta e^{\pm 3i\varphi}$

Table 3.1: Spherical harmonics for $\ell = 0, 1, 2, 3$.

with φ the azimuthal angle and θ the polar angle[1]. The spherical harmonics are given by [105]

$$Y_\ell^m(\varphi, \theta) = \epsilon \sqrt{\frac{(2\ell + 1)}{4\pi} \frac{(\ell - |m|)!}{(\ell + |m|)!}} e^{im\varphi} P_\ell^m(\cos\theta) \tag{3.2}$$

with ℓ a positive integer, m an integer between -ℓ and +ℓ, and

$$\epsilon = \begin{cases} 1 & \text{if } m \leq 0 \\ (-1)^m & \text{if } m > 0 \end{cases} \tag{3.3}$$

$P_\ell^m(\cos\theta)$ is the associated Legendre function, defined by

$$P_\ell^m(x) = (1 - x^2)^{|m|/2} \left(\frac{d}{dx}\right)^{|m|} P_\ell(x) \tag{3.4}$$

with

$$P_\ell(x) = \frac{1}{2^\ell \ell!} \left(\frac{d}{dx}\right)^\ell (x^2 - 1)^\ell \tag{3.5}$$

the ℓth Legendre polynomial. The first few spherical harmonics are listed in table 3.1. The spherical harmonics constitute a complete set of orthonormal functions

$$\int\limits_{\varphi=0}^{2\pi} \int\limits_{\theta=0}^{\pi} Y_\ell^m(\varphi, \theta) Y_{\ell'}^{m'}(\varphi, \theta)^* \sin\theta d\theta d\varphi = \delta_{\ell\ell'} \delta_{mm'} \tag{3.6}$$

that can be used to construct any φ- and θ-dependence, and are therefore very suitable to describe the (angular) symmetry of the order parameter.

In general, the spherical harmonics $Y_\ell^m(\varphi, \theta)$ are complex functions. However, an alternative but equivalent set of spherical harmonics $X_\ell^m(\varphi, \theta)$ comprising only real basis functions can be constructed from (3.2) by using the sum and difference of Y_ℓ^m and Y_ℓ^{-m} rather than the functions themselves:

$$X_\ell^m(\varphi, \theta) = \begin{cases} Y_\ell^0(\varphi, \theta) & m = 0 \\ \frac{1}{\sqrt{2}} \left[Y_\ell^m(\varphi, \theta) + (-1)^m Y_\ell^{-m}(\varphi, \theta) \right] & m > 0 \\ \frac{1}{\sqrt{2}i} \left[Y_\ell^m(\varphi, \theta) - (-1)^m Y_\ell^{-m}(\varphi, \theta) \right] & m < 0 \end{cases} \tag{3.7}$$

---

[1] The angular coordinates are not to be confused with the phase θ and gauge invariant phase drop φ that were introduced earlier

From equations (3.2) through (3.5) one can easily derive that the complex conjugate of $Y_\ell^m(\varphi,\theta)$ is related to $Y_\ell^{-m}(\varphi,\theta)$ via

$$Y_\ell^m(\varphi,\theta)^* = (-1)^m Y_\ell^{-m}(\varphi,\theta) \tag{3.8}$$

so the spherical harmonics in equation (3.7) can be rewritten as

$$X_\ell^m(\varphi,\theta) = \begin{cases} Y_\ell^0(\varphi,\theta) & m=0 \\ \sqrt{2}\Re\left\{Y_\ell^m(\varphi,\theta)\right\} & m>0 \\ \sqrt{2}\Im\left\{Y_\ell^m(\varphi,\theta)\right\} & m<0 \end{cases} \tag{3.9}$$

With $\Re\left\{Y_\ell^m(\varphi,\theta)\right\}$ and $\Im\left\{Y_\ell^m(\varphi,\theta)\right\}$ the real and imaginary parts of $Y_\ell^m(\varphi,\theta)$, respectively. As a last refinement, we can redefine the basis functions such that only the spherical harmonics Y_ℓ^m with $m \geq 0$ are required. Making use of the fact that

$$\Im\left\{Y_\ell^{-m}\right\} = (-1)^{m+1}\Im\left\{Y_\ell^m\right\} \tag{3.10}$$

we see that the imaginary parts for positive and negative m are related only via a minus-sign when m is even, and therefore build up exactly the same function space. Thus if we redefine the basis functions $X_\ell^m(\varphi,\theta)$ for $m<0$ by incorporating this factor $(-1)^{m+1}$ we obtain a complete set of functions $Z_\ell^m(\varphi,\theta)$ which is equivalent to the spherical harmonics in equation (3.2) but consists of only real functions making use of Y_ℓ^m with $m \geq 0$:

$$Z_\ell^m(\varphi,\theta) = \begin{cases} Y_\ell^0(\varphi,\theta) & m=0 \\ \sqrt{2}\Re\left\{Y_\ell^{|m|}(\varphi,\theta)\right\} & m>0 \\ \sqrt{2}\Im\left\{Y_\ell^{|m|}(\varphi,\theta)\right\} & m<0 \end{cases} \tag{3.11}$$

The functions $Z_\ell^m(\varphi,\theta)$ obey the normalization condition

$$\int\limits_{\varphi=0}^{2\pi}\int\limits_{\theta=0}^{\pi} Z_\ell^m(\varphi,\theta) Z_{\ell'}^{m'}(\varphi,\theta)^* \sin\theta d\theta d\varphi = \delta_{\ell\ell'}\delta_{mm'} \tag{3.12}$$

(the complex conjugate in this equation is actually superfluous because all $Z_\ell^m(\varphi,\theta)$ are real functions). A graphical representation of the order parameter symmetries for the first four values of the quantum number ℓ is depicted in figure 3.1. The figures are labelled by the commonly used names s-, p- d- and f-wave which originate from atomic spectroscopy.

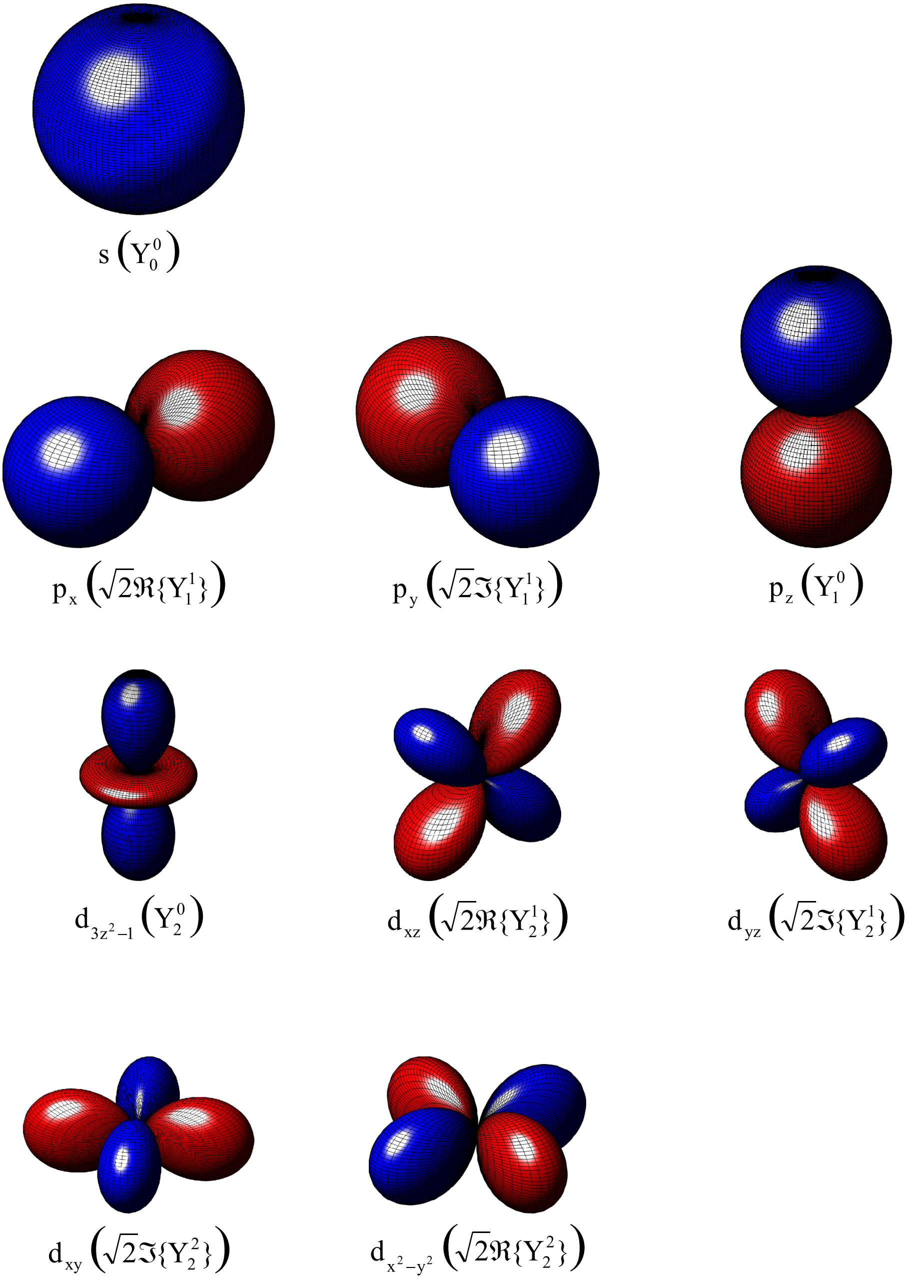

Figure 3.1: Graphical representation of the *s*-, *p*- and *d*-wave order parameter symmetries. The amplitude and phase are indicated by the radius and color, respectively. Blue and red lobes have a relative phase difference π.

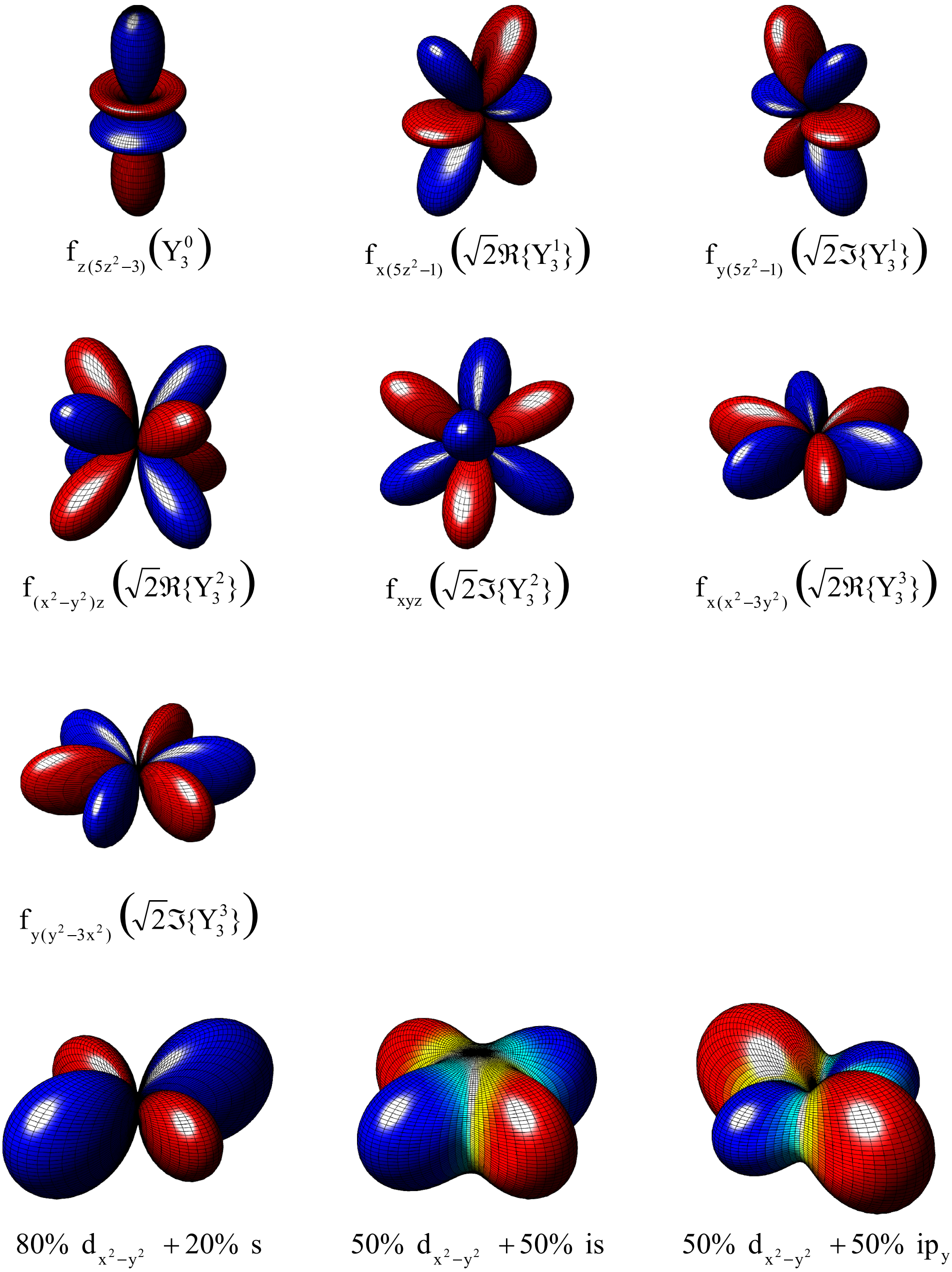

$f_{z(5z^2-3)}\left(Y_3^0\right)$

$f_{x(5z^2-1)}\left(\sqrt{2}\Re\{Y_3^1\}\right)$

$f_{y(5z^2-1)}\left(\sqrt{2}\Im\{Y_3^1\}\right)$

$f_{(x^2-y^2)z}\left(\sqrt{2}\Re\{Y_3^2\}\right)$

$f_{xyz}\left(\sqrt{2}\Im\{Y_3^2\}\right)$

$f_{x(x^2-3y^2)}\left(\sqrt{2}\Re\{Y_3^3\}\right)$

$f_{y(y^2-3x^2)}\left(\sqrt{2}\Im\{Y_3^3\}\right)$

80% $d_{x^2-y^2}$ + 20% s

50% $d_{x^2-y^2}$ + 50% is

50% $d_{x^2-y^2}$ + 50% ip_y

Figure 3.1: (continued) f-wave order parameter symmetry and three linear combinations of order parameters. The phases differ from 0 and π only for linear combinations involving imaginary and real parts.

3.2.2 Linear combinations of spherical harmonics

The last three plots in figure 3.1 show linear combinations of the spherical harmonics. In the context of order parameter symmetry these linear combinations are often referred to as *admixtures* to the order parameter. For example, as will be discussed in more detail in chapter 5, the general consensus currently is that the order parameter symmetry in YBCO is predominantly $d_{x^2-y^2}$-wave with a small s-wave component (admixture).

In general an order parameter symmetry $\Omega(\varphi, \theta)$ comprising N spherical harmonics can be written as

$$\Omega(\varphi, \theta) = \sum_{n=1}^{N} c_n Z_n(\varphi, \theta) \tag{3.13}$$

The choice of coefficients c_n is fixed by two conditions: the (relative) weight factors w_n of the different components and the normalization of $\Omega(\varphi, \theta)$. If the coefficients c_n are defined as

$$c_n = \frac{w_n}{\sqrt{\sum\limits_{n=1}^{N} |w_n|^2}} \tag{3.14}$$

both conditions are satisfied: the coefficients are proportional to the weight factors and the normalization condition is satisfied because

$$\sum_{n=1}^{N} |c_n|^2 = 1 \tag{3.15}$$

By allowing imaginary values for the weight factors, one can construct complex admixtures to the order parameter symmetry, as is shown in the last two plots of figure 3.1. In general, these complex admixtures differ from real admixtures by the absence of nodes and a phase different from 0 or π. The functions for the linear combinations shown in figure 3.1 are

$$\left.\begin{array}{l} 80\%\ d_{x^2-y^2} \\ 20\%\ s \end{array}\right\} \quad \tfrac{4}{\sqrt{17}} Z_2^2 + \tfrac{1}{\sqrt{17}} Z_0^0 \tag{3.16}$$

$$\left.\begin{array}{l} 50\%\ d_{x^2-y^2} \\ 50\%\ is \end{array}\right\} \quad \tfrac{1}{\sqrt{2}} Z_2^2 + \tfrac{i}{\sqrt{2}} Z_0^0 \tag{3.17}$$

$$\left.\begin{array}{l} 50\%\ d_{x^2-y^2} \\ 50\%\ ip_y \end{array}\right\} \quad \tfrac{1}{\sqrt{2}} Z_2^2 + \tfrac{i}{\sqrt{2}} Z_1^{-1} \tag{3.18}$$

3.2.3 2D order parameter symmetry

The order parameter symmetry of the cuprate superconductors is usually described in two-dimensional (k_x,k_y)-space. To describe the order parameter symmetry in two dimensions, the spherical harmonics can be projected onto the 2D plane by setting the polar angle θ to $\pi/2$. This will eliminate all solutions for which $|m| \neq \ell$, as can readily be seen from equations (3.2) through (3.5). The ℓth Legendre polynomial (3.5) always has a highest term of order x^ℓ. Thus for $x = \cos\theta = 0$ the associated Legendre function (3.4) can only have non-zero solutions when $|m| = \ell$. More precisely,

$$P_\ell^m(0) = \begin{cases} \frac{(2\ell)!}{2^\ell \ell!} & |m| = \ell \\ 0 & |m| \neq \ell \end{cases} \tag{3.19}$$

	ℓ	m	$z_\ell^m(\varphi)$	$\frac{\Delta(\varphi)}{\Delta_{max}}$
s	0	0	$\frac{1}{\sqrt{2\pi}}$	1
p_x	1	1	$\frac{1}{\sqrt{\pi}}\cos\varphi$	$\cos\varphi$
p_y	1	-1	$\frac{1}{\sqrt{\pi}}\sin\varphi$	$\sin\varphi$
$d_{x^2-y^2}$	2	2	$\frac{1}{\sqrt{\pi}}\cos(2\varphi)$	$\cos^2\varphi-\sin^2\varphi$
d_{xy}	2	-2	$\frac{1}{\sqrt{\pi}}\sin(2\varphi)$	$2\cos\varphi\sin\varphi$
$f_{x(x^2-3y^2)}$	3	3	$\frac{1}{\sqrt{\pi}}\cos(3\varphi)$	$\cos\varphi(\cos^2\varphi-3\sin^2\varphi)$
$f_{y(y^2-3x^2)}$	3	-3	$\frac{1}{\sqrt{\pi}}\sin(3\varphi)$	$-\sin\varphi(\sin^2\varphi-3\cos^2\varphi)$

Table 3.2: Two-dimensional order parameter symmetries for $\ell = 0, 1, 2, 3$. Both the normalized functions $z_\ell^m(\varphi)$ and the ratio of the superconducting gap $\Delta(\varphi)$ to its maximum absolute value Δ_{max} are tabulated.

The projection of the spherical harmonics (3.2) can thus be written as

$$Y_\ell^m(\varphi, \frac{\pi}{2}) = \begin{cases} \frac{\epsilon}{2^\ell \ell!}\sqrt{\frac{(2\ell+1)!}{4\pi}}e^{im\varphi} & |m| = \ell \\ 0 & |m| \neq \ell \end{cases} \tag{3.20}$$

The projection has greatly simplified the basis functions: besides the normalization constant (which will have to be redefined for the two-dimensional case anyway) we are left with either a constant for the s-wave or $e^{im\varphi}$ for higher-order symmetries. In analogy to the derivation of the spherical harmonics $Z_\ell^m(\varphi, \theta)$ in subsection 3.2.1 we can construct a real set of orthonormal basis functions $z_\ell^m(\varphi)$ by using the sum and difference of $Y_\ell^m(\varphi, \frac{\pi}{2})$ and $Y_\ell^{-m}(\varphi, \frac{\pi}{2})$:

$$z_\ell^m(\varphi) = \begin{cases} \frac{1}{\sqrt{2\pi}} & m = 0 \\ \frac{1}{\sqrt{\pi}}\cos(\ell\varphi) & m > 0 \\ \frac{1}{\sqrt{\pi}}\sin(\ell\varphi) & m < 0 \end{cases} \tag{3.21}$$

This set of functions follows the normalization condition

$$\int_{\varphi=0}^{2\pi} z_\ell^m(\varphi) z_{\ell'}^{m'}(\varphi)^* d\varphi = \delta_{\ell\ell'}\delta_{mm'} \tag{3.22}$$

with δ the Kronecker delta. In table 3.2 the $z_\ell^m(\varphi)$ are displayed for the first four values of the quantum number ℓ.

3.2.4 Normalization of the 2D order parameter symmetry

In literature the order parameter symmetry in superconductors is mostly used in relation to the superconducting gap Δ. Because the gap is proportional to the superconducting order parameter it follows the same symmetry (therefore the order parameter symmetry is also often referred to as the *gap symmetry*). This leads to a slightly different definition of the symmetry functions. Instead of using normalized functions as used in the above, it is convention to define symmetry functions as the ratio of the superconducting gap to its maximum absolute value $\Delta_{max} \equiv \max(|\Delta(\varphi)|)$. Thus the functional forms are still the same as $z_\ell^m(\varphi)$, but they are 'normalized' to have a maximum amplitude of 1. The basis functions (expressed in terms of $\cos\varphi$ and $\sin\varphi$) that follow from this convention are listed in the last column of table 3.2.

A quick glance at table 3.2 reveals that it makes a big difference as to which convention is used for the description of the order parameter. When considering the 'pure' order parameters there is no problem because the different symmetry functions only differ by a proportionality constant. However, when considering admixtures there *is* an important difference between the two sets of symmetry functions, because of the different ratio of prefactors within each set. It can easily be shown that $\sin(\ell\varphi)$ and $\cos(\ell\varphi)$ have a normalization constant of $1/\sqrt{\pi}$ for all ℓ, so this difference only occurs for the s-wave symmetry.

Also the coefficients when considering linear combinations will differ when using non-normalized basis functions. When using the normalized functions $z_\ell^m(\varphi)$ any linear combination $\Omega(\varphi)$ can be created, in analogy to equation (3.13), by using the coefficients in equation (3.14). This ensures that $\Omega(\varphi)$ is also a normalized function in which the basis functions $z_\ell^m(\varphi)$ are represented according to their weight factors. The convention in literature for the admixtures is to use coefficients $c_n^\dagger$ that are proportional to the weight factors w_n and add up to 1

$$c_n^\dagger = \frac{w_n}{\sum\limits_{n=1}^{N} |w_n|} \tag{3.23}$$

As can be seen by comparing equations (3.14) and (3.23) this will only result in a different proportionality constant (except, as mentioned above, for admixtures involving an s-wave component). The obtained linear combination will not necessarily be normalized to 1, however.

The choice to use normalized or non-normalized basis functions for the description of the order parameter symmetry has serious consequences when considering admixtures containing an s-wave and one or more higher-order symmetries. To illustrate these consequences, let us consider the 50% s + 50% $d_{x^2-y^2}$ gap symmetry. In figure 3.2(a) this gap is constructed using non-normalized functions

$$\frac{\Delta(\varphi)}{\Delta_{max}} = \frac{1}{2} + \frac{1}{2}\cos(2\varphi) \tag{3.24}$$

In figure 3.2(b) the gap is constructed using the normalized functions z_ℓ^m

$$\frac{\Delta(\varphi)}{\Delta_{max}} = \frac{1+\sqrt{2}\cos(2\varphi)}{1+\sqrt{2}} \tag{3.25}$$

It is clear that the choice of basis functions has a significant effect on the resulting interpretation of the gap symmetry. To prevent ambiguous interpretations such as that presented in the example above, it is imperative that the convention used for the construction of such admixtures is clear. Though one could argue that using normalized functions is a 'cleaner' approach, we will follow the convention used in literature and from this point on use the non-normalized basis functions shown in the last column of table 3.2.

In figure 3.3 the amplitude and phase of several symmetry functions are plotted. The polar plots of these functions have also been added for clarity. The functions shown are the

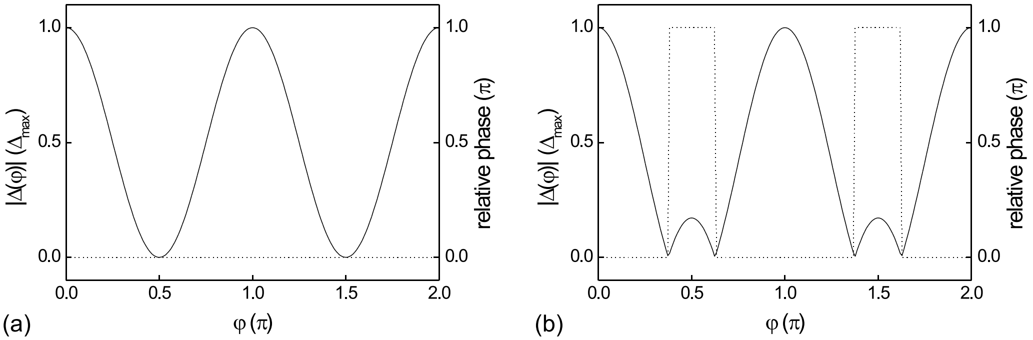

Figure 3.2: Graphical representation of a 50% s + 50% $d_{x^2-y^2}$ symmetry using (a) Non-normalized symmetry functions (b) normalized symmetry functions, as mentioned in the text. Solid lines: amplitude, dotted lines: (relative) phase.

s-, p-, and d- wave symmetries and (complex) admixtures to the $d_{x^2-y^2}$-wave symmetry (80% $d_{x^2-y^2}$-wave and 20% admixture). The last two figures display the somewhat exotic anisotropic s-wave and extended s-wave, which can be written as[2]

$$\text{anisotropic } s\text{-wave:} \quad \frac{\Delta(\varphi)}{\Delta_{max}} = \left(1 - \frac{\Delta_{min}}{\Delta_{max}}\right)\cos^4(2\varphi) + \frac{\Delta_{min}}{\Delta_{max}} \tag{3.26}$$

and

$$\text{extended } s\text{-wave:} \quad \frac{\Delta(\varphi)}{\Delta_{max}} = \left(1 + \gamma^2\right)\cos^2(2\varphi) - \gamma^2 \tag{3.27}$$

respectively. The anisotropic s-wave was proposed in 1993 by Chakravarty *et al.* as a possible gap symmetry which followed from a model based on a tunnelling mechanism between the copper-oxygen planes in the cuprate superconductors [106]. At that time, no phase-sensitive experiments had been performed and the model seemed consistent with the then available angle-resolved photoemission spectroscopy (ARPES) measurements. It is now widely accepted that indeed there is a sign change between perpendicular directions in k-space and the idea of anisotropic s-wave has been abandoned at least for the cuprate superconductors.

The extended s-wave symmetry was proposed around the same period by scientists who believed that the strong suppression of the order parameter along the (2n+1)45° directions (n being an integer) would lead to a sign change in the order parameter for a range of angles along those directions. Like with the anisotropic s-wave, this concept has been abandoned now.

The names anisotropic- and extended s-wave are a bit unfortunate considering the fact that s-wave is normally used for the *isotropic* component of a symmetry function. Moreover, this nomenclature is also completely unnecessary, because any symmetry function can be expressed as a linear combination of the symmetry functions (3.21). For the extended s-wave symmetry, for example, also the more appropriate name s+g-wave is used, where the s-wave indeed represents the isotropic part.

---

[2] These functions were adapted from Van Harlingen [103], who uses yet another convention to describe the order parameter symmetry, which will not be discussed here

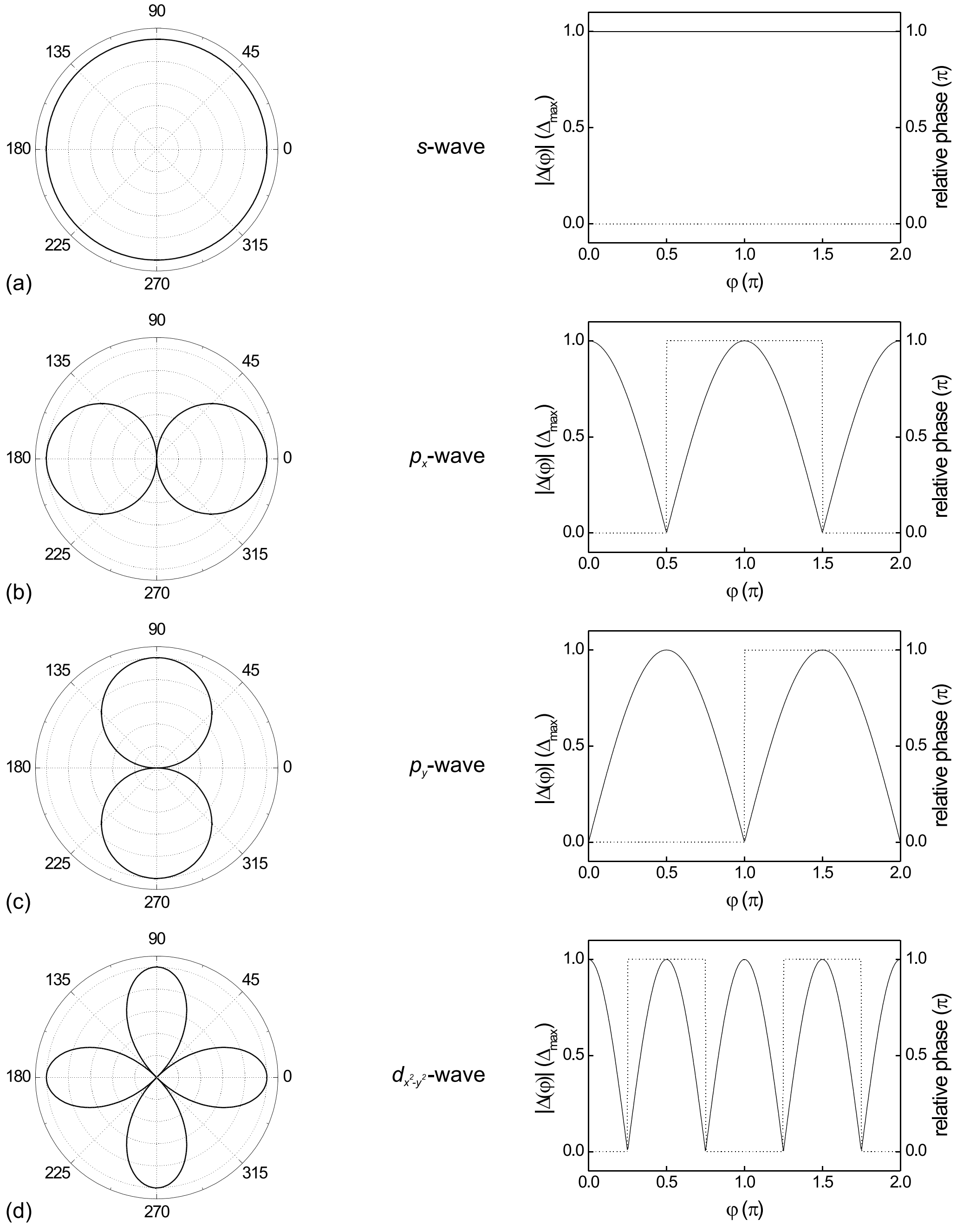

Figure 3.3: (a) s-wave, (b) p_x-wave, (c) p_y-wave, and (d) $d_{x^2-y^2}$-wave gap symmetries. Left: polar plots, right: amplitude (solid lines) and relative phase (dotted lines).

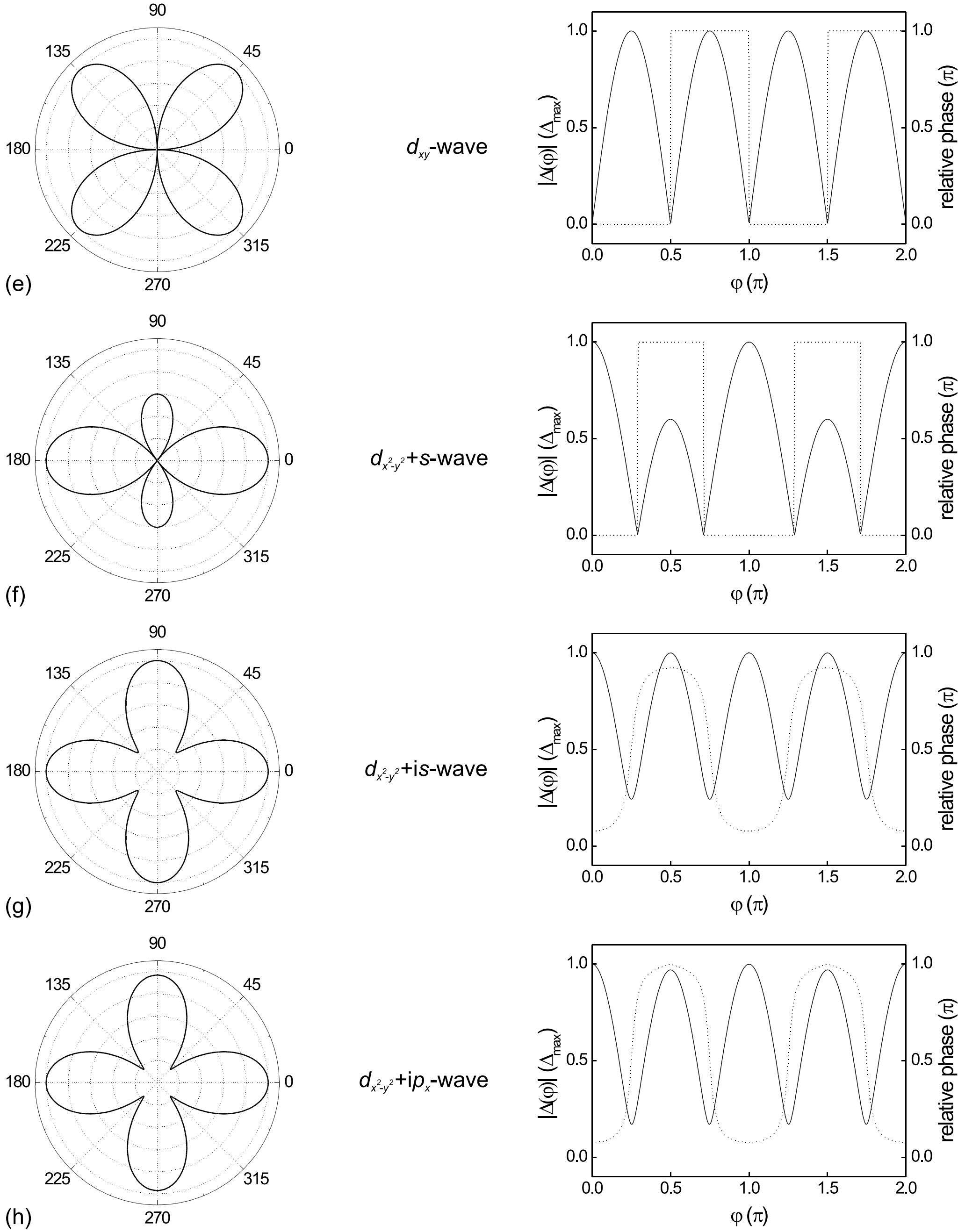

Figure 3.3: (continued) (e) d_{xy}-wave, (f) $d_{x^2-y^2}$+s-wave, (g) $d_{x^2-y^2}$+is-wave, and (h) $d_{x^2-y^2}$+ip_x-wave gap symmetries. The ratio d-wave : admixture is 80% : 20%.

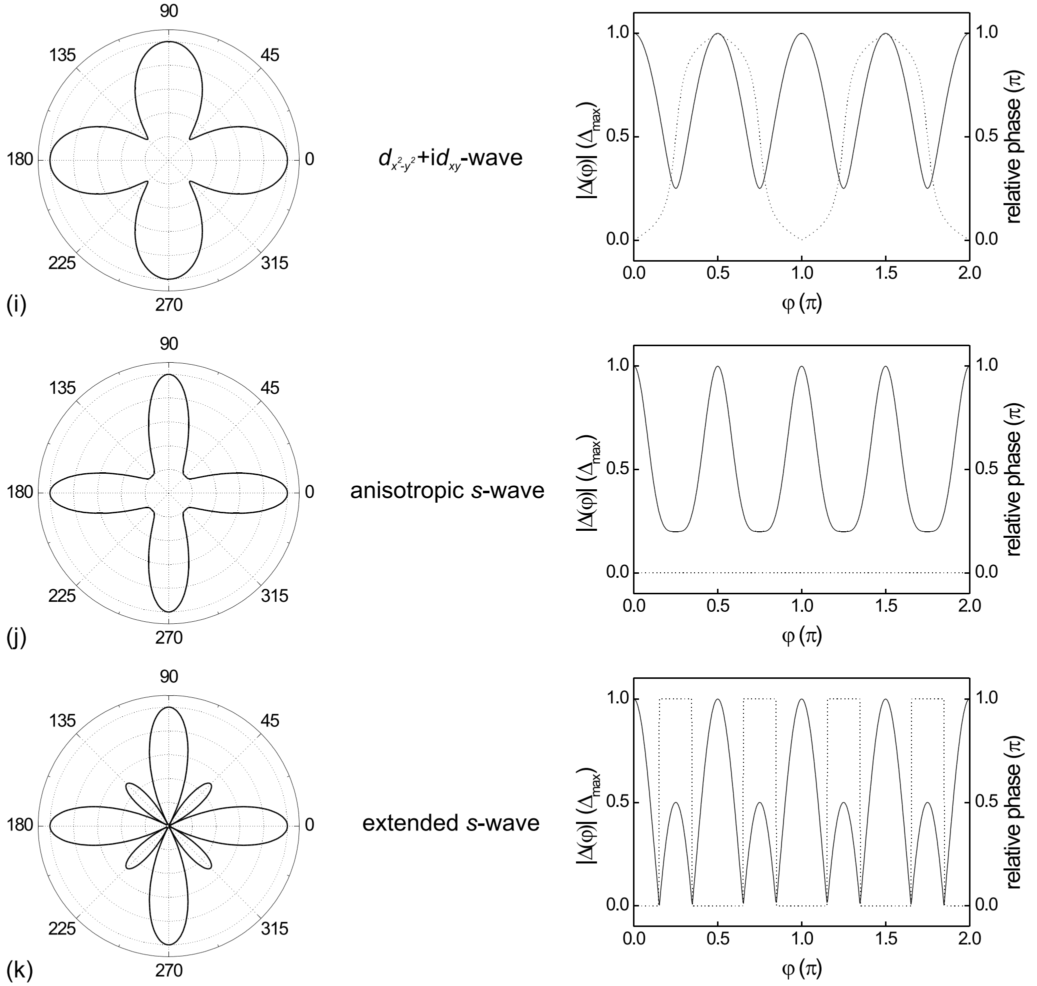

Figure 3.3: (continued) (i) $d_{x^2-y^2}$+id_{xy} (the ratio d-wave : admixture is 80% : 20%), (j) anisotropic s-wave ($\Delta_{min} = 0.2\Delta_{max}$), and (k) isotropic s-wave ($\gamma = 1/\sqrt{2}$).

3.3 d-wave-induced π-phase shifts

The pairing symmetry in YBCO is widely believed to be predominantly $d_{x^2-y^2}$-wave[3]. The d-wave symmetry results in a maximum gap amplitude along the main crystal axes and a strong suppression in the nodal directions (2n+1)45°. Moreover the phase difference between orthogonal directions is π and it is exactly this property which can be exploited to realize rings with an intrinsic π-phase shift. A ring made out of pure single crystalline YBCO will not suffice, however, because for such a ring the wavefunction will experience a 0-π transition four times when going around a closed loop, where an odd number

---

[3] For the present discussion possible admixtures to this symmetry are neglected, though in chapter 5 this issue will be readdressed

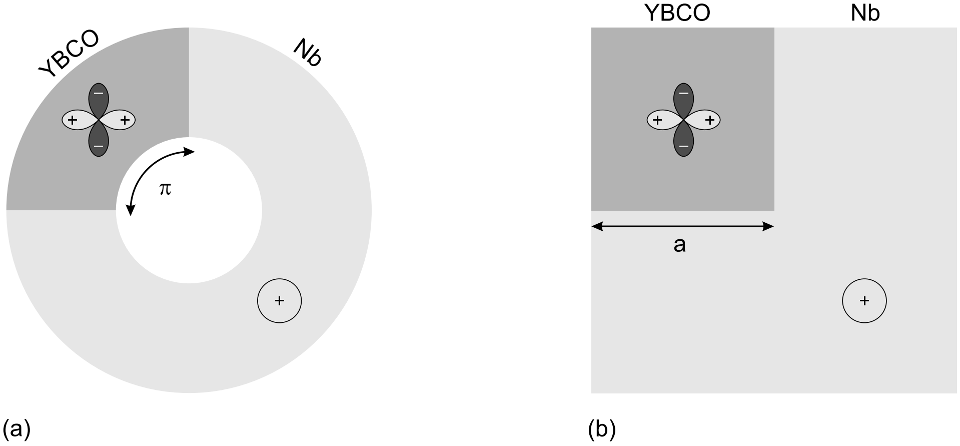

Figure 3.4: Schematic representation of (a) a π-ring and (b) a corner junction.

is required to obtain a π-ring. To exploit the d-wave symmetry for the spontaneous generation of half-integer flux quanta, superconducting structures have to be engineered such that the '0-lobe' of a superconductor is connected to the 'π-lobe' of another.

The first experimental realization of the half-integer magnetic flux quantum effect in a controlled geometry was by Tsuei *et al.* in 1994, through the use of tricrystals [104, 107]. In these samples a YBCO film was deposited on a tricrystal substrate and a three-junction ring was patterned around the tricrystal intersection. For reference, two control rings were defined across two bicrystal lines and one control ring was patterned on a single crystalline part of the substrate. The different relative orientations of the substrate are adopted by the crystal structure of the epitaxially grown YBCO film, and are such that the ring at the tricrystal intersection experiences an odd number of 0-π transitions. The sample was imaged using scanning SQUID microscopy (which will be discussed in section 5.5) and a spontaneously generated flux corresponding to a half-integer flux quantum was observed in the π-ring whereas no flux was observed in the control rings. This experiment has also been conducted on plain (unstructured) films, where a half-integer magnetic flux quantum was observed at the tricrystal intersection [104, 108–111].

A disadvantage of the tricrystal technique is the fact that only one half-integer flux quantum can be generated per sample, and that its position is fixed by the tricrystal intersection. Moreover the alignment of the central ring is by no means a trivial task and the tricrystal rings are relatively expensive. For most applications a more flexible method to generate the half-integer flux quantum is desirable. By connecting a conventional (s-wave) superconductor to a d-wave superconductor the intrinsic π-phase shift can be obtained in a much easier way. This technique has been used in several phase-sensitive experiments, for example by Wollman *et al.* [112, 113], Brawner and Ott [114] and Mathai *et al.* [115]. In 2003, Hilgenkamp *et al.* employed this technique to demonstrate the first arrays of half-integer flux quanta [116]. The hybrid superconductors can be used to fabricate π-rings and so-called *corner junctions*, which will be shortly discussed in the following sections.

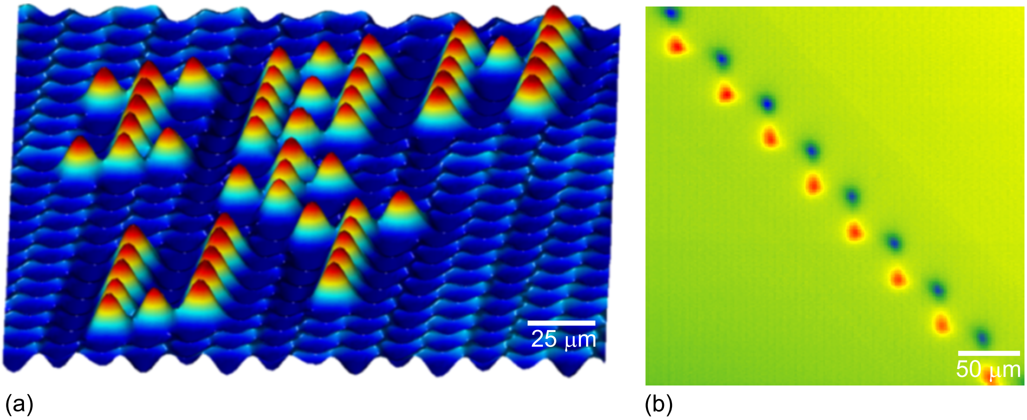

Figure 3.5: Scanning SQUID microscopy images of (a) a 2D array of corner junctions which have been manipulated to form the words 'IBM+UT' and (b) a zigzag junction.

3.3.1 YBCO/Nb π-rings

The concept in its most basic form is sketched in figure 3.4(a). By making use of two different order parameter symmetries, the '0-lobe' and the 'π-lobe' of the d-wave superconductor YBCO can be directly connected via the s-wave superconductor niobium. This results in an intrinsic π-phase shift (which is picked up in the YBCO) for any closed path around the loop. As was discussed in section 2.10, when such a ring is in the large inductance limit, its ground state is characterized by a spontaneously generated current corresponding to a half-integer flux quantum of positive or negative polarity. The fabrication of these hybrid rings requires special junctions in order to connect the two types of superconductors, which is an art in itself. A discussion of the design- and fabrication considerations of these junctions is given in section 4.4. The precise geometry of hybrid YBCO/Nb rings has large consequences for the ring characteristics. For example, the ring in figure 3.4(a) has its first junction angle at 90° and its second junction angle at 180° and is a π-ring. However, if the first junction angle had been at 0° the ring would have been a standard 0-ring. The transition point lies near the nodal angle of 45° and depends strongly on the precise details of the YBCO order parameter symmetry. Chapter 5 is completely dedicated to exactly this phenomenon.

3.3.2 YBCO/Nb corner junctions

When the hole of the ring is made smaller and smaller until it eventually vanishes, what remains is a so-called *corner junction*, which is depicted in figure 3.4(b). A fractional flux quantum will form in a corner junction when the facet length, which is labelled a in figure 3.4(b), is longer than the so-called *Josephson penetration depth*, or λ_J (7.13). A more thorough description of corner junctions in terms of the sine-Gordon equation will be given in subsection 7.2.1. Samples containing up to 75.000 working π-rings (150.000 junctions) on a single chip have already been fabricated and used as a model spin system [117, 118]. Also the controlled manipulation of half-integer flux quanta through the application of a local magnetic field has been demonstrated in corner junctions as can be seen from the scanning SQUID microscopy image in figure 3.5(a).

One special type of corner junction that should be mentioned here is the so-called *zigzag junction.* Zigzag junctions are a special type of corner junction: they consist of multiple corners arranged as a staircase. When the facet length is larger than the Josephson penetration depth these corners contain antiferromagnetically coupled half-integer flux quanta. A scanning SQUID microscopy image of a zigzag junction is depicted in figure 3.5(b). Chapter 7 of this thesis is devoted to the controlled manipulation of the flux polarities in a *double* corner junction though the application of a bias current.

3.4 Summary

One of the more striking differences between the conventional superconductors and the cuprates is the symmetry of the order parameter. In this chapter we have discussed the concept of order parameter symmetry. Starting with the spherical harmonics, several symmetry functions which are commonly used were presented, both for two- and three-dimensional waveforms. It has been shown how high-T_c and low-T_c superconductors can be combined to fabricate structures with intrinsic π-phase shifts, originating from the d-wave symmetry of the high-T_c superconductors. In these rings a flux corresponding to $\pm\Phi_0/2$ can arise spontaneously, i.e. without any applied current or magnetic field. Whereas this chapter was mainly concerned with the principles which lead to the half-flux quantum effect in high-T_c/low-T_c structures, in the next chapter the practical realization of such devices will be discussed. It should be mentioned that the half-flux quantum effect is by no means limited to hybrid superconducting structures such as the ones discussed in this thesis. The same result can in principle be obtained by any technique capable of inducing a π-phase shift in a superconducting ring.

Chapter 4

Experimental realization of High-T_C/Low-T_C devices

4.1 Introduction

This chapter is concerned with the fabrication of devices which combine the high-T_c cuprate superconductor YBCO and the low-T_c superconductor niobium. Even though superconductivity in these materials may rely on completely different principles, rings combining high-T_c and low-T_c superconductors exhibit fluxoid quantization (2.31) and the contacts between the superconductors satisfy the Josephson relations (2.24) and (2.26). Interestingly, as was discussed in the previous chapter, in such rings the difference in order parameter symmetry can be exploited in order to obtain spontaneously generated magnetic half-integer flux quanta, which may be used for fundamental studies or the development of novel circuit elements in superconducting electronics. In this chapter the YBCO/Nb devices are considered more from a materials science point-of-view. Some general aspects of the materials themselves are discussed, followed by a review of the used thin-film processing technology.

4.2 $YBa_2Cu_3O_{7-\delta}$

Yttrium barium copper oxide (YBCO) exists in several stoichiometric phases, such as $YBa_2Cu_3O_{7-\delta}$ (T_c=93 K), $YBa_2Cu_4O_8$ (80 K), and $Y_2Ba_4Cu_7O_{14+x}$ (95 K) [119–121]. The 123 phase of YBCO is most often used because it is easier to fabricate. In fact, since its discovery in 1987 [4] $YBa_2Cu_3O_{7-\delta}$ has been widely recognized as the 'workhorse' in the field of high-T_c superconductivity. The crystal structure of the 123 phase is depicted in figure 4.1(a). The structural and electronic properties of YBCO[1] are strongly related to the oxygen deficiency [122]. For $YBa_2Cu_3O_6$ ($\delta = 1$) the crystal structure is tetragonal (spacegroup P4/mmm): the a- and b crystal axes are equal but differ from the c-axis. Four oxygen atoms are located in the two copper-oxide planes and two more atoms are surrounding the two barium atoms. The sites in the ab-plane (at the top and bottom of the unit cell in figure 4.1) are empty for $\delta = 1$. With increasing oxygen content the

---

[1] Throughout this thesis, YBCO will refer to the 123 phase, i.e. $YBa_2Cu_3O_{7-\delta}$

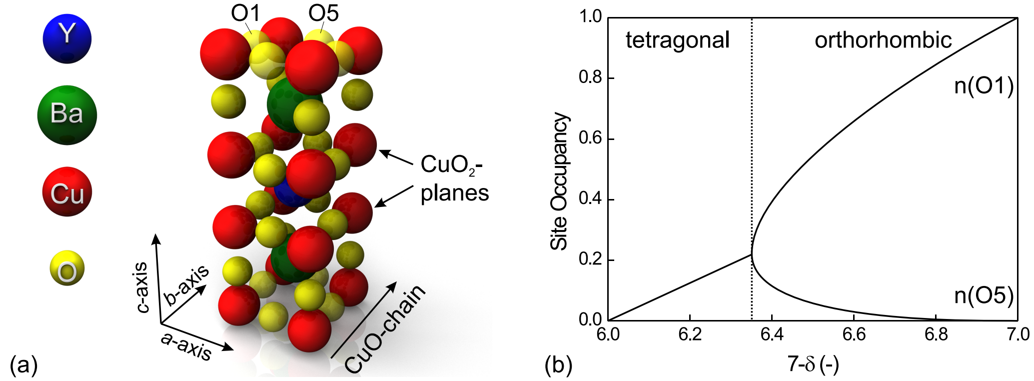

Figure 4.1: (a) Schematic representation of the unit cell of $YBa_2Cu_3O_{7-\delta}$. The oxygen sites at the top and (equivalently) bottom of the unit cell, indicated with a slight transparency, can be separated in two pairs: the O1 sites are located on the *b*-axis and the O5 sites are located on the *a*-axis. (b) Occupancy of the O1 and O5 sites as a function of the oxygen content $7-\delta$ (figure adapted from Jorgensen *et al.* [123]).

occupancy of these states increases and the oxygen divides evenly between sites that are located on the *a*-axis (the O5 sites) and sites that are located on the *b*-axis (the O1 sites). When $7-\delta$ reaches a value of approximately 6.35 a phase transition from the non-superconducting tetragonal phase to the superconducting orthorhombic phase occurs. For the orthorhombic crystal structure (space group Pmmm) the *a*-, *b*- and *c* axes are all different. When the oxygen content $7-\delta$ is increased even further the occupancy of the O1 sites increases but the occupancy of the O5 sites starts to decrease, as indicated in figure 4.1(b) [123]. When δ reaches its minimum value 0 for $YBa_2Cu_3O_7$ the oxygen has vanished from the O1 sites and the O5 sites are fully occupied, resulting in the formation of so-called CuO-chains in the *b*-axis direction. The cell constants and critical temperature of YBCO depend strongly on the oxygen deficiency. Though early studies seemed to suggest a plateau in the doping-dependence of T_c for $\delta < 0.2$, later experiments provided evidence for a maximum around $\delta = 0.13$ [124–126]. All YBCO thin films described in this thesis were at or close to optimal doping, resulting in a critical temperature of approximately 92 K and cell constants $a = 3.82$ Å, $b = 3.89$ Å, and $c = 11.65$ Å.

Though the mechanism of high-T_c superconductivity is currently not understood, it is generally believed that superconductivity in YBCO takes place in the copper-oxygen planes (in fact, all cuprate superconductors contain one or more copper-oxygen planes in the unit cell). There is some speculation about the role of the copper-oxygen chains in superconductivity, though many scientists believe that these act as charge reservoirs for the CuO_2 planes [127–133]. The copper-oxygen planes are not perfectly flat but are slightly buckled towards the Y^{3+}-ion which has a smaller ionic radius (90 pm) than the Ba^{2+} ion (135 pm) [134, 135]. Despite this buckling, superconductivity can still be regarded as a 2D phenomenon, and for this reason it is very important that YBCO thin films are grown epitaxially. The devices described in this thesis contain *c*-axis oriented YBCO films that were epitaxially grown on $SrTiO_3$ substrates. $SrTiO_3$ has a simple cubic crystal structure (space group Pm3m), and its lattice constant 3.905 Å matches well with

	Nb	$YBa_2Cu_3O_{7-\delta}$		Nb	$YBa_2Cu_3O_{7-\delta}$
T_c (K)	9.25	93	κ_{ab} (-)	1	125
λ_{ab} (nm)	39	150	κ_c (-)	-	5333
λ_c (nm)	-	1600	ρ_{ab} ($\mu\Omega$m)	0.152	3.3
ξ_{ab} (nm)	38	1.2	ρ_c ($\mu\Omega$m)	-	140
ξ_c (nm)	-	0.3	Δ (meV)	1.55	20

Table 4.1: Material properties of niobium and optimally doped $YBa_2Cu_3O_{7-\delta}$. Shown are the critical temperature T_c, the London penetration depth λ_L, the coherence length ξ, the Ginzburg-Landau parameter κ, the resistivity ρ, and the energy gap Δ (in-plane). For the anisotropic $YBa_2Cu_3O_{7-\delta}$ in-plane and out-of-plane values are given, for the isotropic only the in-plane value is shown.

the *a*- and *b* axes of YBCO. Several material properties of YBCO such as the London penetration depth, coherence length and Ginzburg-Landau parameter are summarized in table 4.1.

4.3 Niobium

With 9.25 K the low-T_c superconductor niobium has the highest transition temperature of the superconducting elements. This high critical temperature allows for operation at 4.2 K, the boiling point of liquid helium. Niobium oxidizes easily to a variety of oxides, capped by a thin Nb_2O_5 layer, which prevents further oxidation [136]. This natural Nb_2O_5 coating is dense, mechanically hard and stable. The melting point above 2000 K and low diffusivity below 400 K result in long time stability and robustness to thermal cycling. All these factors combined make niobium one of the most popular metallic superconductors. The crystal structure of niobium is BCC (space group Im3m). The niobium films that were used in our experiments consist of polycrystalline niobium (grain size $\approx$ 60-80 nm) which is much easier to fabricate than the epitaxially grown YBCO. The Josephson contacts between YBCO and niobium require some special attention, though. When pure niobium and YBCO are brought into contact the niobium will oxidize at the expense of oxygen in the YBCO. The degradation in these 'native barrier' junctions is so high that the contact is not able to support a supercurrent [137]. For this reason a thin layer of the chemically inert Au is deposited between the two electrodes, as discussed in section 4.4. In table 4.1 several material properties of niobium are summarized. Niobium is the only elemental superconductor which is type II, but with a Ginzburg-Landau parameter κ close to 1 it is near the type I regime. Because niobium is isotropic only the *ab* value has been listed, which is valid for any orientation.

4.4 Ramp-type Josephson junctions

The hybrid YBCO/Nb rings are connected via Josephson junctions. These connections require special attention because of the nature of superconductivity in YBCO. As was already mentioned superconductivity in the cuprate superconductors is generally believed to be a two-dimensional phenomenon, most probably taking place in the copper-oxygen planes. Because of the suppressed gap in the c-axis direction planar junctions are not suitable to connect the YBCO base electrode to the s-wave niobium counter electrode. Studies to Josephson contacts between high-T_c and low-T_c superconductors revealed that ramp-type Josephson junctions can be used to fabricate reliable junctions [137].

The cross section of a ramp-type Josephson junction is sketched in figure 4.2, where the YBCO film is assumed to be c-axis oriented (i.e., with the CuO_2 planes parallel to the substrate). For this geometry, the ab-plane of the YBCO base electrode is aligned with the niobium top electrode. Because of the YBCO d-wave pairing symmetry the coupling will be the largest when the junction edge is aligned with the a- or b-axis of the YBCO crystal structure.

The gold barrier is essential to obtain high-transparency YBCO/Nb junctions[2]. Its primary function is to chemically separate the two superconductors. Transmission electron microscopy (TEM) observations have shown that when niobium is directly deposited on top of YBCO a 6-7 nm insulating NbO_x barrier is formed at the YBCO/Nb interface [138]. The oxygen that is required for the oxidation of niobium is obtained from the neighboring YBCO, resulting in a degraded YBCO layer near the interface. The deposition of a thin layer of gold has been shown to prevent the chemical interaction between the two superconductors, increasing the critical current density by orders of magnitude [138, 139]. Other barrier metals such as Ag or Pt have also been successfully implemented as a chemical barrier [137]. A minimum gold thickness of 8 nm was experimentally found to be required to ensure a good wetting of the junction interface [137].

The overlap, which was typically a few μm for the samples discussed in this thesis, serves to compensate for small misalignments between the top- and bottom electrodes in the direction of the current transport. The STO capping layer prevents current transport in the c-axis direction, which is assumed to be negligible anyway because of the small coherence length in this direction[3]. Therefore the size of the overlap, unlike for planar junctions, will not have an influence on the junction critical current in this ramp-type geometry. However, the overlap does act as a shunting capacitance which has STO as the dielectric. This will be further discussed in subsection 7.4.1. During the design stage, the overlap was always designed such that the niobium overlap has a smaller width (i.e. the out-of-plane direction in figure 4.2) than the YBCO base electrode. This smaller width serves to allow for small in-plane misalignment errors between the top- and bottom electrodes in the direction *perpendicular* to current transport. Without this precaution a misalignment would result in the formation of an unintended π-facet which could generate unwanted flux (in the large facet limit) or reduce the critical current of the junction (in the small facet limit).

A crucial step in the preparation of the ramp-type interface is the structuring of the bevelled edge in the superconducting base electrode through argon ion milling. This procedure can severely degrade the quality of the base electrode near the interface. High resolution transmission electron microscopy studies on YBCO/Au interfaces clearly show an amorphous layer with a thickness of approximately 1.5 nm which resides at the interface between the high-T_c base electrode and the Au layer deposited at the freshly milled ramp edge [140–142]. Energy dispersive X-ray (EDX) analysis of this layer revealed a copper

---

[2] Though strictly speaking it would be more appropriate to speak of YBCO/Au/Nb junctions, throughout this thesis the 'Au' will be dropped and the junctions are simply referred to as YBCO/Nb junctions

[3] The STO layer will often not be mentioned explicitly, but is silently assumed to be present when the bottom electrode is referred to as 'YBCO'

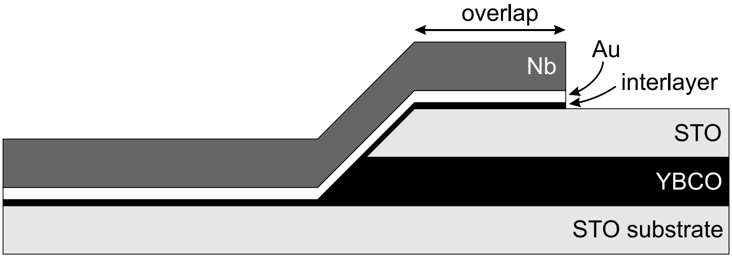

Figure 4.2: Schematic cross section of a ramp-type Josephson junction connecting the high-T_c superconductor YBCO to the low-T_c superconductor niobium.

content of nearly zero and an Y:Ba atomic ratio close to 1:1, which was attributed to preferential etching. Such an amorphous layer strongly suppresses the critical current density of the Josephson junction. For this reason a restoring interlayer is deposited and annealed *in situ* prior to the deposition of the gold barrier. This interlayer, with a typical thickness of 7 nm, restores the surface and leads to clean, reproducible and well-defined interfaces [143].

4.4.1 Definition of the junction area

Some electric properties, such as the critical current density j_c or the $R_N A$-product, are defined with respect to the junction area. However, there is no clear consensus on what area one is to use for the ramp-type geometry described in this section. The fact that superconductivity in the cuprate superconductor YBCO takes place in the two-dimensional (*ab*-oriented) CuO_2 planes leads some scientists to the conclusion that the junction area should be defined as the junction area perpendicular to current transport in the cuprate superconductor. Other scientists are more inclined to use the area of the physical junction barrier because of the *s*-wave nature of the niobium electrode and the fact that the shortest path between the two electrodes is perpendicular to this area.

Often, the precise definition will not be of much importance because in most cases one is interested in the critical current I_c. In a typical scenario the critical current density is determined from a measurement of I_c and then used as a parameter to design junctions with a specific critical current. Since this approach only relies on the relative junction sizes the exact definition of j_c will have no influence on the end result. For properties that rely directly on the critical current *density*, such as the Josephson penetration depth (7.13), the result will depend directly on the convention which is used.

4.5 Fabrication

This section is concerned with the practical realization of the YBCO/Nb ramp-type Josephson junctions. We will briefly discuss the deposition techniques and conditions that were used for the devices described in this thesis. Though we only describe YBCO/Nb junctions, the fabrication process is not necessarily restricted to these materials. The same facilities have been used to realize for example $Nd_{2-x}Ce_xCuO_{4-y}$ (NCCO)/Au/Nb, YBCO/$SrRuO_3$, and YBCO/$La_{1-x}Sr_xMnO_3$ junctions. Also preliminary experiments

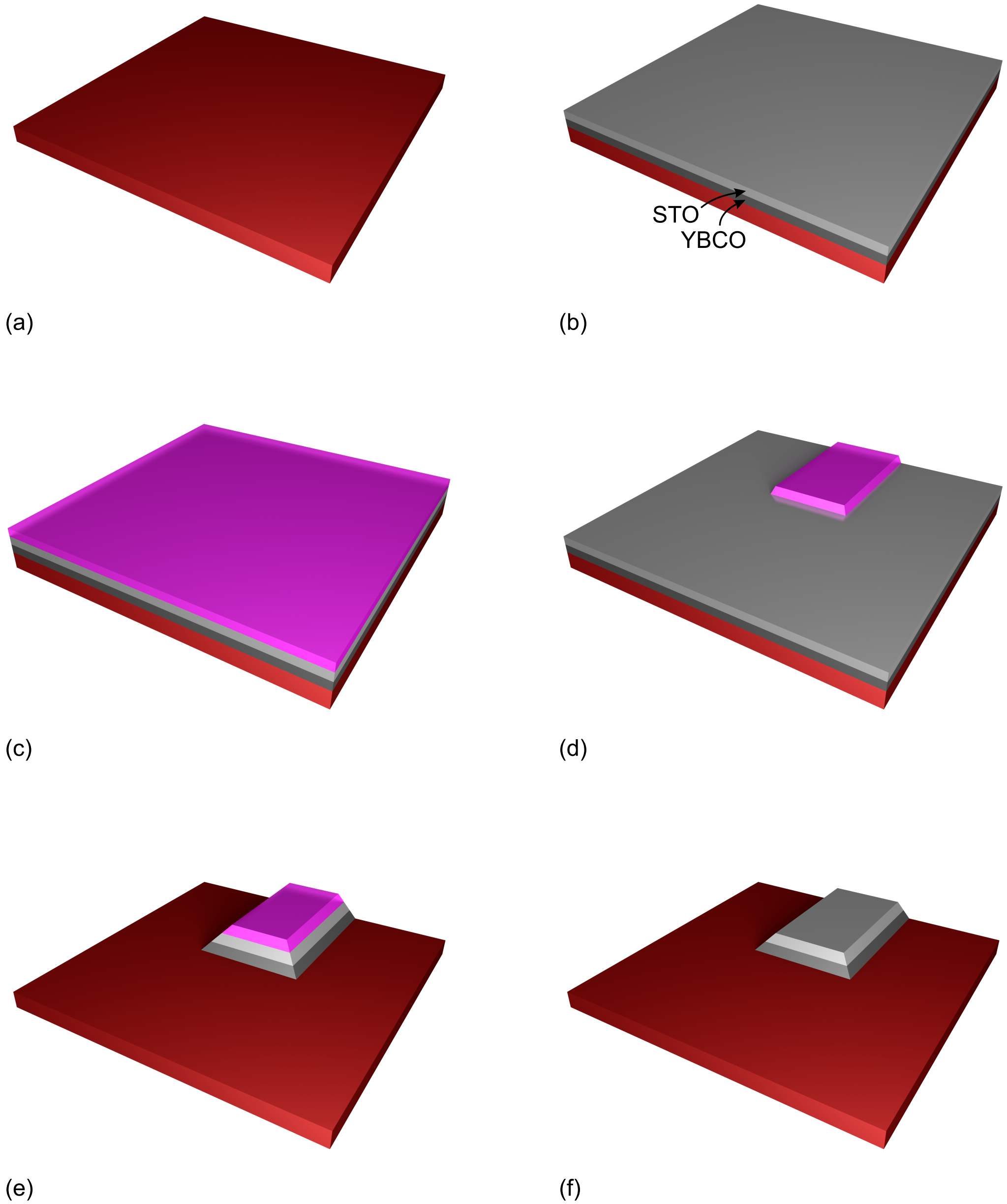

Figure 4.3: Processing steps for the fabrication of YBCO/Nb ramp-type Josephson junctions. (a) Treated STO substrate. (b) Pulsed laser deposition of the YBCO-STO bilayer. (c) Application of photoresist. (d) Patterning of photoresist. (e) Argon ion milling. (f) Resist removal.

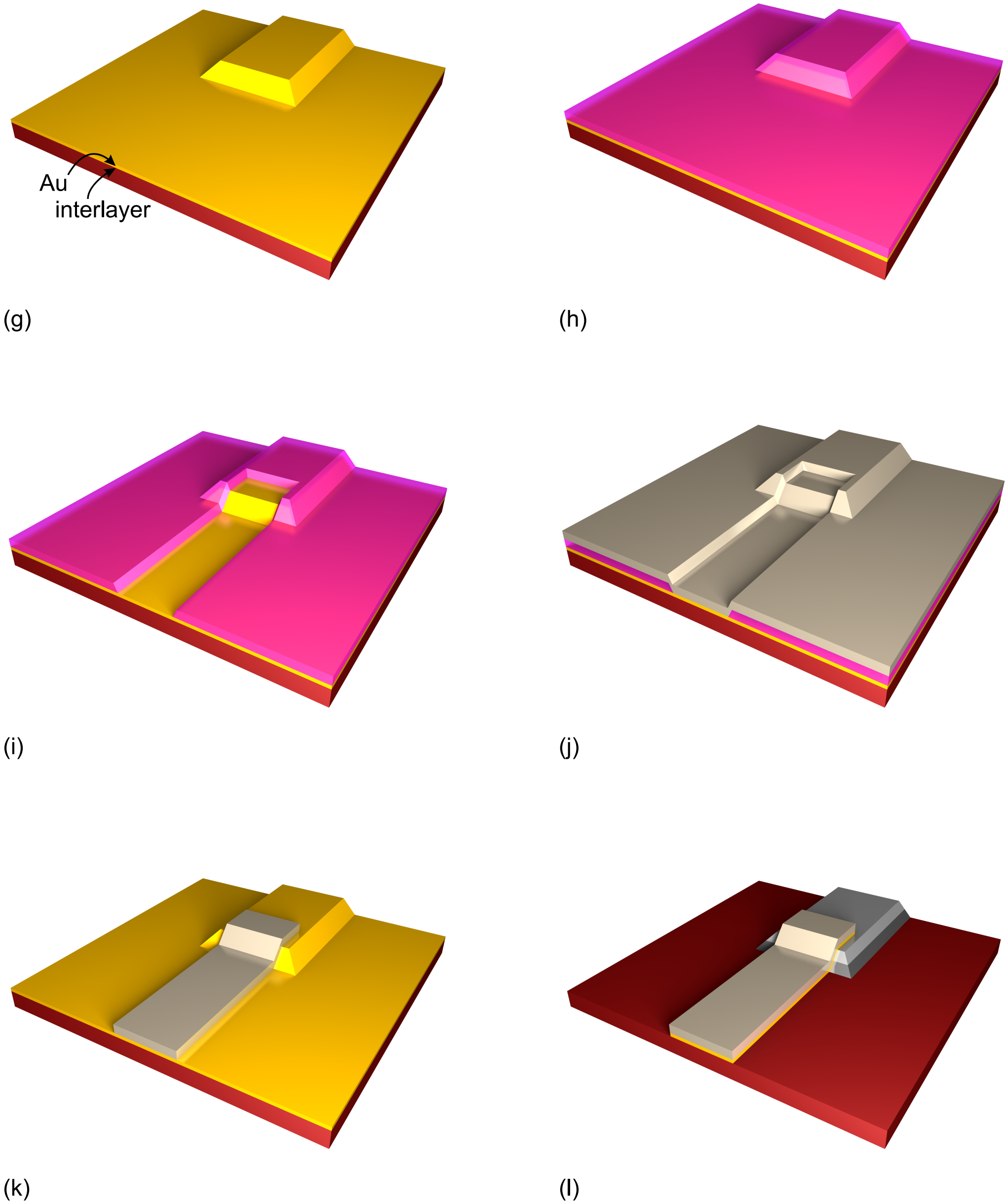

Figure 4.3: (continued) Processing steps for the fabrication of YBCO/Nb ramp-type Josephson junctions. (g) Pulsed laser deposition of the YBCO interlayer and gold barrier. (h) Application of photoresist. (i) Patterning of photoresist. (j) Sputter-deposition of niobium. (k) Lift-off. (l) Removal of redundant Au and YBCO.

involving silver- or platinum barriers have been conducted. First the general fabrication procedure will be outlined, then several processing steps will be discussed in more detail.

4.5.1 Fabrication procedure

The fabrication procedure is schematically illustrated in figure 4.3. After cleaning and a surface treatment step a [001]-oriented YBCO film is epitaxially grown on the STO substrate using pulsed laser deposition (PLD). During the same fabrication step an STO layer is deposited on top of the YBCO film. Then a layer of resist is spun on the sample in which the shape of the base electrode is patterned using optical lithography. Next the parts of the bilayer that are not covered by resist are etched away using argon ion milling. To ensure a well-defined ramp for all junction angles, the sample is rotated during etching and oriented at an angle of 45° with respect to the argon ion beam. After the resist is removed, a thin (~7 nm) YBCO layer is grown (again using PLD) and annealed in order to restore the ramp which has been damaged during the argon ion milling process. After this restoration step the gold barrier is applied *in situ*, also using PLD. On top of the gold layer a resist layer is spun in which the shape of the counter electrode is defined using optical lithography. In the final deposition step niobium is sputtered onto the sample. Lift-off is used to remove the resist and unwanted niobium. In the last step, the redundant uncovered YBCO/Au layer is removed by argon ion milling.

4.5.2 Substrate treatment

All devices described in this thesis were fabricated on 10x5x1 mm^3 $SrTiO_3$ substrates, because of the good lattice match between STO (lattice constant 3.905 Å) and YBCO (lattice constants a = 3.82 Å, b = 3.89 Å) and the comparable coefficient of thermal expansion ($14 \cdot 10^{-6}$/K for YBCO and $11 \cdot 10^{-6}$/K for STO [144]). Considering the d-wave order parameter symmetry in the YBCO base electrode, the junction-orientation with respect to the underlying YBCO crystal lattice is of great importance in our experiments. Thus a good alignment of the STO crystal structure with respect to the edge is highly desirable. The substrates had an edge-alignment better than 1°. Low-miscut ($\alpha < 0.1°$) substrates were used for the experiments where twinning behavior was not of importance. The experiments described in chapter 5, which require untwinned YBCO films, were performed using samples with a miscut α of 1.10°.

Before deposition of the first bilayer the STO substrates were cleaned and prepared in order to obtain a smooth surface and reproducible fabrication circumstances. The cleaning step involves immersing the substrates in acetone and ethanol for 10 minutes using ultrasound. When required, micro-mechanical cleaning was performed. Next the cleaned sample was immersed in demiwater for 10 minutes, also using ultrasound, in order to form strontium-hydroxide:

$$\mathrm{SrO} + \mathrm{H_2O} \rightarrow \mathrm{Sr(OH)_2}$$

The $Sr(OH)_2$ is then removed by immersing the substrate in a buffered HF solution, consisting of 12.5% HF and 87.5% NH_4F. After rinsing the substrate in demiwater for a few minutes the substrate is annealed for 90 minutes at a temperature of 950°C under an oxygen-flow of 200 l/h to allow surface recrystallization. Thus a TiO_2-terminated substrate is obtained with clearly visible terrace steps, as can be seen in the atomic

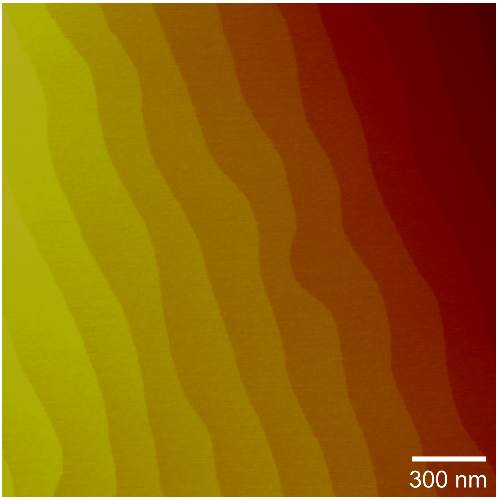

Figure 4.4: AFM image of the step-edges on a treated $SrTiO_3$ substrate.

force microscopy (AFM) image shown in figure 4.4. A more detailed description of the termination process is given in Koster *et al.* [145].

4.5.3 Photolithography

For the optical lithography MICROPOSIT S1813 (Shipley) photoresist was used. After distributing the resist uniformly such that it covers the entire surface, the sample is spun for 30 seconds at 5000 rotations per minute, which results in a resist layer with a thickness of approximately 1.2 μm. To harden the resist the sample is baked on a hotplate for 10 minutes at 100°C. Next, the lithography-mask is carefully positioned over the sample in order to ensure a good alignment of the structures to be patterned. In many experiments only the alignment between different layers, required for proper interconnections between the top- and bottom electrodes across the sample, is of importance. However, for the experiments described in this thesis also the alignment of the YBCO base electrode with respect to the STO substrate (and thus the underlying crystal structure) is of crucial importance because of the d-wave pairing symmetry in YBCO. When mask and sample are properly aligned, the sample is exposed for 5-10 seconds to UV light with an energy density of 10 mW/cm^2. After exposure the sample is developed in the NaOH-based developer MICROPOSIT 351, which is diluted with demiwater (1 developer : 5 water). The sample is developed for 60 seconds under constant stirring and then rinsed twice in demiwater for 30 seconds and 60 seconds, respectively.

As was mentioned in the above, we use etching to structure the YBCO base electrode and lift-off for the Nb top electrode. These two different techniques also require slightly different resist-masks in the sense that for the etching mask resist is removed everywhere except for the structures whereas for the lift-off mask the resist is removed only where the structures are to be fabricated. This difference in resist-mask has led to two small deviations in the lithography steps. For the lift-off mask the sample is spin-coated at 4000 rpm instead of the aforementioned 5000 rpm, which corresponds to a resist thickness of approximately 1.3 μm. Though the resist thickness is only a fraction thicker, we experienced a much easier lift-off for this spinning speed[4]. The second modification has to do with the fact that for our 10x5x1 mm^3 substrates a substantial amount of resist builds up at the corners and (though to a lesser extent) at the edges. This resist cannot be removed using the nominal dose and for edge masks this can lead to islands of superconducting material at the corners of the sample, which is of course highly undesirable. Moreover the resist at the corners can reduce precision when the mask aligner is used in contact mode. Since the dose that is required to remove this resist would overexpose the structures that are of interest, the photolitography for an etch mask is performed in two steps. First the sample is exposed through a mask that covers the entire sample except for the corners and the edges, using a much higher dose (an exposure time of 2 minutes). Then the sample is developed and the photolitography for the actual structures is performed using the nominal dose. For lift-off masks this extra step is not included of course because it would lead to a superconducting ring around the sample. However, for lift-off masks the necessity to get rid of the extra resist is less high because the lift-off in itself will not be hampered by the fact that the resist is thicker at the corners.

After the etching step the resist is removed by immersing the sample in acetone using ultrasound for 5 minutes and then immersing the sample in ethanol, also for 5 minutes using ultrasound. After the lift-off step the sample is also immersed in acetone and ethanol, but without the use of ultrasound to spare the junction and avoid a release of the gold, which is only weakly attached.

4.5.4 Pulsed laser deposition

The YBCO-, STO- and Au films were deposited using pulsed laser deposition. The pulses were generated by a Lambda Physik Compex 205 KrF excimer laser (with a wavelength of 248 nm and a 20-30 ns pulsewidth), and led via a mask, mirror and lens (focal length $\approx$ 45 cm) into the deposition chamber. The mask contains several rectangular openings with an effective window area of 98 mm^2 which are projected onto the target in the deposition chamber. The purpose of this mask is to achieve a more homogeneous distribution of ablated material at the sample.

The deposition chamber is a homebuilt vacuum system in which several process parameters (pressure, temperature, background gas) can be tuned for optimal film growth. The system is equipped with an etching chamber, which allows the user to perform subsequent etching- and deposition jobs without having to break the vacuum. This extra etching step (argon ion milling) is always performed just before the restoration of the ramp, because then the YBCO at the ramp has been in contact with air and the solvants used to remove the resist layer. A few etch pulses can be applied to clean the degraded YBCO before the *in situ* deposition of the YBCO interlayer. The interlayer-concept has been worked out in more detail by Smilde *et al.* [143]. The standard background pressure of the system is $\sim 10^{-7}$ mbar, and the pressure of the background gasses can be controllably varied between 10^{-4} mbar and 0.5 mbar using a combination of mass-flow controllers and a variable valve.

In the following paragraphs, the pulsed laser deposition of the materials used for the devices discussed in this thesis (YBCO, STO and Au) will briefly be discussed. A summary of all deposition conditions can be found in table 4.2.

---

[4] The reported values for resist thickness have been taken from the data sheet and were not actually measured

	YBCO	STO	Au
Fluency (J/cm^2)	1.5	1.5	3.5
Energy (mJ)	96	100	100
Frequency (Hz)	4	4	4
Temperature (°C)	780	740	100
Pressure (mbar)	0.25	0.10	0.22
O_2-flow (ml/min)	25	10	-
Ar-flow (ml/min)	-	-	30
Deposition rate (Å/pulse)	1.0	0.64	1.8

Table 4.2: Deposition conditions for pulsed laser deposition of YBCO, STO and Au.

YBCO growth

Before the deposition can occur, the sample has to be brought to the right deposition conditions in order to obtain the correct stoichiometry. The sample is mounted on a heater and (after degassing the silver paint used to attach the sample to the heater) loaded into the vacuum clock via a load-lock system. Then the sample is heated to a temperature of 200°C. When the background pressure drops below $7 \cdot 10^{-7}$ mbar the oxygen-flow and pressure are set to 25 ml/min and 0.25 mbar, respectively. When the pressure is stable the temperature is slowly increased to the actual deposition temperature of 780°C with short stops at 450°C and 600°C.

When the sample is at the right deposition conditions first the target is cleaned by performing a pre-ablation: for 2 minutes the laser is pulsed with a frequency of 10 Hz and at the desired fluency (1.5 J/cm^2 for YBCO) but a shutter is placed between the plasma plume and the sample. After pre-ablation the same procedure is repeated with the shutter open and at the desired frequency (4 Hz was used for the base electrode and 1 Hz for the interlayer).

STO growth and annealing

The deposition of the STO film is performed *in situ* after the deposition of the YBCO base electrode, at slightly different deposition conditions (a temperature of 740°C, an O_2-flow of 10 ml/min and a pressure of 0.10 mbar). After the STO deposition the sample is annealed in an oxygen environment of 1 bar for 30 minutes at 600°C and for 30 minutes at 450°C. After the annealing step the heater is switched off and the sample is allowed to cool down even further. When the temperature has dropped below 100°C the system is pumped vacuum again and the sample can be taken out of the system. The same annealing procedure was followed between the deposition of the YBCO interlayer and the gold barrier.

Au deposition

The pulsed laser deposition of gold requires a much higher fluency (we use 3.5 J/cm^2) than the ablation of the oxide materials YBCO and STO, due to gold's high thermal conductivity and strong reflectance for UV-laser radiation [146]. At this fluency the ions in the plasma plume can reach kinetic energies up to several tens of eV [147]. These high-energy ions can seriously damage the surface and structures deposited in earlier processing steps when exposed to the sample directly. To reduce the speed of the incoming high-energy particles the gold depositions were carried out using argon as a background gas. A more detailed analysis of the deposition circumstances has been given by Smilde [137]. The argon was let into the system at a flow of 30 ml/min and at a pressure of 0.22 mbar. The deposition temperature of 100°C was chosen to ensure the same deposition conditions for different runs. The pulsed laser deposited Au films often showed gold droplets, see for example figure 5.2(b). This is a recognized problem, especially with the deposition of metals [137, 148, 149]. Under the aforementioned deposition conditions the density of these droplets was so low that the droplets were not considered a problem.

4.5.5 Sputter deposition of niobium

The deposition of niobium was performed in a Nordiko sputter system which has a background pressure of 10^{-7} mbar. Prior to the actual deposition the gold surface is cleaned *in situ* during an RF sputtering step in which the shutter in front of the target is closed. Thus no material is deposited but the sample surface is etched by the argon ions. The pressure during this etching step was $1.3 \cdot 10^{-2}$ mbar and the applied RF power 50W, which induces a self-bias voltage of 310V. Under these circumstances the sample was etched for approximately 1 minute which results in the removal of ~1 nm Au [150].

After this cleaning step the actual niobium deposition is performed by DC sputtering at a pressure of $7.3 \cdot 10^{-2}$ mbar and DC voltage and power of 365 V and 250 W, respectively. These process parameters result in a deposition rate of 80 nm/min. Before sputtering directly on the sample the target is sputtered while a shutter is placed in front of the sample in order to clean the target and reduce the partial pressure of oxygen through the formation of niobium oxide.

4.5.6 Argon ion milling

Argon ion milling was used for the ramp definition and for the removal of redundant gold and YBCO in the last processing step (the cleaning of the gold will be discussed in the sputtering section). Before starting the etching process the system is pumped down to a background pressure of approximately $5 \cdot 10^{-7}$ mbar. Then argon gas is let in and the actual etching is performed at a pressure of approximately $5 \cdot 10^{-3}$ mbar using a beam voltage and -current used of 500 V and 15 mA respectively. During the cleaning step just before the interlayer deposition a soft-etch step is performed at 50 V and 5 mA. To reduce sample heating all etching processes are performed in a pulsed mode: each pulse the beam is off for 12 seconds and then on for 8 seconds. During the definition of the junction ramp in the base electrode the sample is placed under an angle and rotated to obtain a ramp in all directions.

The ramp-angle α is not uniquely determined by the angle β under which the sample is etched, but also by the relative etching speeds of the resist and the material to be etched. This is illustrated in figure 4.5. When the sample is etched during a time Δt, the material will be etched by an amount $\Gamma_M \Delta$t, where Γ_M is the etching speed of the material that is etched. All points on the left-hand side of **A** will therefore experience a vertical displacement of $\Gamma_M \Delta \mathrm{t} \sin\beta$. In the same way the resist will diminish by an amount $\Gamma_R \Delta \mathrm{t} \sin\beta$ with Γ_R the etching speed of the resist. While the resist is retracting

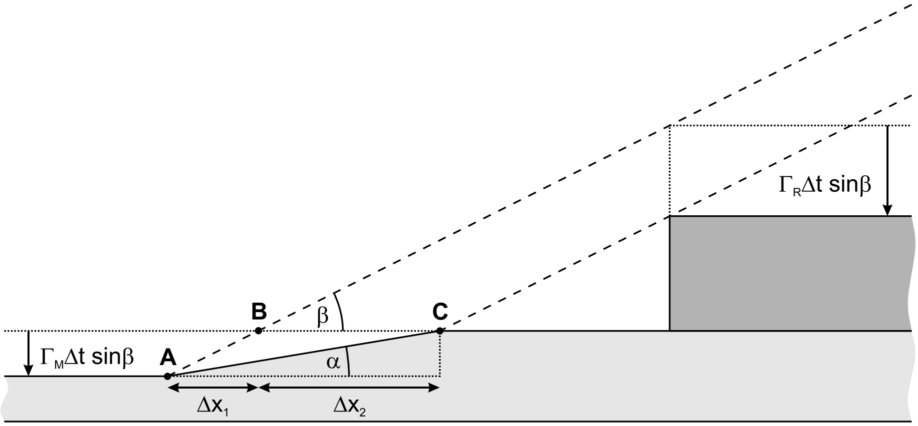

Figure 4.5: Schematic representation of the ramp definition using argon ion milling. The dotted lines represent the resist- and material surfaces at the beginning and end of the time interval Δt as indicated in the text. The dashed lines represent the 'horizon' of the incoming argon beam at the corresponding times.

the 'horizon' of the incoming argon beam moves from **B** to **C**, and the actual ramp is formed between **A** and **C**. Now let us denote the horizontal distance between **A** and **B** by Δx_1 and the horizontal distance between between **B** and **C** by Δx_2. From figure 4.5 it is easy to see that

$$\tan\alpha = \frac{\Gamma_M \Delta t \sin\beta}{\Delta x_1 + \Delta x_2} \tag{4.1}$$

and

$$\tan\beta = \frac{\Gamma_M \Delta t \sin\beta}{\Delta x_1} = \frac{\Gamma_R \Delta t \sin\beta}{\Delta x_2} \tag{4.2}$$

Substituting Δx_1 and Δx_2 from equation (4.2) into equation (4.1) we find

$$\alpha = \arctan\left(\frac{\tan\beta}{1+x}\right) \tag{4.3}$$

with

$$x \equiv \frac{\Gamma_R}{\Gamma_M} \tag{4.4}$$

the ratio of the etching speeds.

Equation (4.3) should be used with some caution. First, the above derivation is for a stationary situation, while in the actual experiments the sample is rotated during ramp definition to ensure a ramp in all directions. Secondly in our experiments the YBCO in the base electrode is always covered with an STO top layer, which also acts as an etching mask for the underlying YBCO. Interestingly, these two effects seem to have a small effect on the ramp angle [151]. For the samples described in this thesis the etching angle was 45°, which, together with $x = 2$ [137] results in a ramp angle of 18.4°.

4.6 Summary

In this chapter the practical realization of YBCO/Nb superconducting structures has been discussed. The properties of the cuprate superconductor $YBa_2Cu_3O_{7-\delta}$ depend critically on the oxygen deficiency. Niobium, on the other hand, oxidizes easily. To ensure high-quality barriers a gold barrier is deposited to chemically separate the two electrodes. The ramp-type geometry which is necessary for good transport properties in the *ab*-plane has been discussed as well as the and the interlayer concept which significantly enhances the junction transparencies. The different deposition and preparation techniques such as pulsed laser deposition, sputtering, (rotating) etching and lithography have been briefly described.

Chapter 5

Angle-resolved determination of the YBCO gap symmetry

5.1 Introduction

More than twenty years after the discovery of high-T_c superconductivity there is still no theory that can satisfyingly explain all experimentally observed phenomena. In the process of trying to unravel the mysteries of high-T_c superconductors pieces and bits of the puzzle have been identified and attempts are made to fit them into a single coherent and consistent theory. One of these pieces is the order parameter symmetry of the wave function in the cuprates. The initial debate of s-wave versus d-wave pairing symmetry has been settled in favor of a predominantly d-wave symmetry by a variety of techniques [103, 104]. For YBCO some controversy still exists over the size of the in-plane gap asymmetry and the possibility of broken time reversal symmetry. Studies on the order parameter symmetry can roughly be divided in phase-insensitive techniques such as angle-resolved photoemission spectroscopy (ARPES), Raman scattering and nuclear magnetic resonance (NMR), and phase-sensitive techniques such as SQUID interferometry and tricrystal magnetometry. The first techniques provide information about the amplitude of the order parameter, and can for example identify nodes in the pair wave function. To get a complete picture of the pairing symmetry phase-sensitive experiments are also necessary. Previous phase-sensitive experiments were performed in a limited number of geometries, whereas experiments performed as a function of the in-plane momentum are desirable if one is to demonstrate an imaginary admixture to the order parameter [152, 153].

5.2 Amplitude-sensitive experiments

Several theoretical studies have predicted that the orthorhombicity of the YBCO unit cell should result in an s-wave admixture to the predominantly $d_{x^2-y^2}$-wave order parameter symmetry [154–158]. The addition of an s-wave admixture creates an anisotropy in the d-wave symmetry. This can be understood intuitively by realizing that the constant amplitude of the s-wave adds in phase to one pair of lobes, and out-of-phase to the other pair of lobes. In other words, the s-wave adds to the blue (0-phase) lobes and subtracts

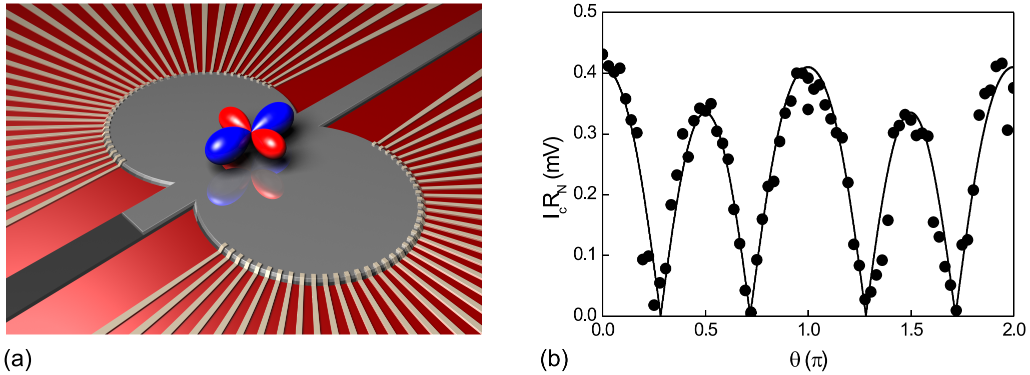

Figure 5.1: (a) Layout of the sample used for angle-resolved electron tunnelling measurements. (b) I_cR_N-product as a function of the angle with respect to the b-axis θ. Solid points represent the measured data and the line is the fit as described in the text (figure adapted from Smilde *et al.* [166]).

from the red (π-phase) lobes in figure 3.1. The anisotropy is often expressed as the ratio of the gap values in the a- and b-direction, Δ_b/Δ_a.

Experimental evidence for the predicted s-wave component has been found by several groups using a variety of techniques. Tunnelling experiments by Polturak *et al.* [159] and Engelhardt *et al.* [160] show an in-plane anisotropy of $\Delta_b/\Delta_a = 1.48$ and $\Delta_b/\Delta_a = 1.2-2$, respectively (where we have assumed that the larger gap corresponds to the b-axis direction and not to the a-axis direction as stated in the respective papers). Interestingly, these measurements are in sharp contrast to tunnelling experiments performed by Wei *et al.* [161], who place an upper limit to any s-wave component (real or imaginary) of 5%, which corresponds to $\Delta_b/\Delta_a \approx 1.1$. ARPES measurements [162] show a substantial gap-anisotropy of $\Delta_b/\Delta_a = 1.5$, whereas in Raman scattering experiments a much smaller value is observed: $\Delta_b/\Delta_a = 1.1 - 1.2$ [162–164]. Measurements on the thermal conductivity of YBCO in a rotating magnetic field [165] provided an upper limit on the s-wave component of 10%, corresponding to $\Delta_b/\Delta_a = 1.25$. It is safe to conclude that the discussion about the magnitude of the s-wave component is far from settled.

The size of the s-wave admixture was also determined by Smilde *et al.* using angle-resolved electron tunnelling [166]. The experimental layout of the sample is depicted in figure 5.1(a)[1]. The base electrode consists of a nearly circular YBCO polygon with edge facets that change orientation from side to side by 5°. Niobium leads contact the base electrode via YBCO/Nb ramp-type Josephson junctions. The critical current I_c and the normal state resistance R_N were probed as a function of the in-plane angle θ. The resulting I_cR_N-product, which is directly related to the superconducting gap [167], is shown in figure 5.1(b). The $I_cR_N(\theta)$ dependence was best fitted by an order parameter symmetry consisting of 83% $d_{x^2-y^2}$-wave, 15% isotropic s-wave and 2% anisotropic s-wave.

---

[1] Note that the graphical representation of the d-wave clover as a 3D object was chosen for artistic reasons. One should keep in mind that the order parameter symmetry of the cuprates is generally accepted as being two-dimensional in nature

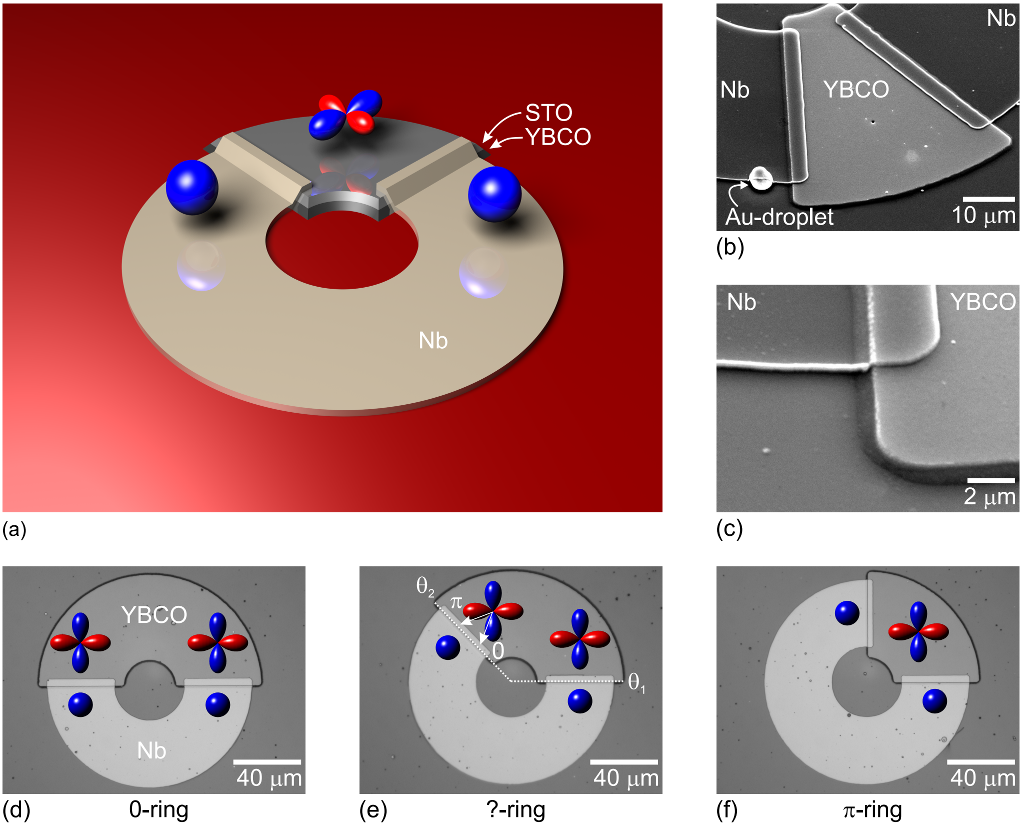

(a) (b) (c)

(d) 0-ring (e) ?-ring (f) π-ring

Figure 5.2: (a) Schematic of the YBCO/Nb rings used for the phase-sensitive determination of the order parameter symmetry of YBCO. (b) Scanning electron microscopy (SEM) picture of the YBCO 'island' which is contacted by the niobium counter electrode via two Josephson junctions. (c) SEM picture of the ramp-type junction between YBCO and niobium. (d)-(f) Optical micrographs of superconducting YBCO/Nb rings in three different geometries. The angle of the first junction is fixed at an angle $\theta_1 = 0$ degrees. By tuning the angle θ_2 of the second junction the ring can be (d) a 0-ring, (e) a ring that can either be a 0- or a π-ring, depending on the details of the YBCO gap symmetry, or (f) a π-ring.

5.3 Phase-sensitive experiments

Angle-resolved phase-sensitive experiments as proposed by Beasley *et al.* [152] and Ng and Varma [153] have until now only been performed with limited success [168, 169]. We have used the half-integer magnetic flux quanta that arise in π-rings as a tool to study the pairing symmetry of YBCO [170]. The layout of the rings that were used is depicted in figures 5.2(a)-(c). The ring connects a YBCO base electrode to a niobium counter electrode via two ramp-type Josephson junctions. Depending on the geometry such a ring can be either a 0-ring which contains a flux $n\Phi_0$, or a π-ring containing a flux $(\mathrm{n}+\frac{1}{2})\Phi_0$ (provided the ring is in the large inductance limit). This is illustrated in figures 5.2(d)-(f). For a predominantly *d*-wave pairing symmetry the rings (d) and (f) will be a 0- and π-ring, respectively, but the behavior around the nodal directions depend critically on the details of the order parameter symmetry. For a pure *d*-wave superconductor, for example, the transition from a 0- to π-ring occurs at an angle of 45 degrees. An *s*-wave admixture will not only cause an anisotropy of the lobes along the *a*- and *b*-directions (see section 3.2), but also shifts the nodal angles, resulting in a shift of the 0- to π-transition. Moreover, an imaginary component to the order parameter symmetry will result in a deviation of the spontaneously generated flux from $\Phi_0/2$, even in the large inductance limit.

An array of 72 rings was fabricated with one junction kept at a constant angle and the second junction angle varying in intervals of 5 degrees. By measuring the flux produced by each of these rings using a scanning SQUID microscope (SSM) the in-plane gap symmetry of YBCO can be probed. The rings were fabricated using the procedure described in section 4.5. The YBCO-STO bilayer has a thickness of 340 nm (YBCO) + 70 nm (STO). The choice for a rather thick YBCO layer was made to enhance the critical current. The critical current of the junctions along the nodal directions will be strongly suppressed. A thick YBCO layer will result in larger critical currents and therefore helps to stay in the large inductance regime, which is crucial for this experiment. The thickness of the gold is 16 nm and the niobium counter electrode has a thickness of 160 nm. The YBCO semi-rings have an inner radius of 15 μm and an outer radius of 65 μm, the niobium rings have an inner radius of 20 μm and an outer radius of 60 μm. The YBCO semi-rings were chosen wider than the niobium semi-rings to ensure a single straight junction: a corner in the YBCO under the niobium overlap results in a corner junction, which in turn can result in a spontaneously generated current (see section 3.3). The 72 rings are spaced by 400 μm in a square array. Using the inductance extraction program FastHenry [171] and the London penetration depths from table 4.1 we estimate a self-inductance of 57 pH and a nearest neighbors mutual inductance of 20 fH. The critical current of the junctions in the rings was estimated from measurements on control junctions that were on the same chip. These junctions, having the same width (40 μm) as the junctions in the rings and oriented along the YBCO main crystal axes, had critical currents of 2.5 mA. From these values we find a screening parameter $\beta_L \approx 433$, which is far in the large inductance regime.

5.4 Twinning

An important aspect for our experiment is the amount of twinning in the YBCO thin films. During film growth the orthorhombic YBCO unit cells align the diagonal of the basal plane with respect to the diagonal of the underlying cubic crystal structure of the strontium titanate substrate. The four different orientations that can be achieved this way can be divided in two twin pairs, denoted by [S_1^+,S_2^-] and [S_1^-,S_2^+]. S_1^+ and S_2^- as well as S_1^- and S_2^+ are correlated by a reflection in a (110) plane, while S_1^+ and S_2^+ as well as S_1^- and S_2^- can be transferred into each other by a rotation through 90°. The difference in orientation between S_1^+ and S_1^- or S_2^+ and S_2^- respectively is given by [172]

$$2\delta = 2\arctan\left(\frac{b}{a}\right) - 90^\circ \tag{5.1}$$

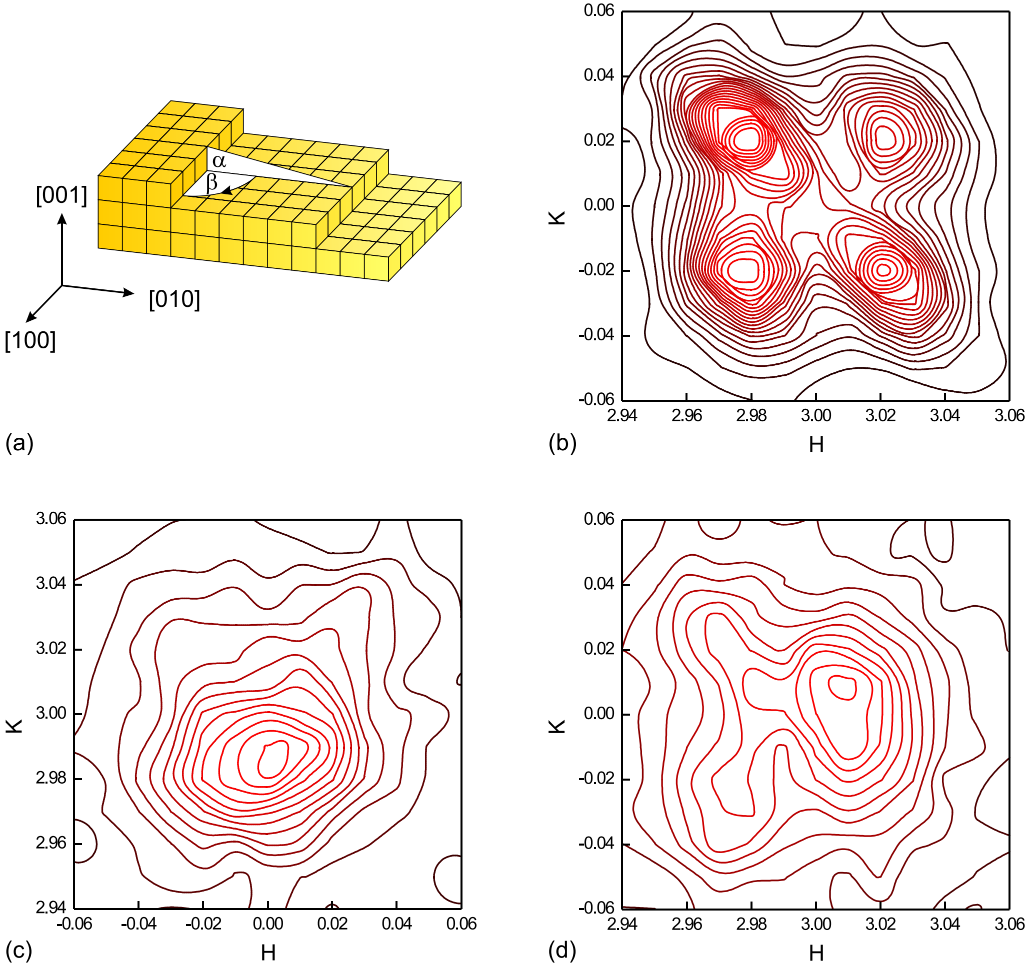

Figure 5.3: (a) Substrate vicinal properties: the angle α and in-plane orientation β of the miscut. (b) Reciprocal space mapping of the YBCO 304 reflection for a fully twinned sample. Reciprocal space mappings of the (c) 034- and (d) 304 reflections of a sample that was used for the angle-resolved determination of the in-plane gap of YBCO.

with a and b the in-plane lattice constants. Inserting the values $a = 3.82$ Å and $b = 3.89$ Å this gives $2\delta \approx 1.04°$. The ratio of the two twin pairs is referred to as twinning. In fully untwinned thin films only one twin pair occurs, whereas in twinned films both twin pairs occur, culminating in a 50%-50% population for fully twinned films.

A strong correlation between the substrate vicinal properties, shown in figure 5.3(a), and the amount of twinning in YBCO films grown on STO by pulsed-laser deposition has been demonstrated experimentally [173, 174]. For substrates with step edges oriented along the [100] crystallographic axis ($\beta = 90°$) a maximum in detwinning has been observed for a miscut angle α of 1.10°. This angle corresponds to a terrace length of 20 nm, which is comparable to the diffusion length of PLD-grown YBCO. The experimental determination of the in-plane gap of YBCO relies heavily on the asymmetry in the *a*- and *b*-axis directions of YBCO. Monocrystalline films are therefore highly desirable: even though the orthorhombic unit cells in themselves are non-isotropic, twinning will average out the effect this has on the superconducting properties of the film as a whole. Therefore the STO substrates that were selected for this experiment have a miscut angle α of 1.10° and are aligned with respect to the [100] axis within an accuracy of 0.5°, which has been confirmed by X-ray analysis.

The twin behavior in our YBCO films was determined using X-ray reciprocal space mapping. Scans were performed around the 304 and 034 reflections. For comparison, a typical reciprocal space mapping of the 304 reflection of a fully twinned sample is shown in figure 5.3(b). In this figure one can clearly distinguish four maxima corresponding to the four orientations discussed previously. The reciprocal space mappings of the YBCO 304 and 034 reflections of one of our samples are shown in figures 5.3(c) and 5.3(d) and show almost completely untwinned YBCO thin films. The bottom half of figure 5.3(c) and the right half of figure 5.3(d) correspond to the same twin pair which is clearly dominant. In general, the inner reflections (small H for the 304 reflections and small K for the 034 reflections) have a lower intensity than the outer reflections. This is consistent with the fact that the reflections of the minority twin directions are only distinguishable in figure 5.3(d).

5.5 Scanning SQUID microscope

Magnetic imaging of the samples was performed at the IBM T.J. Watson Research Center in collaboration with Dr. John Kirtley, employing a high-resolution SSM [175, 176]. In scanning SQUID microscopy the local magnetic field distribution is registered by probing a SQUID over the surface of the sample that is to be measured. The advantage of scanning SQUID microscopy with respect to other techniques is the high sensitivity of the SQUID, the most sensitive magnetic field sensor currently available. The spatial resolution of the scanning SQUID microscope used is approximately 6 μm [86], which is sufficient for our purposes.

A schematic overview of the SSM system is shown in figure 5.4(a). The frame containing the microscope is mounted on top of a mu-metal shielded liquid Helium Dewar in which the microscope is immersed for measurements at cryogenic temperatures. The movement of the scan head (containing the sample) over the SQUID stage is induced by the X- Y- and Z linear actuators located at the top of the setup. The movement is transferred from the linear actuators outside the cryostat to the sample via a pivoting principle.

In figures 5.4(b) and 5.4(c) optical micrographs of the SSM sensor are shown. The sensors were fabricated at Hypres using a conventional Nb-AlO$_x$-Nb trilayer process. The sensor consists of a SQUID which is connected to a pick-up loop coupled inductively to a modulation coil for operation in a flux locked loop. The SQUID washer and the pick-up loop are separated by 1.2 mm long magnetically shielded leads. The separation of pick-up loop and SQUID washer has the advantage that the pick-up loop can be made much smaller than the SQUID, whose dimensions are limited by the available junction technology. The miniaturization of the pick-up loop results in a better spatial resolution and lowers the back-action of the SQUID. The sensor that was used had a square pick-up loop of 8 × 8 μm^2 with a calculated effective pick-up area of 85.3 μm^2 at 4.2 K. To

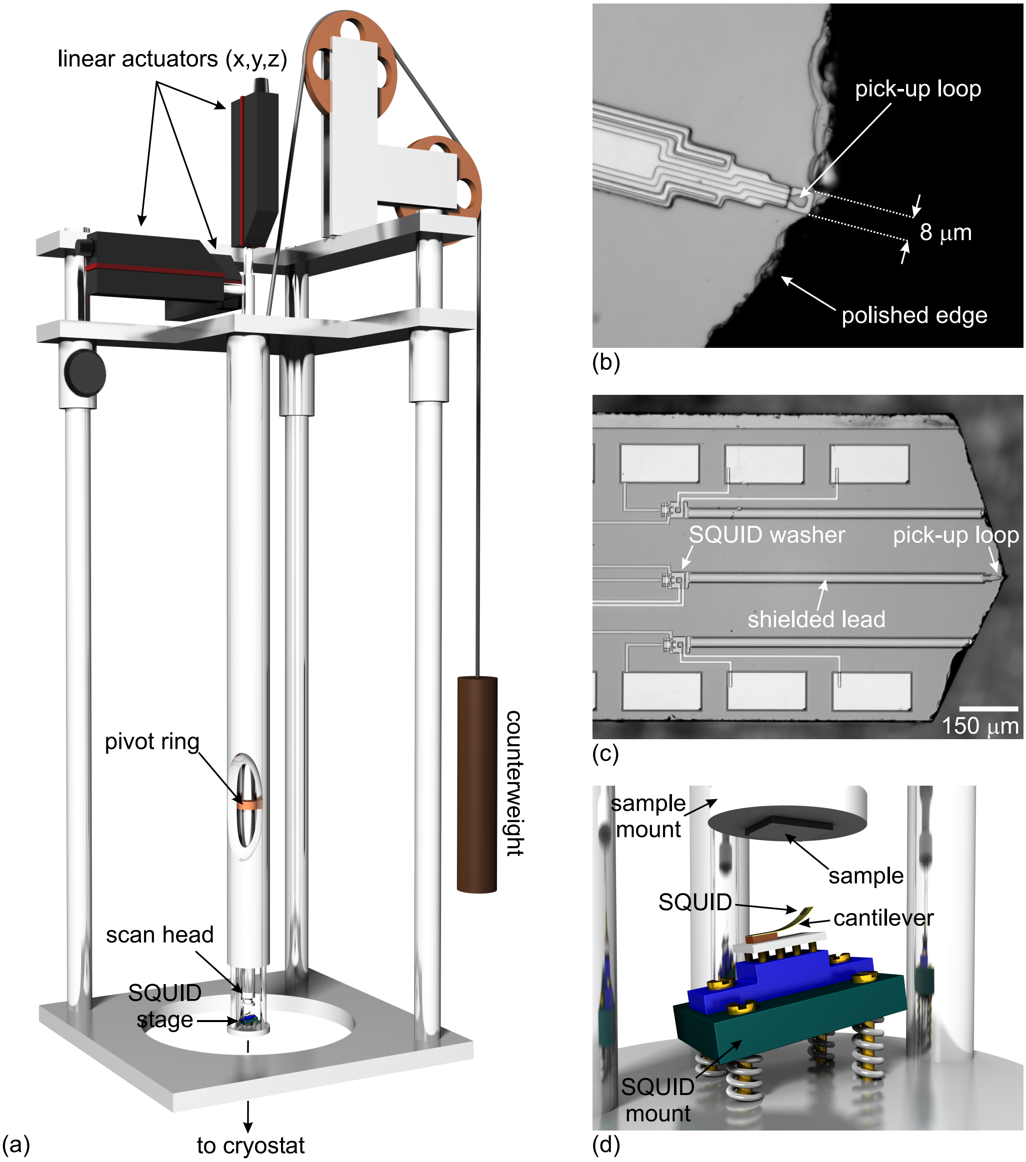

Figure 5.4: (a) Schematic of the IBM scanning SQUID microscope setup. (b) Optical micrograph of the SQUID pick-up loop. (c) Optical micrograph of the SQUID. (d) Schematic of the scan head and the SQUID stage.

decrease the spacing between sensor and sample the silicon substrate is polished to a corner typically one loop diameter from the center of the pick-up loop.

A close-up of the scanner is shown in figure 5.4(d). The SQUID is attached to the end of a thin brass cantilever which is brought in contact with the sample, making the system robust to small variations in the longitudinal direction. The SQUID is positioned under an angle with respect to the sample such that the pick-up loop is closest to the surface. This enhances the spatial resolution because most flux will be picked up by the pick-up loop and moreover has the practical advantage that the bonding wires connected to the SQUID (not shown) are not in contact to the sample that is measured. During the actual measurements a coil (not shown) is placed around the scan area to compensate for stray fields in the Dewar.

The SSM is operated in a flux locked loop at a modulation frequency of 100 kHz. The output of the SQUID electronics is amplified and led to the data acquisition card of the measurement computer. Fully automated imaging of the sample can be performed using software that was developed specifically for this purpose at the IBM T.J. Watson Research Center. The program drives the linear actuators to scan the area of interest while the SQUID output signal is recorded. The noise of this system is typically 2 $\mu\Phi_0/\mathrm{Hz}^{1/2}$, corresponding to a field noise at the pick-up loop of 40 $\mathrm{pT}/\mathrm{Hz}^{1/2}$.

5.6 Measurement results

Results of the magnetic imaging are depicted in figure 5.5. In figure 5.5(a) a schematic of one of the rings is shown, indicating the definitions of the different angles. The first junction angle has the value $\theta_1 = -22.5°$ in all rings of this sample. The angle θ_2 is varied in steps of 5 degrees between -17.5° and 332.5° for different rings. The angle θ of the second junction normal, along which current transport takes place, is defined with respect to the majority twin *a*-axis direction. Figure 5.5(b) shows a typical SQUID microscope image of one of the π-rings, which was cooled and imaged in zero magnetic field and has a full-scale variation of 0.04 Φ_0 flux through the (sensor) SQUID. All measurements were performed at 4.2 K. The spontaneously generated flux (corresponding to $\Phi_0/2$) is clearly visible in the center of the ring, whereas the ring itself is nearly invisible.

Figure 5.5(c) shows the SSM images for all rings on this sample, organized as a polar plot. The images are 150 μm by 150 μm in size and labelled by the angle of the second junction normal with respect to the majority twin *a*-axis direction θ. The outer ring of images was recorded with the sample cooled in zero field. These images have a full-scale variation of 0.04 Φ_0. Clearly, four regimes can be distinguished: in two regimes the rings act as conventional 0-rings (no circulating currents), and in two regimes the rings demonstrate a spontaneously generated flux corresponding to half a flux quantum. The crossovers between 0- and π-rings are indicated by dotted lines and are positioned between the angles $\theta = -42.5°$...-37.5°, 37.5°...42.5°, 137.5°...142.5°, and 217.5°...222.5°. Interestingly, these positions deviate from the (2n+1)45° positions that are to be expected if YBCO has a pure $d_{x^2-y^2}$-wave order parameter symmetry. The deviations cannot be explained by a possible misalignment of the rings with respect to the STO substrate (or equivalently, with respect to the YBCO crystal axes), because this would result in a uniform rotation of all nodes, rather the observed dispersion.

Rings that are at the transition points have their junction normal oriented close to a nodal direction in which the critical current is suppressed. This notion could lead one to believe that those rings are actually still π-rings in the sense that they have a built-in π-phase shift, but do not show the half-flux quantum because the screening parameter β_L of these rings is too small, as was discussed in section 2.10. For this reason the sample was cooled down again but in a background field of 0.2 μT. Once cooled down the magnetic field was removed and the rings were imaged again. The resulting SQUID

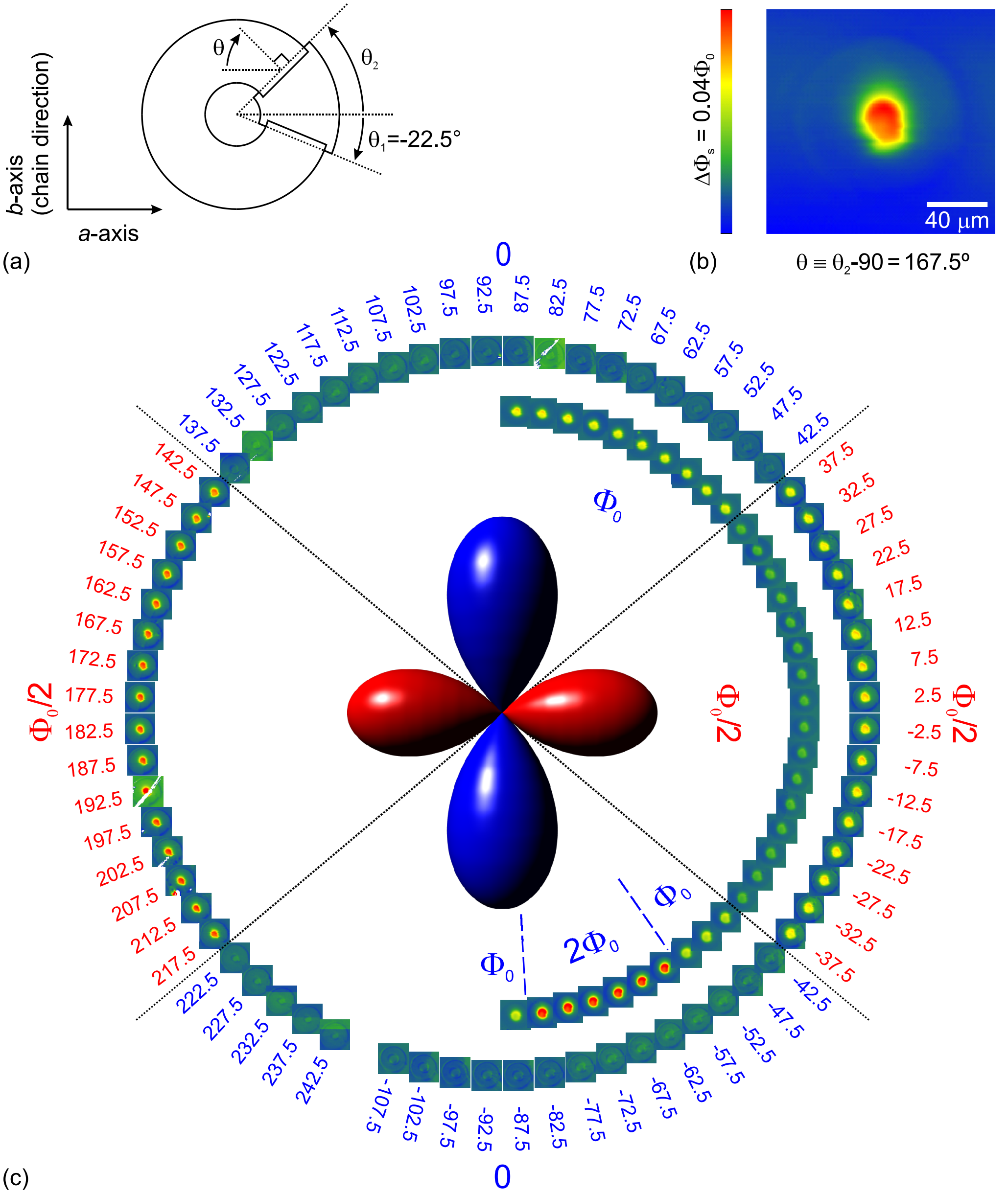

Figure 5.5: (a) Schematic of a ring with the angles θ_1, θ_2 and θ defined. (b) Image of the ring with $\theta_2 = 167.5°$. (c) Polar plot of the SSM images for all rings, labelled by the second junction normal angle θ. The outer circle of images, taken after cooling in zero field, has a full-scale variation of 0.04 Φ_0 flux through the SQUID. The inner ring, taken after the sample was cooled in a field of 0.2 μT, has a full-scale variation of 0.09 Φ_0. The dotted lines indicate the angles at which the transition from 0- to π-rings occurs.

microscope images, 150 μm by 150 μm in size and having a full-scale variation of 0.04 Φ_0, are displayed in the inner semi-circle of figure 5.5(c). The flux in the π-rings is still Φ_0 but the flux in the rings that showed no flux before is one or even sometimes two flux quanta. This elegantly demonstrates that I_c is large enough and these rings are not π-rings.

To quantify the results of figure 5.5 the integrated flux for each of the rings is plotted as a function of the junction normal angle θ in figure 5.6(a). In the following, the method used to integrate the flux from the SSM images is explained. Each image consists of a set of pixels, which have an x-, y- and associated N-value (which is converted to a color scale), see figure 5.6(b). N is proportional to Φ_s, the flux detected by the sensor pick-up loop for that particular pixel. To integrate the flux, first the values N are summed for all pixels within a radius r from the center of the ring. The integration area is given by the sum of all pixels times the area per pixel A_p. In figure 5.6(c), ΣN is plotted as a function of the integration area (black solid points). In the absence of a background magnetic field ΣN should increase with r until r reaches the inner radius of the ring, and then remain constant until the outer diameter is reached. To compensate for constant offsets in the SQUID signal ΣN is fitted to a straight line between an inner radius R_{in} and an outer radius R_{out}, see figure 5.6(b) and the blue line in figure 5.6(c). R_{in} and R_{out} are chosen well within the superconducting material. In figure 5.6(c) the resulting ΣN^* after background subtraction is shown (red solid points).

The flux through a ring is equal to the summation of Φ_p over all pixels within the inner radius of the ring. Each pixel has an area A_p of 3×3 μm^2, which is determined by the scan step size (3 μm for this experiment). However, N^* is related to the flux through the pick-up loop of the sensor Φ_s, with a different area A_s of 85.3 μm^2, which should be taken into account when integrating the flux. In general, the flux Φ_p through a pixel is related to the flux through the sensor pick-up loop Φ_s via

$$\Phi_p = \Phi_s \frac{A_p}{A_s} \tag{5.2}$$

The value N is determined from the flux Φ_s through the SQUID pick-up loop via the flux-to-voltage transfer Φ-to-V of the flux-locked loop, the gain and an analog-to-digital conversion step (16 bits for ± 10 V). Combining this with equation (5.2) we find the following relation between $\Sigma\Phi_p$ and ΣN^*

$$\sum_{r<R_{in}} \Phi_p = \frac{1}{\Phi\text{-to-V} \cdot \text{gain} \cdot \left(\frac{2^{16}}{20}\right)} \frac{A_p}{A_s} \sum_{r<R_{in}} N(r)^* \tag{5.3}$$

Inserting the values for the flux-to-voltage transfer (1.75 V/Φ_0) and gain (50×), the integrated flux $\Sigma\Phi_p$ can be directly calculated as a function of the integration area. The result is shown in figure 5.6(d). Φ_{ring} can be evaluated at any value of r between R_{in} and R_{out}, as by construction it is constant within experimental noise between these values.

5.7 Interpretation

The apparent shift of the nodal positions is in agreement with an s-wave admixture to a predominantly $d_{x^2-y^2}$-wave order parameter symmetry. If we write the angular dependence of the YBCO gap as $\Delta(\theta) = \Delta_s + \Delta_{x^2-y^2}\cos(2\theta)$, where Δ_s is the s-component and $\Delta_{x^2-y^2}$ is the $d_{x^2-y^2}$-component of the in-plane gap, the nodal angle should satisfy

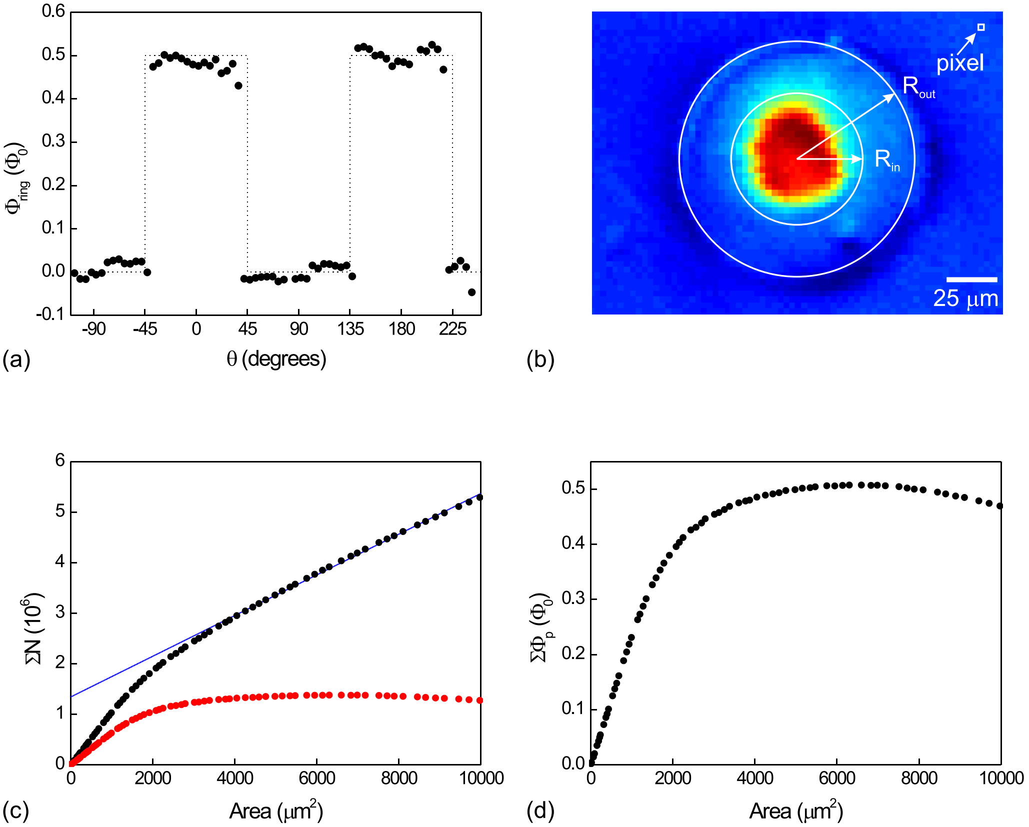

Figure 5.6: (a) Integrated flux through the rings as a function of θ, the angle of the second junction normal with respect to the majority twin-a axis (solid points). The dotted line indicates the expected dependence of a pure $d_{x^2-y^2}$-wave superconductor in the large inductance limit. (b) SSM image for the -12.5° ring, showing the size of a pixel and the inner- and outer radii used for background subtraction. (c) Integrated N as a function of integration area. Black solid points: ΣN, blue line: fit between R_{in} and R_{out}, red solid points: ΣN^*. (d) Integrated flux $\Sigma\Phi_p$ as a function of integration area.

the relation $\theta_{node} = (1/2)\arccos(-\Delta_s/\Delta_{x^2-y^2})$. As the boundary between 0- and π-rings occurs between 37.5° and 42.5°, this implies that $-0.26 < \Delta_s/\Delta_{x^2-y^2} < -0.09$. This should be taken as an underestimate of the gap anisotropy, as twinning would tend to reduce the deviation of the nodal directions from (2n+1)45°.

For a more quantitative analysis a new design was made with smaller increments (0.5°) of the junction angle around the nodal positions. A schematic of this design is shown in figure 5.7(a). The dimensions of the ring are the same as that of the rings mentioned in the previous section except for the junction angles. In the previous design the first junction normal had an angle of 22.5° with respect to the main crystal axis, as suggested by Ng and Varma [153], because in the case of a $d_{x^2-y^2}$+id_{xy} symmetry the phase changes sign at multiples of 90°. Since no considerable deviation of the spontaneously generated flux from $\Phi_0/2$ was observed, the imaginary d_{xy}-wave component was considered negligible.

Samples according to the new design were fabricated and magnetically imaged. In figure 5.7(b) the integrated flux as a function of the second junction normal angle with respect to the majority twin a-axis θ is shown (solid points) and the scanning SQUID microscopy images are depicted in figure 5.7(c). It should be noted that X-ray analysis revealed that the in-plane orientation of the miscut with respect to the 5 by 10 mm^2 STO substrate differs 90° with respect to the miscut orientation of the sample used in the previous measurement. As a consequence the orientation of the rings with respect to the a- and b YBCO crystal axes are interchanged, which explains why half-flux quanta are observed in rings at angles θ that showed integer flux quanta in the previous experiments and vice versa. Note that for this sample the junction angle θ_2 and the junction normal angle θ have the same value by definition, as can be seen from figure 5.7(a). A smooth transition between no spontaneously generated flux and half-flux quanta can be observed because of the small steps in θ.

In the following we try to quantify the order parameter symmetry by fitting the measured data to the theoretical prediction. The fluxoid quantization condition (2.31) for one particular ring reads

$$\frac{1}{2\pi}(\varphi_1 + \varphi_2 + \epsilon) + \frac{\Phi_s}{\Phi_0} = \mathrm{n} \tag{5.4}$$

with the directions as defined in figure 2.10(a). ϵ is the phase difference between the two junctions due to the order parameter symmetry (it will be 0 or π for a $d_{x^2-y^2}$+s-wave symmetry and have intermediate values when complex admixtures such as is, ip or id_{xy} are allowed). Φ_s is the self-generated flux as we consider the case of zero background field. Writing the phases φ_1, φ_2 and the flux Φ_s in terms of the self-generated current I_s we find

$$\arcsin\left(\frac{I_s}{I_{c1}}\right) + \arcsin\left(\frac{I_s}{I_{c2}}\right) + \epsilon + \frac{2\pi L I_s}{\Phi_0} = 2\pi\mathrm{n} \tag{5.5}$$

where we consider only the first solution of (2.53). Normalizing all currents with respect to the nominal junction critical current (which is assumed to be equal for both junctions) and considering the n = 0 state equation (5.5) reduces to

$$\arcsin\left(\frac{i_s}{i_{c1}}\right) + \arcsin\left(\frac{i_s}{i_{c2}}\right) + \epsilon + \beta_L i_s = 0 \tag{5.6}$$

Given the junction normal angles θ_1 and θ_2, equation (5.6) can be solved for i_s using the gap symmetry and β_L as input parameters. Let us denote the superconducting gap $\Delta(\theta)$ as

$$\Delta(\theta) = \Delta_{re}(\theta) + i\Delta_{im}(\theta) \tag{5.7}$$

with

$$\Delta_{re}(\theta) = \Delta_s + \Delta_{d_{x^2-y^2}}\cos(2\theta) \tag{5.8}$$

and

$$\Delta_{im}(\theta) = \Delta_{is} + \Delta_{ip_x}\cos\theta + \Delta_{ip_y}\sin\theta + \Delta_{id_{xy}}\sin(2\theta) \tag{5.9}$$

The junction critical current depends strongly on the orientation when considering an anisotropic superconductor such as YBCO. To incorporate this behavior into our model

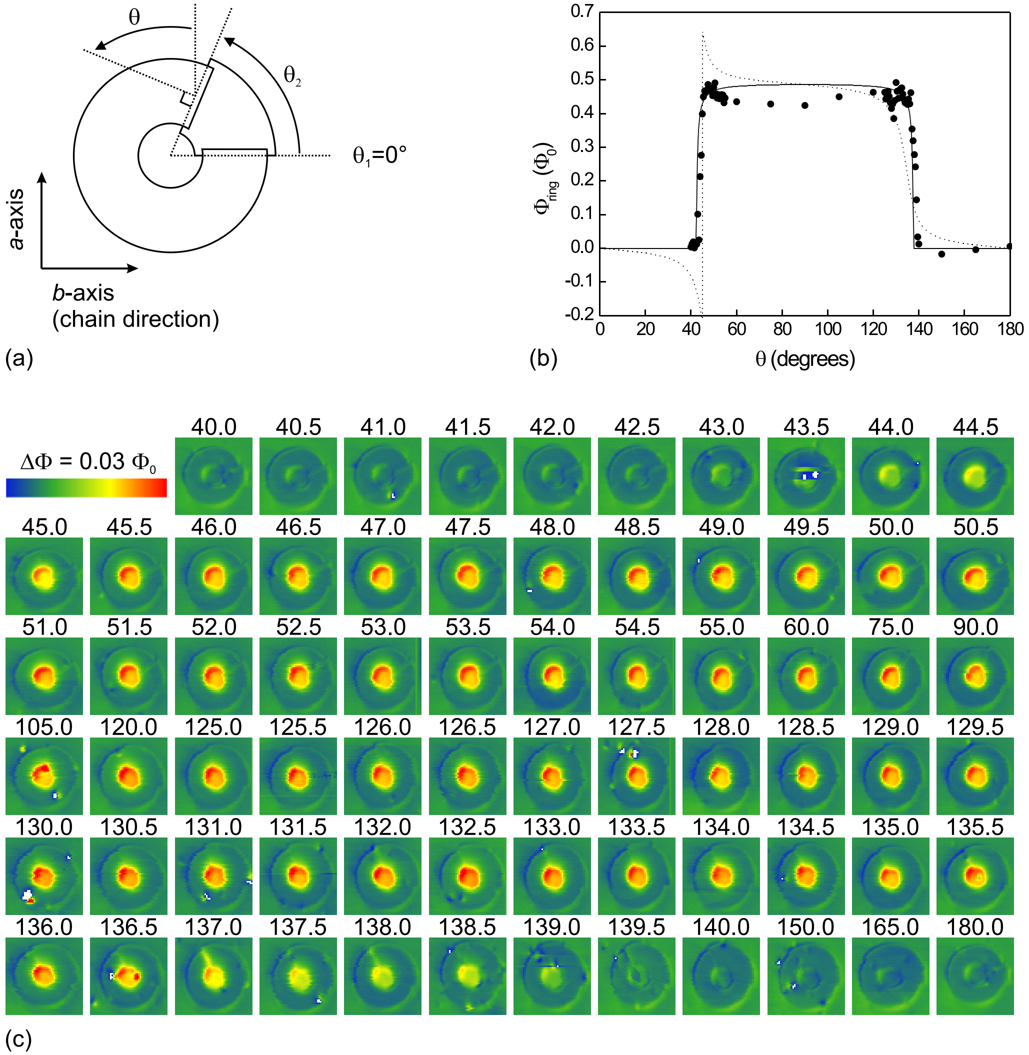

Figure 5.7: (a) Schematic of a ring with the angles θ_1, θ_2 and θ defined. (b) Solid points: integrated flux for the samples with small increments of θ around the nodal angles. Solid line: best fit to the model as described in the text, obtained for a gap symmetry $\Delta(\theta) = \Delta_0[0.91\cos(2\theta) - 0.09]$ and $\beta_L = 67$. Dotted line: expected flux for a gap symmetry $\Delta(\theta) = \Delta_0[0.90\cos(2\theta) - 0.10i\sin(2\theta)]$ and $\beta_L = 67$. (c) Scanning SQUID microscopy images for all rings, labelled by the second junction normal angle θ.

we use the Sigrist-Rice form [177] for the junction critical currents, in which the critical currents are assumed to be proportional to the YBCO gap along the junction normal:

$$i_c(\theta) = \frac{\sqrt{\Delta_{re}(\theta)^2 + \Delta_{im}(\theta)^2}}{\Delta_{max}} \tag{5.10}$$

With Δ_{max} the maximum gap amplitude. The intrinsic phase drop $\epsilon(\theta_1, \theta_2)$ is simply the difference between the arguments of $\Delta(\theta_1)$ and $\Delta(\theta_2)$, and can be written as

$$\epsilon(\theta_1, \theta_2) = i \ln \left(\frac{\Delta(\theta_1)}{\Delta(\theta_2)} \left| \frac{\Delta(\theta_2)}{\Delta(\theta_1)} \right| \right) \tag{5.11}$$

For a given order parameter symmetry and screening parameter β_L equation (5.6) can be solved for i_s (and thus the flux Φ) for all rings. The resulting theoretical prediction for the flux Φ_{th} is then compared to the experimentally determined values Φ_{exp} by minimizing

$$\chi^2 = \sum_{i=1}^{N} (\Phi_{th} - \Phi_{exp})^2 \tag{5.12}$$

with N the total number of rings (70). By changing the screening parameter β_L and the composition of the superconducting gap such as to minimize equation (5.12) we find that the best fit is obtained for $-0.12 < \Delta_s/\Delta_{d_{x^2-y^2}} < -0.08$ and $40 < \beta_L < 150$, using a doubling of χ^2 from its lowest value as a criterion for assigning parameter uncertainties. The observed gap anisotropy is consistent with the value reported for the sample with 5 degrees intervals for the second junction angle ($-0.26 < \Delta_s/\Delta_{x^2-y^2} < -0.09$). The value for the screening parameter is quite different from the value that was estimated in section 5.3: $\beta_L \approx 433$. However, as indicated by the large error margin, the fits are quite insensitive to the value of β_L for large β_L and are highly sensitive to small systematic errors in the integration of the flux. The best fit was obtained for an order parameter symmetry consisting of 91% $d_{x^2-y^2}$-wave and 9% s-wave, indicated by the solid line in figure 5.7(b). We observe no evidence for any imaginary component to the gap (is, ip_x, ip_y, or id_{xy}). This is illustrated by the dashed line in figure 5.7(b) which shows the expected flux for a 10% id_{xy} admixture. The aforementioned model also sets an upper limit of 2.5% to any complex admixture.

It is of interest to compare the observed anisotropy in the gap, $\Delta_b/\Delta_a = 1.2$, to the anisotropy in the YBCO unit cell constants: $b/a \approx 1.02$. The gap anisotropy is about an order of magnitude larger than the lattice anisotropy (20% versus 2%). This may lead one to the conclusion that the observed gap anisotropy is not purely due to the orthorhombicity of YBCO. The question what causes the gap anisotropy is closely connected to the question what causes superconductivity in the cuprate superconductors. Possible sources include energy bands of the CuO chains, which were already mentioned in section 4.2 [178], or a Pomeranchuk instability which breaks the tetragonal symmetry of the Fermi surface [179]. Insights into the relation between the origin of the gap anisotropy and its relation to the underlying crystal structure may prove of crucial importance for modelling high-T_c superconductivity.

5.8 Summary

In this chapter phase-sensitive experiments to study the order parameter symmetry of the cuprate superconductor YBCO have been presented. Arrays of YBCO/Nb rings containing two Josephson junctions have been fabricated and cooled down below the transition temperature of niobium. One of the junctions was kept at a constant angle while the other junction angle was varied for each ring. Depending on the junction angle and the details of the YBCO order parameter symmetry spontaneously generated flux can occur in such superconducting rings. The rings were imaged using a scanning SQUID microscope and from the angular dependence of the produced flux the pairing symmetry in YBCO is found to have $\Delta_s/\Delta_{x^2-y^2} \approx -0.1$, corresponding to a gap which is at least 20% larger in the b-axis (CuO chain) direction: $\Delta_b/\Delta_a = 1.2$. The same anisotropy was also observed by Smilde *et al.* in the I_cR_N-product of similar YBCO/Nb ramp-type Josephson junctions [166]. The gap anisotropy that was estimated from these measurements however was slightly larger: a value of $\Delta_b/\Delta_a = 1.5$ was calculated. The experiments set an upper limit to any imaginary is- ip- or id_{xy} admixture of 2.5%, which indicates that broken time reversal symmetry is not likely to be associated with high-T_c superconductivity in optimally doped YBCO.

Chapter 6

Implementation of half-integer flux quanta in RSFQ

6.1 Introduction

In chapter 3 we described how π-rings can be realized by combining the high-T_c superconductor YBCO and the conventional superconductor niobium. These π-rings are characterized by the spontaneous generation of circulating currents corresponding to half a flux quantum when cooled below the superconducting transition temperature. In chapter 5 we presented how such rings were used for the angle-resolved determination of the in-plane gap symmetry of YBCO. In this chapter we present the application of π-rings in superconducting digital electronics. The natural two-fold degenerate ground state corresponding to a half-flux quantum of positive or negative polarity makes π-rings an excellent candidate for storage of binary information in superconducting information technology. We present the first successful integration of π-rings in superconducting electronics through the realization of a π-ring-based toggle flip-flop (TFF). The incorporation of π-rings leads to improved device symmetry, higher fabrication yield, enhanced operation margins and alleviates the need for bias currents.

6.2 RSFQ

Rapid single flux quantum technology (RSFQ) is a superconducting digital electronics family that was first proposed by Likharev in 1985 [180–182]. In RSFQ, a bit is represented by the presence (for the logic '1') or absence (for the logic '0') of a flux quantum in superconducting loops. An essential element in RSFQ circuits is the Josephson junction, which acts as a gate to transfer flux quanta between loops; it plays a central role in RSFQ much like the transistor does for conventional semiconductor electronics. RSFQ combines a high operation speed (potentially 100 GHz and higher) with low dissipation (typically a few milliWatts), which causes some to believe that RSFQ is an attractive alternative for conventional CMOS technology in a time where Moore's celebrated law seems to come to an end and the demand for higher computing capacity increases. Most superconducting digital electronics devices are low-T_c circuits realized using a niobium-based fabrication process (containing Nb/AlO$_x$/Nb Josephson junctions), which has achieved rapid progress during the last years and is under constant development [17]. Circuits can nowadays be ordered commercially from companies such as the HYPRES foundry or IPHT Jena.

RSFQ has already demonstrated its potential for high-frequency operation. To name but a few accomplishments: a 4-to-1 demultiplexer containing over 500 Josephson junctions that performed up to 56 GHz was realized by Furuta *et al.* [183]. Mukhanov *et al.* demonstrated the correct operation of an RSFQ-based digital receiver system containing approximately 11.000 Josephson junctions which operates at 30 GHz [184]. Yamanashi *et al.* have realized a pipelined 8-bit RSFQ microprocessor containing over 10.000 Josephson junctions and operating at 20 GHz with an estimated peak performance and power consumption of 1400 million operations per second and 3.4 mW, respectively [185]. Work on an improved version of this processor with cache memory, containing over 22.000 Josephson junctions, is currently in progress [186]. H. Akaike *et al.* have demonstrated an SFQ shift register circuit operating at frequencies exceeding 100 GHz [187]. The fastest RSFQ logic cell ever measured is a toggle flip-flop operating at frequencies up to 770 GHz [188]. Though this high speed is also related to the lower complexity of this device, 770 GHz is an impressive speed nonetheless (to make a comparison: a photon travelling at the speed of light, $c = 3.0 \cdot 10^8$ m/s, will travel less than 400 μm during one cycle).

Despite its large potential RSFQ is mainly a research activity and has no commercial applications to date. This can be attributed to a number of factors, such as the high level of integration of the established semiconductor industry (which roughly had a two decades head-start) in current society, the lack of sustained funding to establish the needed infrastructure to make superconductor digital technology a viable commercial product, and the need for a cryogenic environment [189]. Nevertheless, the advantage in performance may well be sufficient to outweigh the cost and inconvenience of the required cryogenic refrigeration for some purposes such as high-end computers, servers, and routers [190]. Moreover, much progress has already been booked in terms of cooling, for example the availability of subKelvin cryogen-free coolers. Besides obvious efforts to increase cooling power and lower the base temperature, current research interests include miniaturization of cryocoolers, improvement of cryopackaging and a reduction of cooler interference (which can be of a mechanical, electromagnetic or thermal nature) [191]. Combined with an improved circuit design (optimized to lower the required cooling power) these efforts may ultimately lower or remove the present barrier that cryogenic refrigeration poses.

6.2.1 Transfer of flux quanta

In RSFQ circuits, Josephson junctions act as gates that transfer binary data stored in the form of magnetic flux quanta between superconducting loops. This process is illustrated in figure 6.1. In figure 6.1(a) a schematic is given of two coupled superconducting loops containing three Josephson junctions, which will be denoted by J_1, J_2 and J_3 for the left, right and middle junction, respectively. The loops are assumed to be in the large inductance limit $\beta_L \gg 1$ and one of the loops has stored one magnetic flux quantum. The circuit diagram of the double loop is presented in figure 6.1(b). Following the conventional notation in RSFQ the loops are represented by open loops connected to ground. It is important to realize that all grounds are connected phase coherently (usually via a superconducting ground plane). For simplicity the self-inductance L of the individual loops and the critical currents I_c of the Josephson junctions are assumed to be equal and the mutual inductance between the loops is neglected. The phase of the wavefunction θ at the grounds and nodes is shown in red font for the initial situation. The values ϵ and

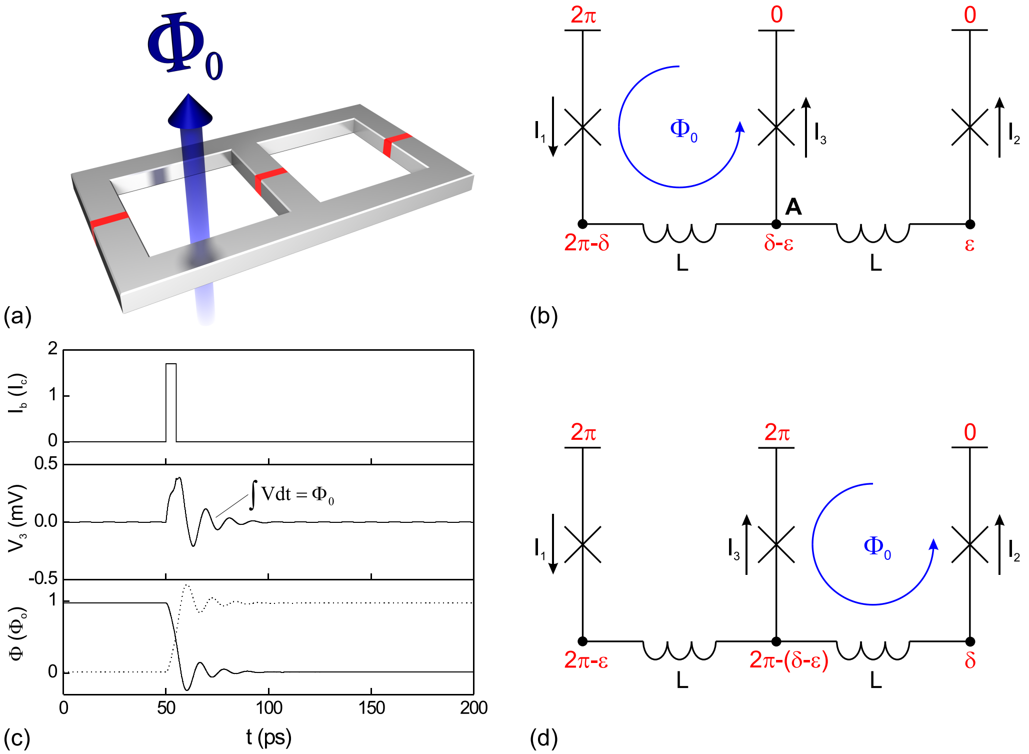

Figure 6.1: (a) Schematic and (b) circuit diagram for two connected storing loops in the large inductance limit ($\beta_L \gg 1$) containing Josephson junctions. In the initial situation the left loop contains one flux quantum and the right loop contains no flux. The phase of the wavefunction θ is indicated in red font. (c) Simulation of a switching event. Top: the current pulse that is applied at the node labelled **A** in figure 6.1(b), Middle: Voltage over junction J_3, Bottom: the flux in the left loop (solid line) and right loop (dashed line). (d) Circuit diagram displaying the current- and phase distributions after the switching event.

δ, given by

$$\epsilon \ll \delta \approx \frac{2\pi}{\beta_L} \ll 1 \tag{6.1}$$

are chosen such that the Josephson relations (2.24)

$$\begin{align} I_1 &= I_c \sin\delta \approx I_c\delta \tag{6.2} \\ I_2 &= I_c \sin\epsilon \approx I_c\epsilon \tag{6.3} \\ I_3 &= I_c \sin(\delta-\epsilon) \approx I_c(\delta-\epsilon) \tag{6.4} \end{align}$$

Kirchhoff's law

$$I_1 = I_2 + I_3 \tag{6.5}$$

and the fluxoid quantization condition (2.31)

$$2\delta - \epsilon + \beta_L \frac{I_1}{I_c} = 2\pi \tag{6.6}$$

$$2\epsilon - \delta + \beta_L \frac{I_2}{I_c} = 0 \tag{6.7}$$

are satisfied. For the definition of signs, directions and dependencies of the phase θ, the gauge invariant phase drop φ and the magnetic flux, refer to sections 2.6 and 2.7[1]. The fact that one of the grounds has a phase 2π whereas the others have a phase 0 merely reflects the fact that for a single valued wavefunction Ψ the phase at any point is only determined up to 2π, which is the basis of the fluxoid quantization condition.

Suppose a current source is connected to the node labelled **A** and ground and a short current pulse exceeding I_c is given. Since junction J_3 provides the smallest impedance path to ground and it is already biased because of the circulating current this junction will switch first (of course the precise details of how large the current pulse should be depends on the circuit parameters). In terms of the pendulum analogon introduced in section 2.8 the current pulse corresponds to a quick jerk on the rope connected to the pulley block. During the switching process the junction produces a transient voltage pulse and changes its phase by 2π, which corresponds to the pendulum making a full rotation.

It should be noted that the bias due to the circulating current plays only a minor role in this example: the phase drop $\delta - \epsilon$ over junction J_3 is considered to be much smaller than one and thus the bias is much smaller than the critical current I_c. The main argument why junction J_3 switches first is therefore the large inductances that are in series with junctions J_1 and J_2. For rings that are not in the large inductance limit, however, the current bias from a flux quantum will be significant. The Josephson transmission line (JTL), which will be discussed in subsection 6.4.2, is actually based on this principle.

The behavior of this system can be analyzed using the circuit simulator JSIM [192]. The result, calculated for junction parameters $I_c = 50\ \mu\text{A}$, $C = 0.5$ pF and $R_N = 10\ \Omega$ and loop inductances of 500 pH, is displayed in figure 6.1(c). In the top graph the applied bias current pulse (85 μA for 5 ps) is depicted. The middle graph shows the voltage over the switching junction. The Stewart-McCumber parameter (2.39) for the junctions is approximately 7.5 so this junction is underdamped[2]. The period of the oscillations corresponds to $2\pi/\omega_p = 11.4$ ps with ω_p the plasma frequency (2.34). The oscillations decay as $e^{-t/2R_N C}$, with an RC-time of 5 ps. In the bottom graph the flux in each of the loops is shown as a function of time. With a screening parameter β_L=76 the loops are in the large inductance limit.

During the switching event, a flux quantum is transferred from the left loop to the right loop, which follows directly from the 2π phase shift that occurs during the switching event. Consider an integration area bound by the superconducting path in the left loop. When Maxwell's equation is integrated over this area we find

$$\int_S (\nabla \times \mathbf{E}) \cdot d\mathbf{S} = -\frac{\partial}{\partial t} \int_S \mathbf{B} \cdot d\mathbf{S} \tag{6.8}$$

---

[1] We assume the flux $\oint \mathbf{A} \cdot d\mathbf{l}$ to be fully stored in the inductor, thereby setting the right-hand side of equation (2.25) equal to zero

[2] Normally overdamped junctions are used in RSFQ but underdamped junctions were chosen for this example to underline the analogy with the mechanical pendulum via the frequency and decay-time of the voltage/flux-oscillations

The left-hand side can be simplified by applying Stokes' Theorem and realizing that $-\oint \mathbf{E} \cdot d\mathbf{l} = V_3$, while the term in the integral of the right hand side is the flux Φ_1 by definition. Thus we find a simple relation between the flux in the left loop and the voltage of the switching junction J_3:

$$V_3 = -\frac{\partial \Phi_1}{\partial t} \tag{6.9}$$

Integrating this equation and substituting the second Josephson equation (2.26) we find

$$\Delta \Phi_1 = -\frac{\Phi_0}{2\pi} \int\limits_0^{2\pi} d\varphi_3 = -\Phi_0 \tag{6.10}$$

The integrated area of the voltage pulse in figure 6.1(c) indeed corresponds to one flux quantum. The net result of the voltage pulse is the transfer of the flux quantum from the left loop to the right loop. This final situation is displayed in figure 6.1(d).

6.3 Storing loop

Because RSFQ is a pulse based logic, the temporary latching of data is an essential task in many RSFQ logic cells. This is typically achieved using a loop containing two Josephson junctions and an asymmetrically applied bias current. Assuming equal critical currents for the Josephson junctions, the free energy of such a storing loop, normalized with respect to the Josephson coupling energy (2.29), is given by

$$u = 2 - \cos\varphi_1 - \cos\varphi_2 - i_b\varphi_1 + \frac{1}{2\beta_L}\left(\varphi_1 - \varphi_2\right)^2 \tag{6.11}$$

with i_b the bias current normalized with respect to the critical current I_c. The last term in this equation represents the energy that is stored in the magnetic field: $\Phi^2/(2LE_J)$ where the magnetic flux is expressed in terms of the phase drops via the fluxoid quantization condition (2.42) [3]. It should be noted that the fluxoid number n is chosen equal to zero, which is justified as long as one implicitly assumes that the phase drops are allowed to differ by more than 2π.

The potential energy landscape of this system is depicted in figure 6.2(a) for a screening parameter $\beta_L = 2\pi$ and in the absence of a bias current i_b. Away from the $\varphi_1 = \varphi_2$ ($\Phi = 0$) line the parabolic term corresponding to the magnetic energy is dominant and no local minima exist. Along the line where the parabolic term has its minimum the cosine-shape of the junction potential energy causes local minima corresponding to 1,3,5,... magnetic flux quanta, depending on the screening parameter of the loop: a larger β_L corresponds to more local minima.

Note that not each point of the potential energy landscape corresponds to a physically allowed (static) state because φ_1 and φ_2 are not independent variables: the phases are linked via the Josephson equations and Kirchhoff's law. At the minima however these relations are satisfied, as can be seen from the sum (or difference) of the partial derivatives of the potential energy with respect to the two phase drops

$$\frac{\partial u}{\partial \varphi_1} + \frac{\partial u}{\partial \varphi_2} = \sin\varphi_1 + \sin\varphi_2 - i_b \tag{6.12}$$

---

[3] In the following discussion we define the flux positive in the $\otimes$ direction, which amounts to adding a minus-sign in front of the flux in equation (2.42)

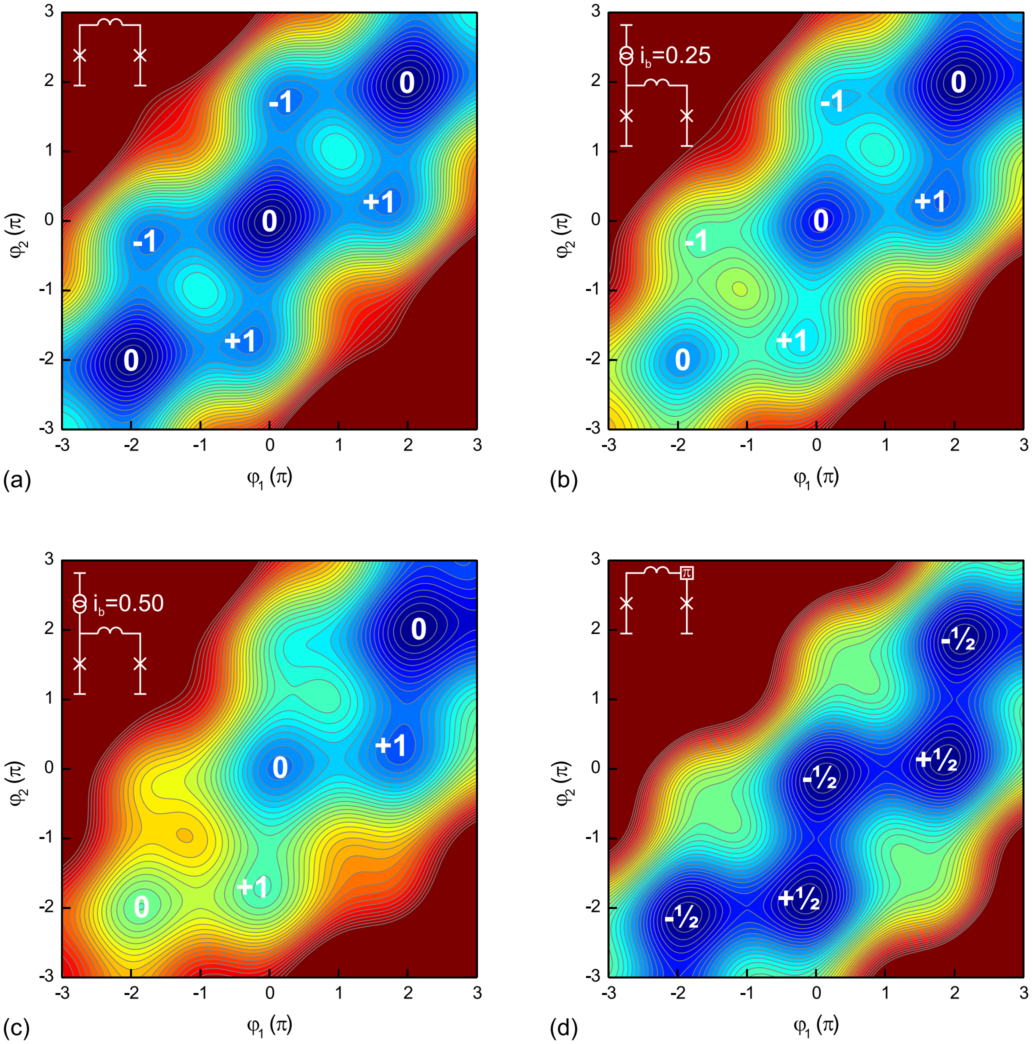

Figure 6.2: (a) Potential energy landscape for a storing loop containing 2 Josephson junctions. The minima are labelled by the corresponding number of flux quanta (which are not necessarily fully formed). (b) Potential energy landscape when a (normalized) bias current $i_b = 0.25$ is asymmetrically applied. (c) Potential energy landscape for a bias current $i_b = 0.50$, which results in a bistable system. (d) Potential energy landscape for a π-ring. All figures were calculated for a screening parameter $\beta_L = 2\pi$.

At the extrema this reduces to

$$i_b = \sin\varphi_1 + \sin\varphi_2 \tag{6.13}$$

which is simply Kirchhoff's law normalized with respect to I_c. Thus the minima correspond to physically allowed stable states.

The two-junction loop without bias current is completely symmetric with respect to the flux polarity. As a result the number of stable states will always be an odd number (1,3,5,...). However, such a loop is not suitable for the storage of binary data, for which a bistable system is preferred. When the asymmetrically applied bias current is increased the potential energy landscape is distorted. This is illustrated in figure 6.2(b) for a bias current $i_b = 0.25$. By increasing the bias current further the potential energy landscape can be tuned such that the $\Phi = -\Phi_0$ state is no longer a stable state. In figure 6.2(c) the potential energy landscape for a bias current $i_b = 0.50$ shows only two stable states: the $\Phi = 0$ and the $\Phi = +\Phi_0$ state. For a bias current $i_b \lesssim 0.50$ the energy states become degenerate and the separating barrier reaches a maximum. This is the ideal configuration for a well designed bistable storage loop in an RSFQ circuit. A further increase of the bias current results finally in the vanishing of the second state and the system is no longer bistable.

6.3.1 Storing π-loop

The artificial generation of a two level system makes the design of RSFQ logic cells strongly asymmetric and acts often as the most critical parameter for correct operation. π-rings have a bistable ground state by nature even for low values of the screening parameter. The potential energy landscape of a π-ring, which can be calculated by simply setting i_b to zero and subtracting an extra π from the parabolic term in equation (6.11), is depicted in figure 6.2(d). Because of its inherent bistability a π-loop does not require an external bias current and is less sensitive to parameter deviations, which presents a strong advantage in RSFQ design, circuit reliability and robustness against thermal noise. It should be noted that this advantage does not hold exclusively for π-loops based on an unconventional order parameter symmetry. The argument also holds when the π-phase shift is realized using different mechanisms such as the π-junctions or rings containing a trapped fluxoid as mentioned in section 2.10.

6.4 Design

We have implemented π-rings in a toggle flip-flop (TFF), a logic circuit in which the fractional flux is controllably toggled by applying single flux quantum (SFQ) pulses at the input channel. The flip-flop was incorporated in a testing circuit and its correct operation demonstrated [193, 194]. The circuit, depicted in figure 6.3, was designed by dr. Thomas Ortlepp at the RSFQ Design Group, University of Technology Ilmenau. It consists of a DC/SFQ converter (input), a Josephson transmission line (transport), the actual toggle flip-flop with integrated π-phase shifts and a read-out SQUID (output). The operation of each of these individual elements will now shortly be discussed. In the design process, a critical current density of 12 μA per μm was assumed.

6.4.1 DC/SFQ converter

The purpose of the DC/SFQ converter is to convert the DC input signal to SFQ pulses. It consists of a loop (designed inductance $L_i = 8.4$ pH) containing two Josephson junctions. The design values of the critical currents are 156 μA for junction J_{i1} and 120 μA for junction J_{i2}. With $LI_c/\Phi_0 \approx 0.5$ this loop is a non-storing loop. The two junctions are biased below their critical current with a bias current I_{b1}. When the input current

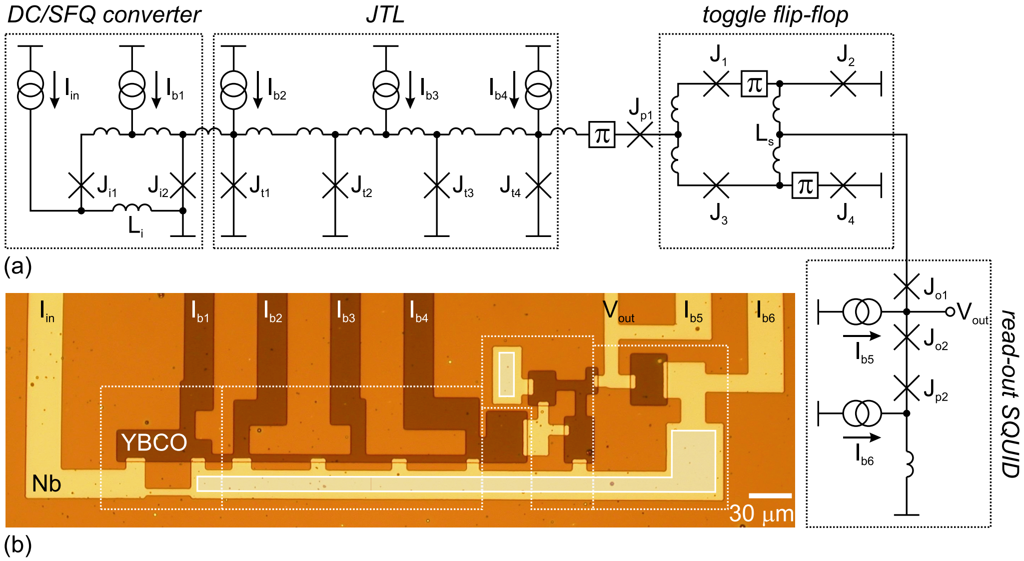

Figure 6.3: (a) Circuit diagram and (b) optical micrograph of the test circuit for the toggle flip-flop with built-in π-phase shifts. The separate elements are highlighted with dashed lines: the DC/SFQ converter provides SFQ pulses which are transferred to the toggle flip-flop via the JTL. The toggling of the internal state of the TFF is detected by a read-out SQUID. The picture was taken before deposition of the ground plane. The two white boxes mark places for the vias to ground.

I_{in} is increased, part of the current flows through these junctions, thereby increasing the bias current of junction J_{i2} and decreasing the bias current of junction J_{i1}. When the total current flowing through junction J_{i2} exceeds the critical current, the junction switches to the voltage state and a flux quantum (of polarity $\otimes$) is released into the Josephson transmission line. Because there was no flux in the loop to begin with and one flux quantum has been transferred into the JTL, the loop contains one flux quantum (of polarity $\odot$) after the switching event. This flux quantum corresponds to a counter-clockwise circulating current which diminishes the bias current of junction J_{i2} below the critical current and it returns to the zero-voltage state (even though the loop is non-storing, the input current I_{in} ensures that the junctions do not switch). When the input current is reduced, the stored flux quantum can escape the system via junction J_{i1}, which has no effect on the JTL. Thus an SFQ pulse can be generated for every rising ramp of a triangular input signal.

The DC/SFQ converter can also be operated such that multiple SFQ pulses are released into the JTL on each rising ramp of the input signal. This can be accomplished by enlarging the input signal. After the release of the first SFQ pulse junction J_{i2} relaxes to the superconducting state and a flux quantum is trapped in the storing loop. By increasing the input current I_{in} even further the junction can be biased to its critical current again and the junction will switch again, thereby sending a second SFQ pulse into the JTL and trapping another flux quantum in the storage loop. By increasing the input current even further more SFQ pulses can be generated.

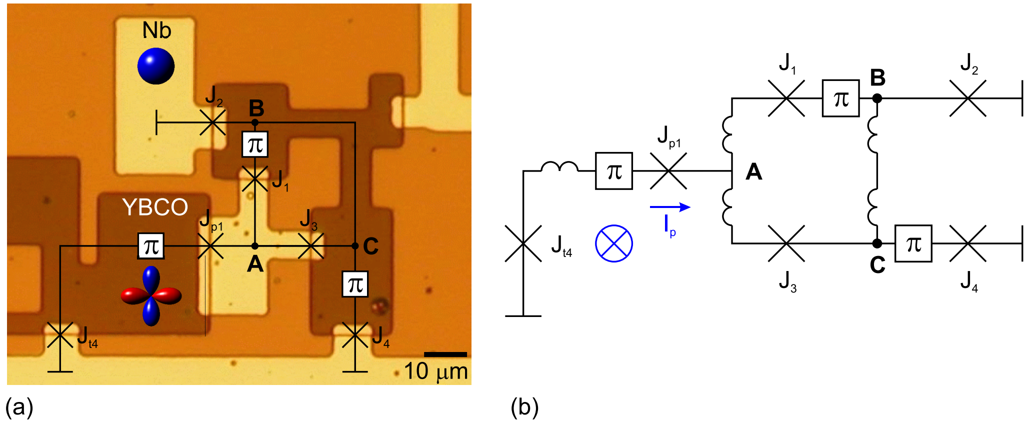

Figure 6.4: (a) Microphoto and circuit diagram of the TFF. (b) Equivalent circuit that was used in figure 6.3. The $\otimes$ and I_p, indicated in blue, represent an incoming SFQ pulse.

6.4.2 Josephson transmission line

The Josephson transmission line is used in RSFQ to transport SFQ pulses between different logic cells. The JTL consists of several electrically coupled two-junction loops. The critical currents of the junctions are designed to be 156 μA for junction J_{t1}, 126 μA for junctions J_{t2} and J_{t3}, and 108 μA for junction J_{t4}. The loop inductances are approximately 8 pH which results in $LI_c/\Phi_0 \approx 0.5$. The operation of a JTL is comparable to the transfer of flux quanta that was discussed in subsection 6.2.1, except that the JTL has in general more than 2 loops and these loops are not able to store a magnetic flux quantum. Suppose an SFQ pulse (polarity $\otimes$) that is generated by the DC/SFQ converter enters the JTL at junction J_{t1}. The circulating current which is associated with this flux quantum will bias junction J_{t2} above its critical current. Consequently, junction J_{t2} switches and the flux quantum is transferred through junction J_{t2} to the next loop in the JTL, where it biases junction J_{t3} above its critical current and so forth. As a result, an SFQ pulse presented at the input of the JTL will, after a cascade of switching events, leave the JTL at the last junction J_{t4}. In principle, a JTL can operate without bias currents but in practice bias currents are added to enhance the overall stability and relax fabrication requirements and operation margins. Many RSFQ designs nowadays make use of passive transmission lines, which were first realized in 1993 by Polonsky *et al.* [195]. These have the advantage that they do not require external bias currents, are faster compared to conventional Josephson transmission lines and are easier to fabricate. For the small JTL which is incorporated in the test circuit these benefits are outweighed by the required driver- and a receiver cells containing two junctions each and the relatively wide lines which are required for good impedance matching.

6.4.3 Toggle flip-flop

A toggle flip-flop is a bistable circuit element that toggles its internal state on every incoming pulse. Toggle flip-flops can be used to divide the clock frequency by a factor of two and are applied in a variety of digital counters. Our TFF consists of two electrically coupled π-rings. The main purpose of having two loops instead of one is to enhance the stability of the device. To clarify the layout of the TFF (in particular the positions of the π-phase shifts) the circuit diagram superimposed on the micrograph and the equivalent network are depicted in figures 6.4(a) and 6.4(b), respectively. All junctions are oriented along the YBCO main crystal axes whose orientation is parallel to the lobes of the *d*-wave clover shown in figure 6.4(a).

The circuit representation of π-phase shifts is not uniquely defined: different schematics may be used to represent the same physical situation provided the π-phase shifts are placed consistently. For example the π-phase shift between junction J_1 and node **B** is equivalent to one π-phase shift just left and one π-phase shift just right of node **B** in figure 6.4(a). Which of these representations 'feels more natural' depends on the direction in which the path between node **A** and the top-left ground is being considered and is therefore completely arbitrary. A similar situation occurs for the π-phase shift located between node **C** and junction J_4. The representation used in figure 6.4 needs the minimum number of π-phase shifts and elegantly shows the TFF as two coupled π-loops. The π-phase shift between the JTL and the TFF was designed there on purpose: it ensures that the loop connecting junctions J_{t4} and J_4 is a standard loop instead of a π-loop. Thus any unwanted currents that are associated with π-loops are prevented.

The design values of the critical currents are 90 μA for junctions J_1 and J_3, 132 μA for junction J_2, and 114 μA for junction J_4. The common storing inductance, L_s is approximately 10 pH which results in a screening parameter $\beta_L \approx 3$ or $LI_c/\Phi_0 \approx 0.5$ for the π-loops. In the ground state the storing loops carry fractional flux quanta of opposite polarity. Let us assume an initial state of a $\otimes$ and $\odot$ half-integer flux quantum in the left and right loop, respectively. When junction J_{t4} emits an SFQ pulse (polarity $\otimes$) from the JTL the associated current pulse I_p will split up at **A** and divide more or less evenly across the two branches to ground. The SFQ pulse is depicted in blue in figure 6.4(b). During the pulse the junctions J_1 and J_4 will be over-biased and will emit a complete flux quantum (of $\otimes$ and $\odot$ polarity, respectively) thereby changing the polarity of the fractional flux quantum stored in the π-loops ($\downarrow \rightarrow \uparrow + \Downarrow$ and $\uparrow \rightarrow \downarrow + \Uparrow$, respectively, where the single arrows denote the fractional flux quanta in the loop, the double arrows denote the emitted flux quanta, up-arrows have $\odot$ polarity and down-arrows have $\otimes$ polarity). Because of the rearrangement of the half-integer flux quanta now junctions J_2 and J_3 are biased. When a new SFQ pulse enters the TFF these junctions will switch under the emission of a full flux quantum (of $\otimes$ and $\odot$ polarity, respectively) and the initial ground state is obtained. Thus on every input pulse one of the junction pairs J_1-J_4 and J_2-J_3 will switch under the emission of a flux quantum and the π-rings toggle their internal state (the polarity of the fractional flux quantum).

6.4.4 Read-out SQUID

The circuit diagram of the read-out SQUID is presented in 6.5(a). To clarify the operation an equivalent circuit bearing more resemblance to the conventional SQUID representation as a two-junction loop is shown in figure 6.5(b). The core of the read-out SQUID consists of a loop containing junctions J_{o1} and J_{o2} which is biased with a current I_{b5}. An extra bias current I_{b6} has been added to the left SQUID branch and the TFF storing loop containing junctions J_2 and J_4 is incorporated in the right SQUID branch. Junction J_{p2} is a passive junction (see next subsection). The SQUID junctions have critical currents

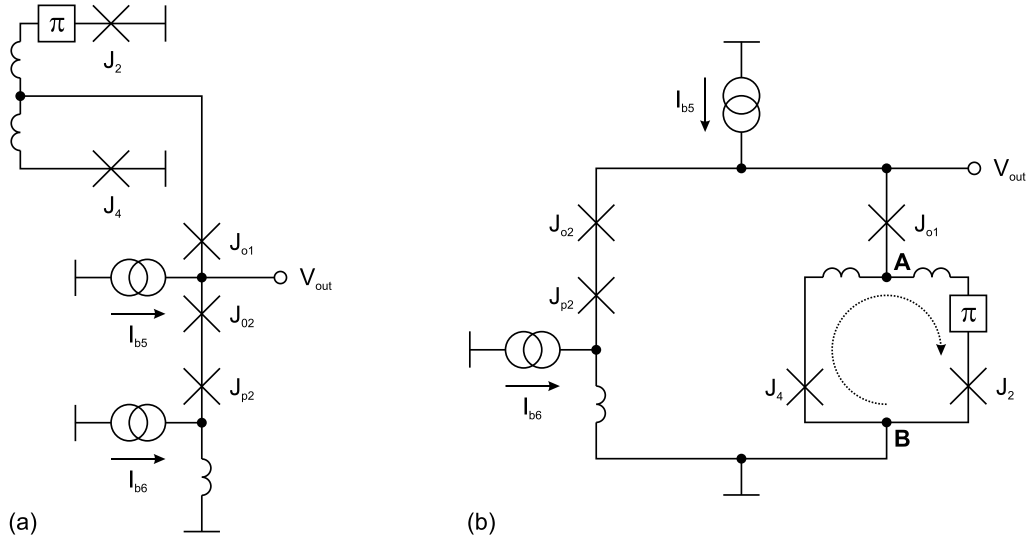

Figure 6.5: (a) Circuit diagram of the read-out SQUID. (b) Equivalent circuit. The dotted arrow indicates a stored half-integer flux quantum.

of 96 μA for junction J_{01} and 114 μA for junction J_{02}. With an estimated self-inductance of 7 pH the SQUID has a screening parameter $\beta_L \approx 2$.

The state of the toggle flip-flop is determined from the polarity of the fractional flux quantum in the TFF storing loop. When the TFF toggles this polarity changes sign, which results in a different phase drop between nodes **A** and **B**. This change in phase drop affects the SQUID properties via the fluxoid quantization condition, in a similar way that an externally applied magnetic field would. The bias current I_{b6} which flows via an inductor to ground provides an extra phase shift and can be used to set the SQUID operation point to a position where it is most sensitive to variations in the phase caused by the toggling of the TFF. The operation of the read-out SQUID can conveniently be explained in terms of figure 2.9(b). First, bias current I_{b5} is used to tune the overall shape of the V-Φ-curve. Then bias current I_{b6} is used to set the position on this bias curve. Thus, these two bias currents have defined the operation point and the signal coming from the TFF, which corresponds to a small change in Φ, can directly be translated into a change of V_{out} for a proper choice of bias currents. In the experiment the bias currents I_{b5} and I_{b6} were chosen such as to bias the SQUID at the edge of a steep flank in figure 2.9(b). The resulting output signal is therefore expected to toggle between zero and a finite voltage.

6.4.5 Passive junctions

The π-phase shifts in this design are obtained by exploiting the difference in order parameter symmetry of the superconductors YBCO and niobium, and as a result the circuit consists of YBCO parts and niobium parts which are connected via Josephson junctions. Most of these junctions are actively participating in the device operation. There are also

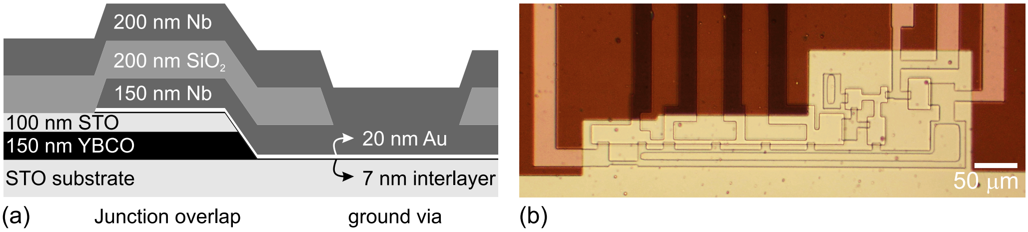

Figure 6.6: (a) Schematic cross section showing a Josephson junction and a via to ground. The layer thicknesses are indicated. (b) Optical micrograph of the TFF test circuit after deposition of the niobium ground plane.

two passive junctions, labelled J_{p1} and J_{p2}, whose purpose is more of a practical nature. Because the circuit consists of two types of superconductor, during the design stage the situation can arise where two nodes, which are in different superconductors, have to be connected. Consider for example the loop containing junctions J_{t4}, J_{p1}, J_3 and J_4 in figure 6.4(a). The left electrode of junction J_3 and the top electrode of junction J_{t4} have to be connected (horizontally to ensure the π-phase shift). Because the two electrodes are not made of the same superconducting material an extra junction is necessary. This junction, labelled J_{p1}, is a passive junction in the sense that it is not designed to switch. Its only purpose is to connect the two superconductors. A similar situation occurs for the passive junction J_{p2}: as can be seen from figure 6.3 the base electrode of junction J_{o2} cannot be connected to ground without the introduction of an extra Josephson junction. The non-switching junctions J_{p1} and J_{p2} are typically three times larger than the other junctions in the circuit and behave like small parasitic inductors (the Josephson inductance of a 300 μA junction corresponds to roughly 1 pH).

6.4.6 Fabrication

The first layers of the sample were fabricated using the standard fabrication process described in section 4.5. However, to ensure well defined inductances the standard fabrication process was modified by the addition of a niobium upper ground plane. The ground plane was deposited in the last fabrication step on top of the existing structures for the practical reason that the YBCO structures need to be epitaxially grown on top of the STO substrate.

A cross section indicating the layer thicknesses is shown in figure 6.6(a). The base electrodes of the ramp-type Josephson junctions consist of a YBCO/STO bilayer with thicknesses 150 nm (YBCO) and 100 nm (STO). A 7 nm YBCO interlayer and 20 nm gold barrier separate the ramped base electrode from the 160 nm niobium top electrode. The overlap of the junctions is 3 μm. On top of the structures a 200 nm SiO$_2$ insulating barrier was deposited in which vias were etched for contact to the ground plane. In the final fabrication step a 200 nm niobium ground plane was deposited using DC sputtering. A picture of the device after the deposition of the ground plane is shown in figure 6.6(b).

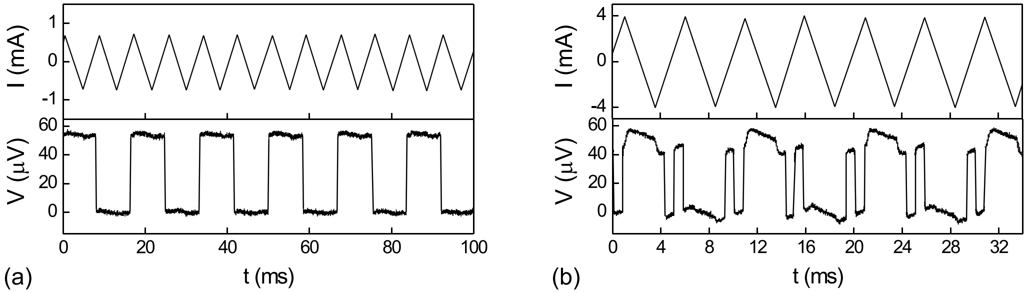

Figure 6.7: Measurement results for (a) a triangular input current corresponding to 1 SFQ pulse per rising ramp of the input signal and (b) a triangular input current corresponding to three SFQ pulses per rising ramp of the input signal.

6.5 Measurement results

The sample was cooled down to 5.3 K in a well-shielded flow cryostat to demonstrate the correct operation both in normal and in oversteered operation mode. Figure 6.7(a) shows the experimental results for the normal operation mode. In the top graph the input current I_{in} is shown as a function of time. The input current is a triangular signal with an amplitude of approximately 1 mA at a frequency of ∼100 Hz. The bottom graph shows the output voltage V_{out} over the read-out SQUID. The voltage clearly jumps between the zero-voltage state to a voltage just below 60 μV on every rising edge of the input signal. Thus the flip-flop toggles its internal state on every incoming pulse.

The circuit was also operated in the mode, where multiple flux quanta where generated at the rising ramp of the input signal, as mentioned in subsection 6.4.1. The experimental results are shown in figure 6.7(b). The applied current signal was increased to an amplitude of 4 mA, where the DC/SFQ converter releases three SFQ pulses per rising ramp of the input signal. In the SQUID output voltage V_{out} three switching events per rising ramp of the input signal can clearly be distinguished, which shows again that the TFF switches its state for every incoming SFQ pulse. The deviations in the voltage level in the oversteered mode of operation in figure 6.7(b) are caused by a parasitic coupling between adjacent lines in the experimental setup. With these experiments we have demonstrated for the first time the correct digital operation of a logic circuit element with integrated π-phase shifts [193, 194].

6.6 Summary

The fractional flux quanta that can arise in YBCO/Nb hybrid superconducting structures have been incorporated in a superconducting logic element: a toggle flip-flop. The polarity of the fractional flux quanta was controllably toggled by applying SFQ pulses at the input channel. The correct digital operation of a circuit containing a DC/SFQ converter, Josephson transmission line, toggle flip-flop with intrinsic π-phase shifts and a read-out SQUID has been demonstrated. This realization needed only a quarter of the size of a standard TFF in established Nb technology with the same feature size of 2.5 μm.

Chapter 7

Manipulation of semifluxons in double corner junctions

7.1 Introduction

In this chapter the on-chip manipulation and detection of spontaneously generated magnetic flux quanta in double corner junctions is investigated. Corner junctions, which were briefly introduced in subsection 3.3.2, have been used in a variety of experiments, both individually and coupled in a zig-zag geometry. Corner junctions in the small facet limit (facet length $a \ll \lambda_J$ with λ_J the Josephson penetration depth) have been used for phase-sensitive studies of the order parameter symmetry [113, 196, 197]. Corner junctions in the large facet limit ($a \gg \lambda_J$) have been used to study the coupling between the *d*-wave-induced half-integer magnetic flux quanta that arise in such structures [116, 118].

The manipulation (flipping) of half-integer flux quanta in individual corner junctions has already been demonstrated [116]. However, until now the detection and manipulation of half-integer flux quanta in corner junctions has only been performed using scanning SQUID microscopy (where a built-in susceptometer was used to provide a local magnetic field to flip the semifluxons). Though the SSM is a powerful tool in the study of the magnetic phenomena in corner junctions, an on-chip solution for manipulation and detection is highly desirable if the corner junction is to be used in any practical application.

Theoretical studies have predicted that the polarity of two coupled flux quanta in a 0-π-0 junction can be changed by applying a transport current through the junction itself [198]. We have used this property to realize a switchable double corner junction and combined it with two SQUIDs for an on-chip read-out. Thus, we have observed the controlled switching between the $\uparrow\downarrow$- and $\downarrow\uparrow$-states in a double corner junction using an on-chip transport current. The design, experimental results and challenges are described in this chapter.

7.2 Theory

The previous chapters were mainly concerned with spontaneously generated flux in π-rings. As was already briefly mentioned in section 3.3, when the inner diameter of such a ring is decreased to zero, a corner junction results, which is still characterized by a spontaneously generated flux in the ground state. Whereas for π-rings the requirement for spontaneously generated flux is a sufficiently large screening parameter, for corner junctions the requirement is a sufficiently large facet length (larger than the Josephson penetration depth). The phase profile (and, by derivation, the magnetic flux- and current profiles) of a conventional long Josephson junction can be described mathematically by the so-called sine-Gordon equation. With the introduction of junctions containing intrinsic π-phase shifts and the intriguing accompanying spontaneously generated flux, many theoretical papers were published on this subject, containing equally interesting mathematics [198–213]. Most of these papers are based on a perturbed sine-Gordon equation. In this section, a derivation of this perturbed sine-Gordon equation is presented. Then the phase profile of fractional flux quanta in both single- and double corner junctions is derived. We conclude by a short review of the response of a double corner junction to a transport current.

7.2.1 Sine-Gordon equation for corner junctions

In this section we will derive the sine-Gordon equation for a corner junction. The perturbed sine-Gordon for a long one dimensional Josephson junction containing π-phase shifts equation was first derived by Xu *et al.* [199] and later by Goldobin *et al.* [202], whose derivation is closely followed here. A small deviation exists concerning the location of the π-phase shift. Due to the nature of the d-wave-induced π-phase shift it is placed *outside* of the actual junction, as opposed to the intrinsic 0-π junctions discussed by the aforementioned authors. This has only a minor effect on some signs in the equations and does not change the final result. Because of the large similarities, some of the terminology of π-junctions is also used for the corner junctions.

The phase φ along a long Josephson junction is a function of the position x. Though the practical realization of 0-π zig-zag or corner junctions involves 2 dimensional junctions in which the different corner facets are oriented perpendicular with respect to each other, the junction can be described along a one dimensional curvilinear coordinate x. A long Josephson junction can be modelled as the parallel connection of short Josephson junctions. A circuit diagram of this so-called *distributed Josephson junction* model is displayed in figure 7.1. In this figure the current flowing through the junction $I(x)$, the externally applied current $I_e(x)$, the current flowing through the inductance $I_L(x)$, the gauge invariant phase drop over the junction $\varphi(x)$ and the intrinsic phase drop caused by the order parameter symmetry $\epsilon(x)$ are indicated.

The fluxoid quantization condition (2.31) for a single loop of length dx reads

$$\frac{1}{2\pi}\left[\varphi(x) - \varphi(x+dx) + \epsilon(x) - \epsilon(x+dx)\right] + \frac{\Phi(x)}{\Phi_0} = \mathrm{n} \tag{7.1}$$

With $\Phi(x)$ the magnetic flux through the loop (defined positive in the $\odot$ direction). Without loss of generality the fluxoid number n can be taken zero, which is justified as long as the phase drops are allowed to differ by more than 2π. The flux penetrating the loop can be written as the sum of the externally applied flux Φ_e and the self-generated flux $L(x)I_L(x)$:

$$\Phi(x) = \Phi_e(x) - L(x)I_L(x) \tag{7.2}$$

Using Kirchhoff's law we find

$$I_e(x) + I_L(x-dx) = I(x) + I_L(x) \tag{7.3}$$

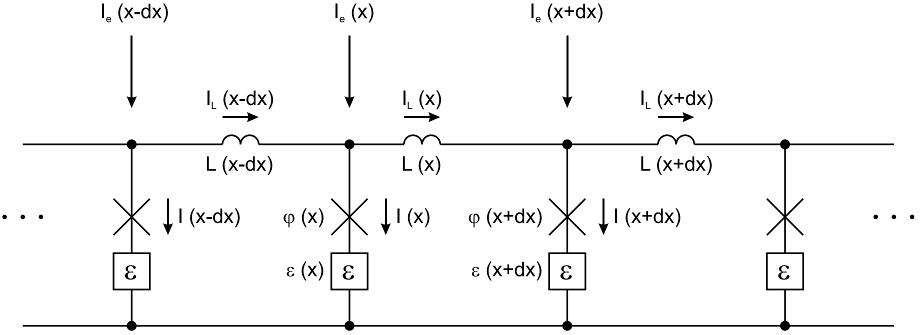

Figure 7.1: Schematic of a distributed Josephson junction.

For a junction thickness t (perpendicular to the current transport direction) the currents are related to the current densities as

$$I(x) = j(x)t dx \tag{7.4}$$

$$I_e(x) = j_e(x)t dx \tag{7.5}$$

$\Phi_e(x)$ is related to the externally applied magnetic field via

$$\Phi_e(x) = B_e(x)d_{eff}\, dx = \mu_0 H(x) d_{eff}\, dx \tag{7.6}$$

with d_{eff} the effective barrier thickness (along the current transport direction). The inductance $L(x)$ between the coordinates x and $x + dx$ can be written as [214]

$$L = \frac{\mu_0 d_{eff}}{t} dx \tag{7.7}$$

Inserting equation (7.2) into equation (7.1) and combining with equations (7.6) and (7.7) gives

$$\varphi_x = \frac{2\pi\mu_0 d_{eff}}{\Phi_0}\left[H - \frac{I_L}{t}\right] - \epsilon_x \tag{7.8}$$

where the subscript x denotes the derivative with respect to position. For the derivative with respect to time the subscript t will be used. Combining (7.3) with equations (7.4) and (7.5) gives

$$\frac{dI_L}{dx} = t(j_e - j) \tag{7.9}$$

Differentiating equation (7.8) with respect to position and substituting equation (7.9) yields

$$\varphi_{xx} = \frac{2\pi\mu_0 d_{eff}}{\Phi_0}\left[H_x - (j_e - j)\right] - \epsilon_{xx} \tag{7.10}$$

Using the RCSJ model, in particular equation (2.33), to rewrite the current density j in terms of the time derivatives of the phase we find

$$\frac{j}{j_c} = \omega_p^{-2}\left[\varphi_{tt} + \frac{1}{RC}\varphi_t\right] + \sin\varphi \tag{7.11}$$

Inserting this into equation (7.10) and rearranging terms yields

$$\lambda_J^2\varphi_{xx} - \omega_p^{-2}\varphi_{tt} - \sin\varphi = \frac{\omega_p^{-2}}{RC}\varphi_t - \frac{j_e}{j_c} + \frac{H_x}{j_c} - \lambda_J^2\epsilon_{xx} \tag{7.12}$$

with

$$\lambda_J = \sqrt{\frac{\Phi_0}{2\pi\mu_0 j_c d_{eff}}} \tag{7.13}$$

the *Josephson penetration depth.* ω_p is the plasma frequency, as defined in equation (2.34). The Josephson penetration depth and the plasma frequency are the typical length- and timescales of variations in the junction phase. A junction is generally considered to be in the long junction limit when the size of the junction is larger than typically 1-4 λ_J. Equation (7.12) is the (perturbed) sine-Gordon equation for a long Josephson junction containing π-phase shifts. When the position- and time coordinates are normalized with respect to the Josephson penetration depth λ_J and the inverse plasma frequency ω_p^{-1} the normalized sine-Gordon equation is obtained:

$$\varphi_{xx} - \varphi_{tt} - \sin\varphi = \frac{\omega_p^{-1}}{RC}\varphi_t - \frac{j_e}{j_c} + \frac{H_x}{j_c} - \epsilon_{xx} \tag{7.14}$$

Throughout the rest of this section we will use the sine-Gordon equation in normalized coordinates.

7.2.2 Phase profile of a half-integer flux quantum

In this section we consider the phase profile of a spontaneously generated half-integer flux quantum in a single 0-π corner junction. A schematic of such a junction is depicted in figure 7.2(a). The phase difference caused by the *d*-wave order parameter symmetry $\epsilon(x)$ is defined as

$$\epsilon(x) = \begin{cases} 0 & x < 0 \\ \pi & x > 0 \end{cases} \tag{7.15}$$

In the absence of externally applied currents or magnetic fields and considering a static case the normalized sine-Gordon equation (7.14) reduces to

$$\varphi_{xx} - \sin\varphi = -\epsilon_{xx} \tag{7.16}$$

Following Goldobin *et al.* [202] we introduce a 'magnetic phase' $\mu(x,t)$, defined by[1]

$$\mu(x,t) \equiv \varphi(x,t) + \epsilon(x) \tag{7.17}$$

Inserting this in (7.16) and considering (7.15) this gives

$$\mu_{xx} = \begin{cases} \sin\mu & x < 0 \\ -\sin\mu & x > 0 \end{cases} \tag{7.18}$$

---

[1] Actually, Goldobin *et al.* define the magnetic phase $\mu(x,t)$ as the total phase drop over the junction $\varphi(x,t)$ minus the order parameter related phase drop $\epsilon(x)$. The sign-difference of $\epsilon(x)$ can be attributed to the fact that for the corner junctions this phase shift is not considered to be *intrinsic*, as was discussed in subsection 7.2.1

Multiplying both sides with $2\mu_x$ and integrating with respect to x we find

$$\mu_x^2 = \begin{cases} -2\cos\mu + C_1 & x < 0 \\ 2\cos\mu + C_2 & x > 0 \end{cases} \tag{7.19}$$

The integration constants C_1 and C_2 can be determined from the boundary conditions $\varphi(\pm\infty) = \varphi_x(\pm\infty) = 0$, or equivalently: $\mu(-\infty) = 0$, $\mu(+\infty) = \pi$ and $\mu_x(\pm\infty) = 0$. This gives $C_1 = C_2 = 2$. Inserting the integration constants and using some trigonometry we find

$$\mu_x^2 = \begin{cases} 4\sin^2(\mu/2) & x < 0 \\ 4\cos^2(\mu/2) & x > 0 \end{cases} \tag{7.20}$$

We solve for the positive semifluxon, whose phase profile monotonically increases from $\mu = 0$ at $x = -\infty$ to $\mu = \pi$ at $x = +\infty$. Since both $\sin(\mu/2)$ and $\cos(\mu/2)$ are positive in this range, the positive square root of (7.20) has to be taken on the entire interval. Separating variables we obtain

$$dx = \begin{cases} \dfrac{d\mu}{2\sin(\mu/2)} & x < 0 \\ \dfrac{d\mu}{2\cos(\mu/2)} & x > 0 \end{cases} \tag{7.21}$$

Integrating with respect to x and μ we find the solution

$$x = \begin{cases} C_3 + \ln\tan(\mu/4) & x < 0 \\ C_4 - \ln\tan(\pi/4 - \mu/4) & x > 0 \end{cases} \tag{7.22}$$

which can be verified easily by differentiation. $\mu(x)$ increases monotonically from 0 at $x = -\infty$ to π at $x = \infty$. Considering the symmetry of the problem $\mu(0) = \pi/2$, which can be used to solve for the integration constants C_3 and C_4:

$$C_3 = \ln\frac{1}{\mathcal{G}} \tag{7.23}$$

$$C_4 = \ln\mathcal{G} \tag{7.24}$$

with $\mathcal{G}$ defined by

$$\mathcal{G} = \tan\left(\frac{\pi}{8}\right) = \sqrt{2} - 1 \tag{7.25}$$

Inserting the integration constants C_3 and C_4 into equation (7.22), $\mu(x)$ can be written as

$$\mu(x) = \begin{cases} 4\arctan(\mathcal{G}e^{x}) & x < 0 \\ \pi - 4\arctan(\mathcal{G}e^{-x}) & x > 0 \end{cases} \tag{7.26}$$

Combining this with equations (7.15) and (7.17), we finally obtain the phase profile of a half-integer flux quantum in a 0-π long Josephson junction:

$$\varphi(x) = -4\,\mathrm{sgn}(x)\arctan\left(\mathcal{G}e^{-|x|}\right) \tag{7.27}$$

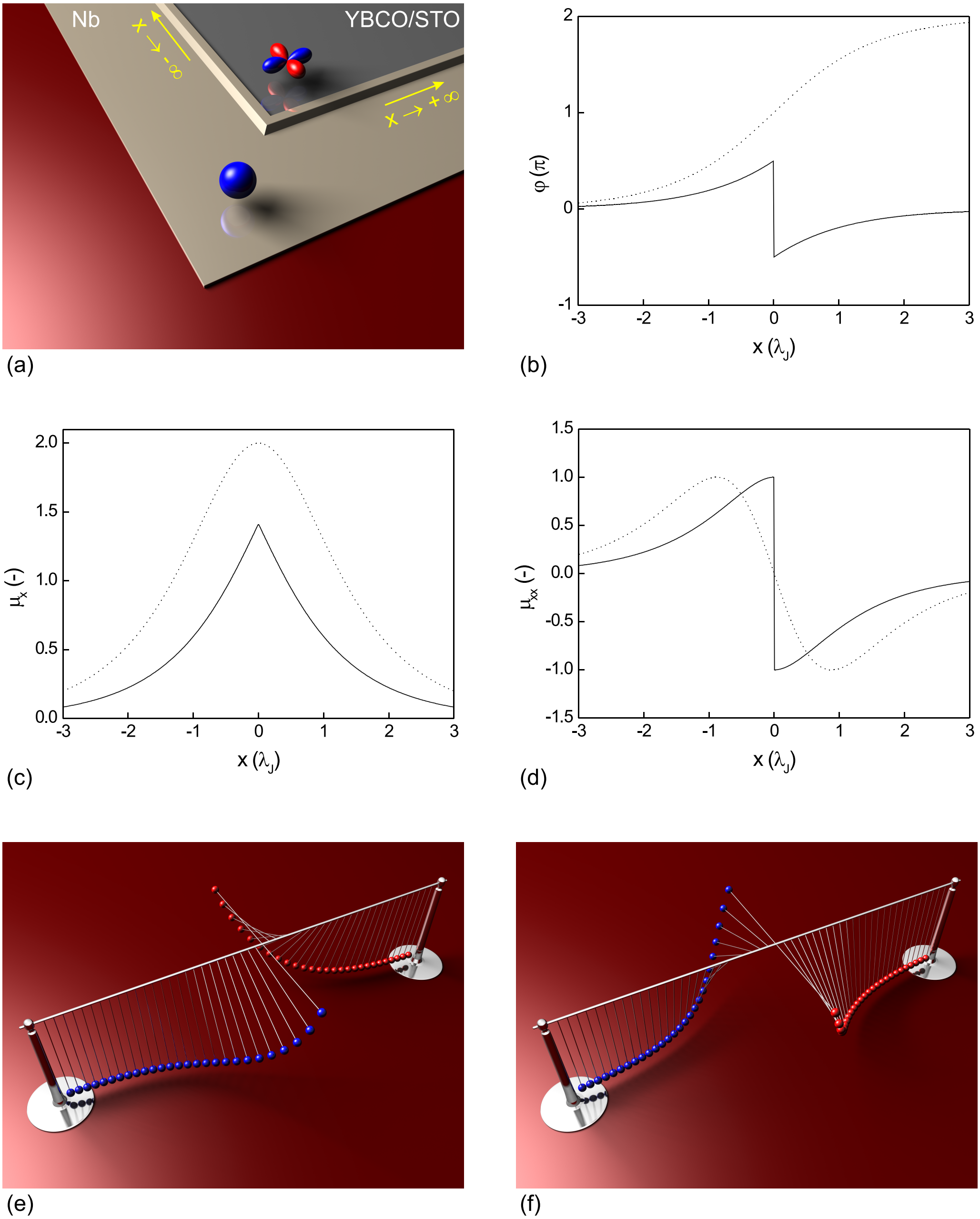

Figure 7.2: (a) Schematic of an infinite 0-π ramp-type Josephson junction. (b) Phase profile $\varphi(x)$, (c) magnetic field profile μ_x and (d) current profile μ_{xx} of an infinitely long 0-π Josephson junction (solid lines) and for a full flux quantum (dotted lines). (e) Positive and (f) negative semifluxon represented in terms of the pendulum-analogon.

From equations (7.1) and (7.17) it follows that the magnetic field produced by the spontaneously generated current is proportional to μ_x. Differentiating equation (7.27) with respect to x we obtain

$$\mu_x = \frac{2}{\cosh\left(|x| - \ln \mathcal{G}\right)} \tag{7.28}$$

The normalized current profile can be calculated by taking the sine of equation (7.27) or, following (7.16) and (7.17), by taking the derivative of μ_x. Differentiating (7.28) with respect to x we find

$$\mu_{xx} = \sin\varphi = -2\ \mathrm{sgn}(x)\frac{\sinh\left(|x| - \ln \mathcal{G}\right)}{\cosh^2\left(|x| - \ln \mathcal{G}\right)} \tag{7.29}$$

The phase-, field- and current profile of the half-integer flux quantum are displayed as solid lines in figures 7.2(b)-(d). The phase profile can be understood intuitively by considering the distributed junction as a series of interconnected pendulums, as is schematically illustrated in figures 7.2(e) and 7.2(f). At the center the phases are separated by a π-phase shift and in the end points the pendulums have zero deflection. Note that in the above calculations the rounding of the corner has not been taken into account. This rounding, in combination with the angular dependence of the order parameter symmetry, will result in a smooth transition of the critical current density to zero at the 45° nodal angle.

In conventional long Josephson junctions one allowed solution of the sine-Gordon equation is the so-called *soliton*, where the phase makes a 2π rotation. This phase profile corresponds to a full flux quantum, which, unlike the half-integer flux quantum produced in the 0-π junction, is not bound to a discontinuity. The phase-, magnetic field- and current profiles of a stationary soliton are shown as dotted lines in figures 7.2(b)-(d).

7.2.3 Double corner junctions

In this section the 0-π-0 corner junction will be discussed. In analogy to a 0-π junction the properties of a double corner junction can be described using the sine-Gordon equation. The static phase-, current- and flux profiles for such a junction are derived in the appendix. The phase profile is shown in terms of the pendulum-analogon in figure 7.3(a) for the $\uparrow\downarrow$-, $\downarrow\uparrow$-, $\uparrow\uparrow$- and $\downarrow\downarrow$-configurations. Note that the phase profiles $\varphi(x)$ which are presented here differ from the magnetic phase profiles $\mu(x)$ depicted in figure A.1 by an amount of π between the two 0-π discontinuities, as defined in equation (A.2). The derivative of the magnetic phase, which is proportional to the magnetic field, is shown in figures 7.3(b) and 7.3(c) for both the ferromagnetic and the antiferromagnetic configurations.

The realization of a 0-π-0 junction using YBCO/Nb ramp-type junction technology is schematically depicted in figure 7.4(a). This configuration will also be referred to as a *double corner junction* for obvious reasons and was used in the experiments presented in this chapter. The first theoretical study of a current-biased 0-π-0 junction was published in 1997 by Kato and Imada [198], who predicted the possibility of macroscopic quantum tunnelling in such a junction. In 2005 the 0-π-0 junction was proposed as a candidate for qubits by Goldobin *et al.* [212].

An important parameter in 0-π-0 junctions is the distance between the two 0-π discontinuities (or the separation distance between the two corners in our experiment), which will be denoted by d. Kato and Imada [198] showed that, in the absence of a magnetic field or transport current, the junction is in the so-called flat-phase state when the corner separation d is smaller than a certain crossover-distance d_c. The flat-phase state is

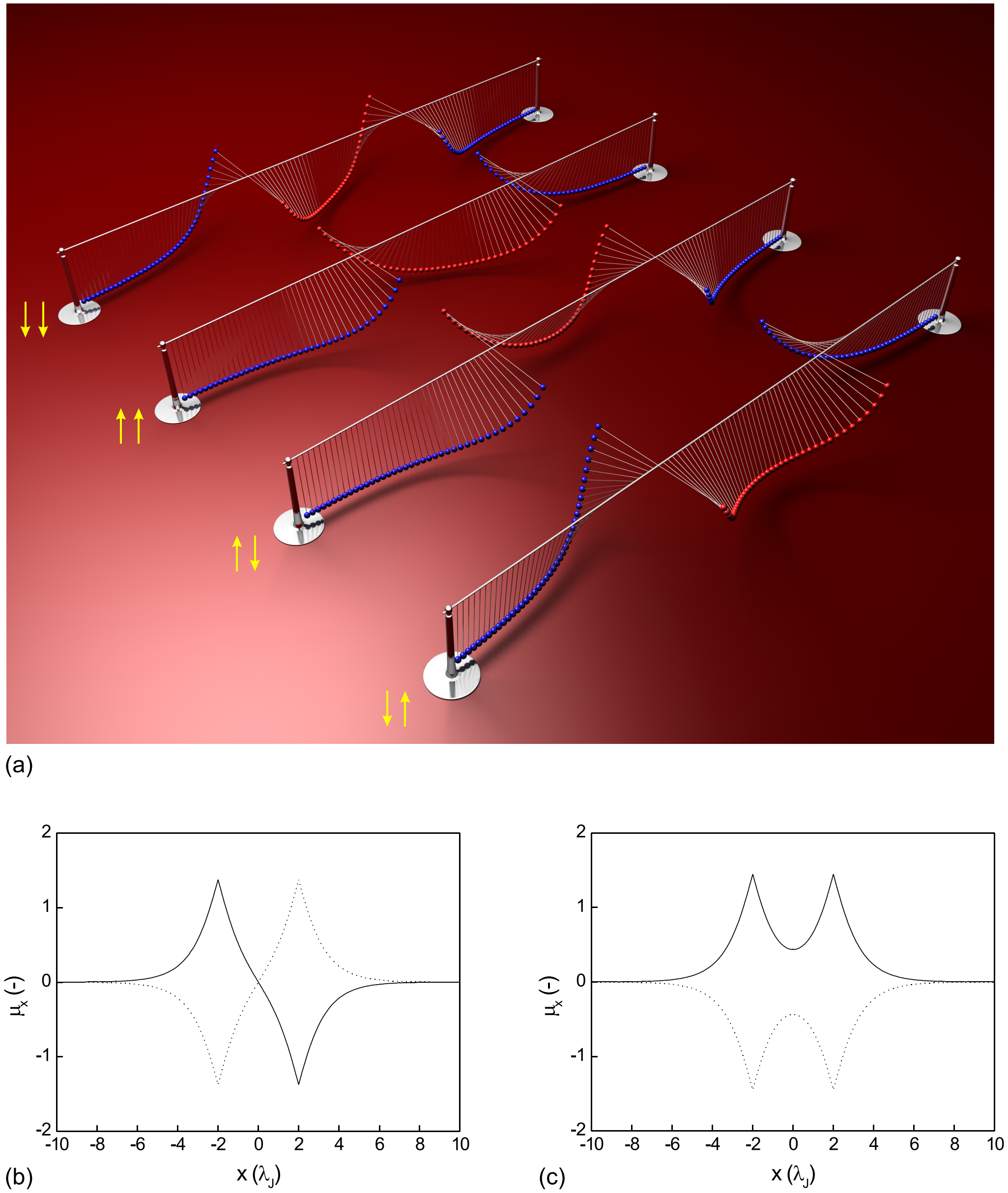

Figure 7.3: (a) Phase profile for a double corner junction represented in terms of the pendulum-analogon. (b) Magnetic field profile μ_x for the antiferromagnetic ↑↓ (solid line) and ↓↑ (dotted line) configuration. (c) Magnetic field profile μ_x for the ferromagnetic ↑↑ (solid line) and ↓↓ (dotted line) configuration.

characterized by a constant (magnetic) phase profile and the absence of spontaneously generated magnetic flux. Numerical calculations revealed a crossover-distance (normal-

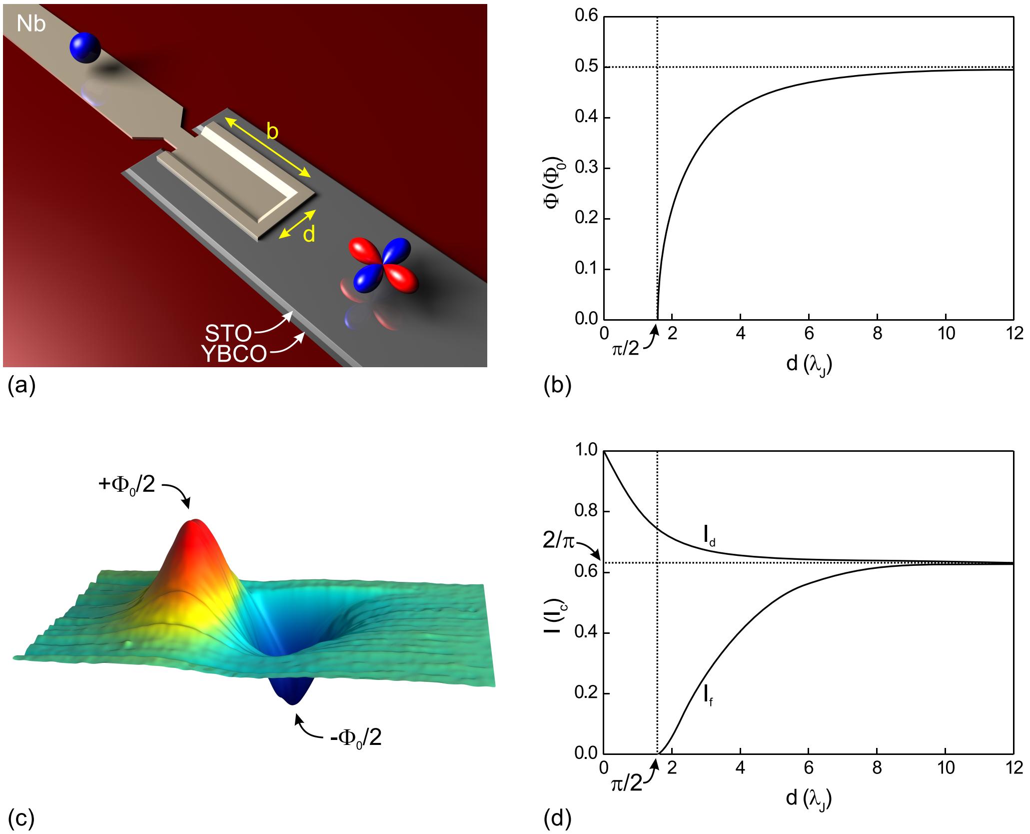

Figure 7.4: (a) Schematic representation of a 0-π-0 ramp-type junction. d represents the distance between the corners and b is the length of the side-facets. (b) Spontaneously generated flux produced on each corner versus the 0-facet length d. (c) Scanning SQUID microscopy image of an $\uparrow\downarrow$ semifluxon pair. (d) Flipping current I_f and depinning current I_d shown as a function of the corner separation d. Figures (b) and (d) were adapted from Kato and Imada [198] and Susanto *et al.* [205]. Note that the corner distance d, used in figures (b) and (d) is twice the parameter a which is used in the original articles. This is only a matter of definition: in the original articles the '0-facet' was defined between -a and -a and therefore has a length $d = 2a$.

ized with respect to λ_J) of $\pi/2$, which was later independently obtained from phase-plane analysis by Susanto *et al.* [205]. When the separation distance between the corners is larger than the crossover-distance, the ground state of the junction is given by two antiferromagnetically coupled vortices, which are denoted as $\uparrow\downarrow$ and $\downarrow\uparrow$. The flux carried by the vortices grows asymptotically to $\Phi_0/2$ for $d \gg d_c$ as shown in figure 7.4(b). A scanning SQUID microscopy image of the $\uparrow\downarrow$-configuration is shown in figure 7.4(c).

Besides the corner separation d, also the length of the side-facets, which is denoted by b in figure 7.4(a), is of importance. Figure 7.4(b) was calculated for infinitely long side-facets. However, Zenchuk and Goldobin demonstrated [206] that the crossover-distance depends crucially on the ratio b/d, and even vanishes to 0 for $b = d/2$. For b larger than ∼1 the crossover-distance quickly approaches $\pi/2$. For the experiments described in this chapter, which had side facets $b = 4d$, the effect of a finite side-facet length can be neglected and also in the rest of this section infinite side-facets are assumed.

The application of a transport current through a corner junction has a large influence on the junction properties. The crossover-distance d_c, for example, reduces to 0 when a bias current is applied [204, 205]. Moreover, the transport current exerts a Lorentz-force on the vortices, pushing them towards each other or pulling them apart, depending on the polarity of the transport current. For small currents both the $\uparrow\downarrow$- and the $\downarrow\uparrow$-states are stable. However, when the transport current exceeds a certain value that will be denoted as the *flipping current* I_f, only one state is stable. If the system resides in the unstable state and the transport current exceeds the flipping current (which is smaller than the critical current of the junction), the half-integer flux quanta will change sign: $\downarrow\uparrow\rightarrow\uparrow\downarrow$. This process, which can be regarded as the transport of a full flux quantum from one corner to the other, is accompanied by a voltage pulse. Thus, the ground state can be 'flipped' from $\uparrow\downarrow$ to $\downarrow\uparrow$ by applying a transport current [198, 204, 205].

The flipping current depends on the length of the middle facet as depicted in figure 7.4(d). Starting from zero at the critical facet length d_c, the flipping current increases monotonically and asymptotically grows to $(2/\pi)I_c$. In figure 7.4(d) also the depinning current I_d is plotted as a function of d. When the current through the junction exceeds the depinning current, there are no stable stationary states available: the vortices are torn from their pinning sites and the junction enters the voltage state. For $d \gg d_c$ the depinning current asymptotically approaches $(2/\pi)I_c$ [198, 205].

7.3 Design

In this chapter we present the successful switching between the $\uparrow\downarrow$- and the $\downarrow\uparrow$-states by means of a transport current. The read-out was performed using an on-chip SQUID. The design of our sample is shown schematically in figure 7.5. The film thicknesses that were used are 100 nm YBCO and 65 nm STO for the base electrode, a 7 nm YBCO interlayer, 50 nm for the gold barrier and an 80 nm Nb top electrode. The rather large thickness of the gold barrier was chosen to suppress j_c, which was approximately 4.5 kA/cm^2 for the experiments described in this chapter[2]. With an effective barrier thickness of approximately 240 nm this results in a Josephson penetration depth $\lambda_J \approx 4.9\ \mu$m.

The 0-π-0 double corner junction has a total length of 108 μm. It consists of a center facet of 12 μm which is flanked by two 48 μm long side facets. As mentioned in the previous section this ratio of 4 allows us to neglect effects due to the finite size of the edge facets. The 12 μm corner separation corresponds to approximately 2.4 λ_J. From figure 7.4(d) it follows that in this regime the flipping- and depinning current are well-separated and the fractional flux quanta have formed substantially (∼0.3 Φ_0, but for convenience these fractional flux quanta will still be referred to as half-integer flux quanta or semifluxons).

Two SQUIDs are connected to read out the flux of the half-integer flux quanta. To improve the flux-coupling between the corners and the SQUIDs, an integrated design was chosen, in which the SQUIDs are coupled to the corners directly. The SQUID junctions

---

[2] This value of j_c is larger than the value reported by [215] due to the choice of definition mentioned in subsection 4.4.1

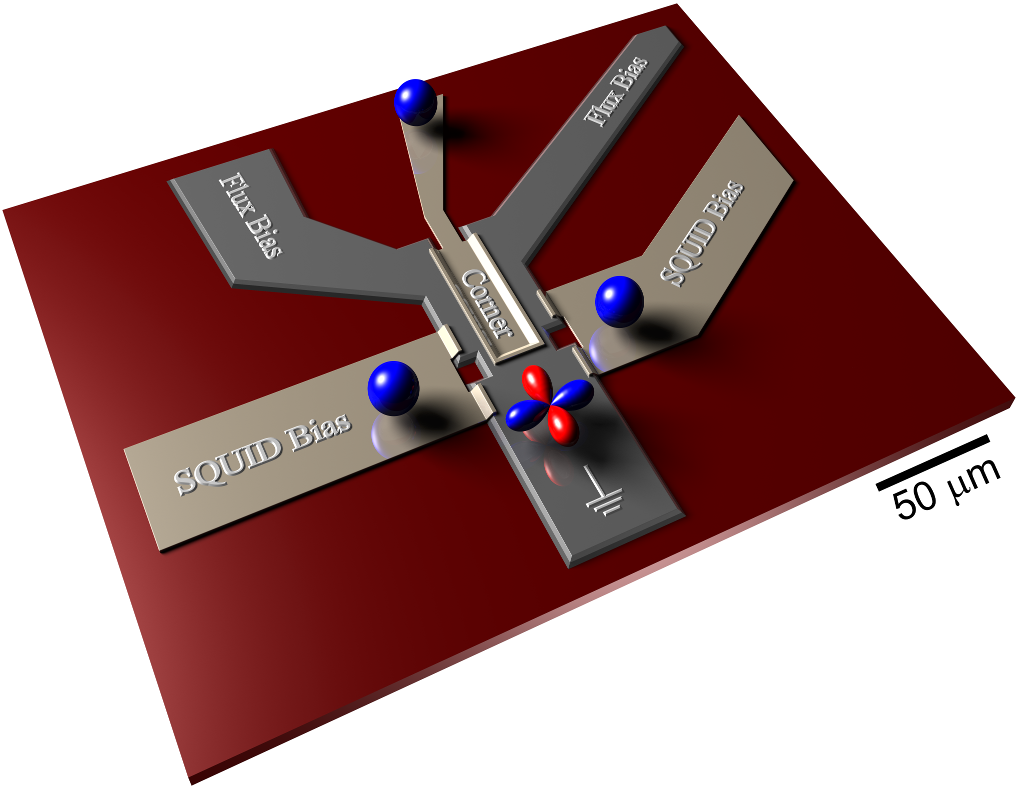

Figure 7.5: Schematic representation of the sample used for the on-chip manipulation and read-out of two coupled half-integer flux quanta.

have a width of 12 μm, and the total SQUID critical current is 115 μA. A crude estimation of the SQUID self-inductance can be obtained from the relation

$$L = 1.25\mu_0 d_{hole} \tag{7.30}$$

which is valid for square washers with a hole width d_{hole} smaller than the edge width [216]. With $d_{hole} \approx 10$ μm a SQUID self-inductance of 15.7 pH is obtained. More detailed simulations in FastHenry [171] reveal a larger value of 21 pH. This gives a screening parameter $\beta_L \approx 3.7$. To bias the SQUIDs at their operating points, two flux bias lines were added, as well as an external coil for the application of an external magnetic field perpendicular to the sample (not shown).

7.4 Measurement results

All measurements described in this chapter were performed in a flow cryostat with a Cryoperm inner-shielding and a mu-metal outer shielding. Instead of using the temperature controller usually the cryostat was cooled down to its base temperature. Because this base temperature changed between different cool-downs, the operation temperature and thus the critical current densities can differ between different measurement runs.

7.4.1 SQUID characterization

First, experiments involving only one read-out SQUID were performed. The behavior of the right SQUID was measured as a function of the bias current I_b applied through the left flux bias line. The IV characteristics are shown in figure 7.6(a). The current through the flux bias line was increased from -1 mA to 1 mA with increments of 10 μA. For clarity, the current-voltage characteristics have been offset by 5 μV. A clear modulation of the SQUID critical current with respect to the applied flux bias is observed. From the modulation the mutual inductance between the flux bias line and the SQUID is estimated to be 4.5 pH, which is 20% less than the 5.6 pH that was numerically obtained using FastHenry. The modulation of the critical current is only partial, as is to be expected for a SQUID with large β_L (see subsection 2.9.1). From the modulation depth and the critical current of approximately 140 μA a self-inductance $L_{sq} \approx 15$ pH is estimated, which is in excellent agreement with the crude estimation from equation (7.30). In figure 7.6(b) the voltage response of the SQUID to the flux bias is shown for different values of the SQUID bias current. The SQUID bias current was increased from 50 μA to 150 μA using increments of 5 μA. For clarity, the curves have been smoothed using adjacent point averaging. On top of the SQUID modulation a much slower modulation due to the Josephson junction itself can be distinguished.

The resonances mentioned in subsection 2.9.3 are clearly visible. From the resonance voltage $V_r \approx 45$ μV and a self inductance $L_{sq} \approx 15$ pH the junction capacitance is estimated to be 7 pF. This is, in fact, evidence that the junction capacitance cannot be (fully) attributed to the parallel-plate configuration of the junction overlap (where the YBCO and Nb electrodes are separated by an STO dielectric). The capacitance of this overlap can be estimated by

$$C_J = \epsilon_0 \epsilon_{STO} \frac{w \cdot ov}{t_{STO}} \tag{7.31}$$

with w the junction width (12 μm), ov the overlap (3 μm) and t_{STO} the thickness of the STO layer (65 nm). To account for a junction capacitance of 7 pF a relative permittivity of 1458 would have to be assumed for the STO, which is an order of magnitude higher than the typical dielectric constant for STO thin films (in bulk the dielectric constant of STO can indeed be much larger) [217]. This discrepancy indicates that the overlap is only partially responsible for the junction capacitance. This has been independently observed in different experiments where the capacitance was extracted from the Stewart-McCumber parameter, which was obtained from the ratio of the switching- and retrapping- current following Zappe [218]. In this experiment we observed a scaling of the calculated ϵ_{STO} with the dimensions of the overlap, indicating a faulty modelling. Evidence that the junction capacitance cannot solely be attributed to the overlap has also been given by Smilde who suggests significant contributions from the substrate and a depleted layer in the junction [137].

Careful inspection of graphs 7.6(a) and 7.6(b) shows that the critical current in the latter is smaller and closer to the design value. The discrepancy originates from the fact that these measurements were performed in different cool-downs and therefore at different temperatures, which results in a slightly different critical current density. Finally, it should be noted that both the current-voltage characteristics and the SQUID-voltage

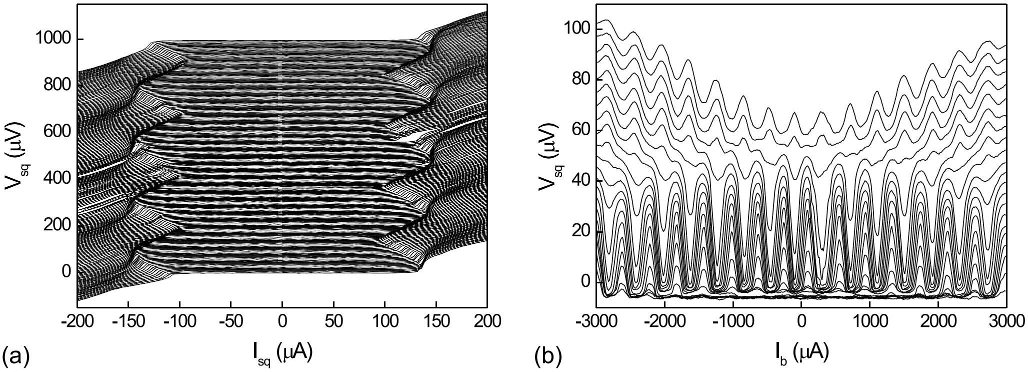

Figure 7.6: (a) IV-characteristics of the right SQUID for different values of the current applied through the left flux bias line I_b, which is increased from -1 mA to 1 mA in steps of 10 μA. IV's have been offset by 5 μV. (b) V_{sq} versus I_b for different SQUID bias currents I_{sq}. I_{sq} was increased from 50 μA to 150 μA in steps of 5 μA.

measurement show 'jumps' as the bias current is ramped up (though smeared out in the voltage measurement). These jumps are attributed to a rearrangement of the flux in the corner, and will be revisited in subsection 7.4.3.

7.4.2 Flipping experiments

To test the on-chip manipulation of the half-integer flux quanta we performed 'flipping experiments', which will be described below. First the SQUID was biased just above its critical current and the flux through the SQUID was set such that the SQUID was sensitive to small changes in the magnetic field (I_{sq} = 125 μA, I_b = 142 μA for this particular measurement). Then a current pulse I_p was applied to the corner and the SQUID voltage V_{sq} registered. Next, a current pulse of the same amplitude but opposite sign was applied and again V_{sq} was measured. This was repeated for different amplitudes of the current pulse. The result of this procedure is shown in figure 7.7, where the black solid points represent the measured SQUID voltage and the red lines represent the current pulses. Though the SQUID voltage was also measured during the pulse, these points have been removed to clarify the SQUID response. The time on the horizontal axis is shown in arbitrary units. This has to do with the static operation mode of the measurement system, which consists of a set of current sources and voltmeters which are driven by a measurement program on a computer. The program sets all current sources to the first value set in the stimulus file and waits to be sure the signals are stable. Then the output voltages are registered and the procedure is repeated for the next points in the stimulus file (it is possible to set a delay and/or averaging). Thus the unit of time of the measurement system is actually 'a measurement'. The measurements shown in figure 7.7 typically took a few tens of seconds to run. The waveform that was used for the pulses was two measurements (points) high current, six points no current, two points negative current and then again six times no current.

For small current pulses the measured output voltage (when the pulse is off) remains steady at a value of ~43 μV, as can be seen in figure 7.7(a). This can be explained

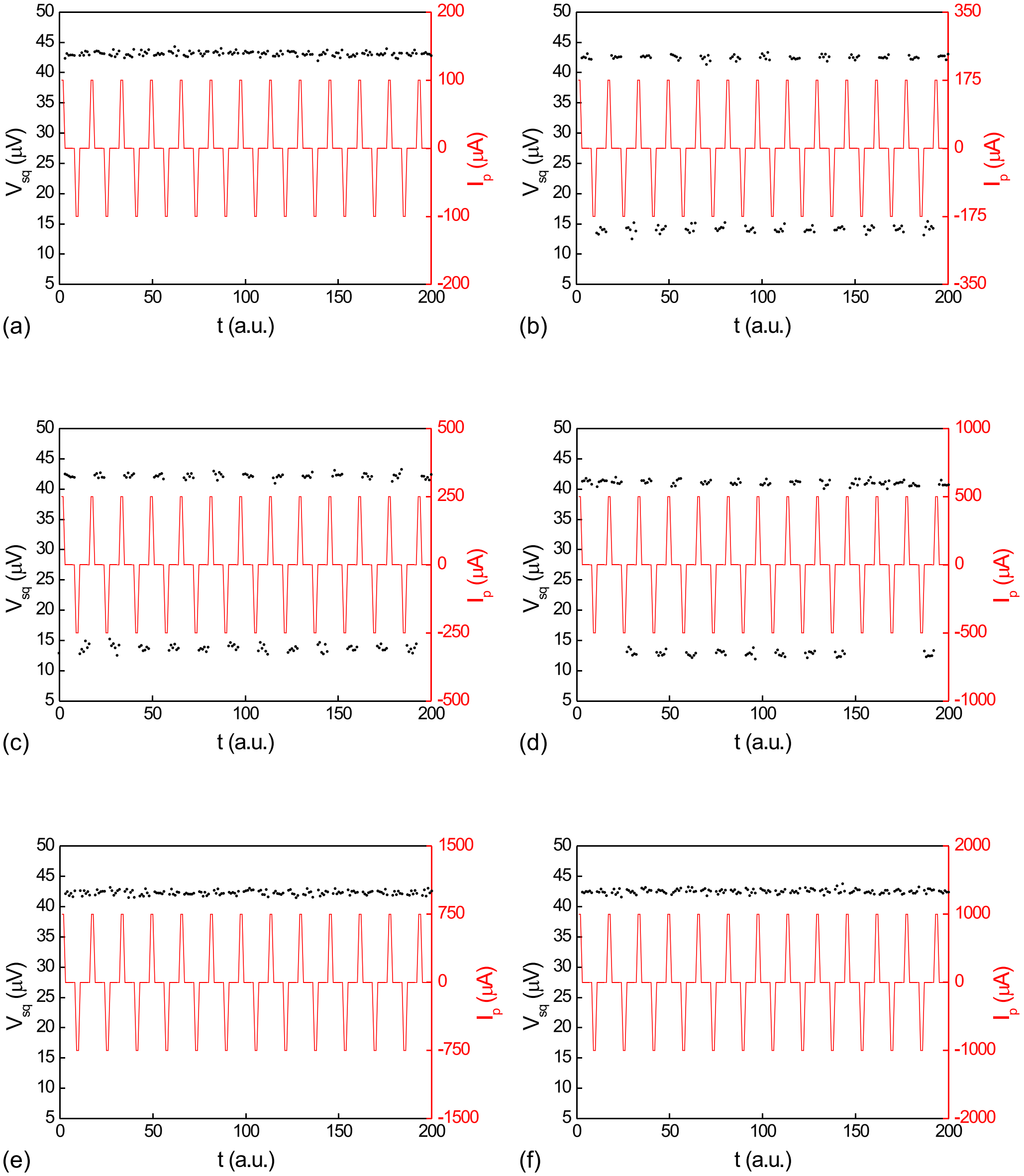

Figure 7.7: SQUID response V_{sq} (black solid points) to the current pulses I_p applied to the double corner junction (red lines). The amplitudes of the current pulses are (a) 100 μA, (b) 175 μA, (c) 250 μA, (d) 500 μA, (e) 750 μA and (f) 1000 μA. For all measurements the SQUID was current-biased at $I_{sq} = 125$ μA flux-biased with $I_b = 142$ μA.

by the fact that for these currents the current that is sent through the corner does not exceed the flipping current and both states remain stable. When the amplitude of the applied pulses is increased however, the pulse amplitude exceeds the flipping current and

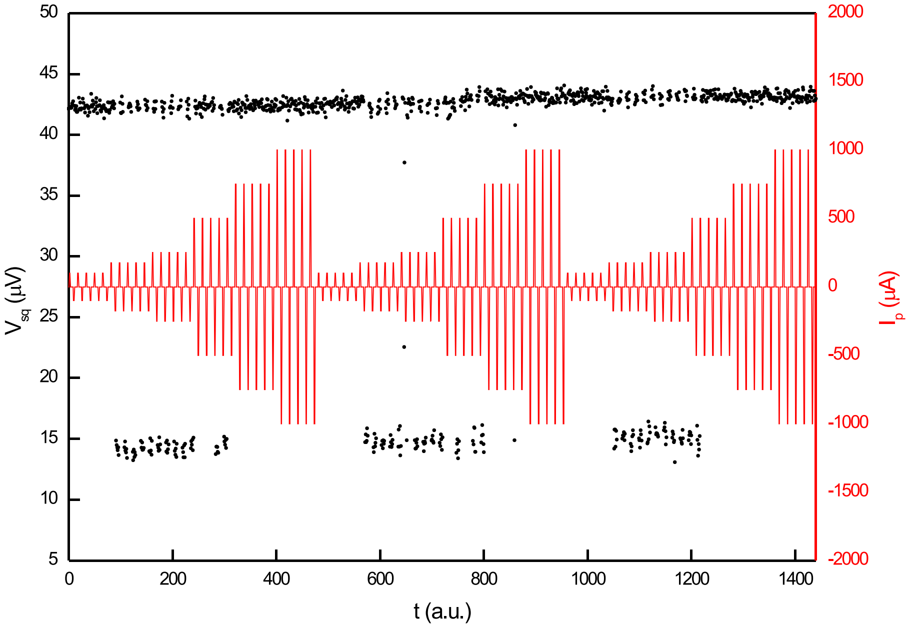

Figure 7.8: Flipping behavior for increasing pulse height. During this measurement the SQUID had a current bias $I_{sq} = 125\ \mu$A and a flux bias $I_b = 142\ \mu$A.

the measured voltage switches between ∼14 μV and ∼43 μV after each pulse, as can be seen in figures 7.7(b) and 7.7(c). The observed switching of the voltage is consistent with a rearrangement of the half-integer flux quanta. Interestingly, in the 500 μA-pulse measurement shown in figure 7.7(d) the output voltage 'fails' to switch occasionally, and when the current is increased even further V_{sq} remains steady at ∼43 μV, as shown in figures 7.7(e) and 7.7(f).

An estimate of the flipping current I_f can be deduced by examining the transition between non-flipping and flipping behavior. This transition occurs when the applied current pulses are between 100 μA and 175 μA . The depinning current I_d, which is simply the current at which the corner switches to the voltage state, was experimentally found to be 490 μA. Thus, the ratio of the flipping- and depinning current lies in the range $0.204 < I_f/I_d < 0.357$. The corner separation was designed to be $d = 2.4\ \lambda_J$. From figure 7.4(d) we see that this distance corresponds to a ratio $I_f/I_d \approx 0.22$, which is in good agreement with the range deduced from the flipping current.

The reason why, starting from current pulses of approximately 500 μA, the output voltage does not flip any more is not yet understood. To rule out the possibility that a change in the conditions between different measurements is responsible, a stimulus containing pulses of increasing height was applied so the effect can be studied in a single continuous measurement run. The result is plotted in figure 7.8 and shows a systematic reluctance to switch for pulses above 500 μA. Interestingly, 500 μA is very close to the depinning current. For pulses smaller than the depinning current, there is always at least one well-defined static stable state. When the current pulses exceed the depinning current, no stationary states are available and the corner junction enters the voltage mode. This may lead one to the conclusion that certain processes in the voltage state are responsible for the lack of switching at these pulse amplitudes. An argument against this line of thought is the fact that the timescale on which the current drops (larger than a microsecond) is orders of magnitude larger than the typical timescale of the corner junction, which is of the order of a picosecond. Thus the drop of the current trough the double corner junction can be considered an adiabatic process and by the time this current reaches the flipping current, the junction has already spent a considerable amount of time in the regime where only one stable state exists, and it has already 'forgotten' it was ever in the voltage state. Note that the state which is favored for high pulse amplitudes is the state that, for lower pulse amplitudes, corresponds to a positive pulse. Interestingly, the bias currents of both the SQUID and the flux bias line have the same direction as a positive pulse.

7.4.3 Magnetic field sweeps

We analyzed the SQUID response to the magnetic field sweeps where we used

- The corner junction
- The flux bias line
- An external coil

to sweep the magnetic field. In all three cases a hysteresis was observed, which will be discussed below. Figure 7.9(a) shows the response when the magnetic field was sweeped using the corner junction with the SQUID biased at a current of 125 μA. Unlike the other two experiments, in this experiment the transport current completely flows through the corners and thus affects the half-integer flux quanta directly as described in subsection 7.2.3. The observed hysteresis is consistent with a rearrangement of the two half-integer flux quanta. Referring to figure 7.5, the most stable configuration for the pair of semifluxons when a positive current is applied is the $\uparrow\downarrow$-configuration. When the system would reside in the $\downarrow\uparrow$-configuration and the transport current exceeds the flipping current I_f, the semifluxons will rearrange to the more stable state $\uparrow\downarrow$. This rearrangement is accompanied by a change in field picked up by the SQUID corresponding to a *larger* transport current which corresponds to the hysteresis observed in figure 7.9(a). In this argumentation we have silently assumed that the SQUID signal picked up is that of the semifluxon closest to the SQUID, which seems like reasonable assumption. The hysteresis is observed in a highly asymmetric interval: between -35 μA and +140 μA. Only when the current pulses in the flipping-experiments exceed both boundaries a full flipping will be observed. The transition between non-flipping and flipping behavior is therefore expected to occur when the pulse heights cross 140 μA, which is consistent with the 100-175 μA interval that was found in subsection 7.4.2.

The source of the large asymmetry in hysteresis is likely to be the SQUID bias. This becomes especially clear from the measurement shown in figure 7.9(b). Here the same sweep was carried out for a positive ($I_{sq} = 125$ μA) and a negative ($I_{sq} = -125$ μA) SQUID bias. The hysteresis occurs between -80 μA and +180 μA for the positive current bias and between -180 μA and +80 μA for the negative current bias. This large effect had not been taken into account when this sample was designed. The SQUIDs were galvanically coupled to the corner junction in order to obtain a good magnetic coupling.

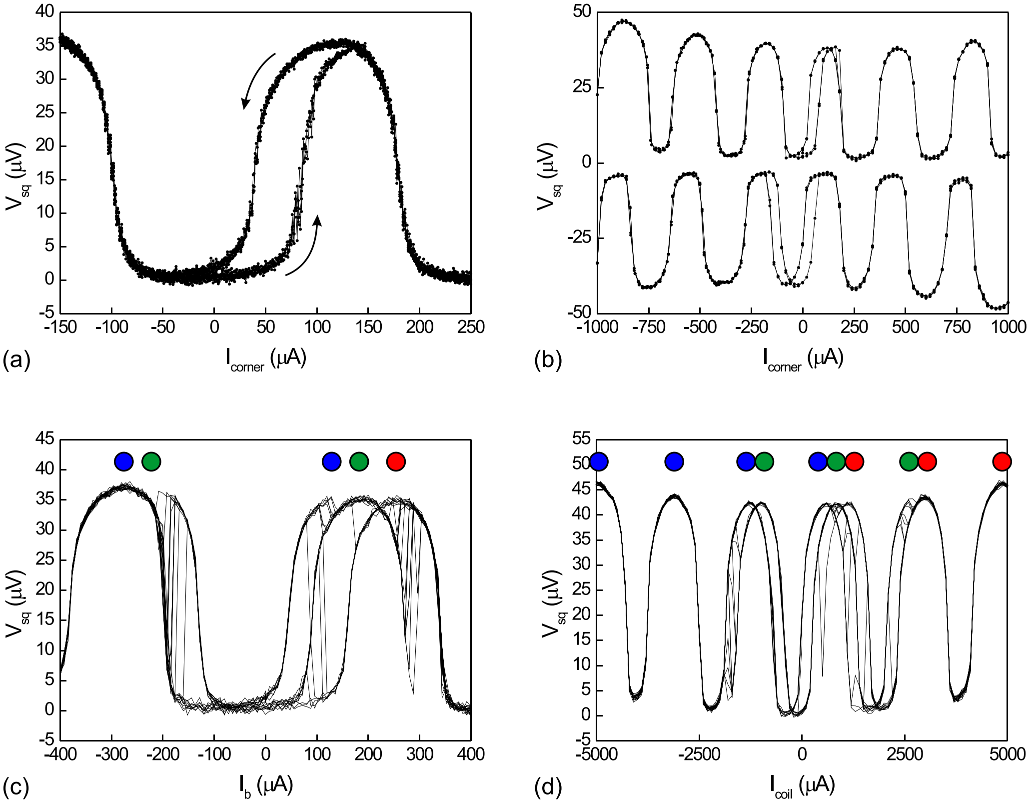

Figure 7.9: Magnetic field sweep experiments. In figures (a) and (b) the magnetic field is applied via the corner junction, in figure (c) via the flux bias line, and in figure (d) via an external coil. In all experiments the SQUID was biased at 125 μA, except for the measurement with negative bias in figure (b) for which a bias of -125 μA was used. The blue, green and red circles shown in figures (c) and (d) indicate three potential states of the system.

Considering the rather large effect of the SQUID bias on the junction properties this choice of coupling may have to be reconsidered.

The SQUID- and corner-response to an external magnetic field was also examined, see figures 7.9(c) and 7.9(d). In both experiments a double hysteresis was observed, which is interpreted as three different states. In the graphs these states have been color-coded by a blue, green and red circle. During the sweeps the voltage always cycled through these three states in the same way: on the positive ramp the registered voltage first followed the 'blue path', then went via green to red, and on the negative ramp the reverse path was chosen: from red via green to blue. The transitions indicate that the system 'switches' between different states which are separated roughly by 0.15 Φ_0, just like the experiments where the magnetic field was sweeped using the corner junction. An important difference can be found in the *direction* of the switches. In the latter two field-sweep experiments the system always jumps to a state that corresponds to a smaller bias current. In other words, the magnetic field gets counteracted. One obvious explanation would be that a flux quantum gets trapped in the opposite SQUID. This explanation can be dismissed however by considering the fact that the hysteretic behavior is the same whether the magnetic field is applied via an external coil or via the flux bias line. The fact that the flux bias line is located between the two SQUIDs provides a subtle difference in the way flux is applied to both SQUIDs. Whereas the external coil provides each SQUID with the same magnetic field, the magnetic field generated by the flux bias line has a different sign for both SQUIDs. Therefore, if the jumps are to be explained by trapped flux, this flux has to be trapped on the side of the bias line where the active SQUID is located. To investigate the nature of the three states SSM measurements are a very useful tool. A new design with structures optimized for this purpose was designed and fabricated but unfortunately due to an earlier planned complete overhaul of the SSM measurement setup these experiments have not yet been performed.

7.5 Summary

Long Josephson junctions containing one or multiple 0-π discontinuities give rise to spontaneously generated fractional flux quanta that are located at the transition points. These vortices are completely determined by their phase profile, which can be solved from a perturbed sine-Gordon equation. In this chapter we have discussed the 0-π-0 junction, which was realized as a YBCO/Nb ramp-type Josephson junction containing two corners. In the ground state antiferromagnetically coupled fractional flux quanta arise at the corners. It has been predicted that by sending a transport current through the double corner junction the half-integer flux quanta can be flipped from the $\uparrow\downarrow$-configuration to the $\downarrow\uparrow$-configuration, provided the transport current exceeds a certain threshold value. This behavior has been confirmed by experiments in which pulses of different polarity and amplitude were applied to the double corner junction, as well by experiments in which a transport current was swept continuously. A controlled rearrangement between two states was observed using an on-chip read-out SQUID. To enhance inductive coupling the read-out SQUID was galvanically coupled to the double corner junction, which is shown to have a substantial effect on the junction properties. A study to the effect of external magnetic fields revealed a third state. This state has not been identified yet and requires further investigation.

Appendix A

Phase profile of a double corner junction

In this appendix the phase profile of spontaneously generated half-integer flux quanta in a double corner junction is derived. Static solutions for the ↑↓-, ↓↑-, ↑↑- and ↓↓-configurations in the absence of external currents or magnetic fields are calculated. In analogy to the derivation in subsection 7.2.2 the calculations are performed using a (continuous) magnetic phase $\mu(x)$, defined by

$$\mu(x) \equiv \varphi(x) + \epsilon(x) \tag{A.1}$$

The corners (or, equivalently, the 0-π discontinuities) are located at $x = \pm a$, with $a \equiv d/2$ half the length of the middle facet. For simplicity the side facets are assumed to be infinitely long. For a double corner junction $\epsilon(x)$ can be written as

$$\epsilon(x) = \begin{cases} 0 & x < -a \\ \pi & |x| < a \\ 0 & x > a \end{cases} \tag{A.2}$$

In analogy to equation (7.18) the sine-Gordon equation reduces to

$$\mu_{xx} = \begin{cases} \sin\mu & x < -a \\ -\sin\mu & |x| < a \\ \sin\mu & x > a \end{cases} \tag{A.3}$$

which can be integrated to

$$\mu_x^2 = \begin{cases} C_1 - 2\cos\mu & x < -a \\ C_2 + 2\cos\mu & |x| < a \\ C_3 - 2\cos\mu & x > a \end{cases} \tag{A.4}$$

First, let us consider the solutions for $|x| > a$. C_1 and C_3 can be determined from the boundary conditions for $\mu(x)$ and $\mu_x(x)$ at $x = \pm\infty$, which yields

$$C_1 = C_3 = 2 \tag{A.5}$$

	$\uparrow\downarrow$	$\downarrow\uparrow$	$\uparrow\uparrow$	$\downarrow\downarrow$
$\mu(-\infty)$	0	0	0	0
$\mu(+\infty)$	0	0	2π	-2π
$\mu_x(-\infty)$	0	0	0	0
$\mu_x(+\infty)$	0	0	0	0
$\mu(0)$	$*$	$*$	π	$-\pi$
$\mu_x(0)$	0	0	$*$	$*$
$\mu_{xx}(0)$	$*$	$*$	0	0
$\mu(-x)$	$\mu(x)$	$\mu(x)$	2π-$\mu(x)$	-2π-$\mu(x)$

Table A.1: Boundary conditions for $\mu(x)$ and its derivatives. The boundary conditions follow from energy (1-4) and symmetry (5-8) considerations. Values which cannot be determined *a priori* are indicated with an asterisk ($*$). The last boundary conditions, not shown in the table, are the continuity of μ and μ_x at $x = \pm a$.

for all configurations (the boundary conditions are listed in table A.1). Thus, using the identity $\cos\mu = 1 - 2\sin^2(\mu/2)$, μ_x^2 can be written as

$$\mu_x^2 = 4\sin^2\left(\frac{\mu}{2}\right) \qquad x > |a| \tag{A.6}$$

μ_x can be obtained by taking either the positive or the negative square root, which depends on the configuration under consideration and the sign of x:

$$\begin{aligned} \mu_x^{\uparrow\downarrow,\downarrow\uparrow} &= \begin{cases} +2\sin\left(\frac{\mu}{2}\right) & x < -a \\ -2\sin\left(\frac{\mu}{2}\right) & x > +a \end{cases} \\ \mu_x^{\uparrow\uparrow,\downarrow\downarrow} &= \begin{cases} +2\sin\left(\frac{\mu}{2}\right) & x < -a \\ +2\sin\left(\frac{\mu}{2}\right) & x > +a \end{cases} \end{aligned} \tag{A.7}$$

Separation of variables yields

$$dx = \pm\frac{d\mu}{2\sin\left(\frac{\mu}{2}\right)} \tag{A.8}$$

which can be integrated to obtain

$$\begin{aligned} x^{\uparrow\downarrow,\downarrow\uparrow} &= \begin{cases} +\ln\left|\tan\left(\frac{\mu}{4}\right)\right| + x^* & x < -a \\ -\ln\left|\tan\left(\frac{\mu}{4}\right)\right| + x^\dagger & x > +a \end{cases} \\ x^{\uparrow\uparrow,\downarrow\downarrow} &= \begin{cases} +\ln\left|\tan\left(\frac{\mu}{4}\right)\right| + x^* & x < -a \\ +\ln\left|\tan\left(\frac{\mu}{4}\right)\right| + x^\dagger & x > +a \end{cases} \end{aligned} \tag{A.9}$$

as can be verified by differentiation. Using the symmetry of the problem, in particular the relation between $\mu(-x)$ and $\mu(x)$ as shown in table A.1, integration constant $x^\dagger$ can be eliminated. For all configurations symmetry dictates $x^{\dagger} = -x^{*}$. Thus, we obtain

$$\begin{aligned}
\mu(x)^{\uparrow\downarrow} &= \begin{cases} 4\arctan\left[e^{(x-x^*)}\right] & x < -a \\ 4\arctan\left[e^{-(x+x^*)}\right] & x > +a \end{cases} \\
\mu(x)^{\downarrow\uparrow} &= \begin{cases} -4\arctan\left[e^{(x-x^*)}\right] & x < -a \\ -4\arctan\left[e^{-(x+x^*)}\right] & x > +a \end{cases} \\
\mu(x)^{\uparrow\uparrow} &= \begin{cases} 4\arctan\left[e^{(x-x^*)}\right] & x < -a \\ 4\arctan\left[e^{(x+x^*)}\right] & x > +a \end{cases} \\
\mu(x)^{\downarrow\downarrow} &= \begin{cases} -4\arctan\left[e^{(x-x^*)}\right] & x < -a \\ -4\arctan\left[e^{(x+x^*)}\right] & x > +a \end{cases}
\end{aligned} \tag{A.10}$$

Where we have used the fact that removing the absolute value sign adds an extra minus-sign for the ↓↑- and ↓↓-configurations. With the two 'tails' of the phase profile solved (up to a constant), let us move to the phase profile in the center facet. The expression for μ_x^2 is given in equation (A.4). Using some trigonometry and introducing a new constant

$$k \equiv \frac{2}{\sqrt{C_2 + 2}} \tag{A.11}$$

this can be written as

$$\frac{k^2}{4}\mu_x^2 = 1 - k^2 \sin^2\left(\frac{\mu}{2}\right) \tag{A.12}$$

Again, special care has to be taken as to use the correct root

$$\begin{aligned}
\tfrac{k}{2}\mu_x^{\uparrow\downarrow} &= \begin{cases} +\sqrt{1 - k^2\sin^2\left(\frac{\mu}{2}\right)} & -a < x < 0 \\ -\sqrt{1 - k^2\sin^2\left(\frac{\mu}{2}\right)} & 0 < x < a \end{cases} \\
\tfrac{k}{2}\mu_x^{\downarrow\uparrow} &= \begin{cases} -\sqrt{1 - k^2\sin^2\left(\frac{\mu}{2}\right)} & -a < x < 0 \\ +\sqrt{1 - k^2\sin^2\left(\frac{\mu}{2}\right)} & 0 < x < a \end{cases} \\
\tfrac{k}{2}\mu_x^{\uparrow\uparrow} &= \begin{cases} +\sqrt{1 - k^2\sin^2\left(\frac{\mu}{2}\right)} & -a < x < 0 \\ +\sqrt{1 - k^2\sin^2\left(\frac{\mu}{2}\right)} & 0 < x < a \end{cases} \\
\tfrac{k}{2}\mu_x^{\downarrow\downarrow} &= \begin{cases} -\sqrt{1 - k^2\sin^2\left(\frac{\mu}{2}\right)} & -a < x < 0 \\ -\sqrt{1 - k^2\sin^2\left(\frac{\mu}{2}\right)} & 0 < x < a \end{cases}
\end{aligned} \tag{A.13}$$

Separation of variables yields

$$dx = \pm k \frac{d\mu}{2\sqrt{1 - k^2\sin^2\left(\frac{\mu}{2}\right)}} \tag{A.14}$$

Integrating between zero and x gives

$$\int_0^x d\xi = \pm k \int_{\frac{\mu_0}{2}}^{\frac{\mu}{2}} \frac{d\theta}{\sqrt{1 - k^2\sin^2\theta}} \tag{A.15}$$

Using the incomplete elliptic integral of the first kind, defined by [219]

$$F(m,k) = \int_0^m \frac{d\theta}{\sqrt{1-k^2\sin^2\theta}} \tag{A.16}$$

equation (A.15) can be written as

$$\begin{aligned}
\frac{x}{k}^{\uparrow\downarrow} &= \begin{cases} F\left(\frac{\mu}{2},k\right) - F\left(\frac{\mu_0}{2},k\right) & -a < x < 0 \\ F\left(\frac{\mu_0}{2},k\right) - F\left(\frac{\mu}{2},k\right) & 0 < x < a \end{cases} \\
\frac{x}{k}^{\downarrow\uparrow} &= \begin{cases} F\left(\frac{\mu_0}{2},k\right) - F\left(\frac{\mu}{2},k\right) & -a < x < 0 \\ F\left(\frac{\mu}{2},k\right) - F\left(\frac{\mu_0}{2},k\right) & 0 < x < a \end{cases} \\
\frac{x}{k}^{\uparrow\uparrow} &= \Big\{ \; F\left(\frac{\mu}{2},k\right) - F\left(\frac{\mu_0}{2},k\right) \quad -a < x < a \\
\frac{x}{k}^{\downarrow\downarrow} &= \Big\{ \; F\left(\frac{\mu_0}{2},k\right) - F\left(\frac{\mu}{2},k\right) \quad -a < x < a
\end{aligned} \tag{A.17}$$

Thus we find for $\mu(x)$

$$\begin{aligned}
\mu(x)^{\uparrow\downarrow} &= \begin{cases} 2\,\mathrm{am}\left[F\left(\frac{\mu_0}{2},k\right) + \frac{x}{k},k\right] & -a < x < 0 \\ 2\,\mathrm{am}\left[F\left(\frac{\mu_0}{2},k\right) - \frac{x}{k},k\right] & 0 < x < a \end{cases} \\
\mu(x)^{\downarrow\uparrow} &= \begin{cases} 2\,\mathrm{am}\left[F\left(\frac{\mu_0}{2},k\right) - \frac{x}{k},k\right] & -a < x < 0 \\ 2\,\mathrm{am}\left[F\left(\frac{\mu_0}{2},k\right) + \frac{x}{k},k\right] & 0 < x < a \end{cases} \\
\mu(x)^{\uparrow\uparrow} &= \Big\{ \; 2\,\mathrm{am}\left[F\left(\frac{\mu_0}{2},k\right) + \frac{x}{k},k\right] \quad -a < x < a \\
\mu(x)^{\downarrow\downarrow} &= \Big\{ \; 2\,\mathrm{am}\left[F\left(\frac{\mu_0}{2},k\right) - \frac{x}{k},k\right] \quad -a < x < a
\end{aligned} \tag{A.18}$$

with $\mathrm{am}(u,k)$ the *Jacobi amplitude*, which is defined as the inverse of the elliptic integral in equation (A.16) [219]

$$\begin{aligned} u &= F(m,k) \\ \mathrm{am}(u,k) &= m \end{aligned} \tag{A.19}$$

With equations (A.10) and (A.18) the sine-Gordon equation has been solved on the entire interval. All that remains is the determination of the integration constants μ_0, k and x^*, which will be done in the remainder of this appendix. The approach that will be used is the following: first we will express both μ_0 and x^* in terms of k and then we use the continuity of $\mu(x)$ at the corners to solve for k.

The phase at $x = 0$, μ_0, can be derived using the symmetry of the problem. One can immediately see that μ_0 is π when the half-integer flux quanta are in the ↑↑-configuration and -π when they are in the ↓↓-configuration. For the ↑↓- and ↓↑-states μ_0 can be obtained from the argument that $\mu_x(0) = 0$. From equation (A.12) we find $\mu_0 = \pm 2\arcsin\left(\frac{1}{k}\right)$ where the positive value is for the ↑↓-state and the negative value for the ↓↑-state. Thus we obtain for μ_0 in terms of k:

$$\begin{aligned} \mu_0^{\uparrow\downarrow} &= +2\arcsin\left(\tfrac{1}{k}\right) \\ \mu_0^{\downarrow\uparrow} &= -2\arcsin\left(\tfrac{1}{k}\right) \\ \mu_0^{\uparrow\uparrow} &= +\pi \\ \mu_0^{\downarrow\downarrow} &= -\pi \end{aligned} \tag{A.20}$$

It can be shown [219] that the Jacobi amplitude $\mathrm{am}(u, k)$ is symmetric around

$$u_0 = F(\pm \arcsin(k^{-1}), k) \tag{A.21}$$

This property can be used to simplify equation (A.18) to

$$\begin{aligned} \mu(x)^{\uparrow\downarrow} &= 2\,\mathrm{am}\left[F\left(\tfrac{\mu_0}{2}, k\right) + \tfrac{x}{k}, k\right] \\ \mu(x)^{\downarrow\uparrow} &= 2\,\mathrm{am}\left[F\left(\tfrac{\mu_0}{2}, k\right) - \tfrac{x}{k}, k\right] \\ \mu(x)^{\uparrow\uparrow} &= 2\,\mathrm{am}\left[F\left(\tfrac{\mu_0}{2}, k\right) + \tfrac{x}{k}, k\right] \\ \mu(x)^{\downarrow\downarrow} &= 2\,\mathrm{am}\left[F\left(\tfrac{\mu_0}{2}, k\right) - \tfrac{x}{k}, k\right] \end{aligned} \quad |x| < a \tag{A.22}$$

Next, we will express the integration constant x^* in terms of k. Taking the derivative of the magnetic phase for $|x| > a$ from equation (A.10) and squaring we find:

$$\mu_x^2 = \begin{cases} \dfrac{4}{\cosh^2(x - x^*)} & x < -a \\ \dfrac{4}{\cosh^2(x + x^*)} & x > +a \end{cases} \tag{A.23}$$

for all configurations. Combining this with equation (A.4) and making use of the continuity of μ and μ_x at $x = \pm a$ we can express C_2 as

$$C_2 = 2\mu_x^2(\pm a) - 2 = \frac{8}{\cosh^2(a + x^*)} - 2 \tag{A.24}$$

Substituting C_2 from equation (A.11) we obtain the following relation between x^* and k:

$$x^* = \operatorname{arccosh}\left(\sqrt{2}k\right) - a \tag{A.25}$$

With μ_0 and x^* from equations (A.20) and (A.25) we can write the phase profile as a function of x and k only:

$$\begin{aligned} \mu(x)^{\uparrow\downarrow} &= \begin{cases} 4\arctan\left[e^{x+a-\operatorname{arccosh}\left(\sqrt{2}k\right)}\right] & x < -a \\ 2\,\mathrm{am}\left[F\left(\arcsin\left(\tfrac{1}{k}\right), k\right) + \tfrac{x}{k}, k\right] & |x| < a \\ 4\arctan\left[e^{-x+a-\operatorname{arccosh}\left(\sqrt{2}k\right)}\right] & x > a \end{cases} \\ \mu(x)^{\downarrow\uparrow} &= \begin{cases} -4\arctan\left[e^{x+a-\operatorname{arccosh}\left(\sqrt{2}k\right)}\right] & x < -a \\ -2\,\mathrm{am}\left[F\left(\arcsin\left(\tfrac{1}{k}\right), k\right) + \tfrac{x}{k}, k\right] & |x| < a \\ -4\arctan\left[e^{-x+a-\operatorname{arccosh}\left(\sqrt{2}k\right)}\right] & x > a \end{cases} \\ \mu(x)^{\uparrow\uparrow} &= \begin{cases} 4\arctan\left[e^{x+a-\operatorname{arccosh}\left(\sqrt{2}k\right)}\right] & x < -a \\ 2\,\mathrm{am}\left[K(k) + \tfrac{x}{k}, k\right] & |x| < a \\ 4\arctan\left[e^{x-a+\operatorname{arccosh}\left(\sqrt{2}k\right)}\right] & x > a \end{cases} \\ \mu(x)^{\downarrow\downarrow} &= \begin{cases} -4\arctan\left[e^{x+a-\operatorname{arccosh}\left(\sqrt{2}k\right)}\right] & x < -a \\ -2\,\mathrm{am}\left[K(k) + \tfrac{x}{k}, k\right] & |x| < a \\ -4\arctan\left[e^{x-a+\operatorname{arccosh}\left(\sqrt{2}k\right)}\right] & x > a \end{cases} \end{aligned} \tag{A.26}$$

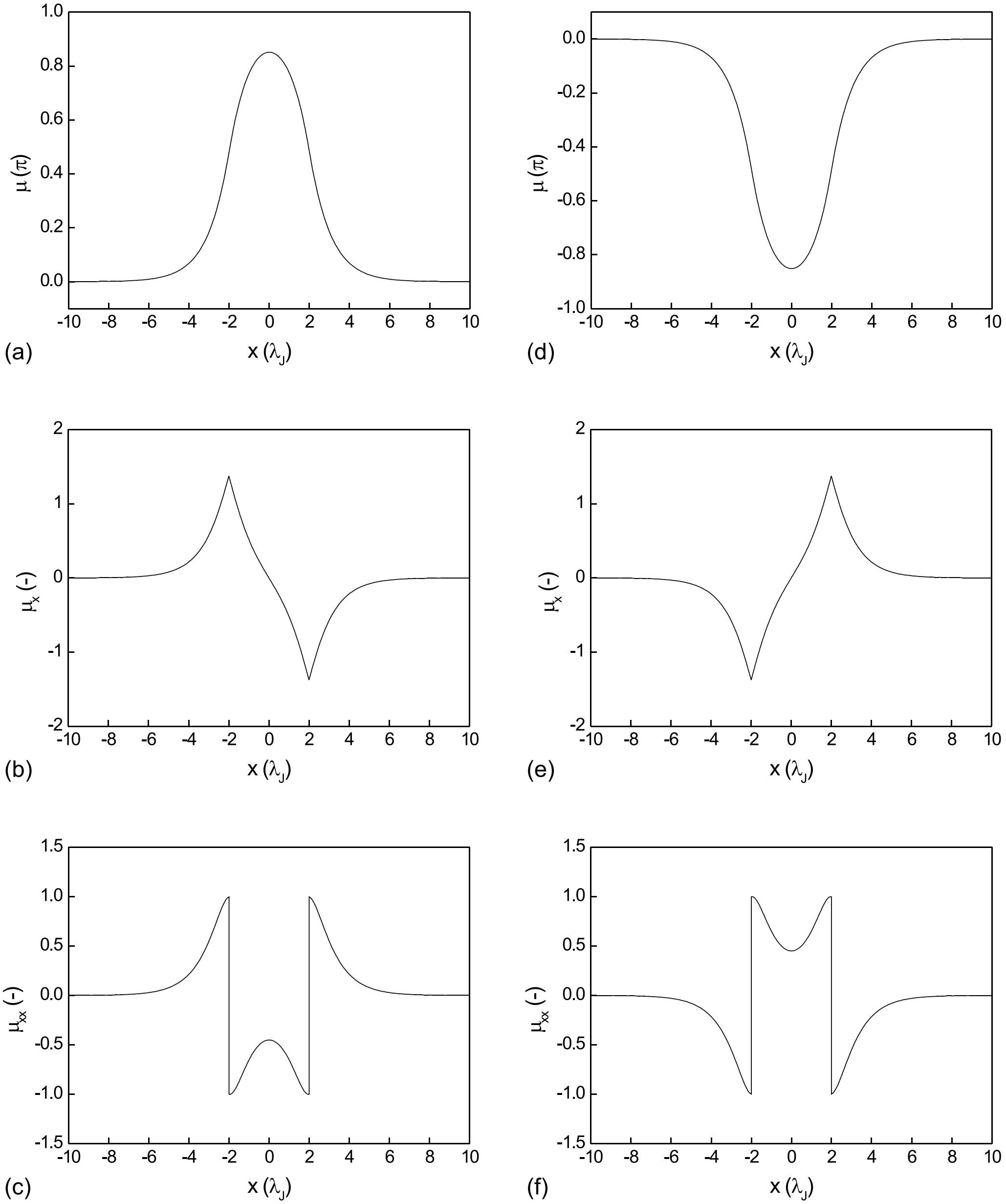

Figure A.1: Magnetic phase- (μ), flux- (μ_x), and current-distribution for (a)-(c) the ↑↓-state and (d)-(f) the ↓↑-state.

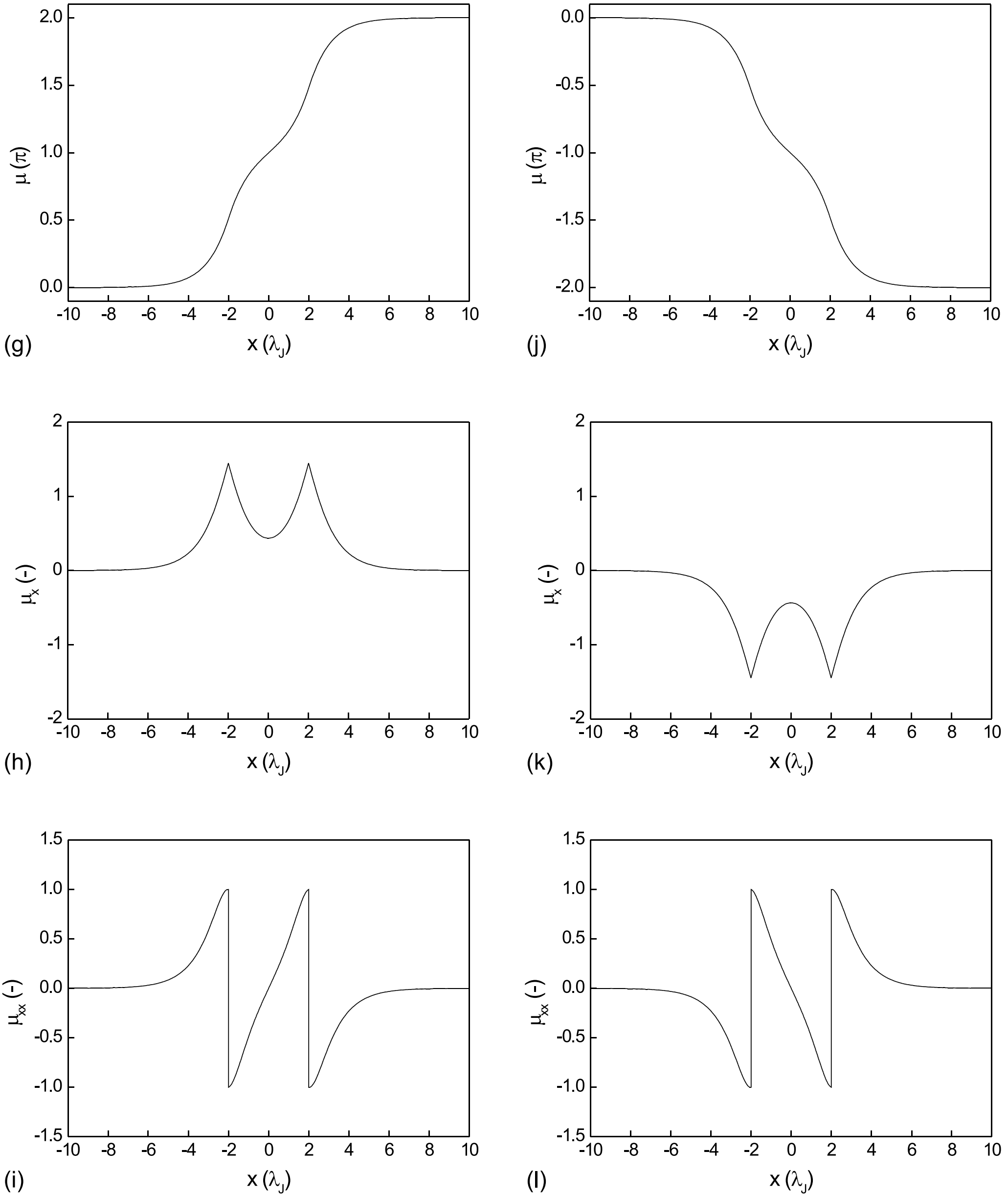

Figure A.1: (continued) Magnetic phase-, flux- and current-distribution for (g)-(i) the $\uparrow\uparrow$-state and (j)-(l) the $\downarrow\downarrow$-state.

where we have used the sign-reversal properties $\tan(-x)=-\tan(x)$, $F(-m,k)=-F(m,k)$, $\mathrm{am}(-u,k)=-\mathrm{am}(u,k)$, and

$$K(k) \equiv F\left(\frac{\pi}{2}, k\right) \tag{A.27}$$

is the complete elliptic integral of the first kind [219]. The last integration constant k can be obtained from the continuity of μ at $x = \pm a$. For a given facet length $d = 2a$ we find the following implicit relations for the antiferromagnetically aligned ($k > 1$) and ferromagnetically aligned semifluxons ($k < 1$):

$$\begin{aligned} \uparrow\downarrow, \downarrow\uparrow: \quad & \mathrm{am}\left[F\left(\arcsin\left(\tfrac{1}{k}\right), k\right) + \tfrac{a}{k}, k\right] = 2\arctan\left[e^{-\operatorname{arccosh}\left(\sqrt{2}k\right)}\right] \\ \uparrow\uparrow, \downarrow\downarrow: \quad & \mathrm{am}\left[K(k) + \tfrac{a}{k}, k\right] = 2\arctan\left[e^{\operatorname{arccosh}\left(\sqrt{2}k\right)}\right] \end{aligned} \tag{A.28}$$

Equations (A.26) and (A.28) can be used to construct the phase profiles for the ↑↓-, ↓↑-, ↑↑- and ↓↓-configuration of the half-integer magnetic flux quanta. The flux- and current profiles follow from taking the first- and second derivatives, respectively. To obtain the 'real' phase profile $\varphi(x)$ the d-wave-induced phase shift of π should be subtracted from the middle facet, in accordance with equation (A.2). The phase $\mu(x)$ and its derivatives are plotted in figure A.1 for a half-facet length a=2 (k was calculated to be 1.027958 for the antiferromagnetic orientation and 0.977071 for the ferromagnetic orientation).

Summary

This thesis is concerned with a remarkable phenomenon which occurs in rings connecting the high-T_c superconductor $\mathrm{YBa_2Cu_3O_{7-\delta}}$ (YBCO) to the low-T_c superconductor niobium. In such hybrid rings a spontaneously generated current leads to the formation of fractional flux quanta. These fractional flux quanta have been used for a fundamental study of the order parameter symmetry in YBCO and for the realization of a novel superconducting logic circuit element. Also the first controlled on-chip manipulation and read-out of two antiferromagnetically coupled fractional flux quanta in a long YBCO/Nb ramp-type Josephson junction containing two corners has been demonstrated.

The cuprate superconductor YBCO has a predominantly $d_{x^2-y^2}$-wave pairing symmetry. Superconductivity is assumed to occur in the quasi two-dimensional copper-oxygen planes. The superconducting gap has a maximum along the a- and b main crystal axes and is suppressed to zero in the nodal directions (diagonally between the crystal axes). An important property of the $d_{x^2-y^2}$-wave order parameter symmetry is a π-phase difference between orthogonal directions. It is this phase difference which can be exploited to realize π-rings which contain a spontaneously generated flux corresponding to a fraction of a flux quantum of positive or negative polarity.

The fluxoid quantization condition for loops containing Josephson junctions states that the sum of the phase differences (normalized by 2π) of the junctions and the enclosed magnetic flux (normalized by the flux quantum Φ_0) has to be an integer. For a standard loop this condition is satisfied when the phase drops over the junctions and the enclosed magnetic field are both zero. Also a single-crystalline YBCO ring is characterized by this currentless ground state because the number of d-wave-induced π-phase shifts picked up when going around the loop will always be an even number. By using hybrid structures which connect the anisotropic (d-wave) superconductor YBCO to the isotropic (s-wave) superconductor niobium, rings can be realized that contain an odd number of π-phase shifts, and for which the solution of zero flux and zero phases would violate the fluxoid quantization condition. In these rings the current, phases and enclosed flux redistribute in such a way that the fluxoid quantization condition is satisfied. For rings in the small-inductance limit ($LI_c \ll \Phi_0$) the d-wave-induced π-phase shift will be compensated mainly by the phases and the magnetic field is negligible. As the inductance increases the effect of the phases becomes smaller and the self-generated flux takes over, growing asymptotically to a half-flux quantum in the large inductance limit.

The precise composition of the order parameter symmetry in the cuprates is not yet established. The order parameter symmetry of YBCO is predominantly $d_{x^2-y^2}$-wave, but contains additional admixtures, on which no general agreement has been reached. The orthorhombic crystal structure of YBCO, and in particular the presence of so-called CuO chains, has lead several theorists to the proposition of an s-wave admixture, which

results in an anisotropy between the *a*- and *b*-axis orientations. The precise magnitude (values ranging from Δ_a/Δ_b=1.1 to 2 have been reported) and the possibility of additional complex admixtures (which allow for phase differences different from 0 or π) are however heavily debated. Insight into the symmetry properties with respect to the underlying crystal structure may lead to a significant contribution to the model of high-T_c superconductivity, one of the 'holy grails' in current-day materials science. For this purpose phase-sensitive experiments probing the pairing symmetry as a function of momentum are desirable, but until now such experiments have only been performed in a limited number of geometries.

The hybrid YBCO/Nb π-rings discussed in this thesis provide an excellent tool for an angle-resolved phase-sensitive study of the order parameter symmetry. Arrays of two-junction rings were fabricated with the angle of one of the junctions varying for each ring. The intrinsic phase shift of each ring, and the associated presence or absence of a fractional flux quantum, depends strongly on the geometry of the ring and the details of the order parameter symmetry of the YBCO base electrode. The rings were cooled down below the superconducting transition temperature of niobium and imaged using scanning SQUID microscopy (SSM). From the observed angular dependence of the spontaneously generated flux it is concluded that the in-plane gap in YBCO is at least 20% larger in the *b*-axis direction. This value is to be taken as an underestimate of the gap anisotropy because the samples were not fully untwinned. Moreover, no evidence for complex admixtures was observed. Based on the measurements it is concluded that any imaginary component of the gap, if at all present, should be smaller than 2.5%.

The two-fold degenerate ground state of π-rings makes them attractive candidates for storage of binary data in superconducting digital electronics. Rapid single flux quantum technology (RSFQ) is a superconducting logic family in which binary data is represented by the presence (for the logic '1') or absence (for the logic '0') of a flux quantum. Because RSFQ is a pulse-based technology, many cells require storing loops for the temporary latching of data. In conventional RSFQ technology the standard storing element is a two-junction loop, which is symmetric with respect to the flux polarity and thus always has an odd number of states (the exact number depending on the inductance of the loop). To make such rings suitable for storage of binary data these rings have to be asymmetrically biased in order to deform the potential energy landscape such that the Φ=0 and the $\Phi=\Phi_0$ states become degenerate. This artificial transformation to a two-level system acts as a critical factor in the design- and operation stage of circuits. Rings containing an intrinsic π-phase shift have a bistable ground state by nature, which alleviates the need for bias lines, increases design- and operation margins and boosts the overall robustness of circuits.

A novel circuit element, based on *d*-wave-induced π-phase shifts, was designed, fabricated and its successful operation demonstrated. The test-circuit consisted of a DC/SFQ converter, which converts the rising ramp of a DC input current to a single flux quantum (SFQ) pulse, a Josephson transmission line (JTL) which is used for the transport of single flux quanta, a π-ring based toggle flip-flop (TFF), which toggles its internal state (corresponding to the $\uparrow\downarrow$- and $\downarrow\uparrow$- configuration of two antiferromagnetically coupled fractional flux quanta in the π-rings) on every incoming SFQ pulse, and a DC SQUID which was used for the read-out of the internal state of the TFF. The measurements demonstrated a controlled change in the SQUID-voltage on every rising ramp of a triangular DC input current. The circuit was also operated in a mode where the DC/SFQ converter released multiple flux quanta into the JTL for every rising ramp. The SQUID registered the toggling of the TFF internal state for each flux quantum.

The spontaneously generated fractional flux quanta were not only studied in π-rings but also in so-called 'double corner' junctions. These are long YBCO/Nb ramp-type Josephson junctions containing two 90° in-plane angles. The symmetry of the (predominantly) d-wave order parameter in YBCO induces an intrinsic phase difference π between perpendicular facets in the junction which results in the spontaneous formation of fractional flux quanta at the corners. In the ground state the fractional flux quanta are ordered in an antiferromagnetic arrangement. The static phase profiles of such a 0-π-0 junction have been derived by making use of a perturbed sine-Gordon equation.

Earlier studies on fractional flux quanta in single and multiple (zig-zag) corner geometries relied heavily on scanning SQUID microscopy, which is undesirable if corner junctions are to be implemented in any practical application. In this thesis the first successful on-chip manipulation and read-out of fractional flux quanta in a long 0-π-0 junction is presented. The experimental results confirm the theoretical prediction that the polarity of two antiferromagnetically coupled fractional flux quanta in such a junction can be inverted through the application of a transport current. Controllable toggling between the two ground states has been observed both in pulse experiments and in magnetic field sweeps using the double corner junction as a field bias. In field sweep experiments using an external coil or an on-chip bias line a third state was observed which requires further investigation.

The work described in this thesis provides a solid basis for the application of half-integer flux quanta both for fundamental studies of the order parameter symmetry and for applications in superconducting digital electronics. The angle-resolved phase-sensitive experiments that have been used to study the in-plane gap symmetry of YBCO can also be used for different materials or to study the pairing behavior as a function of doping and temperature. The advantages of π-phase shifts in superconducting digital electronics is not merely restricted to d-wave-induced π-phase shifts but can be extended to circuits involving for example SFS-junctions or trapped fluxoids. The π-phase shifts increase device symmetry, relax design requirements and improve the operation margins. With the study of the on-chip manipulation and read-out of coupled fractional flux quanta in a double corner junction the first step has been taken for the incorporation of corner junctions in superconducting circuits.

Samenvatting

Dit proefschrift gaat over een opmerkelijk verschijnsel dat zich voordoet in ringen die de hoge-T_c supergeleider $YBa_2Cu_3O_{7-\delta}$ (YBCO) met de lage-T_c supergeleider niobium verbinden. In dergelijke hybride ringen gaat spontaan een stroom lopen die leidt tot de vorming van fractionele flux quanta. Deze fractionele flux quanta zijn gebruikt voor een fundamentele studie naar de ordeparametersymmetrie in YBCO en voor de realisatie van een nieuw supergeleidend logisch circuit element. Tevens is de eerste gecontroleerde on-chip manipulatie en uitlezing van twee antiferromagnetisch gekoppelde fractionele flux quanta in een lange YBCO/Nb hellingstype Josephson junctie met twee hoeken gedemonstreerd.

De cupraatsupergeleider YBCO heeft een overwegend $d_{x^2-y^2}$-wave paarvormingssymmetrie. Aangenomen wordt dat supergeleiding zich afspeelt in de quasi twee-dimensionale koperoxide vlakken. De supergeleidende 'gap' heeft een maximum langs de a- en b hoofdkristalassen en wordt volledig onderdrukt langs de 'nodal directions' (diagonaal tussen de kristalassen). Een belangrijke eigenschap van de $d_{x^2-y^2}$-wave ordeparametersymmetrie is een π-faseverschil tussen orthogonale richtingen. Het is dit faseverschil dat benut kan worden om π-ringen te realiseren die een spontaan gegenereerde flux bevatten, overeenkomend met een fractie van een flux quantum van positive of negatieve polariteit.

De 'fluxoid' kwantiseringsvoorwaarde voor ringen met Josephson juncties stelt dat de som van de faseverschillen (genormaliseerd met 2π) van de juncties en de ingesloten flux (genormaliseerd met het flux quantum Φ_0) een geheel getal moet zijn. Voor een standaard ring is aan deze voorwaarde voldaan wanneer de faseval over de juncties en het ingesloten magneetveld beide nul zijn. Ook een enkel-kristallijne YBCO ring wordt gekenmerkt door deze stroomloze grondtoestand, omdat het aantal d-wave-geïnduceerde π-faseverschuivingen dat wordt opgepikt bij het rondgaan van de ring altijd een even getal is. Door gebruik te maken van hybride structuren die de anisotrope (d-wave) supergeleider YBCO verbinden met de isotrope supergeleider (s-wave) niobium, kunnen ringen gerealiseerd worden die een oneven aantal π-faseverschuivingen bevatten en waarvoor de oplossing met een flux en fases van nul in strijd zou zijn met de fluxoid kwantiseringsvoorwaarde. In deze ringen zullen de stromen, fases en ingesloten flux herdistribueren op een zodanige wijze dat aan de fluxoid kwantiseringsvoorwaarde wordt voldaan. Voor ringen in de kleine inductie limiet ($LI_c \ll \Phi_0$) zal de d-wave-geïnduceerde π-faseverschuiving voornamelijk door de fases worden gecompenseerd en is het magneetveld te verwaardelozen. Met het toenemen van de inductie wordt het effect van de fases kleiner en neemt de zelfgegenereerde flux het over, daarbij asymptotisch groeiend naar een half flux quantum in de grote inductie limiet.

De precieze samenstelling van de ordeparametersymmetrie in de cupraten staat nog niet vast. De ordeparametersymmetrie van YBCO is overwegend $d_{x^2-y^2}$-wave, maar bevat additionele vermengingen, waarover geen algemene overeenstemming is bereikt. De orthorhombische kristalstructuur van YBCO, en in het bijzonder de aanwezigheid van zogenaamde CuO ketens, heeft verschillende theoretici geleid tot het voorstellen van een s-wave vermenging, die resulteert in een anisotropie tussen de a- en b-as oriëntaties. Over de precieze omvang (waarden variërend van $\Delta_a/\Delta_b = 1.1$ tot 2 zijn gerapporteerd) en de mogelijkheid van additionele complexe vermengingen (die faseverschillen anders dan 0 en π toelaten) zijn de meningen echter sterk verdeeld. Inzicht in de symmetrie-eigenschappen met betrekking tot de onderliggende kristalstructuur kan mogelijk leiden tot een belangrijke bijdrage aan het model van hoge-T_c supergeleiding, één van de 'heilige gralen' in de hedendaagse materiaalkunde. Hiervoor zijn fasegevoelige experimenten die de paarvormingssymmetrie als functie van impuls in kaart brengen wenselijk, maar tot nu toe zijn dergelijke experimenten slechts in een beperkt aantal geometrieën uitgevoerd.

De hybride YBCO/Nb π-ringen die in dit proefschrift worden besproken bieden een uitstekend instrument voor een hoekopgeloste fasegevoelige studie naar de ordeparametersymmetrie. Arrays van ringen met twee juncties zijn gefabriceerd waarbij de hoek van één der juncties gevarieerd werd. De intrinsieke faseverschuiving van elke ring, en de bijbehorende aanwezigheid dan wel afwezigheid van een fractioneel flux quantum, hangt sterk af van de geometrie van de ring en de details van de ordeparametersymmetrie van de YBCO basiselectrode. De ringen zijn afgekoeld tot onder de supergeleidende overgangstemperatuur van niobium en afgebeeld met behulp van scanning SQUID microscopie (SSM). Uit de waargenomen hoekafhankelijkheid van de spontaan gegenereerde flux wordt geconcludeerd dat de 'in-plane' gap in YBCO minstens 20% groter is in de b-as richting. Deze waarde moet als ondergrens gezien worden voor de gap-anisotropie omdat de samples niet volledig 'untwinned' waren. Er is bovendien geen bewijs gevonden voor complexe mengvormen. Op basis van de metingen is geconcludeerd dat een eventuele imaginaire component van de gap, als die al aanwezig is, kleiner moet zijn dan 2.5%.

De tweevoudig ontaarde grondtoestand van π-ringen maakt hen aantrekkelijke kandidaten voor de opslag van binaire data in supergeleidende digitale electronica. Rapid single flux quantum technologie (RSFQ) is een supergeleidende logica familie waarin binaire gegevens worden gerepresenteerd door de aanwezigheid (voor de logische '1') dan wel afwezigheid (voor de logische '0') van een flux quantum. Omdat RSFQ een puls-gebaseerde technologie is, hebben veel cellen opslagringen nodig voor het tijdelijk vasthouden van data. In conventionele RSFQ is het standaard opslagelement een ring met twee juncties, die symmetrisch is met betrekking tot de flux polariteit en dus altijd een oneven aantal toestanden heeft (waarbij het precieze aantal afhangt van de inductie van de ring). Om dergelijke ringen geschikt te maken voor de opslag van binaire data moeten deze ringen asymmetrisch aangedreven worden om het potentiaallandschap zodanig te vervormen dat de Φ=0 en de Φ=Φ_0 toestanden ontaard worden. Deze artificiële transformatie naar een twee-niveau systeem is een kritieke factor in de ontwerp- en operatiefase van circuits. Ringen die een intrinsieke π-faseverschuiving bevatten hebben van nature al een bistabiele grondtoestand, hetgeen de behoefte aan aandrijflijnen vermindert en bovendien de ontwerp- en operatiemarges alsmede de algemene robuustheid van circuits vergroot.

Een nieuw circuit element, gebaseerd op d-wave-geïnduceerde π-faseverschuivingen, is ontworpen, gefabriceerd en de correcte werking ervan aangetoond. Het testcircuit bestond uit een DC/SFQ omzetter, die de stijgende helling van een DC ingangsstroom converteert naar een 'single flux quantum' (SFQ) puls, een Josephson transmissie lijn (JTL), die gebruikt wordt voor het transport van SFQ pulsen, een π-ring-gebaseerde 'toggle flip-flop' (TFF), die zijn interne toestand (bestaande uit de $\uparrow\downarrow$- en $\downarrow\uparrow$- configuratie van twee antiferromagnetisch gekoppelde fractionele flux quanta in de π-ringen) bij elke inkomende SFQ puls omschakelt, en een DC SQUID dat gebruikt werd voor de uitlezing van de interne toestand van de TFF. De metingen toonden een gecontroleerde verandering in het SQUID-voltage aan bij elke stijgende helling van een driehoekige DC ingangsstroom. Het circuit is ook gebruikt in een modus waarbij de DC/SFQ omzetter meerdere flux quanta naar de JTL liet gaan voor elke stijgende helling. Het SQUID registreerde het schakelen van de interne toestand van de TFF voor elk flux quantum.

De spontaan gegenereerde fractionele flux quanta zijn niet alleen bestudeerd in π-ringen maar ook in zogenaamde 'dubbele hoekjuncties'. Dit zijn lange YBCO/Nb hellingstype Josephson juncties die twee in-plane hoeken van 90° bevatten. De symmetrie van de (voornamelijk) d-wave ordeparameter in YBCO induceert een intrinsiek faseverschil π tussen haaks op elkaar staande facetten in de junctie, hetgeen resulteert in de spontane formatie van fractionele flux quanta op de hoeken. In de grondtoestand zijn de fractionele flux quanta antiferromagnetisch geordend. De statische faseprofielen van een dergelijke 0-π-0 zijn afgeleid door gebruik te maken van een verstoorde sine-Gordon vergelijking.

Eerdere studies aan fractionele flux quanta in enkele en meervoudige (zig-zag) hoekgeometrieën steunden sterk op scanning SQUID microscopie, hetgeen onwenselijk is voor het gebruik van hoekjuncties in een praktische toepassing. In dit proefschrift is de eerste succesvolle on-chip manipulatie en uitlezing van fractionele flux quanta in een lange 0-π-0 junctie gepresenteerd. De experimentele resultaten bevestigen de theoretische voorspelling dat de polariteit van twee antiferromagnetisch gekoppelde fractionele flux quanta in een dergelijke junctie omgeklapt kan worden door het aanleggen van een transportstroom. Het controleerbaar schakelen tussen de twee grondtoestanden is waargenomen in pulsexperimenten en magneetveldexperimenten waarbij de dubbele hoekjunctie gebruikt werd om het magneetveld te variëren. In magneetveld-experimenten waar een externe spoel of een on-chip aandrijflijn werd gebruikt is een derde toestand ontdekt die nader onderzoek vereist.

Het werk dat beschreven wordt in dit proefschrift levert een solide basis voor de toepassing van halftallige flux quanta zowel voor fundamentele studies naar de ordeparametersymmetrie als voor applicaties in supergeleidende digitale electronica. De hoekopgeloste fasegevoelige experimenten die gebruikt zijn voor de studie naar de in-plane gap symmetrie van YBCO kunnen ook gebruikt worden voor andere materialen of voor de studie naar het paarvormingsgedrag als functie van dotering en temperatuur. De voordelen van π-faseverschuivingen in supergeleidende digitale electronica zijn niet slechts beperkt tot de d-wave-geïnduceerde π-faseverschuivingen maar kunnen worden uitgebreid naar circuits die gebruik maken van bijvoorbeeld SFS juncties of ingevangen fluxoids. De π-faseverschuivingen verhogen de symmetrie van de schakeling, verlagen de ontwerpeisen en verbeteren het werkbereik. Met de studie van de on-chip manipulatie en uitlezing van gekoppelde fractionele flux quanta in een dubbele hoekjunctie is de eerste stap gezet voor de integratie van hoekjuncties in supergeleidende circuits.

Dankwoord

Met de totstandkoming van dit proefschrift wordt een periode van onderzoek afgesloten waar ik nog lang en met veel plezier aan terug zal denken. Niet alleen vanwege de fascinerende verschijnselen waarmee ik mij heb mogen bezighouden, maar vooral ook vanwege de omgeving waarin dit onderzoek heeft plaatsgevonden. In iets ruimere zin doel ik hiermee op de stad Enschede en de groene campus van de Universiteit Twente, wat specifieker denk ik aan de gezellige en collegiale sfeer binnen de vakgroep Lage Temperaturen. Deze hebben er alle toe bijgedragen dat ik de laatste jaren met veel genoegen aan het onderzoek, dat in dit proefschrift is beschreven, heb gewerkt. Uiteraard heb ik dit onderzoek niet alleen uitgevoerd, en ik ben dan ook veel dank verschuldigd aan de talloze personen die, direct of indirect, aan dit proefschrift hebben bijgedragen.

In de eerste plaats gaat mijn dank uit naar Horst Rogalla, voor het bieden van de mogelijkheid dit promotie-onderzoek binnen de vakgroep Lage Temperaturen uit te voeren. Ook wil ik graag mijn promotor Hans Hilgenkamp bedanken voor het in mij gestelde vertrouwen. Ik heb altijd veel respect gehad voor je heldere uitleg van complexe problemen. Het inmiddels legendarische colloquium over het Fractional Quantum Hall effect tijdens het zeiluitje in Heeg is hier een goed voorbeeld van. Ook je toegankelijkheid heeft me altijd enorm aangesproken. Stichting FOM ben ik erkentelijkheid verschuldigd voor de detachering binnen de vakgroep Lage Temperaturen en de door hen geleverde ondersteuning gedurende het gehele promotietraject.

The experiments described in chapter 5 would not have been possible without the fruitful collaboration with Chang Tsuei and John Kirtley at the IBM T.J. Watson Research Center in Yorktown Heights (USA). It has been an honor and a privilege to have worked with two such distinguished scientists. I wish to express my gratitude to Chang for accepting to become a member of my Ph.D. committee and reading the draft version of my thesis. John, thanks for your invaluable scanning SQUID microscopy studies, it has been a pleasure seeing you operate the scanning SQUID microscope during your visits in Twente. I would also like to thank you for many interesting discussions ranging from order parameter symmetry to the finer details of Dutch.

I would also like to take this opportunity to thank Thomas Ortlepp and Olaf Mielke from the RSFQ Design Group at the University of Ilmenau (Germany) who played a crucial role in the experiments described in chapter 6. Thomas, I would like to thank you for teaching me almost everything I know about RSFQ. Explaining things comes very natural to you, and I am happy to see that this talent is currently being employed to train young students at the University of Ilmenau, as I have witnessed during one of your classes. It was a pleasure to find somebody with the same interest in riddles, and I enjoyed supporting the 'Kusshand'-team during the Bettenrennen in Friedrichroda. Olaf I would like to thank for many interesting discussions on Josephson structures and potential energy landscapes and the last-minute support during the final stages of my thesis.

I would like to thank Hadi Susanto from the School of Mathematical Sciences at the University of Nottingham (UK) for useful discussions on the sine-Gordon equation and checking the derivation presented in the appendix. In dit verband wil ik ook graag Hans Bosschker bedanken, die ik tijdens mijn promotie heb mogen begeleiden bij zijn afstudeeronderzoek. Ik heb met verbazing gekeken hoe snel je de stof tot je nam en jouw inspanningen zijn van onschatbare waarde geweest voor de in hoofdstuk 7 gepresenteerde resultaten.

A considerable amount of time during my stay in Twente was spent on the attempt to witness Macroscopic Quantum Tunnelling (MQT) in our YBCO/Nb ramp-type Josephson junctions. Though the results obtained in these experiments were not substantial enough for publication in this thesis, I would like to thank the people that have collaborated on this project. My gratitude goes to Thilo Bauch for performing the switching experiments on our samples in his dilution refrigerator at Chalmers University of Technology (Sweden). Takeo è tò Kato (University of Tokyo, Japan) I owe thanks for discussions about MQT in general and his support for writing a program to numerically calculate the crossover-temperature. I would also like to thank Shiro Kawabata (National Institute of Advanced Industrial Science and Technology, Japan) for the many stimulating discussions.

Zoals gezegd heb ik mijn periode bij de vakgroep Lage Temperaturen als bijzonder aangenaam ervaren. Graag wil ik in dit verband nog enkele mensen noemen. Om alle zaken waarvoor ik Ans Veenstra en Inke in de Wal dankbaar ben te benoemen zou ik minstens een extra appendix nodig hebben, dus ik beperk mij tot een kleine greep. Dank voor de hulp bij het organiseren van reizen en hotels, voor al die administratieve klusjes, en voor de gezellige gesprekken waar ik bij jullie nog wél begrip vond (mijn agenda-tik, kamperen, fietsuitjes). Mijn dank gaat ook uit naar Frank Roest- en Dick Veldhuis, die eigenlijk altijd in één adem genoemd worden (vinden jullie dat nou niet vervelend?): bedankt voor alles wat jullie me geleerd hebben op het gebied van pulsed laser depositie, sputteren, etsen, lithografie, en al die andere zaken die zoal bij samplefabricage komen kijken. Ik heb ook erg genoten van de gezellige gesprekken aan de koffietafel die soms helemaal nergens over gingen.

Dat laatste lijkt mij een mooi bruggetje naar Harry Steffens en Jan Talman. Een Brabander heeft van nature sterk de neiging om te willen 'ouwehoeren', en het is dan ook wonderbaarlijk om te zien hoe bij rasechte Tukkers zoals Harry en Jan in die behoefte kan worden voorzien, waarvoor mijn dank! Het spreekt natuurlijk voor zich dat ik ook jullie noeste arbeid doordeweeks én in het weekeinde om de heliumproductie op peil te houden enorm heb gewaardeerd, alsmede de hulp met de flow-cryostaat. In het paragraafje, laat ik het beleefd houden, 'medium aged', mag natuurlijk ook 'Syboltosaurus' Harkema niet ontbreken. Sybolt, ik heb altijd enorm genoten van jouw scherpe opmerkingen aan de koffietafel en tijdens de werkbesprekingen, waar je mij sterk deed denken aan die oude mannetjes op het balkon bij de Muppet-show. Ook wil ik jou en Gerrit van Hummel bedanken voor alle hulp bij de metingen met de röntgendiffractometer. Jullie technische expertise is van onschatbare waarde geweest!

Graag wil ik Alexander Brinkman bedanken voor de theoretische discussies. Ik heb het altijd erg prettig gevonden dat je, hoe druk je het ook had, voor een wetenschappelijk probleem altijd tijd vrij wilde maken. Alexander (Sasha) Golubov wil ik in dit verband ook graag bedanken. Hoewel ik geen directe professionele relatie had met Jaap Flokstra, voelde ik mij altijd wel sterk bij hem betrokken, mede omdat onze kamer zich naast die van hem bevond en Jaaps dragende stem zich niet erg veel aantrekt van dunne wandjes. Iets waarvan ik overigens zelf ook weer ben beschuldigd toen Sybolt mij op het gehoor feilloos in een menigte mensen wist op te sporen tijdens een conferentie.

Gedurende mijn promotieperiode heb ik met verschillende collega's en studenten het kantoor gedeeld. Graag wil ik hier mijn kamergenoten bedanken voor de gezellige periode: Joska Broekmaat, ondernemer in hart en nieren. Na je promotie heb je met een aantal collega's het bedrijf SolMateS opgericht. Ik wens je alle goeds toe om van dit bedrijf een groot succes te maken. Agnès Roussy heb ik maar een korte periode mee mogen maken, maar je was een kleurrijke toevoeging voor het kantoor. Je lerares Nederlands kan trots op je zijn als je deze tekst na al die tijd nog begrijpt, maar ik vermoed dat Dick het voor je zal vertalen. Vedran 'Linux' Vonk wil ik graag bedanken voor de discussies over de kristallografische eigenschappen van YBCO, en Aleksandar Andreski voor de discussies over Josephson-structuren en beurskoersen. Menno Veldhorst moet ik complimenteren met zijn immer netjes opgeruimde bureau. Veel succes met de gekuiste Andreev reflectie! Tim Lammens (ook wel Lamme Tim of Timmay genoemd), Rob Bijman (bedankt voor de cursus hakken), Sander Wenderich, en Marcel Hoek wil ik hier ook graag bedanken voor het aangename gezelschap.

I would like to express my special thanks to Ari Ando, who tricked the whole group into believing that he had only one name but exposed himself by labelling his sample boxes with 'AA'. You have helped me from the start and taught me almost everything I know about sample fabrication. It has been a real pleasure working with you and I enjoyed our discussions both on-duty and off-duty. My gratitude also goes to Karthikeyan Shunmugavel for explaining to me the finer details of Indian culture. Thank you for teaching me the hard way that indeed what I had always considered as 'spicy food' was, in fact, not spicy at all. I would also like to say thanks to Kelvin Foo for teaching me how to count (which I already forgot) and say 'Coca Cola' (which I did not forget) in Cantonese.

De juweeltjes in mijn werkdag waren vaak toch de lunches in de Bastille met het vaste clubje Martin van Essen, Johannes 'de Koala' Pleikies en Reinder Cuperus, waarvoor ik jullie hier graag wil bedanken. Om met de laatste te beginnen: Reinder, ik zeg het niet graag, maar voor een Fries ben je zwaar OK! Vooral het weglaten van nautische termen tijdens het zeiluitje heeft je enorm in mijn achting doen stijgen. Bedankt ook voor je hulp met programmeren in Matlab en zo'n beetje alles wat met enen en nullen werkt. Johannes wil ik graag bedanken voor de vele discussies over onderwerpen als juncties en SQUIDs, maar ook over films, politiek en Oost-Duitsland. Je onverstoorbare werkhouding heeft altijd respect bij mij afgedwongen. Met Martin heb ik behalve interesses in onder andere talen, schaken, mosterd, en (om maar eens wat te noemen) Ome Henk, ook een neiging naar perfectionisme gemeen. De voorbeelden hiervan waren vaak een feest van herkenning en werkten zo op de lachspieren dat ik hier met veel plezier aan terugdenk.

Verder gaat mijn dank uit naar alle overige medewerkers en studenten die samen voor een fantastische sfeer hebben gezorgd: Aico 'ass-o-vision' Troeman (bedankt voor je hulp met de SSM metingen), Maarten 'gewoon GMR' van Zalk (die ik langzaam heb zien transformeren naar de koning van de practical jokes), Kristiaan Kuit (zonder jou zat ik nu nog kleurcoderingen op weerstanden te ontcijferen), de '2 Brothers on the 4th Floor' Mark & Jeroen Huijben (bedankt voor de hulp in het lab en met LightWave en uiteraard de discussies over games), Joost 'glovebox' Beukers (de EuO koning), Martin Sobik, Theo Thijssen, Pieter Lerou, Marcel ter Brake, Harry Holland, Johannes Burger, Robert-Jan Meijer, Harald van Weeren, Hendrie Derking, Gerard Willering, Manon Kok, Peter Bosch, Diederik Jekel, Michelle Kruize, Thijs 'mijnenveger' Veening , 'Taxi' Bert Borger, Imdat Yikilmaz, Robert van Tankeren en Ingrid Oomen: allen bedankt voor een onvergetelijke tijd.

Ook buiten de Universiteit Twente ben ik dank verschuldigd aan mensen die mij op verschillende manieren hebben bijgestaan. I would like to thank Adrian Lupaşcu (Institute of Quantum Computing, University of Waterloo, Canada) for helpful discussions and proofreading the draft-version of my thesis. I wish you all the best in setting up your own research group. Mijn oud-collega's aan de Technische Universiteit Delft Benoit Witkamp en Paul van Rossum wil ik graag bedanken voor het bemachtigen van artikelen die hier lastig te verkrijgen waren. Ben wil ik bovendien bedanken voor zijn hulp met LabVIEW. Voor de broodnodige ontspanning was ik altijd welkom aan de Haringvliet in Rotterdam: ik wil hier graag Coen Gebuis, Albart 'vissen' Grasman en Ben 'muntjes' Feringa bedanken voor de onvergetelijke kaartavonden. Ook mijn collega-'schnickelfilosofen' Paul van Rossum, Khoa Do, Iddo Heller en Joost Dijkers wil ik hartelijk danken voor het mij aansmeren van de schoppenmiet. Op deze plaats wil ik ook Gerda van Tongeren bedanken voor de dagelijkse support, de gezellige uurtjes online en de maffe mailtjes. Pieter Kramer wil ik graag bedanken voor de discussies tijdens onze lange wandelingen. Dat er maar vele mogen volgen! Tenslotte gaat mijn dank uit naar mijn familie die mij tijdens deze periode altijd heeft gesteund en waar ik mij altijd welkom heb geweten. Mijn (groot)ouders wil ik graag bedanken voor onvoorwaardelijke liefde die ik vanuit Steenbergen heb mogen ontvangen. Ook mijn zus en zwager wil ik bedanken voor de gezellige weekeinden en veel succes toewensen met het grootbrengen van mijn twee fantastische neefjes.

π

De π-faseverschuiving die verantwoordelijk is voor de spontaan gegenereerde halftallige magnetische flux quanta loopt als rode draad door dit proefschrift. Het getal π bleek zich tijdens mijn promotie echter ook op allerlei andere manieren te manifesteren. Het kantoor dat ik betrok had het telefoonnummer $3_0 14$ (π). Het laboratorium met de bad-cryostaat had als telefoonnummer π onafgerond (3141), het laboratorium met de flow-cryostaat had als telefoonnummer π afgerond (3142), het telefoonnummer van de aangrenzende kamer was 3122 (2+2=4), wat door elkaar gehusseld weer de code op de koffie-automaat was voor café-au-lait met extra suiker (2123). Het telefoonnummer van de collega-promovendi aan het einde van de gang kon ik pas onthouden toen ik mij realiseerde dat ook dat uit π te herleiden was: $31_{4159}26$. De reistijd Enschede-Roosendaal bedroeg volgens de NS dienstregeling 3:14, de lunch kostte regelmatig 3.14 Euro, tijdens mijn promotie-onderzoek leerde ik dat er ongeveer $\pi \cdot 10^7$ seconden in een jaar gaan en dat men voor een zachtgekookt ei het water 3'14" moet laten koken.

Bibliography

[1] H.K. Onnes, *Further experiments with liquid helium. C. On the change of electric resistance of pure metals at very low temperatures etc. IV. The resistance of pure mercury at helium temperatures*, Communication N^0 120^b from the Physical Laboratory at Leiden (1911)

[2] H.K. Onnes, *Further experiments with liquid helium. D. On the change of the electrical resistance of pure metals at very low temperatures, etc. V. The disappearance of the resistance of mercury*, Communication N^0 122^b from the Physical Laboratory at Leiden (1911)

[3] H.K. Onnes, *Further experiments with liquid helium. G. On the electrical resistance of pure metals, etc. VI. On the sudden change in the rate at which the resistance of mercury disappears*, Communication N^0 124^c from the Physical Laboratory at Leiden (1911)

[4] M.K. Wu, J.R. Ashburn, C.J. Torng, P.H. Hor, R.L. Meng, L. Gao, Z.J. Huang, Y.Q. Wang and C.W. Chu, *Superconductivity at 93 K in a new mixed-phase Y-Ba-Cu-O compound system at ambient pressure*, Physical Review Letters **58**, 908 (1987)

[5] J. Bardeen, L.N. Cooper and J.R. Schrieffer, *Theory of superconductivity*, Physical Review **108**, 1175 (1957)

[6] V.B. Geshkenbein and A.I. Larkin, *The Josephson effect in superconductors with heavy fermions*, Journal of Experimental and Theoretical Physics Letters **43**, 395 (1986)

[7] V.B. Geshkenbein, A.I. Larkin and A. Barone, *Vortices with half magnetic flux quanta in "heavy-fermion superconductors"*, Physical Review B **36**, 235 (1987)

[8] H.K. Onnes, *The liquefaction of helium*, Communication N^0 108 from the Physical Laboratory at Leiden (1908)

[9] A. Mourachkine, *Room-temperature superconductivity*, Cambridge International Science Publishing (2004)

[10] M.J. de Vries, F.K. Boersma, *80 years of research at the Philips Natuurkundig Laboratorium 1914-1994*, Pallas Publications (2005)

[11] H.K. Onnes, *Further experiments with liquid helium. H. On the electrical resistance etc. (continued). VIII. The sudden disappearance of the ordinary resistance of tin,*

and the super-conductive state of lead, Communication N^0 133^d from the Physical Laboratory at Leiden (1913)

[12] *Nobel lectures in physics 1901-1921*, World Scientific Publishing (1998)

[13] P.J. Lee, *Engineering superconductivity*, John Wiley & Sons (2001)

[14] W. Meissner and H. Franz, *Supraleitfähigkeit von Carbiden und Nitriden*, Naturwissenschaften **18**, 418 (1930)

[15] W. Meissner and H. Franz, *Messungen mit Hilfe von flüssigem Helium. IX. Supraleitfähigkeit von Carbiden und Nitriden*, Zeitschrift für Physik **65**, 30 (1930)

[16] W. Meissner and H. Franz, *Messungen mit Hilfe von flüssigem Helium. VIII. Supraleitfähigkeit von Niobium*, Zeitschrift für Physik **63**, 558 (1930)

[17] L.A. Abelson and G.L. Kerber, *Superconductor integrated circuit fabrication technology*, Proceedings of the IEEE **92**, 1517 (2004)

[18] W. Meissner and R. Ochsenfeld, *Ein neuer Effekt bei Eintritt der Supraleitfähigkeit*, Die Naturwissenschaften **21**, 787 (1933)

[19] F. London and H. London, *The electromagnetic equations of the supraconductor*, Proceedings of the Royal Society of London **149**, 71 (1935)

[20] V.L. Ginzburg and L.D. Landau, *Phenomenological theory of superconductivity*, Zh. Eksp. Teor. Fiz. **20**, 1064 (1950)

[21] *Nobel lectures in physics 1971-1980*, World Scientific Publishing (1992)

[22] B.T. Matthias, T.H. Geballe, S. Geller and E. Corenzwit, *Superconductivity of* Nb_3Sn, Physical Review **95**, 1435 (1954)

[23] A. Godeke, *A review of the properties of* Nb_3Sn *and their variation with A15 composition, morphology and strain state*, Superconductor Science and Technology **19**, R68 (2006)

[24] A. Godeke, *Performance boundaries in* Nb_3Sn *superconductors*, Ph.D. Thesis, University of Twente (2005)

[25] B.T. Matthias, T.H. Geballe, L.D. Longinotti, E. Corenzwit, G.W. Hull, R.H. Willens and J.P. Maita, *Superconductivity at 20 degrees Kelvin*, Science **156**, 645 (1967)

[26] G. Arrhenius, E. Corenzwit, R. Fitzgerald, G.W. Hull jr., H.L. Luo, B.T. Matthias and W.H. Zachariasen, *Superconductivity of* $Nb_3(Al,Ge)$ *above 20.5° K*, Proceedings of the National Academy of Sciences of the United States of America **61**, 621 (1968)

[27] W.L. McMillan, *Transition temperature of strong-coupled superconductors*, Physical Review **167**, 331 (1968)

[28] L.M. Falicov, *Superconductivity: a brief introduction to its phenomenology and theories*, IEEE Journal of Quantum Electronics **25**, 2358 (1989)

[29] C.W. Chu, *High-temperature superconducting materials: a decade of impressive advancement of* T_c, IEEE Transactions on Applied Superconductivity **7**, 80 (1997)

[30] J.G. Bednorz and K.A. Müller, *Possible high T_c superconductivity in the Ba-La-Cu-O system*, Zeitschrift für Physik B **64**, 189 (1986)

[31] C.P. Poole jr., *Handbook of superconductivity*, Academic Press (2000)

[32] *Nobel lectures in physics 1981-1990*, World Scientific Publishing (1993)

[33] R.M. Hazen, L.W. Finger, R.J. Angel, C.T. Prewitt, N.L. Ross, H.K. Mao, C.G. Hadidiacos, P.H. Hor, R.L. Meng and C.W. Chu, *Crystallographic description of phases in the Y-Ba-Cu-O superconductor*, Physical Review B **35**, 7238 (1987)

[34] H. Maeda, Y. Tanaka, M. Fukutomi and T. Asano, *A New High-T_c Oxide superconductor without a rare earth element*, Japanese Journal of Applied Physics **27**, L209 (1988)

[35] C.W. Chu, J. Bechtold, L. Gao, P.H. Hor, Z.J. Huang, R.L. Meng, Y.Y. Sun, Y.Q. Wang and Y.Y. Xue, *Superconductivity up to 114 K in the Bi-Al-Ca-Sr-Cu-O compound system without rare-earth elements*, Physical Review Letters **60**, 941 (1988)

[36] Z.Z. Sheng and A.M. Hermann, *Bulk superconductivity at 120 K in the Tl-Ca/Ba-Cu-O system*, Nature **332**, 138 (1988)

[37] R.M. Hazen, L.W. Finger, R.J. Angel, C.T. Prewitt, N.L. Ross, C.G. Hadidiacos, P.J. Heaney, D.R. Veblen, Z.Z. Sheng, A. El Ali and A.M. Hermann, *100-K Superconducting phases in the Tl-Ca-Ba-Cu-O system*, Physical Review Letters **60**, 1657 (1988)

[38] S.S.P. Parkin, V.Y. Lee, E.M. Engler, A.I. Nazzal, T.C. Huang, G. Gorman, R. Savoy and R. Beyers, *Bulk superconductivity at 125 K in $Tl_2Ca_2Ba_2Cu_3O_x$*, Physical Review Letters **60**, 2539 (1988)

[39] D.D. Berkley, E.F. Skelton, N.E. Moulton, M.S. Osofsky, W.T. Lechter, V.M. Browning and D.H. Liebenberg, *Pressure dependence of the superconducting transition temperature in single crystals of $Tl_2Ba_2Ca_2Cu_3O_{10-x}$*, Physical Review B **47**, 5524 (1993)

[40] A. Schilling, M. Cantoni, J.D. Guo and H.R. Ott, *Superconductivity above 130K in the Hg-Ba-Ca-Cu-O system*, Nature **363**, 56 (1993)

[41] C.W. Chu, L. Gao, F. Chen, Z.J. Huang, R.L. Meng and Y.Y. Xue, *Superconductivity above 150 K in $HgBa_2Ca_2Cu_3O_{8+\delta}$*, Nature **365**, 323 (1993)

[42] L. Gao, Y.Y. Xue, F. Chen, Q. Xiong, R.L. Meng, D. Ramirez, C.W. Chu, J. Eggert and H.K. Mao, *Superconductivity up to 164 K in $HgBa_2Ca_{m-1}Cu_mO_{2m+2+\delta}$*, Physical Review B **50**, 4260 (1994)

[43] L.F. Mattheiss, E.M. Gyorgy and D.W. Johnson jr., *Superconductivity above 20 K in the Ba-K-Bi-O system*, Physical Review B **37**, 3745 (1988)

[44] R.J. Cava, B. Batlogg, J.J. Krajewski, R. Farrow, L.W. Rupp jr., A.E. White, K. Short, W.F. Peck and T. Kometani, *Superconductivity near 30 K without copper: the $Ba_{0.6}K_{0.4}BiO_3$ perovskite*, Nature **332**, 814 (1988)

[45] A.F. Hebard, M.J. Rosseinsky, R.C. Haddon, D.W. Murphy, S.H. Glarum, T.T.M. Palstra, A.P. Ramirez and A.R. Kortan, *Superconductivity at 18 K in potassium-doped* C_{60}, Nature **350**, 600 (1991)

[46] K. Holczer, O. Klein, S.-M. Huang, R.B. Kaner, K.-J. Fu, R.L. Whetten and F. Diederich, *Alkali-fulleride superconductors: synthesis, composition, and diamagnetic shielding*, Science **252**, 1154 (1991)

[47] M.J. Rosseinsky, A.P. Ramirez, S.H. Glarum, D.W. Murphy, R.C. Haddon, A.F. Hebard, T.T.M. Palstra, A.R. Kortan, S.M. Zahurak and A. V. Makhija, *Superconductivity at 28 K in* Rb_xC_{60}, Physical Review Letters **66**, 2830 (1991)

[48] C.-C. Chen, S.P. Kelty and C.M. Lieber, $(Rb_xK_{1-x})_3C_{60}$ *Superconductors: formation of a continuous series of solid solutions*, Science **253**, 886 (1991)

[49] A.Y. Ganin, Y. Takabayashi, Y.Z. Khimyak, S. Margadonna, A. Tamai, M.J. Rosseinsky and K. Prassides, *Bulk superconductivity at 38 K in a molecular system*, Nature Materials **7**, 367 (2008)

[50] R. Nagarajan, C. Mazumdar, Z. Hossain, S.K. Dhar, K.V. Gopalakrishnan, L.C. Gupta, C. Godart, B.D. Padalia and R. Vijayaraghavan, *Bulk superconductivity at an elevated temperature* ($T_c \approx 12$ *K) in a nickel containing aloy system Y-Ni-B-C*, Physical Review Letters **72**, 274 (1994)

[51] R.J. Cava, H. Takagi, B. Batlogg, H.W. Zandbergen, J.J. Krajewski, W.F. Peck jr., R.B. van Dover, R.J. Felder, T. Siegrist, K. Mizuhashi, J.O. Lee, H. Eisaki, S.A. Carter and S. Uchida, *Superconductivity at 23 K in yttrium palladium boride carbide*, Nature **367**, 146 (1994)

[52] R.J. Cava, H. Takagi, H.W. Zandbergen, J.J. Krajewski, W.F. Peck jr., T. Siegrist, B. Batlogg, R.B. van Dover, R.J. Felder, K. Mizuhashi, J.O. Lee, H. Eisaki and S. Uchida, *Superconductivity in the quaternary intermetallic compounds* $LnNi_2B_2C$, Nature **367**, 252 (1994)

[53] T. Siegrist, H.W. Zandbergen, R.J. Cava, J.J. Krajewski and W.F. Peck jr., *The crystal structure of superconducting* $LuNi_2B_2C$ *and the related phase LuNiBC*, Nature **367**, 254 (1994)

[54] H.C. Ku, C.C. Lai, Y.B. You, J.H. Shieh and W.Y. Guan, *Superconductivity at 15 K in the metastable* $ScNi_2B_2C$ *compound*, Physical Review B **50**, 351 (1994)

[55] R.J. Cava, B. Batlogg, T. Siegrist, J.J. Krajewski, W.F. Peck jr., S. Carter, R.J. Felder, H. Takagi and R.B. van Dover, *Superconductivity in* RPt_2B_2C, Physical Review B **49**, 12384 (1994)

[56] C.C. Lai, M.S. Lin, Y.B. You and H.C. Ku, *Systematic variation of superconductivity for the quaternary borocarbide system* RNi_2B_2C *(R=Sc, Y, La, Th, U, or a lanthanide)*, Physical Review B **51**, 420 (1995)

[57] J. Nagamatsu, N. Nakagawa, T. Muranaka, Y. Zenitani and J. Akimitsu, *Superconductivity at 39 K in magnesium diboride*, Nature **410**, 63 (2001)

[58] Z.K. Tang, L. Zhang, N. Wang, X.X. Zhang, G.H. Wen, G.D. Li, J.N. Wang, C.T. Chan and P. Sheng, *Superconductivity in 4 Angstrom single-walled carbon nanotubes*, Science **292**, 2462 (2001)

[59] Y. Kamihara, T. Watanabe, M. Hirano and H. Hosono, *Iron-based layered superconductor* $La[O_{1-x}F_x]FeAs$ *(x = 0.05-0.12) with* $T_c = 26$ *K*, Journal of the American Chemical Society **130**, 3296 (2008)

[60] X.H. Chen, T. Wu, G. Wu, R.H. Liu, H. Chen and D.F. Fang, *Superconductivity at 43 K in* $SmFeAsO_{1-x}F_x$, Nature **453**, 761 (2008)

[61] G. Aschermann, E. Friederich, E. Justi and J. Kramer, *Supraleitfähige Verbindungen mit extrem hohen Sprungtemperaturen (NbH und NBN)*, Physikalische Zeitschrift **42**, 349 (1941) [The reported transition temperature is believed to be over-optimistic [62]. The more realistic value of 15 K was used in figure 2.2]

[62] G.F. Hardy and J.K. Hulm, *Superconducting silicides and germanides*, Physical Review **89**, 884 (1953)

[63] G.F. Hardy and J.K. Hulm, *The superconductivity of some transition metal compounds*, Physical Review **93**, 1004 (1954)

[64] J.R. Gavaler, *Superconductivity in Nb-Ge films above 22 K*, Applied Physics Letters **23**, 480 (1973)

[65] J.R. Gavaler, M.A. Janocko and C.K. Jones, *Preparation and properties of high-*T_c *Nb-Ge films*, Journal of Applied Physics **45**, 3009 (1974)

[66] C.W. Chu, P.H. Hor, R.L. Meng, L. Gao, Z.J. Huang and Y.Q. Wang, *Evidence for superconductivity above 40 K in the La-Ba-Cu-O compound system*, Physical Review Letters **58**, 405 (1987)

[67] C.W. Chu, P.H. Hor, R.L. Meng, L. Gao and Z.J. Huang, *Superconductivity at 52.5K in the lanthanum-barium-copper-oxide system*, Science **235**, 567 (1987)

[68] T.P. Orlando and K.A. Delin, *Foundations of applied superconductivity*, Addison-Wesley (1991)

[69] H. Goldstein, *Classical mechanics*, second edition, Addison-Wesley (1980)

[70] L.P. Gor'kov, Zh. Eksp. Teor. Fiz. **36**, 1918 (1959)

[71] B.S. Deaver jr. and W.M. Fairbank, *Experimental evidence for quantized flux in superconducting cylinders*, Physical Review Letters **7**, 43 (1961)

[72] V.V. Schmidt, *The physics of superconductors*, Springer-Verlag (1997)

[73] A.A. Abrikosov, Zh. Eksp. Teor. Fiz. **32**, 1442 (1957)

[74] B.D. Josephson, *Possible new effects in superconductive tunnelling*, Physics Letters **1**, 251 (1962)

[75] B.D. Josephson, *Supercurrents through barriers*, Advances in Physics **14**, 419 (1965)

[76] P.K. Hansma and G.I. Rochlin, *Josephson weak links: shunted-junction and mechanical-model results*, Journal of Applied Physics **43**, 4721 (1972)

[77] W.C. Stewart, *Current-voltage characteristics of Josephson junctions*, Applied Physics Letters **12**, 277 (1968)

[78] D.E. McCumber, *Effect of AC impedance on DC voltage-current characteristics of superconductor weak-link junctions*, Journal of Applied Physics **39**, 3113 (1968)

[79] M. Tinkham, *Introduction to superconductivity*, second edition, McGraw-Hill (1996)

[80] W.J. Johnson, *Nonlinear wave propagation on superconducting tunneling junctions*, Ph.D. Thesis, University of Wisconsin (1968)

[81] S.H. Strogatz, *Nonlinear dynamics and chaos: with applications to physics, biology, chemistry, and engineering*, Addison-Wesley (1994)

[82] V.N. Belykh, N.F. Pedersen and O.H. Soerensen, *Shunted-Josephson-junction model. I. The autonomous case*, Physical Review B **16**, 4853 (1977)

[83] F.M.A. Salam and S.S. Sastry, *Dynamics of the forced Josephson junction circuit: the regions of chaos*, IEEE Transactions on Circuits and Systems **32**, 784 (1985)

[84] A. Barone and G. Paternò, *Physics and applications of the Josephson effect*, John Wiley & Sons (1982)

[85] J.E. Lenz, *A review of magnetic sensors*, Proceedings of the IEEE **78**, 973 (1990)

[86] A. Troeman, *NanoSQUID magnetometers and high resolution scanning SQUID microscopy*, Ph.D. Thesis, University of Twente (2007)

[87] J. Clarke and A.I. Braginski, *The SQUID handbook vol. I fundamentals and technology of SQUIDs and SQUID systems*, Wiley-VCH Verlag (2004)

[88] J. Clarke and A.I. Braginski, *The SQUID handbook vol. II applications of SQUIDs and SQUID systems*, Wiley-VCH Verlag (2006)

[89] R. Kleiner, D. Koelle, F. Ludwig and J. Clarke, *Superconducting quantum interference devices: state of the art and applications*, Proceedings of the IEEE **92**, 1534 (2004)

[90] H. Itozaki, *SQUID application research in Japan*, Superconducting Science and Technology **16**, 1340 (2003)

[91] C.D. Tesche and J. Clarke, *DC SQUID: noise and optimization*, Journal of Low Temperature Physics **29**, 301 (1977)

[92] R.H. Koch, J.R. Rozen, P. Wöltgens, T. Picunko, W.J. Goss, D. Gambrel, D. Lathrop, R. Wiegert and D. Overway, *High performance superconducting quantum interference device feedback electronics*, Review of Scientific Instruments **67**, 2968 (1996)

[93] H. Hilgenkamp, *High-T_c DC SQUID magnetometers*, Ph.D. Thesis, University of Twente (1995)

[94] D.B. Tuckerman and J.H. Magerlein, *Resonances in symmetric Josephson interferometers*, Applied Physics Letters **37**, 241 (1980) [addendum: Applied Physics Letters **38**, 581 (1981)]

[95] G. Paternò, A.M. Cucolo and G. Modestino, *Resonant modes in Nb baselayer interferometers with two Josephson junctions*, Journal of Applied Physics **57**, 1680 (1985)

[96] H. Hilgenkamp, *Pi-phase shift Josephson structures*, Superconductor Science and Technology **21**, 034011 (2008)

[97] V.V. Ryazanov, V.A. Oboznov, A.Y. Rusanov, A.V. Veretennikov, A.A. Golubov and J. Aarts, *Coupling of two superconductors through a ferromagnet: evidence for a π junction*, Physical Review Letters **86**, 2427 (2001)

[98] V.V. Ryazanov, V.A. Oboznov, A.V. Veretennikov and A.Y. Rusanov, *Intrinsically frustrated superconducting array of superconductor-ferromagnet-superconductor π junctions*, Physical Review B **65**, 020501 (2001)

[99] T. Kontos, M. Aprili, J. Lesueur, F. Genêt, B. Stephanidis and R. Boursier, *Josephson junction through a thin ferromagnetic layer: negative coupling*, Physical Review Letters **89**, 137007 (2002)

[100] J.J.A. Baselmans, A.F. Morpurgo, B.J. van Wees and T.M. Klapwijk, *Reversing the direction of the supercurrent in a controllable Josephson junction*, Nature **397**, 43 (1999)

[101] J.B. Majer, J.R. Butcher and J.E. Mooij, *Simple phase bias for superconducting circuits*, Applied Physics Letters **80**, 3638 (2002)

[102] D. Balashov, B. Dimov, M. Khabipov, T. Ortlepp, D. Hagedorn, A.B. Zorin, F.-I. Buchholz, F.H. Uhlmann and J. Niemeyer, *Passive phase shifter for superconducting Josephson circuits*, IEEE Transactions on Applied Superconductivity **17**, 142 (2007)

[103] D.J. Van Harlingen, *Phase-sensitive tests of the symmetry of the pairing state in the high-temperature superconductors - evidence for $d_{x^2-y^2}$ symmetry*, Review of Modern Physics **67**, 515 (1995)

[104] C.C. Tsuei and J.R. Kirtley, *Pairing symmetry in cuprate superconductors*, Review of Modern Physics **72**, 969 (2000)

[105] D.J. Griffiths, *Introduction to quantum mechanics*, second edition, Pearson Prentice Hall (2005)

[106] S. Chakravarty, A. Sudbø and P.W. Anderson, *Interlayer tunneling and gap anisotropy in high-temperature superconductors*, Science **261**, 337 (1993)

[107] C.C. Tsuei, J.R. Kirtley, C.C. Chi, L.S. Yu-Jahnes, A. Gupta, T. Shaw, J.Z. Sun and M.B. Ketchen, *Pairing symmetry and flux quantization in a tricrystal superconducting ring of $YBa_2Cu_3O_{7-\delta}$*, Physical Review Letters **73**, 593 (1994)

[108] J.R. Kirtley, C.C. Tsuei, M. Rupp, J.Z. Sun, L.S. Yu-Jahnes, A. Gupta, M.B. Ketchen, K.A. Moler and M. Bhushan, *Direct imaging of integer and half-integer Josephson vortices in high-*T_c *grain boundaries*, Physical Review Letters **76**, 1336 (1996)

[109] J.R. Kirtley, C.C. Tsuei and K.A. Moler, *Temperature dependence of the half-integer magnetic flux quantum*, Science **285**, 1373 (1999)

[110] V.G. Kogan, J.R. Clem and J.R. Kirtley, *Josephson vortices at tricrystal boundaries*, Physical Review B **61**, 9122 (2000)

[111] A. Sugimoto, T. Yamaguchi and I. Iguchi, *Temperature dependence of half flux quantum in* $YBa_2Cu_3O_{7-y}$ *tricrystal thin film observed by scanning SQUID microscopy*, Physica C **367**, 28 (2002)

[112] D.A. Wollman, D.J. Van Harlingen, W.C. Lee, D.M. Ginsberg and A.J. Leggett, *Experimental determination of the superconducting pairing state in YBCO from the phase coherence of YBCO-Pb DC SQUIDs*, Physical Review Letters **71**, 2134 (1993)

[113] D.A. Wollman, D.J. Van Harlingen, J. Giapintzakis and D.M. Ginsberg, *Evidence for* $d_{x^2-y^2}$ *pairing from the magnetic field modulation of* $YBa_2Cu_3O_7$*-Pb Josephson junctions*, Physical Review Letters **74**, 797 (1995)

[114] D.A. Brawner and H.R. Ott, *Evidence for an unconventional superconducting order parameter in* $YBa_2Cu_3O_{6.9}$, Physical Review B **50**, 6530 (1994)

[115] A. Mathai, Y. Gim, R.C. Black, A. Amar and F.C. Wellstood, *Experimental proof of a time-reversal-invariant order parameter with a* π *shift in* $YBa_2Cu_3O7-\delta$, Physical Review Letters **74**, 4523 (1995)

[116] H. Hilgenkamp, Ariando, H.-J.H. Smilde, D.H.A. Blank, G. Rijnders, H. Rogalla, J.R. Kirtley and C.C. Tsuei, *Ordering and manipulation of the magnetic moments in large-scale superconducting* π*-loop arrays*, Nature **422**, 50 (2003)

[117] A.P. Malozemoff, J. Mannhart and D. Scalapino, *High-temperature cuprate superconductors get to work*, Physics Today **58**, 41 (2005)

[118] J.R. Kirtley, C.C. Tsuei, Ariando, H.J.H. Smilde and H. Hilgenkamp, *Antiferromagnetic ordering in arrays of superconducting* π*-rings*, Physical Review B **72**, 214521 (2005)

[119] J.-Y. Genoud, T. Graf, A. Junod, D. Sanchez, G. Triscone and J. Muller, *Preparation, resistivity, magnetic properties and specific heat of the 95 K superconductor* $YBa_2Cu_{3.5}O_{7.5+x}$ *("247")*, Physica C **177**, 315 (1991)

[120] G. Triscone, A.F. Khoder, C. Opagiste, J.-Y. Genoud, T. Graf, E. Janod, T. Tsukamoto, M. Couach, A. Junod and J. Muller, *Reversible magnetization below* T_c *in high-quality superconducting ceramics*, Physica C **224**, 263 (1994)

[121] I.L. Landau and H.R. Ott, *Temperature dependence of the upper critical field of high-*T_c *superconductors from isothermal magnetization data. Application to polycrystalline samples and ceramics*, Physica C **385**, 544 (2003)

[122] K. Yvon and M. François, *Crystal structures of high-T_c oxides*, Zeitschrift für Physik B **76**, 413 (1989)

[123] J.D. Jorgensen, B.W. Veal, A.P. Paulikas, L.J. Nowicki, G.W. Crabtree, H. Claus and W.K. Kwok, *Structural properties of oxygen-deficient $YBa_2Cu_3O_{7-\delta}$*, Physical Review B **41**, 1863 (1990) [erratum: Physical Review B **42**, 995 (1990)]

[124] R.J. Cava, B. Batlogg, C.H. Chen, E.A. Rietman, S.M. Zahurak and D. Werder, *Single-phase 60-K bulk superconductor in annealed $Ba_2Cu_3O_{7-\delta}$(0.3< δ <0.4) with correlated oxygen vacancies in the Cu-O chains*, Physical Review B **36**, 5719 (1987)

[125] J.L. Tallon, C. Bernhard, H. Shaked, R.L. Hitterman and J.D. Jorgensen, *Generic superconducting phase behavior in high-T_c cuprates: T_c variation with hole concentration in $YBa_2Cu_3O_{7-\delta}$*, Physical Review B **51**, 12911 (1995)

[126] N.M. Strickland, A. Semwal, G.V.M. Williams, D.T. Verebelyi and W. Zhang, *Optimizing the doping state of YBCO coated superconductors*, Superconductor Science and Technology **17**, S473 (2004)

[127] R.J. Cava, A.W. Hewat, B. Batlogg, M. Marezio, K.M. Rabe, J.J. Krajewski, W.F. Peck jr. and L.W. Rupp jr., *Structural anomalies, oxygen ordering and superconductivity in oxygen deficient $Ba_2YCu_3O_x$*, Physica C **165**, 419 (1990)

[128] E. Dagotto, *Correlated electrons in high-temperature superconductors*, Review of Modern Physics **66**, 763 (1994)

[129] Z. Trajanovic, R. Shreekala, M. Rajeswari, I. Takeuchi, C.J. Lobb, T. Venkatesan, E. Bauer and F. Bridges, *Controlling the dopant incorporation in a-axis oriented Co doped YBCO thin films*, IEEE Transactions on Applied Superconductivity **7**, 2146 (1997)

[130] M. Velter-Stefanescu, A. Totovana and V. Sandu, *Microwave spectroscopy in YBCO superconductors: influence of neutron irradiation on the 123 phase*, Journal of Superconductivity **11**, 327 (1998)

[131] X.S. Wu and J. Gao, *Comparison of superconductivity-depression for lanthanum and potassium replacing barium in $Yba_2Cu_3O_y$ ceramic cuprate*, Physica C **329**, 285 (2000)

[132] D.H. Ha, S. Byon and K.W. Lee, *On the role of apical oxygen in the charge transfer of YBCO superconductors*, Physica C **340**, 243 (2000)

[133] M. Murugesan, H. Obara, A. Sawa, S. Kosaka, Y. Nakagawa, J.C. Nie and H. Yamasaki, *Microwave surface resistance of under doped Co substituted YBCO films*, Physica C **400**, 65 (2003)

[134] S. Kambe and O. Ishii, *Correlation between T_c, in-plane Cu-O-Cu bond length, and buckling of the CuO_2 plane in cuprate superconductors*, Physica C **341-348**, 555 (2000)

[135] R. D. Shannon, *Revised effective ionic radii and systematic studies of interatomic distances in halides and chalcogenides*, Acta Crystallographica Section A **32**, 751 (1976)

[136] J. Halbritter, *On the oxidation and on the superconductivity of niobium*, Applied Physics A **43**, 1 (1987)

[137] H.J.H. Smilde, *Josephson contacts between high-T_c and low-T_c superconductors*, Ph.D. Thesis, University of Twente (2001)

[138] T. Usagawa, J. Wen, Y. Ishimaru, S. Koyama, T. Utagawa and Y. Enomoto, *Stability of ultrasmooth surface morphology of (110) $YBa_2Cu_3O_{7-\delta}$ homoepitaxial films and Nb/Au/(110) $YBa_2Cu_3O_{7-\delta}$ junctions*, Applied Physics Letters **72**, 3202 (1998)

[139] Q.Y. Ma, M.T. Schmidt, L.S. Weinman, E.S. Yang, S.M. Sampere and S.-W. Chan, *Characterization of bilayer-metal contacts to high T_c superconducting films*, Journal of Vacuum Science and Technology A **9**, 390 (1991)

[140] J.G. Wen, N. Koshizuka, S. Tanaka, T. Satoh, M. Hidaka and S. Tahara, *Atomic structure and composition of the barrier in the modified interface high-T_c Josephson junction studied by transmission electron microscopy*, Applied Physics Letters **75**, 2470 (1999)

[141] J.G. Wen, T. Satoh, M. Hidaka, S. Tahara, N. Koshizuka and S. Tanaka, *TEM study on the microstructure of the modified interface junction*, Physica C **337**, 249 (2000)

[142] T. Satoh, J.G. Wen, M. Hidaka, S. Tahara, N. Koshizuka and S. Tanaka, *High-temperature superconducting edge junctions with modified interface barriers*, Superconductor Science and Technology **13**, 88 (2000)

[143] H.-J.H. Smilde, H. Hilgenkamp, G. Rijnders, H. Rogalla and D.H.A. Blank, *Enhanced transparency ramp-type Josephson contacts through interlayer deposition*, Applied Physics Letters **80**, 4579 (2002)

[144] Y. Yamada, J. Kawashima, J.-G. Wen, Y. Niiori and I. Hirabayashi, *Evaluation of thermal expansion coefficient of twinned $YBa_2Cu_3O_{7-\delta}$ film for prediction of crack formation on various substrates*, Japanese Journal of Applied Physics **39**, 1111 (2000)

[145] G. Koster, B.L. Kropman, G.J.H.M. Rijnders, D.H.A. Blank and H. Rogalla, *Quasi-ideal strontium titanate crystal surfaces through formation of strontium hydroxide*, Applied Physics Letters **73**, 2920 (1998)

[146] H.-U. Krebs and O. Bremert, *Pulsed laser deposition of thin metallic alloys*, Applied Physics Letters **62**, 2341 (1993)

[147] J.G. Lunney, *Pulsed laser deposition of metal and metal multilayer films*, Applied Surface Science **86**, 79 (1995)

[148] S. Fähler, M. Störmer and H.U. Krebs, *Origin and avoidance of droplets during laser ablation of metals*, Applied Surface Science **109-110**, 433 (1997)

[149] T.J. Jackson and S.B. Palmer, *Oxide superconductor and magnetic thin film deposition by pulsed laser ablation: a review*, Journal of Physics D: Applied Physics **27**, 1581 (1994)

[150] Ariando, *Josephson junction arrays with d-wave-induced π-phase-shifts*, Ph.D. Thesis, University of Twente (2005)

[151] T. Thijssen, *Submicron Josephson structures combining high- and low-T_c superconductors*, M.Sc. Thesis, University of Twente (2008)

[152] M.R. Beasley, D. Lew and R.B. Laughlin, *Time-reversal symmetry breaking in superconductors: a proposed experimental test*, Physical Review B **49**, 12330 (1994)

[153] T.-K. Ng and C.M. Varma, *Experimental signatures of time-reversal-violating superconductors*, Physical Review B **70**, 054514 (2004)

[154] Q.P. Li, B.E.C. Koltenbah and R. Joynt, *Mixed s-wave and d-wave superconductivity in high-T_c systems*, Physical Review B **48**, 437 (1993)

[155] C. O'Donovan and J.P. Carbotte, *s- and d-wave mixing in high-T_c superconductors*, Physical Review B **52**, 16208 (1995)

[156] C. O'Donovan and J.P. Carbotte, *In plane anisotropy in optimally doped $YBa_2Cu_3O_{6.95}$*, Journal of Low Temperature Physics **105**, 495 (1996)

[157] K. Maki and M.T. Beal-Monod, *Anisotropic d + s wave superconductivity*, Physics Letters A **208**, 365 (1995)

[158] M.T. Beal-Monod and K. Maki, *Low temperature thermal conductivity in d + s wave superconductivity*, Physica C **265**, 309 (1996)

[159] E. Polturak, G. Koren, D. Cohen and E. Aharoni, *Measurements of the anisotropy and temperature dependence of the in-plane energy gap in $YBa_2Cu_3O_{7-\delta}$ using Andreev reflections*, Physical Review B **47**, 5270 (1993)

[160] A. Engelhardt, R. Dittmann and A.I. Braginski, *Subgap conductance features of $YBa_2Cu_3O_{7-\delta}$ edge Josephson junctions*, Physical Review B **59**, 3815 (1999)

[161] J.Y.T. Wei, N.-C. Yeh, D.F. Garrigus and M. Strasik, *Directional tunneling and Andreev reflection on $YBa_2Cu_3O_{7-\delta}$ single crystals: predominance of d-wave pairing symmetry verified with the generalized Blonder, Tinkham, and Klapwijk theory*, Physical Review Letters **81**, 2542 (1998)

[162] D.H. Lu, D.L. Feng, N.P. Armitage, K.M. Shen, A. Damascelli, C. Kim, F. Ronning, Z.-X. Shen, D.A. Bonn, R. Liang, W.N. Hardy, A.I. Rykov and S.Tajima, *Superconducting gap and strong in-plane anisotropy in untwinned $YBa_2Cu_3O_{7-\delta}$*, Physical Review Letters **86**, 4370 (2001)

[163] M.F. Limonov, A.I. Rykov, S. Tajima and A. Yamanaka, *Raman scattering study on fully oxygenated $YBa_2Cu_3O_7$ single crystals: x-y anisotropy in the superconductivity-induced effects*, Physical Review Letters **80**, 825 (1998)

[164] M.F. Limonov, A.I. Rykov, S. Tajima and A. Yamanaka, *Superconductivity-induced effects on phononic and electronic Raman scattering in twin-free $YBa_2Cu_3O_{7-x}$ single crystals*, Physical Review B **61**, 12412 (2000)

[165] H. Aubin, K. Behnia, M. Ribault, R. Gagnon and L. Taillefer, *Angular position of nodes in the superconducting gap of YBCO*, Physical Review Letters **78**, 2624 (1997)

[166] H.J.H. Smilde, A.A. Golubov, Ariando, G. Rijnders, J.M. Dekkers, S. Harkema, D.H.A. Blank, H. Rogalla and H. Hilgenkamp, *Admixtures to d-wave gap symmetry in untwinned* $YBa_2Cu_3O_7$ *superconducting films measured by angle-resolved electron tunneling*, Physical Review Letters **95**, 257001 (2005)

[167] J.B. Ketterson and S.N. Song, *Superconductivity*, Cambridge University Press (1999)

[168] D.J. van Harlingen, J.E. Hilliard, B.L.T. Plourde and B.D. Yanoff, *Extending SQUID interferometry beyond the cuprates and beyond d-wave symmetry*, Physica C **317-318**, 410 (1999)

[169] Y. Gim, A. Mathai, R.C. Black, A. Amar and F.C. Wellstood, *Symmetry of the phase of the order parameter in* $YBa_2Cu_3O_{7-\delta}$, Journal de Physique I **6**, 2299 (1996)

[170] J.R. Kirtley, C.C. Tsuei, Ariando, C.J.M. Verwijs, S. Harkema and H. Hilgenkamp, *Angle-resolved phase-sensitive determination of the in-plane gap symmetry in* $YBa_2Cu_3O_{7-\delta}$, Nature Physics **2**, 190 (2006) [erratum: Nature Physics **2**, 353 (2006)]

[171] M. Kamon, M.J. Tsuk and J.K. White, *FastHenry: a multipole-accelerated 3-D inductance extraction program*, IEEE Transactions on Microwave Theory and Techniques **42**, 1750 (1994)

[172] D. Schweitzer, T. Bollmeier, B. Stritzker and B. Rauschenbach, *Twinning of* $YBa_2Cu_3O_7$ *thin films on different substrates*, Thin Solid Films **280**, 147 (1996)

[173] J. Brötz and H. Fuess, *Detwinning in* $YBa_2Cu_3O_{7-\delta}$ *films on vicinal* $SrTiO_3$ *(001) due to anisotropic strain at the interface*, Physica C **339**, 75 (2000)

[174] J.M. Dekkers, G. Rijnders, S. Harkema, H.J.H. Smilde, H. Hilgenkamp, H. Rogalla and D.H.A. Blank, *Monocrystalline* $YBa_2Cu_3O_{7-x}$ *thin films on vicinal* $SrTiO_3$ *(001) substrates*, Applied Physics Letters **83**, 5199 (2003)

[175] J.R. Kirtley, M.B. Ketchen, K.G. Stawiasz, J.Z. Sun, W.J. Gallagher, S.H. Blanton and S.J. Wind, *High-resolution scanning SQUID microscope*, Applied Physics Letters **66**, 1138 (1995)

[176] J.R. Kirtley and M.B. Ketchen, *Design and applications of a scanning SQUID microscope*, IBM Journal of Research and Development **39**, 655 (1995)

[177] M. Sigrist and T.M. Rice, *Paramagnetic effect in high* T_c *superconductors - a hint for d-wave superconductivity*, Journal of the Physical Society of Japan **61**, 4283 (1992)

[178] J.H. Ngai, W.A. Atkinson and J.Y.T. Wei, *Tunneling spectroscopy of c-axis* $Y_{1-x}Ca_xBa_2Cu_3O_{7-\delta}$ *thin-film superconductors*, Physical Review Letters **98**, 177003 (2007)

[179] C.J. Halboth and W. Metzner, *d-wave superconductivity and Pomeranchuk instability in the two-dimensional Hubbard model*, Physical Review Letters **85**, 5162 (2000)

[180] K.K. Likharev, O.A. Mukhanov and V.K. Semenov, *Resistive single flux quantum logic for the Josephson-junction technology*, SQUID '85, 1103 (1985)

[181] O.A. Mukhanov, V.K. Semenov and K.K. Likharev, *Ultimate performance of the RSFQ logic circuits*, IEEE Transactions on Magnetics **23**, 759 (1987)

[182] K.K. Likharev and V.K. Semenov, *RSFQ logic/memory family: a new Josephson-junction technology for sub-terahertz-clock-frequency digital systems*, IEEE Transactions on Applied Superconductivity **1**, 3 (1991)

[183] F. Furuta, K. Saitoh and K. Takagi, *High-speed operation of demultiplexer up to 56 GHz*, IEEE Transactions on Applied Superconductivity **13**, 567 (2003)

[184] O.A. Mukhanov, D. Kirichenko, I.V. Vernik, T.V. Filippov, A. Kirichenko, R. Webber, V. Dotsenko, A. Talalaevskii, J.C. Tang, A. Shau, P. Shevchenko, R. Miller, S.B. Kaplan, S. Sarwana and D. Gupta, *Superconductor digital-RF receiver systems*, IEICE Transactions on Applied Superconductivity **E91-C**, 306 (2008)

[185] Y. Yamanashi, M. Tanaka, A. Akimoto, H. Park, Y. Kamiya, N. Irie, N. Yoshikawa, A. Fujimaki, H. Terai and Y. Hashimoto, *Design and implementation of a pipelined bit-serial SFQ microprocessor, CORE1β*, IEEE Transactions on Applied Superconductivity **17**, 474 (2007)

[186] M. Tanaka, Y. Yamanashi, N. Irie, H.-J. Park, S. Iwasaki, K. Takagi, K. Taketomi, A. Fujimaki, N. Yoshikawa, H. Terai and S. Yorozu, *Design and implementation of a pipelined 8 bit-serial single-flux-quantum microprocessor with cache memories*, Superconductor Science and Technology **20**, S305 (2007)

[187] H. Akaike, T. Yamada, A. Fujimaki, S. Nagasawa, K. Hinode, T. Satoh, Y. Kitagawa and M. Hidaka, *Demonstration of a 120 GHz single-flux-quantum shift register circuit based on a 10 kA cm^{-2} Nb process*, Superconductor Science and Technology **19**, (2006)

[188] W. Chen, A.V. Rylyakov, V. Patel, J.E. Lukens and K.K. Likharev, *Rapid single flux quantum T-flip flop operating up to 770 GHz*, IEEE Transactions on Applied Superconductivity **9**, 3212 (1999)

[189] M. Nisenoff, *Bringing superconductor digital technology to the market place*, IEICE Transactions on Applied Superconductivity **E91-C**, 252 (2008)

[190] T. van Duzer, *Superconductor digital electronics past, present, and future*, IEICE Transactions on Applied Superconductivity **E91-C**, 260 (2008)

[191] H.J.M. ter Brake, F.-I. Buchholz, G. Burnell, T. Claeson, D. Crété, P. Febvre, G.J. Gerritsma, H. Hilgenkamp, R. Humphreys, Z. Ivanov, W. Jutzi, M.I. Khabipov, J. Mannhart, H.-G. Meyer, J. Niemeyer, A. Ravex, H. Rogalla, M. Russo, J. Satchell, M. Siegel, H. Töpfer, F.H. Uhlmann, J.-C. Villégier, E. Wikborg, D. Winkler and A.B. Zorin, *SCENET roadmap for superconductor digital electronics*, Physica C **439**, 1 (2006)

[192] E.S. Fang and T. van Duzer, *A Josephson integrated circuit simulator (JSIM) for superconductive electronics application*, extended abstracts of the 1989 International Superconductive Electronics Conference, 407 (1989)

[193] T. Ortlepp, Ariando, O. Mielke, C.J.M. Verwijs, K.F.K. Foo, H. Rogalla, F.H. Uhlmann and H. Hilgenkamp, *Flip-flopping fractional flux quanta*, Science **312**, 1495 (2006)

[194] T. Ortlepp, Ariando, O. Mielke, C.J.M. Verwijs, K.F.K. Foo, A. Andreski, H. Rogalla, F.H. Uhlmann and H. Hilgenkamp, *RSFQ circuitry using intrinsic π-phase shifts*, IEEE Transactions on Applied Superconductivity **17**, 659 (2007)

[195] S.V. Polonsky, V.K. Semenov and D.F. Schneider, *Transmission of single-flux-quantum pulses along superconducting microstrip lines*, IEEE Transactions on Applied Superconductivity **3**, 2598 (1993)

[196] H.J.H. Smilde, Ariando, D.H.A. Blank, G.J. Gerritsma, H. Hilgenkamp and H. Rogalla, *d-wave-induced Josephson current counterflow in $YBa_2Cu_3O_7$/Nb zigzag junctions*, Physical Review Letters **88**, 057004 (1992)

[197] Ariando, D. Darminto, H.-J.H. Smilde, V. Leca, D.H.A. Blank, H. Rogalla and H. Hilgenkamp, *Phase-sensitive order parameter symmetry test experiments utilizing $Nd_{2-x}Ce_xCuO_{4-y}$/Nb zigzag junctions*, Physical Review Letters **94**, 167001 (2005)

[198] T. Kato and M. Imada, *Vortices and quantum tunneling in current-biased 0-π-0 Josephson junctions of d-wave superconductors*, Journal of the Physical Society of Japan **66**, 1445 (1997)

[199] J.H. Xu, J.H. Miller jr. and C.S. Ting, *π-vortex state in a long 0-π Josephson junction*, Physical Review B **51**, 11958 (1995)

[200] D.-X. Chen and A. Hernando, *Magnetization of symmetric 0-π Josephson junctions*, Physical Review B **50**, 10107 (1994)

[201] A.B. Kuklov, V.S. Boyko and J. Malinsky, *Instability in the current-biased 0-π Josephson junction*, Physical Review B **51**, 11965 (1995) [erratum: Physical Review B **55**, 11878 (1997)]

[202] E. Goldobin, D. Koelle and R. Kleiner, *Semifluxons in long Josephson 0-π-junctions*, Physical Review B **66**, 100508 (2002)

[203] A. Buzdin and A.E. Koshelev, *Periodic alternating 0- and π-junction structures as realization of φ-Josephson junctions*, Physical Review B **67**, 220504 (2003)

[204] E. Goldobin, D. Koelle and R. Kleiner, *Ground states and bias-current-induced rearrangement of semifluxons in 0-π long Josephson junctions*, Physical Review B **67**, 224515 (2003)

[205] H. Susanto, S.A. van Gils, T.P.P. Visser, Ariando, H.J.H. Smilde and H. Hilgenkamp, *Static semifluxons in a long Josephson junction with π-discontinuity points*, Physical Review B **68**, 104501 (2003)

[206] A. Zenchuk and E. Goldobin, *Analysis of ground states of 0-π long Josephson junctions*, Physical Review B **69**, 024515 (2004)

[207] E. Goldobin, A. Sterck, T. Gaber, D. Koelle and R. Kleiner, *Dynamics of semifluxons in Nb long Josephson 0-π junctions*, Physical Review Letters **92**, 057005 (2004)

[208] E. Goldobin, N. Stefanakis, D. Koelle and R. Kleiner, *Fluxon-semifluxon interaction in an annular long Josephson 0-π junction*, Physical Review B **70**, 094520 (2004)

[209] E. Goldobin, D. Koelle and R. Kleiner, *Ground state of one and two fractional vortices in long Josephson 0-κ junctions*, Physical Review B **70**, 174519 (2004)

[210] H. Susanto and S.A. van Gils, *Instability of a lattice semifluxon in a current-biased 0-π array of Josephson junctions*, Physical Review B **69**, 092507 (2004)

[211] H. Susanto and S.A. van Gils, *Semifluxons with a hump in a 0-π Josephson junction*, Physica C **408-410**, 579 (2004)

[212] E. Goldobin, K. Vogel, O. Crasser, R. Walser, W.P. Schleich, D. Koelle and R. Kleiner, *Quantum tunneling of semifluxons in a 0-π-0 long Josephson junction*, Physical Review B **72**, 054527 (2005)

[213] H. Susanto, *Josephson junctions with phase shifts*, Ph.D. Thesis, University of Twente (2006)

[214] T. van Duzer and C.W. Turner, *Principles of superconductive devices and circuits*, second edition, Prentice Hall PTR (1999)

[215] J.A. Boschker, *Manipulation and on-chip readout of fractional flux quanta*, M.Sc. Thesis, University of Twente (2006)

[216] J.M. Jaycox and M.B. Ketchen, *Planar coupling scheme for ultra low noise DC SQUIDs*, IEEE Transactions on Magnetics **17**, 400 (1981)

[217] H.-M. Christen, J. Mannhart, E.J. Williams and C. Gerber, *Dielectric properties of sputtered $SrTiO_3$ films*, Physical Review B **49**, 12095 (1994)

[218] H.H. Zappe, *Minimum current and related topics in Josephson tunnel junction devices*, Journal of Applied Physics **44**, 1371 (1973)

[219] P.F. Byrd and M.D. Friedman, *Handbook of elliptic integrals for engineers and scientists*, second edition, Springer-Verlag (1971)

STELLINGEN

Behorende bij het proefschrift

Fractional Flux Quanta in High-T_c/Low-T_c Superconducting Structures

1. Het gebruik van niet-genormaliseerde basisfuncties voor het beschrijven van ordeparametersymmetrieën met mengvormen is als appels met peren vergelijken
   (Hoofdstuk 3 van dit proefschrift)
2. De ordeparametersymmetrie van de cupraatsupergeleider $YBa_2Cu_3O_{7-\delta}$ bevat een s-wave component van tenminste 9% en bevat geen complexe mengvormen
   (Hoofdstuk 5 van dit proefschrift)
3. Het toepassen van π-faseverschuivingen in supergeleidende digitale electronica biedt significante voordelen voor de ontwerp-, realisatie- en operatiefase van circuits
   (Hoofdstuk 6 van dit proefschrift)
4. Een on-chip aandrijving en uitlezing van de flux-toestand in hoekjuncties is cruciaal voor de integratie van dergelijke elementen in supergeleidende electronica
   (Hoofdstuk 7 van dit proefschrift)
5. Een vrouw die door het glazen plafond wil breken kan maar beter de broek aantrekken
6. Het advies “Luister niet naar andermans adviezen” is logischerwijs ongeldig
7. Dat duurzame energie tegenwoordig een *hot topic* is heeft niet zozeer te maken met *global warming* maar veeleer met economische en politieke motieven
8. Het is niet een gebrek aan vertrouwen, maar juist een teveel aan vertrouwen geweest dat heeft geleid tot de crisis in de bancaire sector
9. Ongewenste intimiteiten zijn altijd door tenminste één partij gewenst
10. Mensen die bewust niet aan hypes deelnemen baseren hun keuzes op de keuzes van anderen en vertonen derhalve indirect alsnog kuddegedrag

Deze stellingen worden verdedigbaar geacht en zijn als zodanig goedgekeurd door de promotor, prof. dr. ir. J.W.M. Hilgenkamp

C.J.M. Verwijs
25 juni 2009